ADVANCED FIBRE GRATINGS FABRICATED IN STANDARD AND INFRARED GLASS FIBRES BY ULTRAVIOLET AND NEAR-INFRARED-FEMTOSECOND LASERS

RUI SUO

Doctor of Philosophy

ASTON UNIVERSITY

September 2009

ASTON UNIVERSITY

ADVANCED FIBRE GRATINGS FABRICATED IN STANDARD AND INFRARED GLASS FIBRES BY ULTRAVIOLET AND NEAR-INFRARED-FEMTOSECOND LASERS

Rui Suo
Doctor of Philosophy
September 2009

In this thesis, I describe studies on fabrication, spectral characteristics and applications of tilted fibre gratings (TFGs) with small, large and 45° tilted structures and novel developments in fabrication of fibre Bragg gratings (FBGs) and long period gratings (LPGs) in normal silica and mid-infrared (mid-IR) glass fibres using near-IR femtosecond laser.

One of the major contributions presented in this thesis is the systematic investigation of structures, inscription methods and spectral, polarisation dependent loss (PDL) and thermal characteristics of TFGs with small (<45°), large (>45°) and 45° tilted structures. I have experimentally characterised TFGs, obtaining relationships between the radiation angle, central wavelength of the radiation profile, Bragg resonance and the tilt angle, which are consistent with theoretical simulation based on the mode-coupling theory. Furthermore, thermal responses have been measured for these three types of TFGs, showing the transmission spectra of large and 45° TFGs are insensitive to the temperature change, unlike the normal and small angle tilted FBGs.

Based on the distinctive optical properties, TFGs have been developed into interrogation system and sensors, which form the other significant contributions of the work presented in this thesis. The 10°-TFG based 800nm WDM interrogation system can function not just as an in-fibre spectrum analyser but also possess refractive index sensing capability. By utilising the unique polarisation properties, the 81°-TFG based sensors are capable of sensing the transverse loading and twisting with sensitivities of 2.04μW/(kg/m) and 145.90μW/rad, repectively.

The final but the most important contribution from the research work presented in this thesis is the development of novel grating inscription techniques using near-IR femtosecond laser. A number of LPGs and FBGs were successfully fabricated in normal silica and mid-IR glass fibres using point-by-point and phase-mask techniques. LPGs and 1st and 2nd order FBGs have been fabricated in these mid-IR glass fibres showing resonances covering the wavelength range from 1200 to 1700nm with the strengths up to 13dB. In addition, the thermal and strain sensitivities of these gratings have been systematically investigated. All the results from these initial but systematic works will provide useful function characteristics information for future fibre grating based devices and applications in mid-IR range.

Key words: fibre Bragg grating, tilted fibre grating, optical fibre sensor, femtosecond laser inscription, mid-infrared glass fibre

ACKNOWLEDGMENTS

Firstly of all, I would like to express my gratitude to my supervisor Prof Lin Zhang, who offered me a great opportunity to research in the field of optical fibre grating technology and the guidance throughout my time at Aston University. More importantly, her enthusiasm for science and tireless attention to the research work motivated me in the past years and will inspire me in future. I would like to extend my gratitude to Prof Ian Bennion for his recommendation of ORS scholarship. I also would like to thank Prof Shulian Zhang, Prof Yan Li in Tsinghua University and Dr Fang Xie in Beijing Jiaotong University, who recommended me as a Ph.D. candidate to Aston University.

I would like to thank Dr Xianfeng Chen and Dr Kaiming Zhou, who have helped me to find the way around the laboratory, master the fibre grating fabrication techniques and understand the theories on optical fibre gratings.

I would like to thank Prof Animesh Jha, Dr Joris Lousteau, Mr Xin Jiang in the University of Leeds and Prof Ajoy K Kar, Dr Henry T Bookey, Dr James S Barton, Dr Bill Macpherson, Ms Hongxia Li at Heriot-Watt University for the countless discussions and fruitful collaborations, which are particularly helpful for my studies on fibre grating inscription using femtosecond laser.

I would like to thank Dr Xuewen Shu, Dr Wei Zhang, Dr Yichang Lai, Dr Thomas Allsop, Mr Mykhaylo Dubov, Dr Andrey Okhrimchuk, Mr Chengbo Mou and Ms Hongyan Fu for their ideas, useful discussions and helps throughout my Ph.D. programme. I also would like to thank Dr Kate Sugden, Ms Pouneh Saffari, Mr Edward Davies and Mr Terence Broderick who helped and supported me during my study at Aston University.

Particularly, I am very grateful to Mr Bert Biggs for his great help, without him the labs could not run so smoothly. My thanks also go to Mrs Helen Yard and Ms Yuen Chu for their kind support during my Ph.D programme. Overall, I would like to thank and congratulate everybody from the Photonics Research Group, who made such a great, intuitive and facilitated place to work and study.

Finally, I acknowledge the project studentship awarded from the Engineering and Physical Sciences Research Council (EPSRC), which supported my Ph.D programme.

CONTENTS

LIST OF FIGURES

LIST OF TABLES

ACRONYMS

BBS	Broadband Light Source
B/Ge	Boron/Germanium codoped
CCD	Charge-Coupled Device
CDA	Centroid Detection Algorithm
CW	Continuous Wave
EDFA	Erbium Doped Fibre Amplifier
EMI	Electromagnetic Interference
FBG	Fibre Bragg Grating
GPNG	GeO_2-PbO-Na_2O-Ga_2O_3
IFO	Integrated & Fibre Optical (Gratings)
IR	Infrared
LPG	Long-period Grating
MCF	Multi-Core Fibre
OSA	Optical Spectrum Analyser
PDL	Polarisation Dependent Loss
PM	Polarisation Maintaining
RMS	Root Mean Square
SLD	Super Luminescent Diode
SMF	Single-Mode Fibre
SRI	Surrounding-medium Refractive Index
TIR	Total Internal Reflection
TFG	Tilted Fibre Grating
TZN	TeO_2-ZnO-Na_2O
UV	Ultraviolet
WDM	Wavelength Division Multiplexing

Chapter 1

Introduction and Thesis Structure

1. Introduction and Thesis Structure

1.1. INTRODUCTION

Following the realisation of low loss optical waveguide in the 1960s [1], optical fibres have been developed and widely used in modern communications and optical sensor networks due to their advantages of immunity to electromagnetic interference (EMI), light weight, flexibility, durable and especially, the low transmission loss.

Optical fibre devices based on in-fibre gratings have been exploited for last three decades since they were proposed by Hill *et al* [2] in 1978. A variety of application devices have been developed based on fibre Bragg gratings (FBGs), long-period gratings (LPGs) and tilted fibre gratings (TFGs). In relation to these grating structures, waveguide mode couplings have been extensively studied in order to design better grating structures to suit specific applications [3-5]. Due to their advantages such as immunity to EMI, lightweight and small size, high sensitivity, large bandwidth, and the capability for multiplexing, these gratings have been investigated and developed into applications and devices in optical communications, signal processing and smart optical sensing.

Noticeably, FBGs, as reflection devices, have been widely used in optical communications, including dispersion compensation [7, 8], wavelength selective devices [9-11], network monitoring and optical fibre identification [12], and fibre lasers [13-15]. In more recent years, FBGs have been demonstrated as most effective single-probe and wavelength multiplexable sensornet to measure a wide range of physical parameters, including temperature, strain, pressure, loading, bending and vibration [16-18, 229] for engineering structure health monitoring and projects across industrial sectors, such as military, aerospace, maritime, civil, oil and gas, power, nuclear, *etc.*

In contrast and complementary to FBGs, the broad transmission bands possessed by LPGs make them ideal as loss filters and LPGs have been used as band-rejection filters [19], gain flatteners for Erbium-doped fibre amplifiers (EDFA) [20], dispersion compensators [21], widely tuneable filters [22], broadband add/drop multiplexers [23], as well as various types of optical sensors [24-30].

TFGs have the capability of coupling the light from the core mode to the radiation modes and tapping the light out from the side of the fibre. By utilising this characteristic, TFGs have been developed into in-fibre spectrometer [31], wavelength division multiplexing (WDM) channel monitoring [32], EDFA gain flattening [33] devices, and optical sensor interrogation systems [34-38]. Due to the asymmetry of the grating structure, TFGs exhibit strong polarisation dependent effects. Based on this property, many TFG based applications, such as in-line polarimeter [39, 40], polarisation dependent loss equaliser [41, 42], and high-extinction-ratio polarisers [43] have been implemented.

With the advancement of grating inscription technology, various optical fibre gratings have been inscribed by Ultraviolet (UV) and more recently by femtosecond lasers and their spectral characteristics have been exploited for a wide range of applications. In recently years, a variety of novel optical fibres have been fabricated with different materials to be applied in new areas. Therefore, optical fibre gratings are then desirable to be inscribed in novel fibres as reflectors, sensors, dispersion compensators, filters, *etc.* The increasing demand for high function fibre devices and the wide range of applications are the motivations of the work reported in this thesis.

1.2. *STRUCTURE OF THESIS*

This thesis summarises the work carried out for developing advanced fibre grating structures and applications. It gives detailed description on the inscription methods, spectral characteristics and some applications of fibre gratings, mainly the tilted fibre gratings, fabricated in standard telecom fibres by UV laser inscription. Furthermore, the systematic work on optical fibre gratings in standard telecom fibre and single- and multi-core mid-infrared (mid-IR) glass fibres inscribed by near-IR femtosecond laser is reported. The thesis consists of 7 chapters; the detailed contents for each chapter are listed below.

Chapter 1 provides a brief introduction on development history and applications of all type of fibre gratings and the motivation for the work carried out for my Ph.D programme, followed by the description of the structure of the thesis.

Chapter 2 introduces the fundamental theories of the optical fibre gratings. This Chapter begins with the review the historical perspective of the photosensitivity of the optical fibre. Subsequently, the mode-coupling theory describing the behaviour of optical fibre gratings is introduced followed by a brief introduction on the fibre grating inscription techniques.

Chapter 3 reviews the mechanisms of the femtosecond laser inscription in transparent materials and the applications of femtosecond laser fabrication technology.

Chapter 4 theoretically analyses some characteristics of the cladding modes of TFGs and describes in details of the realisation of TFGs with small, large and 45° tilted structures. Furthermore, transmission-loss profiles and thermal responses of all-angle TFGs fabricated using phase-mask inscription techniques are comparatively discussed.

Based on the spectral characteristics discussed in Chapter 4, Chapter 5 introduces some applications based on TFGs with small and large tilt angles, utilising the unique radiation mode coupling function of the TFGs. As an application example, a TFG with tilted structure at 10° has been developed into a sensor interrogation system at 800nm, which can be utilised as a spectrometer and also as a refractive index sensor system. By employing the unique polarisation properties of coupled cladding modes, a TFG with tilted structure at a large angle of 81° is applied evaluated for twisting and transverse loading sensing.

Chapter 6 reports the FBGs and LPGs inscription using femtosecond laser employing both point-by-point and phase-mask methods in standard telecom fibres and single- and multi-core mid-IR glass fibres. Additionally, the spectral, thermal and strain properties and microscope structures of these gratings are analysed.

The final Chapter 7 concludes the work and gives some detailed suggestions for future research projects further exploring the devices and applications based on TFGs and improving the fibre gratings inscription using femtosecond laser system.

Chapter 2

Theory of Optical Fibre Gratings and Fabrication Methods

2. Theory of Optical Fibre Gratings and Fabrication Methods

2.1. INTRODUCTION

This chapter will introduce the fundamental theories of optical fibre gratings. At the beginning of this chapter, the historical perspective of the photosensitivity of optical fibre, including the photosensitivity mechanisms and photosensitisation techniques, will be reviewed. Subsequently, the mode-coupling theory describing the behaviour of FBGs, LPGs and TFGs will be introduced. Finally, a brief introduction on the fibre grating inscription techniques, including two-beam holographic, phase-mask and point-by-point method, will be given followed by a summary of this chapter.

2.2. *PHOTOSENSITIVITY IN OPTICAL FIBRE*

Photosensitivity of optical fibres refers to the irradiation-induced permanent refractive index change of the fibre core. Since it was firstly observed in germano-silicate (Ge-doped) fibres during the Bragg grating inscription by Hill *et al* in 1978 [2], several theories have been published to explain the mechanism, such as the colour-centre model [44], compaction-densification model [45] and stress relief model [46]. However, photosensitivity was found to be associated with the wavelength and intensity of the irradiation light that depends on the core material; and there is still no single model which can explain photosensitivity in all cases. In this section, the main theories of photosensitivity mechanisms and several methods to enhance the photosensitivity of optical fibres, such as hydrogenation, flame-brushing and using co-dopants, will be briefly reviewed.

2.2.1. PHOTOSENSITIVITY MECHANISMS

There are currently at least seven published theories explaining the mechanism of the photosensitivity: colour-centre model [44], compaction model [45], stress-relief model [46], electron charge migration model [47], permanent electric dipole model [48], ionic migration model [49] and Soret effect [50]. Among all the models, the colour-centre model and compaction densification model are the two main mechanisms which have been regarded for the photosensitivity behaviour for the most common germano-silicate fibre.

2.2.1.1. Colour-centre (point defect) model

It is well known that in germano-silicate fibre cores, germanium (Ge) has two stable oxidation states and can be expected as both GeO_2 and GeO. GeO, sometimes considered to exist as discrete molecules [51], manifests itself in the form of oxygen

vacancy Ge-Si defects, which are linked to the 240nm absorption band [52].

The colour-centre model, firstly proposed by Hand and Russell [44], describes that under the UV irradiation, the Ge-Si wrong bonds breaks, forming the GeE' centre and trapping electrons in neighbouring Ge sites to generate additional absorption centres in the glass, thus, creating other absorption bands. The photo-induced refractive index change associated with colour-centre model follows the Kramers-Kronig relationship [53].

After that, the bleaching of the 240nm band and the growth of absorption features at shorter wavelengths mentioned in the model have been proved by measurements of the UV-induced spectral changes and grating inscription [54-59], supporting the colour centre model for photosensitivity effect.

The colour-centre model contributes greatly to explain the photosensitivity in germano-silicate fibres and can also be applicable for explaining photosensitivity observed in hydrogen loaded germano-silicate fibres [60, 61]. However, it does not completely explain all the experimental observations [62-64], especially not for much higher magnitude refractive index change.

2.2.1.2. Compaction-densification model

The compaction-densification model is based on laser irradiation induced density increase that results in an increase in the refractive index of the glass. Fiori and Devine [45] reported that they irradiated thin-film amorphous silica samples grown on Si wafers using a KrF excimer laser, and found that the thickness of the film reduced approximately 16% after irradiation and the refractive index increased during the irradiation. After annealing the sample for 1 hour at 950°C in vacuum, the compaction disappeared and both the thickness and the refractive index value recovered to the

original states. Continued accumulation of UV irradiation was then been applied. Once the UV irradiation induced compaction beyond the threshold, it became irreversible.

A large part of the UV-induced refractive index change observed in non-hydrogen loaded germano-silicate glasses can be explained by the compaction-densification model [65-67].

2.2.1.3. Stress-relief model

After the fibre is drawn at high temperature, the tension is induced in the fibre core due to the difference in the thermal expansion of the core and the cladding during the cooling down of the glass. The stress-relief model is based on the hypothesis that the refractive index of the fibre core increases in relation to the release of the built-in thermo-elastic stresses [46]. It is proposed that during UV irradiation the wrong bonds break and promote relaxation in the tensioned glass hence increasing the refractive index in the core due to stress-optic effect.

2.2.2. PHOTOSENSITISATION TECHNIQUES

Since the discovery of the photosensitivity in germano-silicate fibres, there have been numerous efforts to increase the photosensitivity of the optical fibres. The photo-induced index modulation can be achieved up to the order of 10^{-3} and even higher by applying the following techniques: co-doping in fibre core [68], hydrogen loading (hydrogenation) [69] and flame brushing [70].

2.2.2.1. Co-doping

The photosensitivity of the germano-silicate fibre can be enhanced by co-doping

certain dopant, such as boron (B) [68] or tin (Sn) [71]. A comparative study on the relative photosensitivity of several different types of fibres including boron co-doping has been done by Williams *et al* [68]. After exposure to continuous wave (CW) radiation at 244nm, the saturated UV-induced index modulation for standard telecom fibre (3 mol% GeO_2) and the fibre with high Ge concentration (20 mol% GeO_2) were ~3×10^{-5} and ~2.5×10^{-4}, however, that for boron co-doping fibre (15 mol% GeO_2) was ~7×10^{-4}. Additionally, the saturated index modulations for the boron co-doping fibre (~ 10 min) were achieved much faster than the former two kinds of fibre (~ 2 hours). All these results demonstrate that the boron co-doping fibre has an excellent photosensitive response, much greater than a fibre with an equivalent Ge concentration without boron. However, boron causes additional loss in the 1550nm window, of the order of ~0.1dB/m, which may not be desirable.

Tin is an alternative co-dopant to increase the photosensitivity of the germano-silicate fibre. It was reported by Don *et al* [71, 72] that the saturated UV-induced index change was 3 times larger than that of normal germano-silicate fibre, which was comparable with that of boron co-doped fibre. Additionally, the tin co-doped fibre has advantages over the boron co-doped fibre: the gratings survive at higher temperature, do not cause additional loss in the 1500nm window.

2.2.2.2. Hydrogen loading (Hydrogenation)

Hydrogen (H_2) loading is a simple technique to enhance the UV-induced photosensitivity of germano-silicate fibres. This technique was firstly reported by Lemaire *et al* [69, 73]. In their experiment, fibres were soaked in hydrogen gas at temperatures ranging from 20 to 75°C and pressures from ~20 to over ~750atm and then exposed to the pulsed radiation at 241nm. Peak-to-peak index modulation of ~6×10^{-3} was achieved in the hydrogen-loaded fibre (3 mol% GeO_2 with 3.3 mol% H_2),

and the average core index increased by ~3.4×10^{-3}.

When the fibre is loaded in high pressure hydrogen gas tube, H_2 molecules are diffused into fibres through the cladding to the core over a time period. Subsequent exposure to UV or intense heat (e.g. a flame or a CO_2 laser) causes the dissolved H_2 to react in the glass, leading to the formation of Si-OH and Ge-OH, in addition to the formation of oxygen-deficient centres and resulting in large permanent index changes in the fibre core. Under UV exposure, an absorption band at ~1.4μm due to OH formation can be observed [74], which is comprised of two closely spaced peaks at 1.39 (Si-OH) and 1.41μm (Ge-OH). Such absorption peaks are unacceptable to some telecommunication network systems. However, by soaking the fibre in deuterium instead of hydrogen, this UV-induced absorption peaks will not appear in the range from 1.3 to 1.6μm of the communication band [75].

Both co-doping and hydrogen loading are widely used to increase the photosensitivity of the optical fibres for UV inscription. Comparing with the co-doped photosensitive fibres, hydrogen loading treatment of standard telecom fibre costs far less while provides high photosensitivity, though it slightly increases the OH loss. Even higher photosensitivity can be achieved by hydrogen loading B/Ge-doped fibre. Using this technique, the photo-induced index modulation can be as high as 10^{-2} [17], but the OH loss is increased much greater than in hydrogen loaded standard telecom fibre.

2.2.2.3. Flame brushing

Flame brushing technique is an alternative method for photosensitising optical waveguides and fibres [70]. The flame brushing is carried out by brushing the waveguides and fibres to be photosensitised repeatedly with a flame fuelled with hydrogen and a small amount of oxygen reaching a temperature of ~1700°C. During the flame brushing progress, the H_2 diffuses into the fibre core very quickly and reacts

with the germano-silicate glass, forming germanium oxygen-deficient centres. For the standard telecom fibre, the flame brush method increases the photosensitivity by a factor greater than 10, achieving UV-induced refractive change > 10^{-3} at 1540nm.

2.2.3. Thermal decay of UV-induced fibre Bragg gratings

The studies on the thermal decay of the UV-induced fibre Bragg grating is essential to ensure that the grating is fit for purpose throughout the applications lifetime. Niay *et al* [64] showed that UV grating inscription using either CW or pulsed sources resulted in gratings possessing the same elevated temperature stability properties. Williams and Smith [76] studied the thermal stability of strong and weak gratings and showed that superior stability can be assured in Bragg gratings by appropriate stabilisation of the gratings and may be expected to last at least 25 years, this result was analysed and confirmed by Kannan *et al* [77].

Erdogan *et al* [78] proposed a "power law" model to explain the thermal degradation characteristics of FBGs written in Ge-doped silica fibre, which accurately described the decay of the UV-induced index for non-hydrogen-loaded fibre. However, Patrick *et al* [79] stated that the UV-induced index modulation in hydrogen-loaded fibre was reduced by 40% after 10 hours at 176°C, whereas it was reduced by only 5% in unloaded fibre under the same conditions, which did not obey the Erdogan's model. Baker *et al* [80] proposed a log-time model which could be used to predict the decay characteristics of gratings written in H_2 loaded fibre and was extended to other fibres in the search for thermally stable FBGs, such as B-doped fibres, Sn-doped fibres, and fluorine-doped fibres [81-83].

2.3. COUPLE-MODE THEORY

Coupled-mode theory was developed to obtain an approximate solution for the propagation of electromagnetic wave in a periodic layered medium. As such, it is one of the most popular techniques utilised in describing the behaviour of Bragg gratings, mainly due to its simplicity and accuracy in modelling the optical properties of most fibre gratings of interest. As the derivation of the coupled-mode theory has been detailed in numerous articles [84, 85], the details of the derivation will not be provided in this thesis. The derivation in this section closely follows the work by Erdogan [86, 87].

In an ideal-mode approximation to coupled-mode theory, the transverse component of the electric field can be written as a superposition of the ideal modes where the modes are in an ideal waveguide with no grating perturbation. Given that the modes are labelled with index m, we then have:

Equation 2.1

$$\vec{E}^T(x,y,z,t) = \sum_m \left[A_m(z)\exp(i\beta_m z) + B_m(z)\exp(-i\beta_m z)\right]\cdot \vec{e}_m^T(x,y)\exp(-i\omega t)$$

where the coefficients $A_m(z)$ and $B_m(z)$ are slowly varying amplitudes of the m^{th} mode travelling in the $+z$ and $-z$ directions, respectively. The transverse mode field $\vec{e}_m^T(x,y)$ might describe the bound-core or radiation LP modes, or they might describe cladding modes. The propagation constant β is:

Equation 2.2

$$\beta = \frac{2\pi}{\lambda} n_{eff}$$

where n_{eff} represents the effect refractive index of m^{th} mode.

The presence of a dielectric perturbation causes the coupling between modes. Therefore the amplitudes A_m and B_m of the m^{th} mode evolve along the z direction

according to:

Equation 2.3

$$\frac{dA_m}{dz} = i\sum_q A_q\left(C_{qm}^T + C_{qm}^L\right)\exp\left[i\left(\beta_q - \beta_m\right)z\right] + i\sum_q B_q\left(C_{qm}^T - C_{qm}^L\right)\exp\left[-i\left(\beta_q + \beta_m\right)z\right]$$

Equation 2.4

$$\frac{dB_m}{dz} = -i\sum_q A_q\left(C_{qm}^T - C_{qm}^L\right)\exp\left[i\left(\beta_q + \beta_q\right)z\right] - i\sum_q B_q\left(C_{qm}^T + C_{qm}^L\right)\exp\left[-i\left(\beta_q - \beta_m\right)z\right]$$

where C_{qm}^T and C_{qm}^L are the transverse and longitudinal coupling coefficients, respectively, between q and m modes. Because the longitudinal component is nearly 2 orders of magnitude smaller than the transverse components for fibre modes, this coefficient is neglected in the coupled-mode analysis. The transverse coupling coefficient C_{qm}^T in the above equations is given by:

Equation 2.5 $$C_{qm}^T(z) = \frac{\omega}{4}\iint_{\infty}\Delta\varepsilon(x,y,z)\cdot\vec{e}_q^T(x,y)\cdot\vec{e}_m^{T*}(x,y)\,dx\,dy$$

where $\Delta\varepsilon(x, y, z)$ is the permittivity perturbation.

Even in the strongest fibre gratings written to date, for example, FBGs in the H_2-loaded Ge-doped fibre, the variation in the (effective) refractive index, δn (the photo-induced index modulation can be achieved up to the order of 10^{-2} [17]) is small compared with the local index in the ideal fibre, n (~1.45). In this case, $\Delta\varepsilon(x, y, z)$ is approximately $2n\delta n$.

For normal UV-inscribed fibre gratings, the refractive index modulation of the grating can be defined as:

Equation 2.6 $$\delta n_{eff}(z) = \overline{\delta n_{eff}}(z)\left[1 + s\cos\left(\frac{2\pi}{\Lambda}z + \phi(z)\right)\right]$$

where $\overline{\delta n_{eff}}(z)$ is the "*dc*" index change spatially averaged over a grating period, s is the fringe visibility of the index change, Λ is the nominal period, and $\phi(z)$ describes grating chirp.

In most fibre gratings, the UV-induced index change is approximately uniform across the core and negligible outside the core. The core index $\overline{\delta n_{eff}}(z)$ can thus be replaced by $\overline{\delta n_{co}}(z)$. Replacing $\Delta\varepsilon(x, y, z)$ by $2n_{co}\delta n_{co}(z)$, based on Equation 2.6, the general coupling coefficient $C_{qm}^{T}(z)$ can be rewritten as:

Equation 2.7 $$C_{qm}^{T}(z) = \zeta_{qm}(z) + 2\kappa_{qm}(z)\cos\left(\frac{2\pi}{\Lambda}z + \phi(z)\right)$$

where $\zeta_{qm}(z)$ is defined as a "*dc*" coupling coefficient and $\kappa_{qm}(z)$ is an "*ac*" coupling coefficient. We have:

Equation 2.8 $$\zeta_{qm}(z) = \frac{\omega n_{co}}{2}\overline{\delta n_{co}}(z)\iint_{core}\vec{e}_{q}^{T}(x,y)\cdot\vec{e}_{m}^{T*}(x,y)\,dx\,dy$$

Equation 2.9 $$\kappa_{qm}(z) = \frac{s}{2}\zeta_{qm}(z)$$

2.3.1. BRAGG GRATINGS

For a Bragg grating, the dominant interaction lies near the wavelength for which reflection of a mode of amplitude $A(z)$ into an identical counter-propagating mode of amplitude $B(z)$. Under such conditions Equation 2.2 and 2.3 may be simplified [86] as follows:

Equation 2.10 $$\frac{dA^{*}}{dz} = i\zeta^{*}A^{*}(z) + i\kappa B^{*}(z)$$

Equation 2.11 $$\frac{dB^{*}}{dz} = -i\zeta^{*}B^{*}(z) - i\kappa^{*}A^{*}(z)$$

where the amplitude $A^{*}(z)$ and $B^{*}(z)$ are:

Equation 2.12 $$A^{*}(z) = A(z)\exp\left(i\delta z - \frac{\phi(z)}{2}\right)$$

Equation 2.13 $$B^{*}(z) = B(z)\exp\left(-i\delta z + \frac{\phi(z)}{2}\right)$$

In Equation 2.10 and 2.11, ζ^{*} is the general "*dc*" self-coupling coefficient defined as:

Equation 2.14 $$\zeta^{*} = \delta + \zeta - \frac{1}{2}\frac{d\phi(z)}{dz}$$

In above equations, the detuning δ is independent of z for all gratings and defined as:

Equation 2.15 $$\delta = \beta - \frac{\pi}{\Lambda} = \beta - \beta_D = 2\pi n_{eff}\left(\frac{1}{\lambda} - \frac{1}{\lambda_D}\right)$$

where $\lambda_D = 2n_{eff}\Lambda$ is the "*design wavelength*" for an infinitesimally weak index of refraction change grating ($\delta n_{eff} \to 0$). For a single-mode Bragg grating, the coupling coefficients ζ and κ can be simplified as:

Equation 2.16 $$\zeta = \frac{2\pi}{\lambda}\overline{\delta n}_{eff}$$

Equation 2.17 $$\kappa = \kappa^{*} = \frac{\pi}{\lambda}s\overline{\delta n}_{eff}$$

If the grating is uniform along z direction and no grating chirp, then δn_{eff} is constant

and $d\phi(z)/dz = 0$. Thus, κ, ζ and ζ^* are constants. This simplifies Equation 2.10 and 2.11 into coupled first-order ordinary differential equations with constant coefficients, and the closed-form solutions may be found when appropriate boundary conditions are specified.

2.3.2. TILTED GRATINGS

For tilted gratings, the grating structure is tilted about the axis normal to the plane by an angle θ as shown in Fig.2.1. The induced index change in the core of a single-mode optical fibre, δn_{co} is:

Equation 2.18 $$\delta n_{co}(x,z) = \overline{\delta n}_{co}(z')\left[1 + s\cos\left(\frac{2\pi}{\Lambda_G}z' + \phi(z')\right)\right]$$

where, the z'-axis, shown in Fig.2.1 is defined as $z' = x\sin\theta + z\cos\theta$. The grating period along the fibre axis that determines the resonant wavelengths for coupling is:

Equation 2.19 $$\Lambda = \frac{\Lambda_G}{\cos\theta}$$

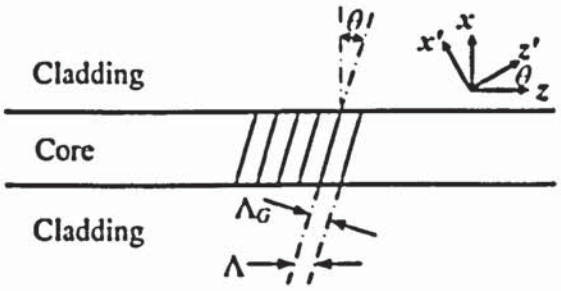

Fig.2.1. Schematic diagram of the core of a step-index optical fibre showing a tilted fibre grating.

For the slowly varying functions $\overline{\delta n}_{co}(z')$ and $\phi(z')$, $z' \equiv z\cos\theta$. By taking the projection of these functions along the fibre axis, the general coupling coefficient in Equation 2.7 becomes:

Equation 2.20 $$C_{\mp\pm}^{T}(z)=\zeta(z)+2\kappa_{\mp\pm}(z)\cos\left[\frac{2\pi}{\Lambda}z+\phi(z\cos\theta)\right]$$

where the subscript m in Equation 2.7 is associated with the forward-propagating mode (+) and q describes the backward-propagating mode (-). Thus the self- and cross-coupling coefficients are modified as:

Equation 2.21 $$\zeta(z)=\frac{\omega n_{co}}{2}\overline{\delta n}_{co}(z\cos\theta)\iint_{core}\vec{e}_{\mp}^{T}(x,y)\cdot\vec{e}_{\pm}^{T*}(x,y)\,dxdy$$

Equation 2.22

$$\kappa_{\mp\pm}(z,\theta)=\frac{s}{2}\frac{\omega n_{co}}{2}\overline{\delta n}_{co}(z\cos\theta)\iint_{core}\exp\left(\pm i\frac{2\pi}{\Lambda}x\tan\theta\right)\cdot\vec{e}_{\mp}^{T}(x,y)\cdot\vec{e}_{\pm}^{T*}(x,y)\,dxdy$$

It is noted that $\kappa_{\pm}=\kappa_{\mp}^{*}$. The effect of the tilt can be described by an "*effective fringe visibility*" $s_{\mp\pm}(\theta)$, which is defined as:

Equation 2.23 $$\frac{s_{\mp\pm}(\theta)}{s}=\frac{\iint_{core}\exp\left(\pm i\frac{2\pi}{\Lambda}x\tan\theta\right)\cdot\vec{e}_{\mp}^{T}(x,y)\cdot\vec{e}_{\pm}^{T*}(x,y)\,dxdy}{\iint_{core}\cdot\vec{e}_{\mp}^{T}(x,y)\cdot\vec{e}_{\pm}^{T*}(x,y)\,dxdy}$$

Thus, the Equation 2.22 can be rewrite as:

Equation 2.24 $$\kappa_{\mp\pm}(z,\theta)=\frac{s_{\mp\pm}(\theta)}{2}\zeta(z)$$

This result states that the effect of grating tilt on single-mode Bragg reflection is to reduce the effective fringe visibility by an amount given in Equation 2.23 and describes how effective the grating perturbation is in backward-scattering.

2.3.3. LONG PERIOD GRATINGS

For long period gratings, close to the wavelength for which a forward-propagating mode of amplitude $A_1(z)$ is strongly coupled into a co-propagating mode with amplitude $A_2(z)$, Equation 2.3 and 2.4 may be modified by retaining only terms that involve the amplitudes of these two modes and making the usual synchronous approximation as:

Equation 2.25
$$\frac{dA^*}{dz} = i\zeta^* A^*(z) + i\kappa B^*(z)$$

Equation 2.26
$$\frac{dB^*}{dz} = -i\zeta^* B^*(z) + i\kappa^* A^*(z)$$

where the new amplitudes A^* and B^* are defined as:

Equation 2.27
$$A^*(z) = A_1(z)\exp\left[-i(\zeta_{11}+\zeta_{22})\frac{z}{2}\right]\exp\left(i\delta z - \frac{\phi(z)}{2}\right)$$

Equation 2.28
$$B^*(z) = A_2(z)\exp\left[-i(\zeta_{11}+\zeta_{22})\frac{z}{2}\right]\exp\left(-i\delta z + \frac{\phi(z)}{2}\right)$$

where ζ_{11} and ζ_{22} are the "*dc*" coupling coefficients defined in Equation 2.8, and κ is the "*ac*" cross-coupling coefficient defined in Equation 2.9. We have $\kappa=\kappa_{21}=\kappa_{12}^*$. Thus the general "*dc*" self-coupling coefficient is now defined as:

Equation 2.29
$$\zeta^* = \delta + \frac{\zeta_{11}-\zeta_{22}}{2} - \frac{1}{2}\frac{d\phi(z)}{dz}$$

The detuning is assumed to be constant along the z axis and can be described as:

Equation 2.30
$$\delta = \frac{1}{2}(\beta_1 - \beta_2) - \frac{\pi}{\Lambda} = \pi\Delta n_{eff}\left(\frac{1}{\lambda} - \frac{1}{\lambda_D}\right)$$

where again $\lambda_D = 2n_{eff}\Lambda$ is the "*design wavelength*" for an infinitesimally weak grating. For Bragg grating, δ=0 corresponds to the grating condition predicted by the qualitative picture of grating diffraction, or $\lambda = \Delta n_{eff}\Lambda$.

For a uniform grating ζ and κ are constants. Like the analogous Bragg-grating equations, Equation 2.25 and 2.26 are coupled first-order ordinary differential equations with constant coefficients. With given the appropriate boundary conditions, closed-form solutions can be found.

2.3.4. PHASE-MATCH CONDITION

If the grating perturbation exists in the fibre, the bound-wave can be coupled to the counter-propagating or co-propagating modes. For the transfer of energy from a mode of amplitude $A_i(z)$ into an counter-propagating or co-propagating mode of amplitude $B_j(z)$, the phase mismatch factor $\Delta\beta$ is referred to a detuning, and is given by:

Equation 2.31 $$\Delta\beta = \beta_i \pm \beta_j - \frac{2\pi}{\Lambda_G} N\cos\theta$$

where β_i and β_j are the propagation constants for the incident and diffracted modes, respectively, Λ_G is the period of the grating, as shown in Fig.2.1, θ is the grating tilt angle and N represents an integer number. It is noteworthy that the "±" sign describes the case wherein the mode propagates in the $\mp z$ direction.

For significant transfer of energy, the phase-matching condition satisfies $\Delta\beta$=0, therefore, Equation 2.31 becomes:

Equation 2.32 $$\beta_i \pm \beta_j = \frac{2\pi}{\Lambda_G} N\cos\theta$$

For the counter-propagating, both β_i and β_j have identical (positive) signs; for co-propagating, they have opposite signs. For most reported cases, first-order diffraction is dominant, therefore, N=1. By substituting Equation 2.2, the resonant wavelength is satisfied:

Equation 2.33 $$\lambda = \left(n'_{eff} \pm n'_{eff}\right)\frac{\Lambda_G}{\cos\theta}$$

In the case of a Bragg grating, the core mode is coupled to the counter-propagating core mode and the Bragg wavelength is given by:

Equation 2.34 $$\lambda_B = 2n_{eff}\Lambda$$

where n_{eff} is the effective index of the core.

In the case of a long period grating, the core mode is coupled to the co-propagating cladding modes, the resonant wavelength of the coupled cladding modes satisfies:

Equation 2.35 $$\lambda_{co-cl} = \left(n_{co} - n_{cl,m}\right)\Lambda$$

where n_{co} is the effective index of the core and $n_{cl,m}$ is the effective index of the m^{th} cladding mode.

In the case of a tilted grating, the core mode can be coupled to counter-propagating or co-propagating modes, the resonant wavelength of the coupled mode is:

Equation 2.36 $$\lambda_{co-cl} = \left(n_{co} \pm n_{cl,m}\right)\frac{\Lambda_G}{\cos\theta}$$

where n_{co} and $n_{cl,m}$ are the effective index of the core and m^{th} cladding mode. The sign is described the same as Equation 2.31-2.33. The mode coupling of TFGs will be systematically discussed in Chapter 4.

2.4. *GRATING FABRICATION TECHNIQUE*

In 1978, the first internal inscribed Bragg grating was reported by Hill and co-workers [2, 88]. In their system, an Ar^+ laser (488 or 514.5nm) was used as the source. The incident laser light interfered with the Fresnel reflection (typically of ~4%) from the cleaved end of the fibre to create a standing wave within the core of the fibre and form a grating due to the photosensitivity of the fibre. This technique is very simple, but the Bragg wavelength is fixed as it is determined by the excitation laser wavelength.

Subsequently, external grating fabrication techniques using UV laser have been reported [2, 89-93]. These techniques overcome the fundamental limitation of the internally fabrication method and allow the Bragg wavelength, λ_B to be chosen. In summary, most fibre gratings are inscribed using one of three major fabrication techniques: two-beam holographic, phase-mask and point-by-point techniques. These are discussed in the following section.

2.4.1. TWO-BEAM HOLOGRAPHIC INSCRIPTION TECHNIQUE

The two-beam holographic inscription technique for side writing fibre gratings was demonstrated by Meltz *et al* [90] in 1989. This inscription system is an amplitude-splitting interferometer, using which gratings can be inscribed over a wide range of wavelengths - typically from 600 to 1700nm. Fig.2.2 shows the schematic diagram of the two-beam holographic grating fabrication setup in our lab.

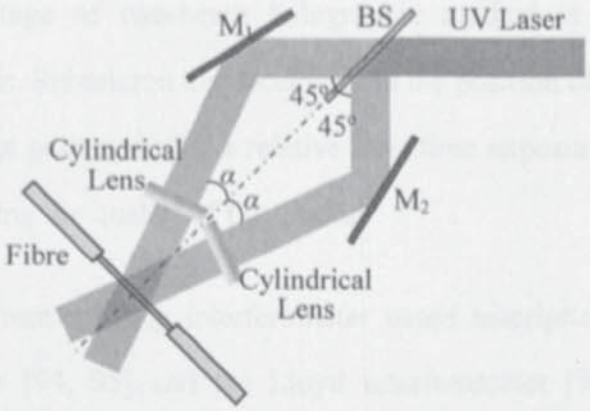

Fig.2.2. Schematic diagram of the two-beam holographic grating fabrication setup in our lab.

The UV beam passes through and is split by a 50:50 beam splitter. The split two beams are then reflected by two similar mirrors, focused by two similar cylindrical lenses and brought together at the fibre core to produce an interference pattern. Thus, a refractive index modulation is induced in the core of the fibre. The period of the Bragg grating depends on both the irradiation wavelength and the half angel α between the two split UV beams and is given by:

Equation 2.37 $$\Lambda = \frac{\lambda_{UV}}{2\sin\alpha}$$

where λ_{UV} is the UV wavelength. For non-tilted gratings, the Bragg wavelength can be written as:

Equation 2.38 $$\lambda_B = \frac{n_{eff}\lambda_{UV}}{\sin\alpha}$$

It is noted that an additional compensating plate is required to be inserted in one of the interference arm for low-coherence sources to compensate for the path imbalance imposed by the beam splitter. But this compensation is almost always omitted in setups using Ar^+ lasers, as their coherence lengths (~60mm for the normal multi-longitudinal mode output of and ion laser) are much longer than the optical path difference of two interference beams induced by the beam splitter (BS).

The main disadvantage of two-beam holographic method is a susceptibility to mechanical vibrations. Submicron displacements in the position of any optical devices will cause poor fringe pattern during a relative long time exposure (several to tens of minutes), thus affecting the quality of the grating.

A number of wavefront-splitting interferometer based inscription systems, such as prism interferometer [94, 95] and the Lloyd interferometer [96], have also been proposed but are not as popular as amplitude-splitting interferometer systems. In these two wavefront-splitting systems, only one optical component is employed, which simplifies the optical setup and reduces its sensitivity to mechanical vibrations. However, compared with the amplitude-splitting interferometer, these systems have disadvantages of limitation on the grating length and Bragg wavelength tuneability.

2.4.2. PHASE-MASK INSCRIPTION TECHNIQUE

Phase-mask inscription technique was firstly reported by Hill and Anderson *et al* [91, 92]. It is widely regarded as one of the most effective method for grating inscription, although this method is only for the inscription of gratings with fixed wavelengths and relatively short lengths.

The phase-mask is a one-dimensional surface-relief grating with the period of Λ_m etched in a fused silica plate, by which the incident UV beam is diffracted into several orders, m=0, ±1, ±2.... The ±1 order phase-mask is most popular employed for UV inscription achieved by suppressing energy diffracted to the 0 order and maximising the diffraction efficiency of ±1 order. With a normal incident beam, a near-field fringe pattern is produced by the interference of the ±1 order diffracted beams as shown in Fig.2.3.

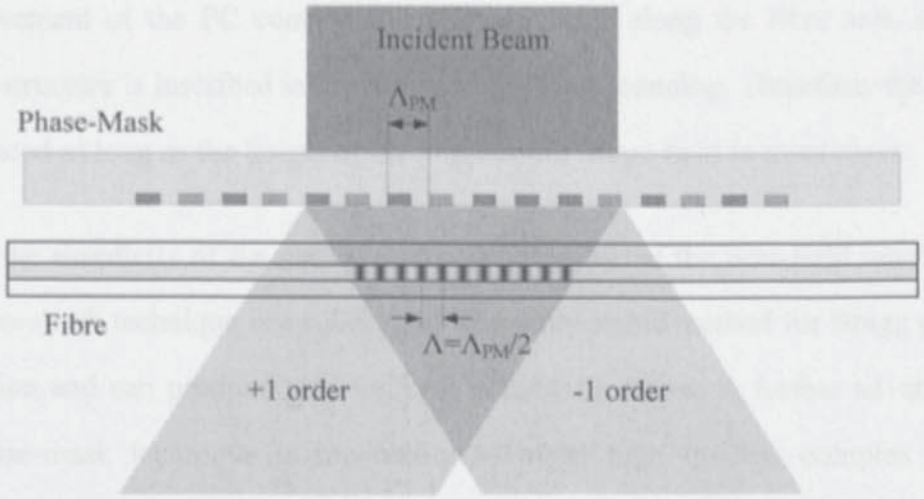

Fig.2.3. Schematic diagram of FBG inscription by UV beam exposure through a phase-mask. Normally incident UV beam diffracted into two ±1 orders.

The period of grating inscribed using ±1 order phase-mask is given by

Equation 2.39 $$\Lambda = \frac{\lambda_{UV}}{2\sin\theta_m} = \frac{\Lambda_{PM}}{2}$$

where θ_m is the diffraction angle for m^{th} order, and Λ_{PM} is the period of the phase-mask.

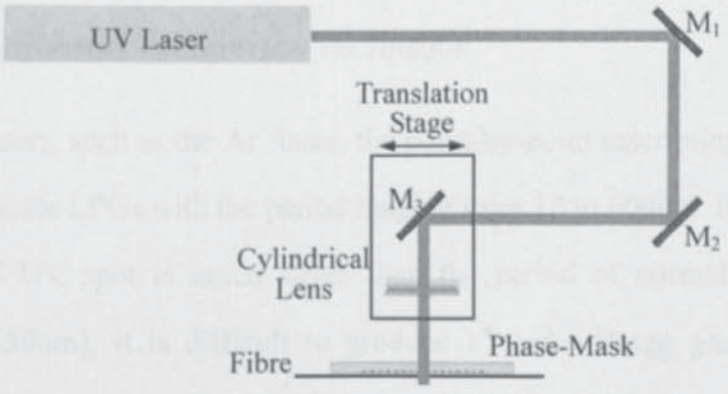

Fig.2.4. Schematic diagram of the experimental phase-mask inscription system in our lab.

Fig.2.4 shows the experimental arrangement of the phase-mask inscription system in our lab. The UV laser is focused by a cylindrical lens along the fibre axis onto the fibre core and passes through the stationary phase-mask to illuminate the fibre. With

the movement of the PC controlled translation stage along the fibre axis, a Bragg grating structure is inscribed in the fibre core by laser scanning. Therefore, the grating is produced as long as the length of the phase-mask fringe field in most cases.

Due to the simplicity of the optical system and the use of the near-field interference, the phase-mask technique is a robust and inherently stable method for Bragg gratings inscription and can produce very uniform grating structures. A further advantage of the phase-mask technique is the ability to make high quality, complex grating structures, including grating arrays, chirped [97], apodized [98, 99], phase-shifted [100, 101], Moire [102, 103] and sampled [104].

The main disadvantage of the phase-mask technique is the limit to variation of the inscribed Bragg wavelength, *i.e.*, separate masks are required for different Bragg wavelength. Several methods have been developed to tune the Bragg wavelength using phase-mask method, such as placing a magnifying lens before the mask [105] and pre-stretching the fibre [106, 107], which have demonstrated up to 7nm-tuning range to the Bragg wavelength.

2.4.3. POINT-BY-POINT INSCRIPTION TECHNIQUE

For CW UV lasers, such as the Ar^+ laser, the point-by-point inscription technique can be used to fabricate LPGs with the period ranging from 10 to 600μm. Because the size of the focused UV spot is much larger than the period of normal Bragg grating (~0.5μm at 1550nm), it is difficult to produce 1st order Bragg grating using this method. Fig.2.5 shows the schematic diagram of the point-by-point technique system employed in our lab.

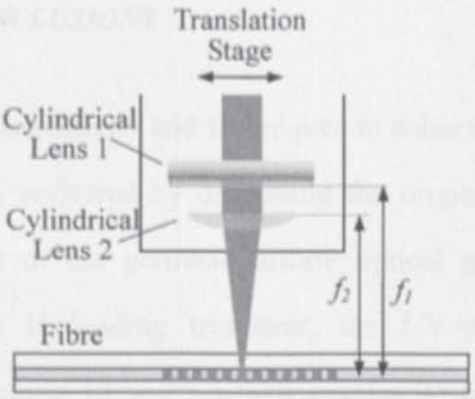

Fig.2.5. Schematic diagram of the point-by-point technique system employed in our lab.

Compared to the phase-mask inscription system described previously, an additional cylindrical lens is employed with the axis normal to the plane to reduce the beam size along the fibre axis. By PC control of the movement of the translation stage and the shutter to modulate the laser power, the parameters of a fibre grating such as the period, duty cycle and grating length could be alternated according to design. Although high order Bragg gratings may also be inscribed using point-by-point inscription method, this technique is generally used for LPG fabrication.

2.5. *CHAPTER CONCLUSIONS*

In this chapter, the photosensitivity and techniques to enhance the photosensitivity of optical fibres have been reviewed by discussing the origins of and the H_2-loading induced photosensitivity of the germano-silicate optical glass fibres. It has been revealed that by using H_2-loading treatment, the UV-induced refractive index modulation may be reaching 10^{-3}-10^{-2}, which enables writing strong, complex and high quality fibre gratings. Coupled mode theories for three different types of gratings, including FBG, TFG and LPG, were then systematically reviewed. The thermal stability studies have also been reviewed with conclusion that such UV-induced fibre grating devices may possess lifetime as long as 25 years. Finally, the fibre grating inscription techniques have been introduced very briefly, with which various fibre gratings, such as, FBGs, TFGs and LPGs can be achieved.

Chapter 3

Inscription of Photonic Devices by Femtosecond Lasers (Review)

3. Inscription of Photonic Devices by Femtosecond Lasers (Review)

3.1. INTRODUCTION

Since femtosecond laser micromachining of silica was first demonstrated in 1994 [108], the use of femtosecond laser pulses to directly induce refractive index changes in transparent dielectric materials has attracted great interest. Unlike the CW or quasi-CW UV exposure methods that are widely used for fibres, the femtosecond laser inscription technique is not limited to UV photosensitive glasses. Although the laser-induced breakdown and damage in transparent materials is not completely understood, various active and passive integrated optics devices in glass have been fabricated using femtosecond laser.

In this chapter, mechanisms of the femtosecond laser inscription in transparent materials will be reviewed firstly, which can be broadly categorised in two regimes: ablation and structural modifications. Subsequently, the applications of femtosecond laser device fabrication will be introduced followed by a summary of this chapter.

3.2. *MECHANISMS OF FEMTOSECOND LASER INSCRIPTION IN TRANSPARENT MATERIALS*

Laser-induced breakdown in optically transparent materials has been studied for decades since the 1960s [109]. Although laser-induced breakdown and damage in transparent materials are well researched subjects, the mechanism that leads to the refractive index changes is not completely understood [110-113].

For most pulsed lasers, the avalanche-breakdown mechanism is believed to be the dominant damage mechanism [110, 114]. The nature of this mechanism is that of thermal excitation, where a small number of free electrons resulting from crystal defects or nonlinear photo-ionisation are created within the optical material. These free electrons serve as seeds to a process called avalanche ionisation, and which ionises other atoms within the material produces additional electrons with high energies. If enough laser energy is deposited into the material by this process, a localised heating of the material will be induced and eventually lead to damage of the material due to cracking or melting.

3.2.1. NONLINEAR PHOTO-IONISATION

Considering the irradiation of a widely used amplified Ti:Sapphire femtosecond laser (800nm output wavelength), in the absence of impurity, there is no linear absorption of the incident laser light in the transparent material with large band-gap. This is because the energy gap between the valence and conduction bands is larger than the energy of the single photon of infrared light. Thus, a single photon does not contain sufficient energy to excite an electron at the ground state. However, an electron can simultaneously absorb the energy from the multiple photons to exceed the band-gap at sufficiently high laser intensities.

For femtosecond laser pulses, nonlinear photo-ionisation plays an important role in the generation of conduction band electrons. Depending on the laser frequency and intensity, there are two different regimes of photo-ionisation described within the same framework: the multi-photon ionisation and the tunnelling ionisation [110].

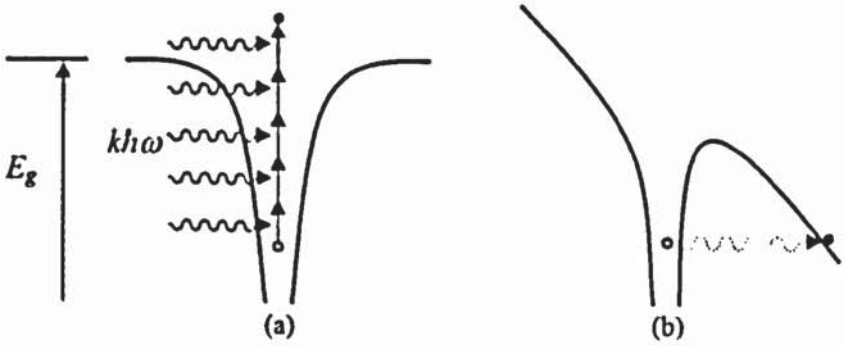

Fig.3.1. (a) Schematic diagram of multi-photon ionisation. An electron is promoted to the conduction band by simultaneous absorption of several photons. (b) Schematic diagram of tunnelling ionisation. The bounded electron can tunnel through the shorter barrier to a free state as the Coulomb well is suppressed enough.

The multi-photon ionisation, as shown in Fig.3.1 (a), refers to promoting an electron to the conduction band by simultaneous absorption of several photons of laser. The multi-photon ionisation rate depends strongly on laser intensity as [115]:

Equation 3.1 $$P(I)=\sigma_k I^k$$

where I is the laser intensity at the focus, σ_k is the multi-photon absorption coefficient for absorption of k-photons [115] and k is minimum number of photons that satisfies the relation $kh\omega \geq E_g$, where E_g represents the band-gap of the material. For example, the 800nm laser inscription in the fused silica is a six-photon absorption process [110], the probability of which is linear to I^6 and extremely dependent on the laser intensity.

The tunnelling ionisation takes place when the electric field is very strong. In this case, the Coulomb well can be suppressed enough that the bound electron tunnels through the short barrier and becomes free, as shown in Fig.3.1 (b).

In the overall femtosecond ionisation process, there is a balance between multi-photon and tunnelling ionisation, which is overall dependent on parameters such as the band-gap of the material, laser frequency and the laser intensity. This balance can be expressed by the adiabatic parameter, (also known as the Keldysh parameter) [110] as:

Equation 3.2 $$\gamma = \frac{\omega}{e}\left(\frac{mcn\varepsilon_0 E_g}{I}\right)^{1/2}$$

where ω is the laser frequency, I is the laser intensity at the focus, m and e are the reduced mass and charge of the electron, c is the velocity of light, n is the refractive index of the material, E_g is the band-gap of the material and ε_0 is the permittivity of free space. When the Keldysh parameter is larger (smaller) than about 1.5, photo-ionisation is a multi-photon (tunnelling) process. If the Keldysh parameter is about 1.5, the photo-ionisation is a mix between tunnelling and multi-photon ionisation.

From Equation 3.2, it is clear that the tunnelling ionisation dominates for strong laser fields at low laser frequency, while multi-photon ionisation mainly occurs at high laser frequencies (but still below that required for single photon absorption).

3.2.2. AVALANCHE IONISATION

Once a small number of electrons are promoted to the conduction band, they serve as seeds to a process called avalanche ionisation. The seed electron initially present within the material linearly absorbs several laser photons sequentially, moving to higher energy states in the conduction band. After the sequential absorption of k photons, where k is minimum number of photons that satisfies the relation $kh\omega \geq E_g$, the electron's energy exceeds the conduction band minimum by more than the

band-gap energy. Therefore, the electron can then collisionally ionise another electron from the valence band as illustrated in Fig.3.2, resulting in two free electrons. This process will repeat itself, leading to an avalanche where the free-electron density grows exponentially from the very low seed electron density.

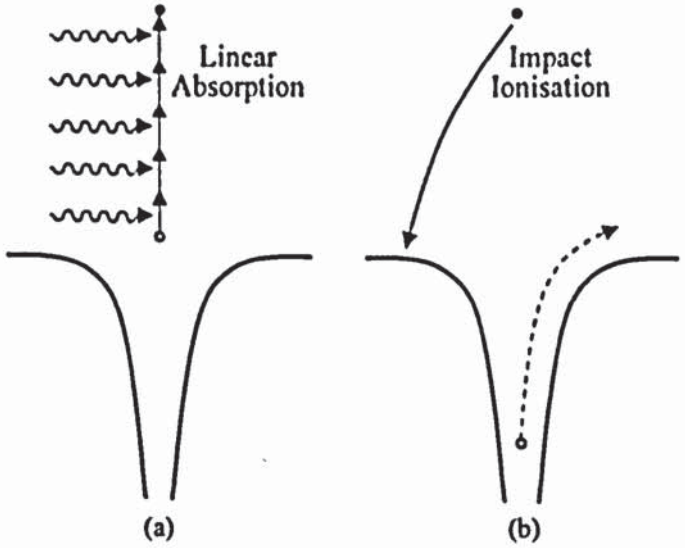

Fig.3.2. Schematic diagram of avalanche ionisation. An initially free electron linearly absorbs several laser photons then impact ionises another electron.

The electron density, N, in the conduction band grows due to the avalanche ionisation can be expressed as [110]:

Equation 3.3 $$\frac{dN}{dt} = \eta N$$

where, the avalanche ionisation rate η depends linearly on the laser intensity and can be expressed as $\eta = \alpha I$, where α represents the avalanche ionisation coefficient [116].

3.2.3. Plasma formation

With femtosecond laser irradiation, free electrons grow exponentially through avalanche ionisation. Because electrons in the conduction band are heated by the laser pulse much faster than they can cool by phonon emission, the density of the electron

plasma, which determines ultimately the nature of the material modification, can be simply expressed as Equation 3.4 [116-119].

Equation 3.4 $$\frac{\partial N}{\partial t} = \sigma_k I^k + \alpha N I$$

The first term in the right hand side of this equation corresponds to multi-photon ionisation and the second term corresponds to avalanche ionisation.

Once the plasma of electron reaches the critical plasma density [116], it becomes strongly absorbent to the incident laser pulses. This high density plasma strongly absorbs laser energy by linear absorption. As the reflectivity of the plasma at the critical density is weak, most of the laser energy is transmitted into the plasma where it can be absorbed. However, the plasma becomes reflective at higher plasma densities. The plasma is micrometer-sized and trapped inside the material. With the efficient absorption of the laser pulses, the highly-excited plasma leads to refractive change of the material. Thus, the density of the plasma is directly related to the refractive index modification and the ablation processes.

The laser-induced breakdown process is dependent on the laser intensity and exhibits a threshold behaviour: at a given laser pulse-width, the irreversible breakdown takes place only when the laser intensity exceeds a certain threshold, and thus, where the plasma density grows to the critical value. This laser intensity threshold, I_{th}, is a very important parameter for laser inscription in dielectrics, and the dependence of this on the pulse-width τ has been explored for values of τ down to 10fs. For $\tau > 10$ps, I_{th} varies as $\tau^{1/2}$, indicating that the initially ionised electrons by linear absorption are responsible for the optical damage [120]. For $\tau < 10$ps, the experimental results show low dependence of I_{th} on τ, which is due to avalanche ionisation: nonlinear ionisation creates only a small number of initial seeds, but the linear dependence of the avalanche process on the laser intensity is responsible for the high plasma density

necessary for laser-induced breakdown [110, 116]. The low dependence of I_{th} on τ provides flexibility in the choice of laser system, which is important for commercial applications of femtosecond laser micromachining.

Additionally, femtosecond laser processing is a deterministic process because no defect electrons are needed to seed the absorption process. For longer pulse laser irradiation, the seeded electrons initially present within the material are created by either thermal excitation or defects in the material. The seed electron density in a normal material is due to impurities, and the actual number can vary greatly due to statistical variations. Therefore, the avalanche ionisation that leads to breakdown for longer pulses thus will exhibit large fluctuations. For femtosecond laser irradiation, nonlinear photo-ionisation provides sufficient free electrons to start avalanche, and does not rely on the impurity seed electrons. In this case, the seed electron density can be quite high and does not exhibit large statistical fluctuation. Consequently, the laser-induced breakdown threshold for femtosecond pulses becomes more deterministic and low dependent on the band-gap energy which makes femtosecond laser induced damage repeatable for abroad range of materials.

3.2.4. FEMTOSECOND LASER INDUCED REFRACTIVE INDEX CHANGE

The refractive index change induced by femtosecond laser varies from material to material, with either positive or negative index contrasts [121-125]. This index change is not spatially homogeneous and the mechanism of which is still under investigation. Many models have been reported to explain the mechanism of the index change, such as stress-induced changes, densification, changes in effective fictive temperature, and colour-centre, varying from different material systems and processing conditions [112, 122, 125-129].

Depending on the level of laser intensity, different types of modification or damage

can be created in the dielectric materials [112, 130]. When the incident energy irradiated on the material is kept close to the threshold energy, a smooth refractive index change (type I) is then produced at focus position. This kind of refractive index change is usually around 10^{-3} [121-125]. If the laser energy is beyond the threshold, both the affected area and the average energy of the plasma will be increased. Thus, ionic shielding will be reduced causing Coulomb repulsion between ions with increased plasma energy. A surge of Coulomb repulsion with sufficient energy will then lead to void formation [127] (type III). By the laser with intermediate intensity, the index change (type II) is produced associated with the birefringence [131]. This kind of refractive index change can be created higher than 10^{-2} [137]. For 800nm femtosecond laser inscription in bulk of fused silica, type I refractive index change is erased at 900°C, while type II refractive index change is survived [130]. Most photonic applications use values of laser energy that are close to the absorption threshold and thus result in changes in the refractive index.

3.3. *APPLICATIONS OF FEMTOSECOND LASER MICROMACHINING IN TRANSPARENT MATERIALS*

Since femtosecond laser was first reported for micrometresized ablation on silica in 1994 [108], it has been widely used for variety of micromachining tasks [132] due to its advantages over previous long pulse lasers.

As mentioned in above section, the laser-induced breakdown threshold for femtosecond pulses is more deterministic than that for longer pulses. Therefore, the micrometresized femtosecond laser pulses can cleanly ablate materials without affecting the surrounding area with molten material, which makes them possible to produce three-dimensional structures within the bulk of the material by producing micro-voids of change the refractive index of a volume inside the material [133].

Another key advantage of femtosecond laser is its nonlinear absorption characteristic and low dependence of laser-induced breakdown threshold on the band-gap energy which makes the femtosecond laser inscription applicable for abroad range of materials without any linear absorption at the wavelength of the femtosecond laser, including glasses, polymers and crystals.

Depending on the level of the laser intensity, femtosecond lasers can create three different types of structure inside dielectric materials: low intensity exposure induces a refractive-index change relative to the unprocessed material (type I), which has been used to achieve waveguides and couplers [134, 135]; intermediate intensity exposure results in birefringent regions which can survive at high temperature (type II); and at high intensity exposure the damage consists of voids embedded into the glass (type III), which has been exploited for data storage [133] and photonic crystals [136].

With the development of ultrafast lasers, many practical applications of femtosecond lasers have been developed in areas involving material removal with submicron

precision, such as micromachining of waveguides [122, 137-141], data storage devices [133, 142-145], microfluidic devices [146-151] and subcellular nanosurgery [152-155]. In this section, some applications of femtosecond laser micromachining in transparent materials, including waveguides, high-density data storage in three dimensions, complex three-dimensional structure and optical fibre gratings, will be reviewed.

3.3.1. WAVEGUIDES

Since waveguides inscribed by femtosecond lasers were first reported in 1996 [137], abundant work has been reported on the fabrication of waveguide in glasses [122, 138, 139] and crystals [140, 141]. Waveguides are best inscribed with pulse energies just exceeding the threshold for the refractive index change. The pulse energy required for fabricating devices can be as low as a few nanojoules, which makes it possible to directly write waveguides in three dimensions into bulk optical materials and opens the door to the fabrication of a wide variety of passive and active optical devices for the telecommunications industry [121, 156] at least at a prototyping level. Functioned as interconnects in a variety of host glasses, waveguides inscribe by femtosecond laser can be applied as the two- or three-dimensional couplers [121, 157-159]. Moreover, active devices based on waveguide inscription in gain substrates such as amplifiers in Nd-doped glass [160] and a laser in Er:Yb glass [161] have been reported.

3.3.2. DATA STORAGE

Along with waveguides [137], data storage was one of the first demonstrations of the potential of femtosecond laser micromachining for photonic applications [133]. Conventional two-dimensional (2D) optical data storage can store the information as

micrometresized binary pattern inside optical media inscribed by highly focused lasers, the data storage density of which is ~10^8 bits/cm^2. The three-dimensional (3D) optical data storage can be achieved by stacking a number of 2D bit arrays. The data density of 3D optical data storage is then multiplied by the number of planes in the 3D stack, achieving >10^{12} bits/cm^3 [142-145]. Optical inscription of 3D optical data storage can be achieved by the use of volume holographic [162] or point-by-point techniques [133]. Femtosecond-laser-induced 3D optical data storage is achieved by creating hundred-nanometresized micro-voids [162], offering higher data storage. Currently, extensive work towards the development of holographic techniques using femtosecond lasers in both glass [163] and polymers [164] have been reported, showing the possibility to inscribe structures with periods in the range of tens to hundreds of nanometres [163, 165].

3.3.3. THREE-DIMENSIONAL COMPLEX STRUCTURES

Recently, more complex 3D structures achieved using femtosecond laser inscription have been reported. Based on the multi-photon absorption, photochemical or photophysical processes material transformations can be localised within the focal volume of a laser beam that has passed through a microscope objective [166]. Complex structures with resolutions lower than 100 nm can be fabricated by moving laser focus in three dimensions relative to the substrate. Typically, a Ti:sapphire laser producing pulses with duration of a few tens of femtoseconds and very high repetition rate (~80MHz) is employed for inscription. Another 3D fabrication method is also based on the multi-photon absorption. This technique offers the 3D fabrication with capability at resolutions better than 100 nm [166, 167].

3.3.4. OPTICAL FIBRE GRATINGS

The first LPG inscribed by femtosecond laser was reported in 1999 [168]. In that experiment, an LPG was written using IR femtosecond laser and point-by-point inscription technique. However, the resulting transmission spectrum was noisy and not regular like UV inscribed gratings. After that, the femtosecond laser inscribed refractive index change was studied by Fertein *et al* [169]. Eventually, LPGs with smooth spectra were successfully inscribed using femtosecond laser in both germano-silica and pure silica fibres by Hindle *et al* [170]. The only problem in their experiment is that the inscription process took over 4 hours, thus the results might highly rely on the stability of the system. Recently, LPGs with smooth transmission spectra and different grating periods have been inscribed using UV femtosecond laser with the wavelengths of 211 and 264nm [171]. A three-layer-structure model was employed to explain the experimental results, demonstrating most energy was absorbed by the fibre cladding.

FBGs inscribed using 800nm femtosecond laser and point-by-point technique was firstly reported by Martinez *et al* in 2004 [172]. In their paper, FBGs with first, second and third order resonance at ~1550nm were written in commercial fibres without any photosensitisation. The gratings were thermally stable up to temperatures of the order of 1000°C, showing a significant improvement compared to the conventional UV-inscribed FBGs [173]. In further studies, the FBGs were achieved by direct inscription in polymer coated fibres, which improved the mechanical strength of the gratings [174]. Recently, Lai *et al* improved the inscription system by immersing the fibre in the index-matching gel, overcoming the fabrication limitation imposed by the intrinsic fibre surface curvature [175]. Thus, high spectral quality FBGs with first-order Bragg resonances within the C-band are realised using point-by-point inscription technique with an IR femtosecond laser were achieved by reducing the pulse energy to tens of nanojoules.

Another method to write FBGs using femtosecond lasers is the phase-mask technique, by which FBGs of different orders were first written by Mihailov *et al* in 2003 [176, 177]. After that, the order walk-off effect which appears in the phase-mask inscription technique was analysed [178, 179], explaining the laser induced structures in the fibre and demonstrating that pure two-beam interference grating structure can be achieved by ultrafast laser inscription. Furthermore, the femtosecond-induced damage was studied for FBGs inscribed in hydrogenated and in non-hydrogenated fibres [180-182]. Recently, FBGs writing through fibre coating with IR femtosecond radiation and phase-mask has been achieved [183].

LPGs and FBGs inscribed by femtosecond laser using both point-by-point and phase-mask techniques developed in this work will be discussed in Chapter 6.

3.4. *CHAPTER CONCLUSIONS*

In this chapter, mechanisms of femtosecond laser inscription in transparent materials have been reviewed. When a femtosecond laser is used to irradiating a transparent material, free electrons created within the optical material through the nonlinear photo-ionisation serves as seeds to the process of avalanche ionisation and ionise other atoms within the material produces additional electrons with high energies, thus free electrons grow exponentially and intensity of the plasma increases. If the density of the plasma moves beyond a critical density, a localised heating of the material will be induced by laser energy deposited in the material and eventually lead to damage of the material due to cracking or melting formation and refractive index change. Femtosecond laser micromachining presents unique capabilities for three-dimensional, material-independent, precise processing.

Subsequently, applications of femtosecond laser micromachining in transparent materials have been introduced, including waveguides, high-density data storage in three dimensions, complex three-dimensional structure and optical fibre gratings. With the development in the micromachining in bulk materials by femtosecond laser, the waveguide fabricating and the three-dimensional structure processing have achieved resolutions of lower than 100 nm and the data density of 3D optical data storage can be improved to $>10^{12}$ bits/cm^3. Additionally, LPGs and FBGs have been successfully femtosecond-inscribed in germano-silica fibres using point-by-point and phase-mask techniques with transmission spectra in good quality.

Chapter 4

Fabrication and Spectral Characteristics of Fibre Gratings with Tilted Structures

4. Fabrication and Spectral Characteristics of Fibre Gratings with Tilted Structures

4.1. INTRODUCTION

The capability of light coupling from core to cladding and radiation modes by TFGs and their polarisation effect have been known since tilted fibre gratings (TFGs) were first demonstrated by Meltz *et al.* in 1990 [93]. In 1996, Erdogan and Sipe gave a detailed theoretical treatment to TFG structures [184]. Limited by the grating inscription techniques at the time, only simulation spectra based on their theory for small angle TFGs were compared with the experimental ones, showing good qualitative agreement.

With advances in UV inscription technology and demands for their application, a variety of TFG structures have been studied and developed in recent years. As reported in Meltz's paper [93], TFGs exhibit relatively strong polarisation-dependent effects when the tilted angles are larger. Based on this effect, TFGs with structures tilted at 45° (named as 45°-TFG) were explored as polarisation-dependent-loss (PDL) equalisers [41], in-line polarimeters [39] and in-line polarisers [43]. Quite recently, Zhou *et al* have reported [43] theoretically simulated transmission-losses of TFGs with structures tilted at different angles for coupled modes with two orthogonal polarisation states, pointing out the maximum PDL can be achieved with the tilt angle of 45°. Zhou *et al* also reported the theoretical and experimental investigation of TFGs with tilted structures larger than 45° [185], revealing the characteristics of forward propagating mode coupling and demonstrating the advantages of temperature, strain and refractive index sensitivities of such tilted gratings [186-188].

In this chapter, some characteristics of the cladding modes of TFGs will be theoretical

analysed and a detailed description of the realisation of TFGs of small (<45°), large (>45°) and 45° tilted structures will be given. Furthermore, transmission-loss profiles and thermal responses of TFGs of small, large and 45° tilt angles fabricated using phase-mask inscription techniques will be comparatively discussed. Based on these characteristics, a range of devices and their applications will be studied and investigated in Chapter 5.

4.2. *TFG CLASSIFICATION AND FABRICATION METHODS*

Fig.4.1 shows the schematic diagram of a TFG, depicting the mode coupling from the core to the cladding. In this figure, Λ_G is the normal period of the grating and Λ represents the grating period along fibre axis.

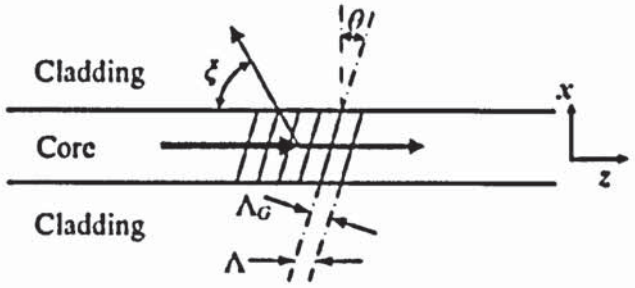

Fig.4.1. The schematic diagram of a TFG structure.

4.2.1. CLASSIFICATION OF MODE COUPLING RANGE OF TFGS

A TFG is capable of coupling light out of the fibre core in diverse directions. As mentioned in section §2.3.4, the strongest coupled wavelength is determined by the phase-match condition:

Equation 2.36 $$\lambda_{co-cl} = \left(n_{co} \pm n_{cl,m}\right) \cdot \frac{\Lambda_G}{\cos\theta}$$

where n_{co} and $n_{cl,m}$ are the effective mode indexes of fundamental core and m^{th} cladding modes, respectively, and the signs of "+" and "-" describe the cases wherein the mode propagates in the $-z$ or $+z$ direction, respectively.

Depending on the tilt angle, θ, TFGs may be classified into three regimes. If $\theta = 45°$ the forward-propagating core mode will be coupled to radiation modes and out from the side of the fibre; if $\theta <$ or $> 45°$ the light will be coupled to the backward-propagating ($-z$ direction) and to forward-propagating ($+z$ direction) cladding and radiation modes, respectively.

4.2.2. FABRICATION METHODS

As illustrated in Fig.4.2 the tilted structures can be achieved either by tilting the phase-mask with respect to the fibre in the phase-mask inscription system, or by rotating the fibre about the axis normal to the plane defined by the two interfering UV beams in the two-beam holographic system.

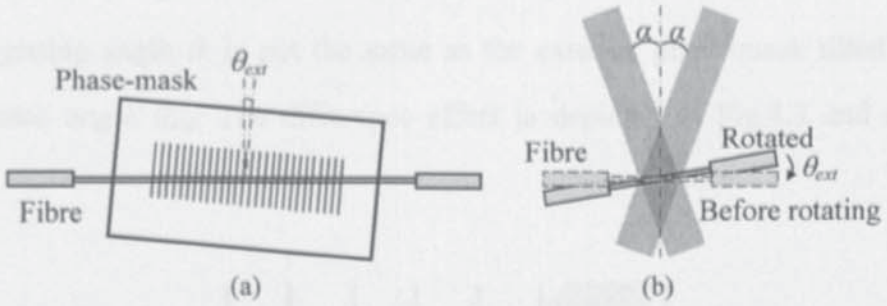

Fig.4.2. (a) Phase-mask and (b) two-beam holographic techniques for TFG fabrication. Note, the mask is tilted in (a) and the fibre is rotated in (b) to realise a tilted fringe structure.

As discussed in section §2.4.2, for a given wavelength, gratings with good quality can be easier achieved using phase-mask inscription method. Therefore, all the TFGs in my thesis were written by this method. The phase-mask technique will be introduced in the following section.

4.3. *TFG STRUCTURES WITH SMALL, LARGE AND 45° TILTED ANGLES - THEORETICAL ANALYSIS*

4.3.1. RELATIONSHIP BETWEEN THE INTERNAL AND EXTERNAL TILTED ANGLES AND THE PERIOD OF TILTED GRATING STRUCTURE

As reported in [189], owing to the cylindrical geometry of the optical fibre, the internal grating angle θ is not the same as the external phase-mask tilted angle or fibre rotated angle θ_{ext}. The difference effect is depicted in Fig.4.3 and discussed below.

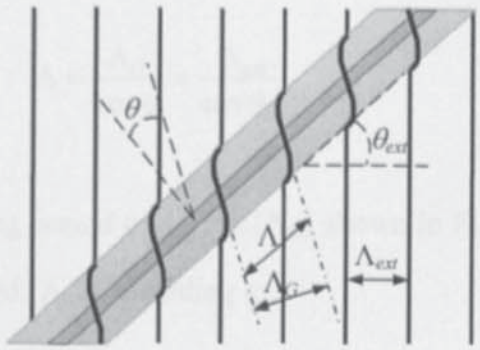

Fig.4.3. Schematic diagram of a TFG structure showing the difference between internal and external tilted angles.

For the phase-mask fabrication, the internal tilted angle θ is related to the external tilted angle θ_{ext} (the angle between the mask and the fibre) by the following relationship [189].

Equation 4.1
$$\theta = \frac{\pi}{2} - \tan^{-1}\left[\frac{1}{n\tan\theta_{ext}}\right]$$

where, n is the refractive index of the fibre. This relationship between the internal and external tilt angle is shown in Fig.4.4.

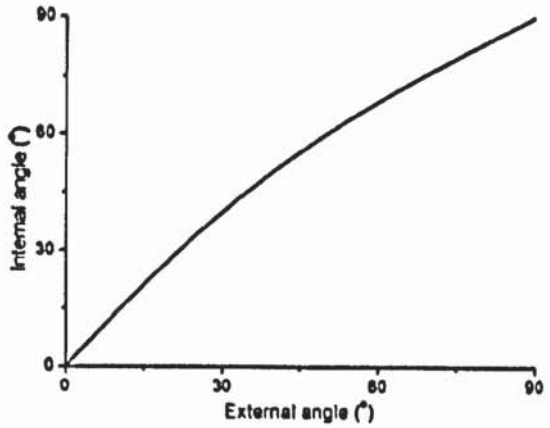

Fig.4.4. Relationship between the internal and external tilt angle of TFGs.

From the geometry relation shown in Fig.4.3 and Equation 2.19 in section §2.3.2, we have

Equation 4.2 $$\Lambda = \frac{\Lambda_G}{\cos\theta} = \frac{\Lambda_{ext}}{\cos\theta_{ext}}$$

Thus, the internal grating period of a TFG (Λ_G) shown in Fig.4.3 is related to the UV interference fringe period (Λ_{ext}) according to:

Equation 4.3 $$\Lambda_G = \frac{\Lambda_{ext}\cos\theta}{\cos\theta_{ext}}$$

where the UV interference fringe period, Λ_{ext} can be expressed as $\Lambda_{ext}=\Lambda_{PM}/2$ according to Equation 2.39 and Λ_{PM} is the pitch length of the phase-mask.

4.3.2. PHASE-MATCHING CONDITION AND MODE COUPLING REGIME

When light composed of various wavelengths encounters a TFG, it is radiated out of the fibre core in different directions with different strengths. As described in Zhou's paper [185], the strongest light coupling only takes place when the phase-match condition is satisfied as shown below:

Equation 4.4 $$K_R = K_C + K_G$$

where K_R, K_C and K_G are wave vectors of the radiated light, core mode and grating itself, respectively. In a general case, the amplitude difference between K_R and K_C can be neglected, since the refractive indices of the core and the cladding are very close.

Fig.4.5 (a), (b) and (c) illustrate graphically the phase-match condition for TFGs with tilt angles < 45°, = 45° and > 45°.

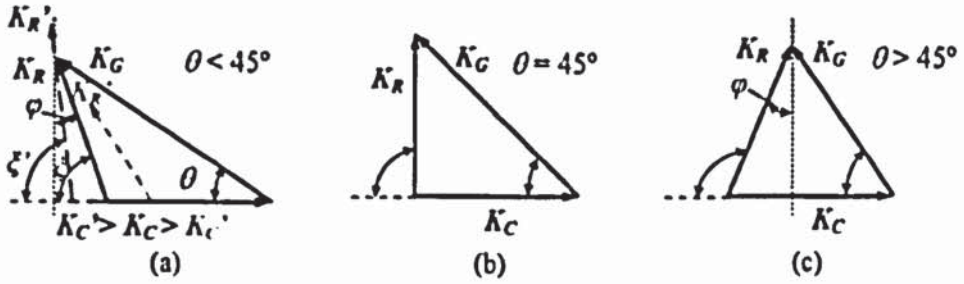

Fig.4.5. Phase-matching conditions for TFGs with tilted angles (a) <, (b) =, and (c) >45°. φ is the incident angle of the radiation beam at the cladding boundary. Note, in (a), K_R' is for non-phase-match condition.

4.3.2.1. Radiation angle

From the Fig.4.5, K_R and K_C are related as

Equation 4.5 $$k_R = \frac{k_G}{2\cos\theta} \quad (\xi = 2\theta)$$

where $k = |K|$, ξ and θ are the radiation angle and tilted angle of the TFG, respectively.

In Zhou's opinion, in Fig.4.5 (a), the main beam, K_R, satisfies the vectorial geometry of the phase-match condition, which will be strongly coupled. For radiated light of other wavelengths, K_R', will be weakly coupled at ξ' direction, at which the mismatch among K_R', K_C and K_G is minimal. From Fig.4.5 (a), the relationship among ξ', θ and K_G can be derived as:

Equation 4.6 $$c\tan\xi' = c\tan\theta - \frac{k_R}{k_G \sin\theta}$$

where, $k_C = k_R' = nk_0$, n represents the refractive index of fibre, $k_G = \frac{2\pi}{\Lambda_G}$.

Substituting $k_0 = \frac{2\pi}{\lambda}$, Equation 4.6 becomes,

Equation 4.7 $$\tan\xi' = \frac{\lambda \sin\theta}{\lambda\cos\theta - n\Lambda_G}$$

Equation 4.7 demonstrates the relationship between the radiation angle ξ' and the tilted angle θ for certain wavelength λ (suitable for both strong and weak coupling).

Substituting $\Lambda_G = \frac{\Lambda_{ext}\cos\theta}{\cos\theta_{ext}}$ and $\Lambda_{ext} = \frac{1}{2}\Lambda_{PM}$, Fig.4.6 (a) plots the relationship between the radiation angle and the internal tilt angle for standard telecom fibre with the parameters of n=1.445, λ=1550nm and Λ_{ext}=1083nm. In this figure, the curve is almost linear when the tilted angle is less than 10°; and the nonlinearity of the curve becomes obvious with the angle increasing. On the other hand, the TFG with given tilted angle couples the incident light out of fibre core in different directions according to its wavelengths. For a 10°-TFG, the relationship between the radiation angle and the wavelength of incident light ranging from 1300 to 1600nm is plotted in Fig.4.6 (b). By applying this relationship, the TFG may be developed into a spectrometer in the wavelength range covered by the radiation profile and such TFG-based in-fibre spectrometer application will be introduced and discussed in Chapter 5.

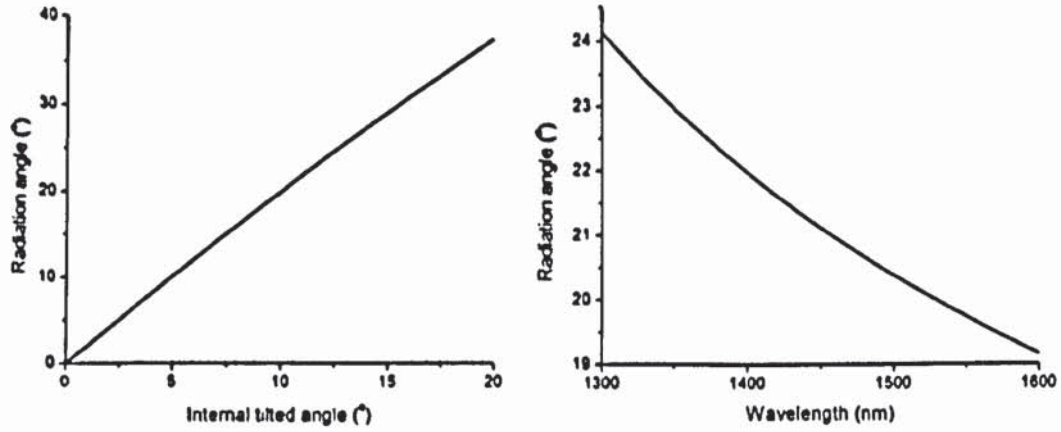

(a) (b)

Fig.4.6. Relationship between the radiation angle and (a) the internal tilted angle; (b) radiation wavelength for normal single mode optical fibre with parameters: n=1.445, Λ_{ext}=1083nm. In (a), λ=1550nm; and in (b) θ=10°.

4.3.2.2. Central wavelength of the radiation profile and the Bragg wavelength

When light composed of various colours encounters a TFG, it is radiated out of the fibre core in different directions with different strengths. Therefore a radiation profile can be measured in transmission spectrum. The strongest light coupling only takes place when the phase-match condition is satisfied. This wavelength is the central wavelength of the radiation profile. From Fig.4.5, we have

Equation 4.8 $$k_G \cos\theta = k_R \cos 2\theta + k_R$$

By substituting $k_G = \frac{2\pi}{\Lambda_G}$, $k_0 = \frac{2\pi}{\lambda}$, $\Lambda_G = \frac{\Lambda_{ext}\cos\theta}{\cos\theta_{ext}}$ and $\Lambda_{ext} = \frac{1}{2}\Lambda_{PM}$, the central wavelength λ_c can derived as:

Equation 4.9 $$\lambda_c = \frac{n\Lambda_{PM}\cos^2\theta}{\cos\theta_{ext}}$$

Although TFGs couple most light from core to cladding modes, a Bragg resonance still exists in small angle TFG appearing at the longer wavelength side of the radiation

profile. The Bragg wavelength, λ_B can be expressed as follows based on Fig.4.5:

Equation 4.10 $$\lambda_B = 2n\Lambda$$

By substituting $\Lambda = \frac{\Lambda_{ext}}{\cos\theta_{ext}}$ and $\Lambda_{ext} = \frac{1}{2}\Lambda_{PM}$, λ_B can be simplified as:

Equation 4.11 $$\lambda_B = \frac{n\Lambda_{PM}}{\cos\theta_{ext}}$$

4.3.3. CRITICAL ANGLE AND RADIATION MODE OUT-COUPLING RANGE

As mentioned in Equation 4.7, the direction of the radiated light depends on the tilt angle of the grating structure and the wavelength. Considering only the phase-matched beam, the radiation angle is related to the tilt angle. As shown in Fig.4.7, when the radiation beam encounters the cladding boundary, the light will be confined in the cladding modes without tapping out of the fibre due to the total internal reflection (TIR) effect if the tilt angle is small (or large) enough. However, if the grating structure's tilt angle is in an appropriate range, the incident angle of the cladding mode coupling at the cladding boundary will be less than the critical angle, thus, the light can overcome TIR and be tapped out intrinsically from the side of the TFG.

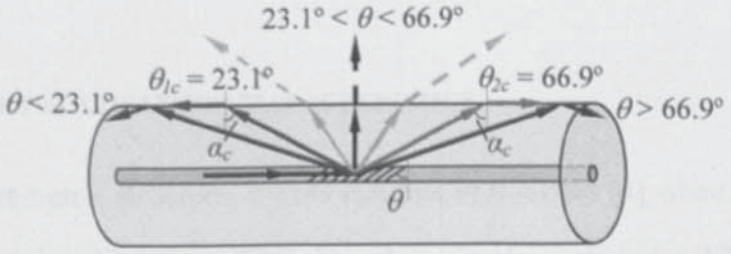

Fig.4.7. Three mode coupling regimes: (a) $\theta < \theta_{1c}$: backward cladding mode coupling; (b) $\theta_{1c} < \theta < \theta_{2c}$: radiation mode coupling; (c) $\theta > \theta_{2c}$: forward cladding mode coupling. For a standard telecom fibre placed in the air, θ_{1c}=23.1° and θ_{2c} =66.9°.

When the fibre is placed in certain medium, this critical angle of the fibre is defined as:

Equation 4.12 $$\alpha_c = \arcsin(n_1 / n_2)$$

where n_1 and n_2 are refractive indices of surrounding medium and cladding, respectively.

In Fig.4.5, if the amplitude difference between K_R and K_C is ignored, the radiation angle of the phase-matched beam ξ can be derived as $\xi=2\theta$, and the incident angle φ of the radiation beam is related to the tilted angle θ by $\varphi = \pi/2 - 2\theta$. If $|\varphi| < \alpha_c$, we have a radiation mode out-coupling range of $\theta_{1c} < \theta < \theta_{2c}$, where θ_{1c} and θ_{2c} can be calculated as:

Equation 4.13 $$\theta_{1c} = \frac{1}{2}\left(\frac{\pi}{2} - \alpha_c\right), \theta_{2c} = \frac{1}{2}\left(\frac{\pi}{2} + \alpha_c\right)$$

When the fibre is placed in vacuum (air, n~1), the critical angle can be calculated as α_c = 43.8°. Thus, for TFGs with tilted angle in the range from 23.1° to 66.9°, the radiation mode will be coupled out of the fibre cladding. If the surrounding is changed to the water based solution (n~1.33), the radiation mode out-coupling range increases from 11.5° to 78.5°.

4.3.4. UNIQUE POLARISATION CHARACTERISTICS

Due to the asymmetric structure, a TFG exhibits PDL effect [4] when the tilted angle is large. By applying this effect, TFGs have been implemented as a PDL equaliser [41] and an in-line polarimeter [39]. Additionally, an in-fibre polariser based on 45°-TFG has been reported by Zhou *et al* [43], showing a polarisation-extinction ratio higher

than 33dB covering a 100nm operation range. In his paper, the spectra of TFGs with various tilt angles have been simulated by the Green's function method [190] and PDL effect for TFGs has been systematic analysed.

Fig.4.8 (a) [43] shows transmission spectra of TFGs with various tilt angles for s-polarised (solid line) and p-polarised (dashed line) incident modes. Here, s- and p-polarised modes are the components of the electric field parallel and perpendicular to the incidence plane. It is clear that although the trends for both polarisation states are similar, the change in amplitude for p-light is most noticeable. It is noted that when the tilt angle is at 45°, the transmission-loss of p-light is almost zero. Fig.4.8 (b) [43] shows the simulation of the maximum transmission-losses at different tilt angles for s- and p-light. The transmission-losses of both polarisation states reach minimum when the tilt angle is 45°. At this unique angle, the loss of p-light is eliminated completely and the loss of s-light remains still high, giving an in-fibre polariser function. From Fig.4.8 (b), it is clear that the PDL reaches maximum when the tilt angle is 45°.

Fig.4.8. (a) Transmission spectra of TFGs with various tilt angles. Dashed curves: p-light; solid curves: s-light. (b) Transmission-losses of TFGs versus tilt angles for s- and p-light. The peak wavelength is set to 1550nm and the period is varied accordingly. [43]

4.4. *SMALL ANGLE TFGS INSCRIPTION AND CHARACTERISTICS*

4.4.1. FABRICATION OF TFGS WITH SMALL TILTED STRUCTURES

For a comparative study of the characteristics of the radiation mode out-coupling of the TFGs, several TFG samples with small tilted structures were UV-written in hydrogen-loaded standard single-mode fibre (SMF) - Corning SMF-28 - using the phase-mask method. The pitch of the phase-mask employed was 1083nm. With external angle change controlled to a precision of 0.1°, a series of TFGs were fabricated with external tilt angles of 0.0°, 0.7°, 1.4°, 2.1°, 3.5°, 4.1° and 4.8°. Therefore, the internal angles of these TFGs were calculated from 0.0° to 7.0°, respectively. Fig.4.9 presents transmission spectra of the TFGs with internal tilt angles from 0° to 7°.

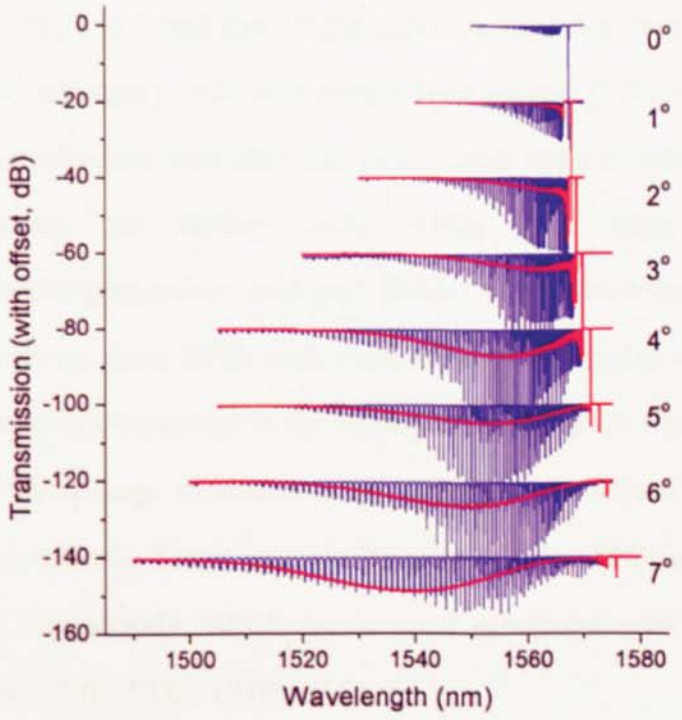

Fig.4.9. Transmission-loss profiles of TFGs with internal tilted angles from 0° to 7° in Corning SMF-28 fabricated using phase-mask method. Note, the resonant profiles were obtained when the TFGs were surrounded by air and the smooth profiles were obtained when the TFGs were immersed in index-matching gel.

As shown in Fig. 4.8, the transmission-loss profiles of the TFGs are strongly dependent on the tilt angle. With the tilt angle increasing, the radiation mode out-coupling (appearing as a broad transmission-loss profile) evolves as a result of blue shift of its central wavelength and increasing its dynamic range; at the same time the Bragg resonance shifts to longer wavelengths whilst its strength decreases. Thus, our analyses in section §4.3.2.2 were proved by above phenomena. It should be pointed out that in order to eliminate the resonant features in the transmission spectrum caused by the cladding-mode coupling effect, the gratings were immersed in index-matching gel to mimic an infinite cladding layer resulting in smooth radiation profiles as the smooth curves shown in Fig.4.9. With the grating internal angle increasing, the light is more and more coupled to the backward-propagating cladding modes by the TFG and not to the backward-propagating core mode, therefore, the strength of the Bragg reflection decreases, as also clearly seen in Fig. 4.8.

During the inscription, it is found that longer exposure time was required to achieve high strength of the radiation profile with certain laser power. This may be caused by the fact that the interference area after the phase-mask reduces with the tilt angle increasing. Therefore, for further study, TFGs have been inscribed in hydrogen-loaded boron/germanium co-doped (B/Ge) fibre which has much higher intrinsic photosensitivity. Four TFGs with even larger tilted angles - θ_{ext}=4.8°, 9.0°, 13.4° and 18.6° - were UV-inscribed in the hydrogen-loaded B/Ge fibre. Fig.4.10 and Fig.4.11 show the microscope structures taken under a 100× objective lens and the spectra of them, respectively. The measured tilt angles of these TFGs are 7.02°, 13.02°, 18.98° and 25.97°, respectively, which are in good agreement with the theoretical design parameters (θ=7.0°, 13.0°, 19.0° and 26.0°).

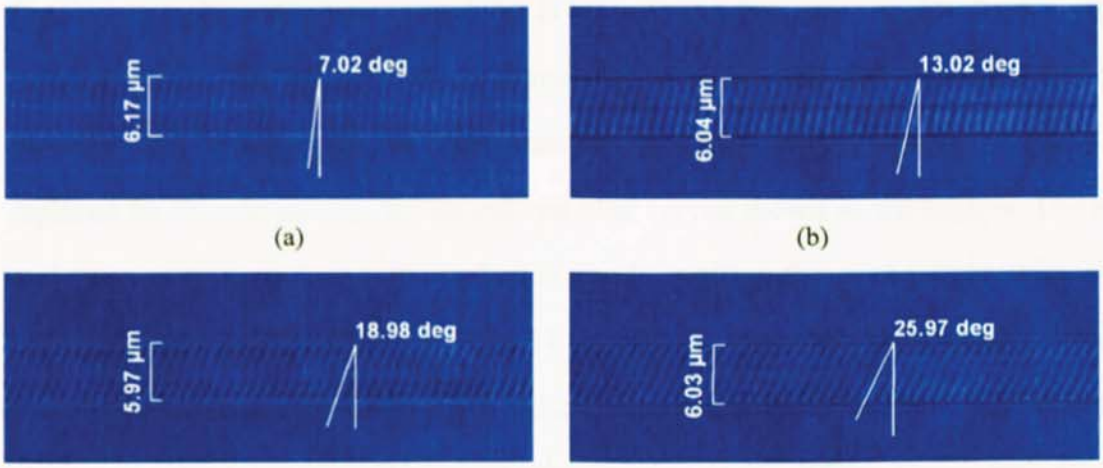

Fig.4.10. Images of photo-induced index modulation of UV-inscribed TFGs in B/Ge fibre with θ_{ext}= (a) 4.8°, (b) 9.0°, (c) 13.4° and (d) 18.6°, showing the internal tilted angles of 7.02°, 13.02°, 18.98° and 25.97°.

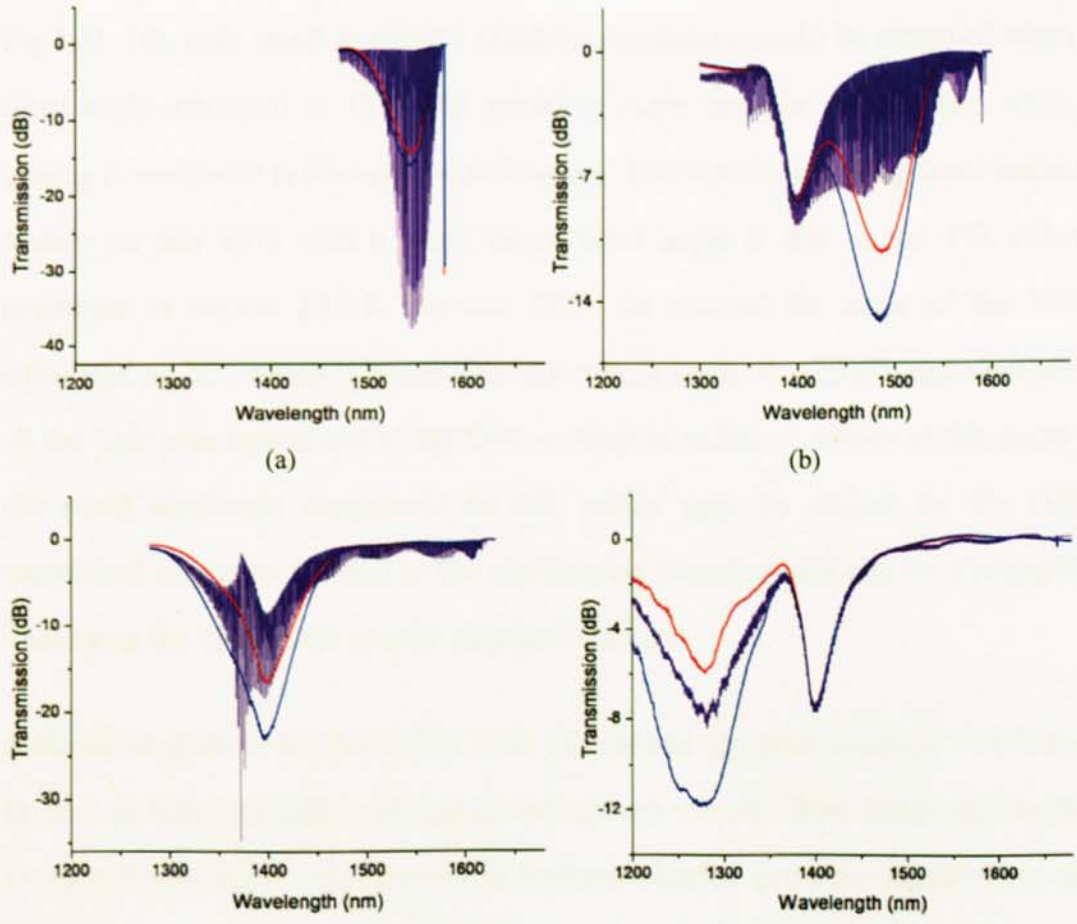

Fig.4.11. Transmission spectra of the UV-inscribed TFGs in B/Ge fibre with θ= (a) 7°, (b) 13°, (c) 19° and (d) 26°. Note, the red and blue curves are the spectra in two polarisation states when the TFG were immersed in index-matching gel.

Fig.4.11. (a), (b) and (c) show that the TFGs with the first three angles display clear cladding-mode coupling profiles as dense-resonance features and when these three gratings were immersed in the index-matching gel, the dense-resonance profiles are replaced by smooth curves, as the red and blue curves shown in the figures. The red and blue curves represent the radiation mode profiles for probe light with two orthogonal polarisation states. In Fig.4.11 (b) and (c), the comb-like resonances have less strength in loss than those of the red and blue smooth curves, because a very low resolution (1nm) was selected for the measurement over ~300nm wavelength range, thus the cladding mode resonances were not fully resolved to show their full strength. Apart from more noticeable strength changes, only small shifts of the central positions of the radiation profiles for the two polarisation states can be seen. It is noticed in Fig.4.11. (d), only small amplitude cladding resonances could be observed when the tilted angle increased to 18.6° and smoother curve can also be obtained when the grating is immersed in the index-matching gel. The reduced cladding mode resonance feature on this TFG with a much larger tilted angle is due to the TIR effect as explained in section §4.3.3. For this TFG, the internal tilt angle of the TFG is calculated as 26°, which is larger than the critical angle θ_{lc} (23.1°), and thus, almost all the light was tapped out of the fibre as coupled radiation modes at this angle and the small amplitude resonances on the profile may be caused by the slightly unmatched refractive indexes at the cladding/air boundary and can be eliminated by immersing the fibre in the exactly matched index gel.

It should be pointed out that in Fig. 4.10. (b), (c) and (d), great losses at ~1400nm can be seen in both comb-like resonances and smooth curves. These losses are attributed to the OH absorption band formed in hydrogen-loaded germano-silicate fibre under UV exposure, which was demonstrated in section §2.2.2.2.

4.4.2. PDL EFFECT OF TFGS WITH SMALL TILTED STRUCTURES

4.4.2.1. PDL of the TFG

In Fig. 4.10, the red and blue curves are the TFGs' transmission-loss profiles of s-(blue curve) and p-polarised (red curve) modes measured by inserting a polariser and polarisation controller in the characterisation system. As expressed in section §4.3.4, these two sets of orthogonal polarised mode profiles were obtained by changing the polarisation controller to reach the maximum and minimum transmission-loss profiles with the TFG immersed in the index-matching gel. PDLs of the TFGs UV-inscribed in B/Ge fibre with four different and relatively larger tilt angles are shown in Fig.4.12. Note, the PDL is actually the subtraction of the maximum and minimum transmission profiles, *i.e.* the red-curve minus the blue-curve in Fig.4.11.

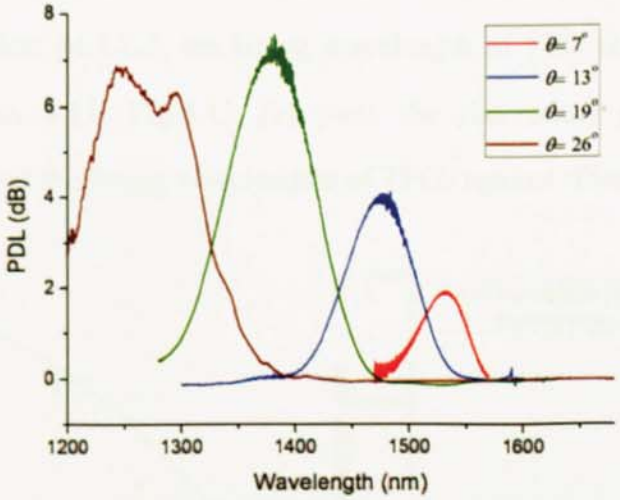

Fig.4.12. The PDL profiles of the TFGs with θ= 7°, 13°, 19° and 26°.

From Fig.4.12, it can be clearly see that there is a dependence of PDL effect on tilt angle of the TFGs - with increasing tilt angle, the PDL increases as well. These experimental results are another examples verifying Zhou's theoretical relationship between the PDL and the tilt angle [43]. In Fig. 4.11, the fact that PDL of the 26°-TFG is not stronger than that of the 19°-TFG might be caused that the maximum and minimum polarisation dependent transmission-losses cannot be measured

accurately in the range from 1200 to 1320nm as the output power of our BBS employed for measurement is not high enough in this wavelength range.

4.4.2.2. Central wavelength of the radiation profile and the Bragg wavelength

From Fig.4.11, it is clear that the transmission-loss characteristics of TFGs are related to the tilt angle. With the internal tilted angle increasing from 7° to 26°, the dynamic range of the radiation mode transmission profile becomes broader, and the central wavelength of radiation profile which can be identified from the maximum PDL point in Fig.4.12 blue shifts greatly; at the same time, the Bragg resonance red shifts slightly. The theoretical relationship between the central wavelength λ_c and the internal tilted angle θ can be obtained by substituting $\theta = \frac{\pi}{2} - \tan^{-1}\left[\frac{1}{n\tan(\theta_{ext})}\right]$ into Equation 4.9. Fig.4.13 (a) depicts the simulated relationship and experimental data. As shown in section §4.3.2.2, the Bragg wavelength of TFG is related to the tilted angle as Equation 4.11. Fig.4.13 (b) plots the theoretical calculation and the experimental data of the Bragg wavelengths of TFGs against tilted angles.

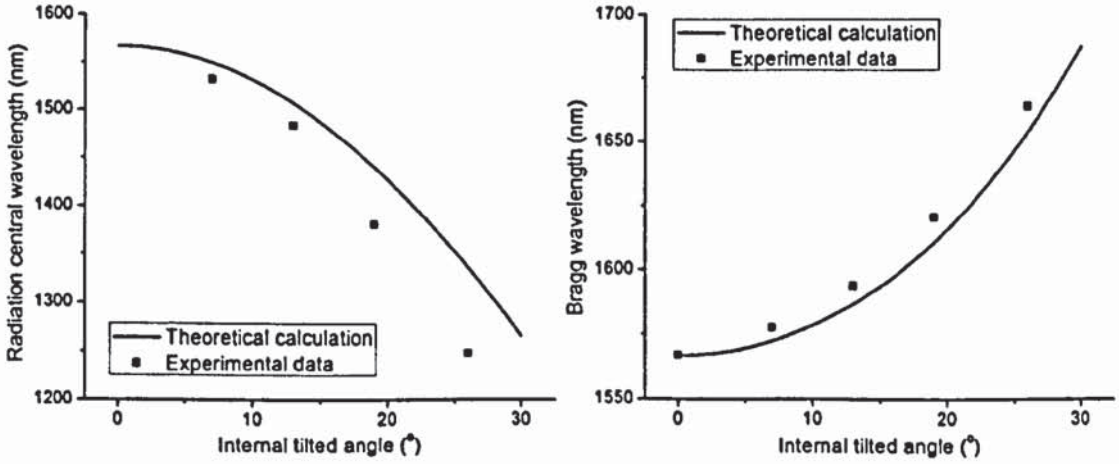

Fig.4.13. The theoretical simulation and experimental data of the relationship between (a) radiation central wavelength and (b) Bragg wavelength and internal tilted angle.

From Fig.4.13, it is clear that the trends of the theoretical calculated radiation central

and Bragg wavelengths of TFGs based on my simplified model change with increasing tilted angle, which is basically in agreement with the experimental results with some discrepancies (see the difference between the curves and the dots in Fig.4.13). The discrepancies could be caused by my relatively simple model, which does not include dispersion and other facts. However, this model can be used to provide guidance for design.

4.4.3. SPECTRAL CHARACTERISTICS OF THE CLADDING MODE RESONANCES

In Fig.4.11 (a) - (c), the cladding mode couplings of the TFGs were comb-like resonances. I then further study the spectral characteristics of these resonances. By inserting the polariser and polarisation controller between the light source and TFG and changing the polarisation state of the incident light, the transmission spectra of the 7°-TFG with light at two orthogonal polarisation states were plotted in Fig.4.14 (a), showing that these comb-like resonances were polarisation dependent.

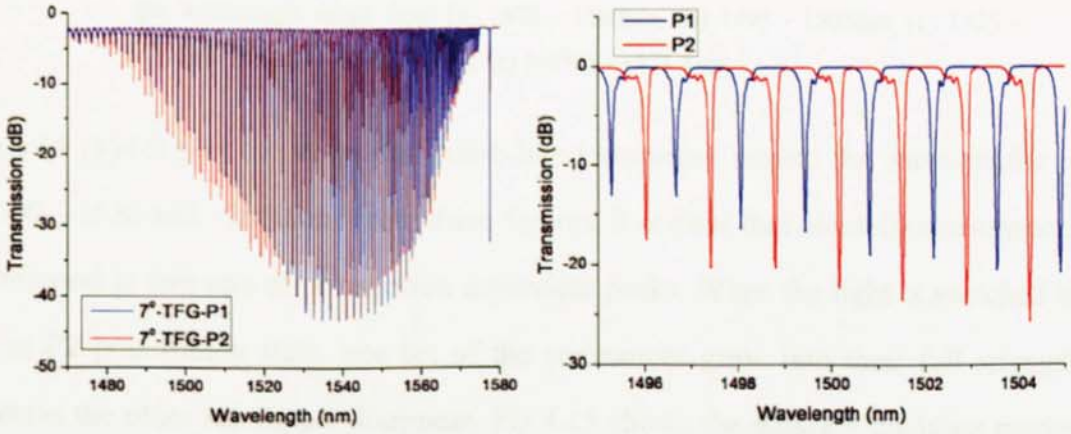

(a) (b)

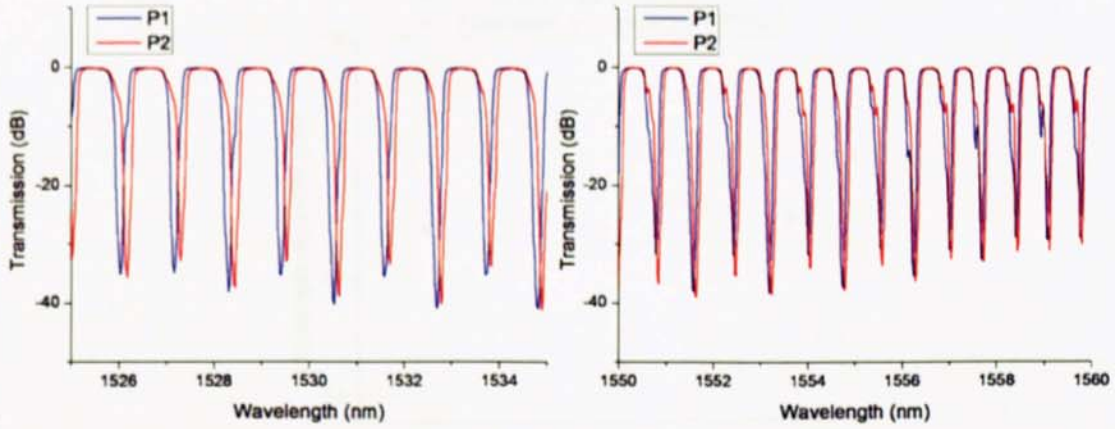

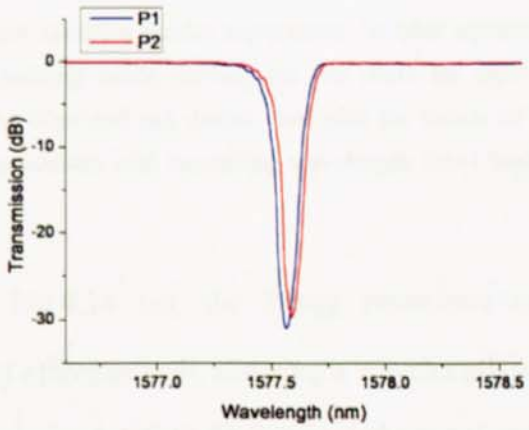

(e)

Fig.4.14. The transmission spectrum of a 7°-TFG in two orthogonal polarisation states in the wavelength range from (a) 1470 - 1580nm, (b) 1495 - 1505nm, (c) 1525 - 1535nm (d) 1550 - 1560nm and (e) 1576.6 - 1578.6nm.

Fig.4.14 (b)-(d) plot the magnified comb-like resonances around the wavelengths of ~1500, ~1530 and ~1550nm. From these figures, it is clear that comb-like resonances correspond to two sets of polarisation dependent peaks. When the light is switched to P1 or P2 polarisation state, one set of the resonances grow into their full strength whereas the other set almost disappear. Fig.4.15 shows the adjacent cladding modes separations (in blue squares) and the polarisation induced cladding mode shifting (in red dots) for three different wavelength ranges, based on which, the trends of these two wavelength separations evolves with increasing wavelength are fitted as the blue and red dotted lines. From this figure, it is clear that these two characteristics are wavelength dependent as they are larger at shorter wavelength side and *vice versa*.

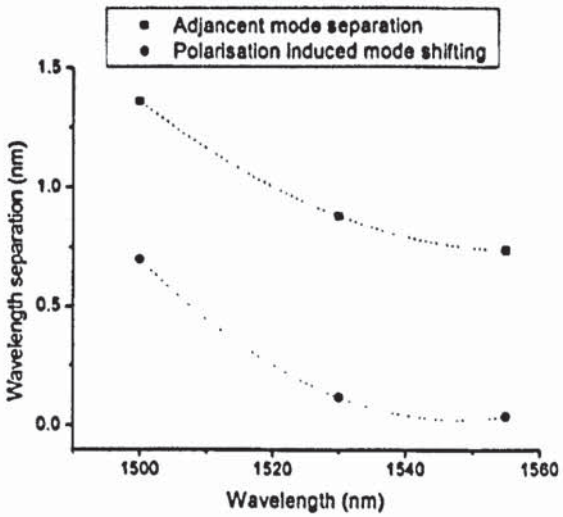

Fig.4.15. The adjacent cladding modes separations (in blue squares) and the polarisation induced cladding mode shifting (in red dots) for three different wavelength ranges. The blue and red dotted lines plot the trends of these two wavelength separations evolves with increasing wavelength fitted based on the experimental data.

It is noted that in Fig.4.14 (e), the Bragg resonance of the 7°-TFG exhibits polarisation dependent effect as well, showing a wavelength separation of 0.02nm and a peak attenuation variation of 1.32dB in two orthogonal polarised states. This may caused by the asymmetric grating structure.

4.5. *LARGE ANGLE TFGS INSCRIPTION AND CHARACTERISTICS*

4.5.1. FABRICATION OF TFGS WITH LARGE TILTED STRUCTURES

In order to study the characteristics of the radiation mode out-coupling of the TFGs with large tilt angles, I then UV-inscribed several TFG samples with~75° and ~81° tilted structures in hydrogen-loaded Corning SMF-28 using a frequency doubled CW Ar^+ laser and the phase-mask method. The custom-designed amplitude mask with a period of 6.6μm from Edmund Optics Ltd was employed and tilted for the fabrication. The phase-mask was tilted at 69.0° and 78.0° to achieve the two designed large internal tilted angles. Therefore, based on Equation 4.1, the internal tilt angles are calculated as 75.17° and 81.66°. Limited by the size of the phase-mask (the length of the mask fringe along the fibre axis is ~13mm), the exposure length for each grating was only 12mm. Fig.4.16 (a) and (b) show the microscope structures of the TFGs taken under a 40× objective lens. The tilt angles of the fringes were measured as 75.08° and 81.55°, which are in good agreement with the designed parameters.

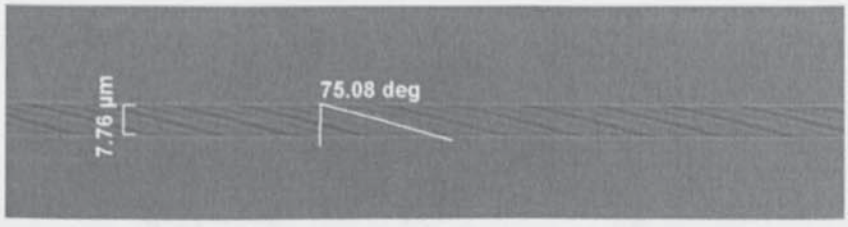

(a)

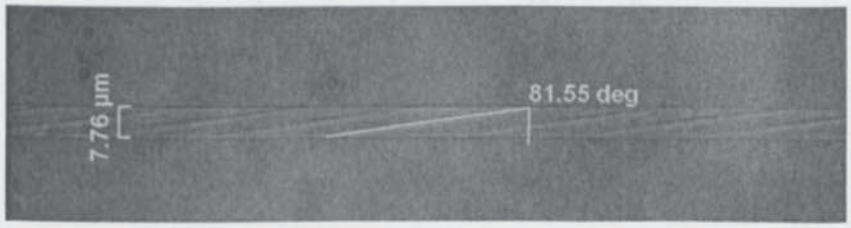

(b)

Fig.4.16. Microscope images of TFGs with θ_{ext}= (a) 69.0° and (b) 78.0° taken under a 40× objective lens.

Comparing with the small angle TFGs, due to the much larger period of the

phase-mask, less grating periods were inscribed in the fibre core for the same exposure length. In order to increase the index modulation, multiple scans were employed in large angle TFGs' inscription. Fig.4.17 shows the transmission spectrum evolution of an 81°-TFG with increasing UV exposure. Since the tilt angle $\theta > \theta_{2c}$ (66.9°), the light was coupled to forward-propagation cladding mode resulting in a series of the resonances with a noticeable dual-peak feature on the spectra. With increasing exposure, the strengths of these dual-peaks increase until ~3dB when randomly polarised light is coupled in. A large angle TFG can couple the light from the fundamental core mode to forward-propagating cladding modes, which is very similar to the LPG except showing the dual-peak feature caused by the tilted structure induced birefringence. As demonstrated in [230], there is a dispersion turning-point corresponding to a certain wavelength for each forward-propagating cladding mode. With increasing refractive index modulation, resonances at either the longer or shorter wavelength side of the turning-point shift towards the turning-point. For cladding modes of the 81°-TFG shown in Fig.4.17, the turning-point may appear at a wavelength less than 1500nm. Therefore, with increasing exposure, these dual-peak resonances shift towards shorter wavelength side.

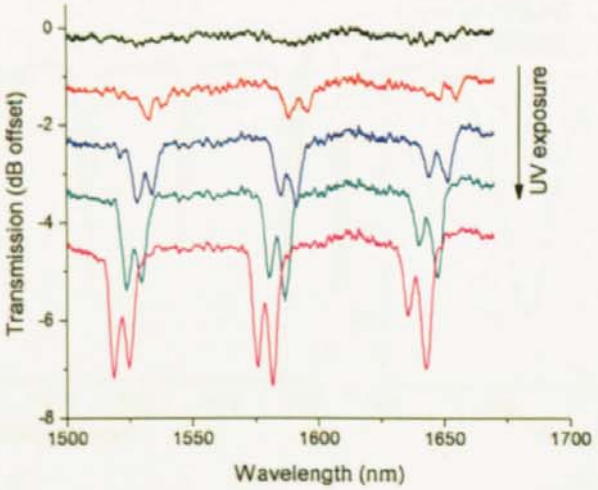

Fig.4.17. Transmission spectrum evolution of an 81°-TFG with UV scanned 1-5 times.

The transmission spectra of a 75°- and an 81°-TFG with random polarised incident

light were measured and plotted in Fig.4.18 (a) and Fig.4.19 (a) in the range from 1400 to 1700 nm, showing clearly a series dual-peak resonance, corresponding to the two sets of coupled cladding modes with orthogonal polarisation states. Fig.4.18 (b) and Fig.4.19 (b) show the transmission spectra of one pair of the dual-peaks for two (labelled as P1 and P2) orthogonally polarised states for these two TFGs. When the light is switched to P1 or P2, one of the dual-peaks grows to its full strength whereas the other almost disappears.

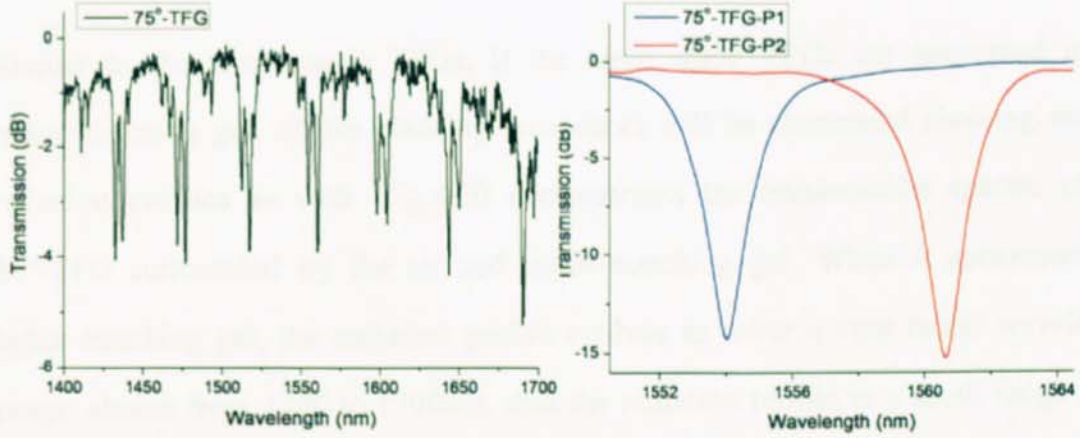

(a) (b)

Fig.4.18. (a) Transmission spectrum of a 75°-TFG with random polarised incident light in the wavelength range from 1400-1700nm. (b) One pair dual-peaks of the 75°-TFG for two orthogonal polarised states at ~1560nm.

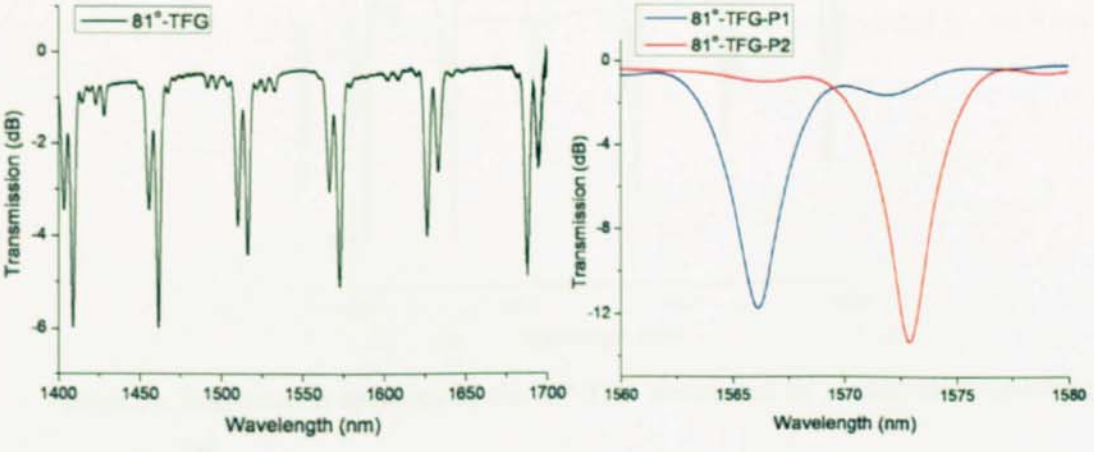

(a) (b)

Fig.4.19. (a) Transmission spectrum of an 81°-TFG with random polarised incident light in the wavelength range from 1400-1700nm. (b) One pair dual-peaks of the 81°-TFG for two orthogonal polarised states at ~1570nm.

In Fig.4.18 and Fig.4.19, the transmission spectra of large tilted TFGs look like that of LPG due to their similar forward-propagation cladding mode coupling except that the former exhibits dual-peaks. Comparing to the small angle TFGs, the wavelength separations between the modes with two polarised states of large angle TFGs are much greater which may be attributed to higher birefringence induced by their more asymmetric structures.

4.5.2. SPECIAL CHARACTERISTICS OF TFGS WITH LARGE TILTED STRUCTURES

Similar to the small angle TFGs, if the large angle TFGs are immersed in the index-matching gel, all the cladding resonances will be eliminated showing smooth radiation profiles as well. Fig.4.20 demonstrates the transmission spectra of the 81°-TFG surrounded by the air and index-matching gel. When it surrounded by index-matching gel, the radiation profile evolves to cover a very broad wavelength range, almost from 1400 to 1700nm, thus the radiation profile in a small range looks flat.

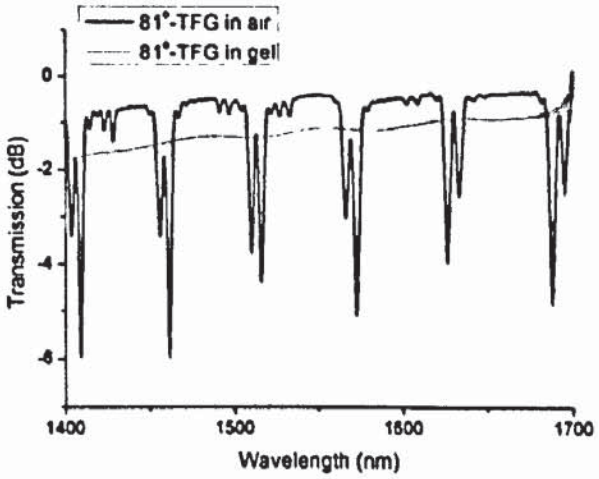

Fig.4.20. Transmission spectrum of the 81°-TFG surrounded by air and index-matching gel.

I further examine the spectral characteristics dependence on wavelength. Fig.4.21 (a) and (b) plot the adjacent cladding modes separations and the polarisation induced

cladding mode shifting of the 75°- and 81°-TFG for different wavelengths. From these two figures, it is clear that spectral characteristics of large TFGs are wavelength dependent, *i.e*, the separation and the shifting are larger at longer wavelength side and *vice versa*, which is opposite to the trends of the small angle TFGs. Additionally, for a comparison between these two large angle TFGs, as shown in Fig.4.21, the separation and the shifting for the 81°-TFG are greater than those for the 75°-TFG.

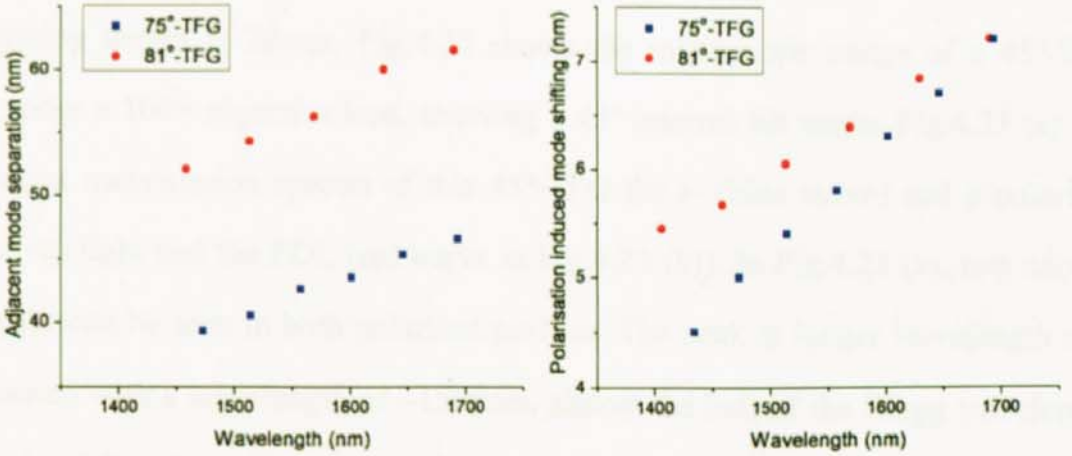

(a) (b)

Fig.4.21. (a) The adjacent cladding modes separations and (b) the polarisation induced cladding mode shifting for the 75°- and 81°-TFG at different wavelengths.

From Fig.4.18 (b) and Fig.4.19 (b), it is clear that the transmission spectra of the large angle TFGs exhibit significant polarisation dependent effect. Some special polarisation properties of this kind of TFGs were studied and applied in twisting and transverse loading sensing, which will be introduced and discussed in Chapter 5.

4.6. 45°-TFGs INSCRIPTION AND CHARACTERISTICS

4.6.1. FABRICATION OF TFGs WITH 45° TILTED STRUCTURES

The 45°-TFGs were UV-written in hydrogen-loaded B/Ge fibre using a commercial phase-mask with 33.7° tilted pitch pattern. The pitch of the phase-mask was 1800nm (the maximum pitch length for a +1/-1 order phase-mask that Ibsen Ltd can produce), which ensures that the central wavelength of the radiation profile is around ~1500nm. The grating length is 28mm. Fig.4.22 shows the microscope image of a 45°-TFG taken under a 100× objective lens, showing a 45° internal tilt angle. Fig.4.23 (a) and (b) present transmission spectra of this 45°-TFG for s- (blue curve) and p-polarised (red curve) light and the PDL (red curve in Fig.4.23 (b)). In Fig.4.23 (a), two narrow loss-peaks can be seen in both polarised profiles. The peak at longer wavelength side is measured with a wavelength of ~1568nm, almost the half of the Bragg wavelength λ_B calculated based on Equation 4.11. This loss-peak could be the 2nd order Bragg resonance of this 45°-TFG. The peak at shorter wavelength side then may be a ghost mode peak caused by the index asymmetry, arising from UV absorption [191]. From Fig.4.23 (b), we can see that the 2nd order Bragg resonance exhibits a polarisation effect, as we see a wavelength separation of 0.08nm for the two orthogonal polarisation states.

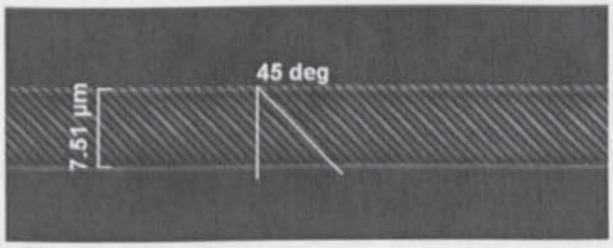

Fig.4.22. Microscope image of a 45°-TFG taken under a 100× objective lens. The measured tilt angle is 45°.

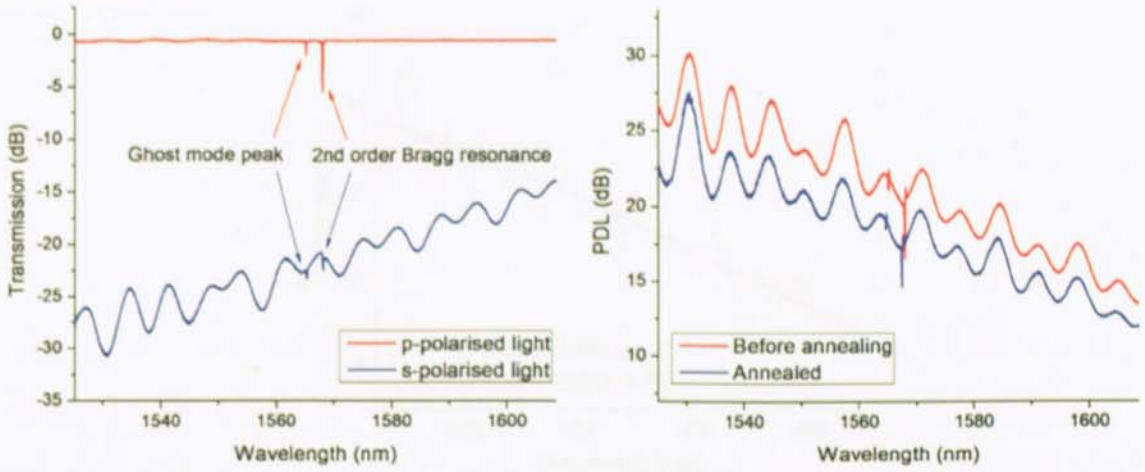

(a) (b)

Fig.4.23. (a) The transmission spectra of a 45°-TFG for s- (red curve) and p-polarised light (blue curve). (b) The PDL of this TFG measured before (red curve) and after (blue curve) annealing.

I then studied the stability of this 45°-TFG by subjecting it into an annealing treatment at 80°C for 48 hours. Fig.4.23 (b) shows the PDL of this TFG measured before and after annealing. From this figure, it is clear that the PDL decreases ~2.4dB and the 2nd Bragg resonance blue shifts ~0.7nm with a reduced Bragg strength.

4.6.2. PDL OF THE 45°-TFG

As described in Zhou's paper [43], the entire PDL profile of the 45°-TFG is near-Gaussian-like and covers a broad wavelength range if a broadband source is used for measurement. Limited by the light source, only the spectrum in the wavelength range from 1525 to 1608nm was measured. The pronounced ripple feature appears in the transmission spectrum is caused by unmatched refractive index at the cladding/air boundary. To eliminate the ripples, the 45°-TFG was immersed in the index-matching gel and a smooth PDL profile was obtained as the blue line shown in Fig.4.24.

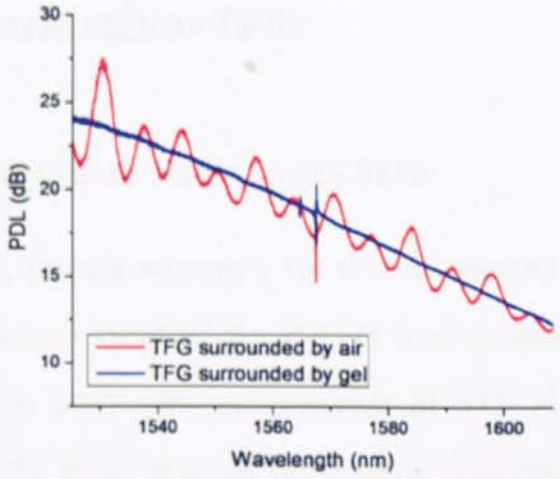

Fig.4.24. The PDLs of the 45°-TFG surrounded by air (red curve) and index-matching gel (blue curve).

From Fig.4.24, it is clear that in the wavelength range from 1525 to 1608nm, the PDL decreases with increasing wavelength except at the wavelength of Bragg resonance and ghost mode peak and the maximum PDL appearing at 1525nm is ~24dB. This great slope may indicate that the maximum PDL is still outside of this wavelength range and on the shorter wavelength side. The slope also suggests that because the broadband source was used it was not possible to achieve maximum PDLs for all wavelengths at the same time with the polariser set at certain status. By employing a tuneable laser and measuring the PDL for different wavelengths as described in [43], an overall PDL profile (TFG surrounded by gel) can be measured with higher amplitude and appear flatter, because the PDLs measured using a broadband source cannot give the maximum values for all wavelengths. Based on the fact that a very high PDL can be achieved over a broad wavelength range, the 45°-TFG can be developed into an in-line polariser. By employing the intrinsic 2^{nd} order Bragg resonance (as shown in Fig.4.23 (a)) and utilising the great PDL of a 45°-TFG as an intracavity component, a fibre laser may be realised giving single wavelength and single polarisation output.

4.7. THERMAL RESPONSES OF TFGS

4.7.1. THERMAL RESPONSES OF SMALL ANGLE TFGS

For small angle TFGs, thermal responses for several selected cladding modes with two orthogonal polarisation states of the 7°-TFG were measured by increasing the temperature from 10 to 60°C with an increment of 5°C. Fig.4.25 (a) shows the wavelength shifts of the three selected polarisation dual-peaks of the 7°-TFG at ~1499.6, 1530.3 and 1555.5nm against temperature changes. Thermal sensitivities for resonances measured from Fig.4.25 (a) are shown in Table 4.1.

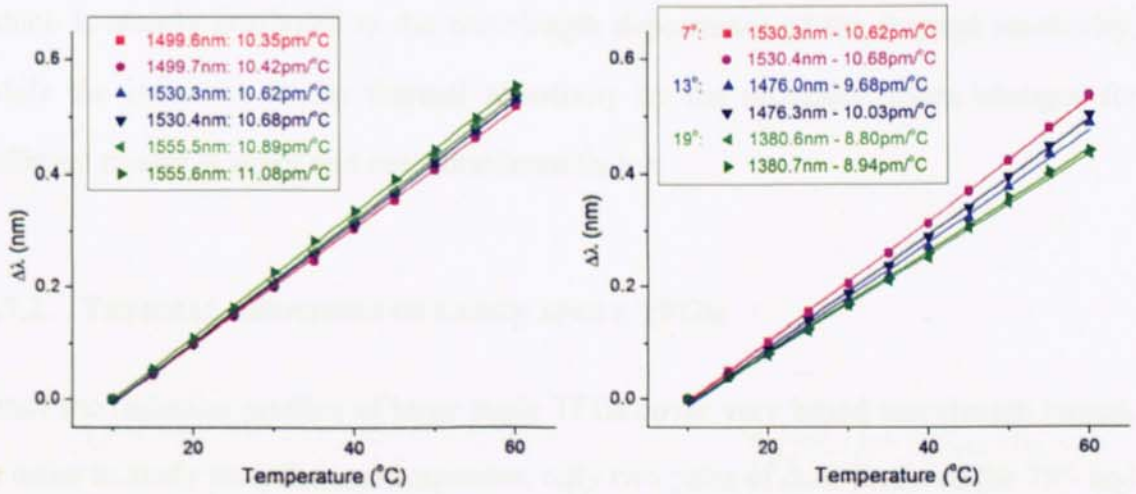

(a) (b)

Fig.4.25. (a) The wavelength shifts of the selected dual-peaks of the 7°-TFG at ~1499.6, 1530.3 and 1555.5nm versus temperature changes. (b) Thermal responses for 7°-, 13°- and 19°-TFG's dual-peaks at central wavelength of the radiation profile.

Table 4.1. Thermal sensitivities for resonances of a 7°-TFG.

Wavelength (nm)	1499.6	1499.7	1530.3	1530.4	1555.5	1555.6
Thermal sensitivity (pm/°C)	10.35	10.42	10.62	10.68	10.89	11.08

All these thermal sensitivities for cladding resonances with wavelengths ranging from 1500-1555nm are in the same order of but slightly lower than reported thermal sensitivities for normal structure FBGs in silica fibre (10.6pm/°C) [18]. From Fig.4.25, it is clear that thermal sensitivities for the same dual-peaks with orthogonal

polarisations are similar but have larger discrepancy for different pairs. The thermal sensitivity increases with increasing wavelength.

Fig.4.24 (b) plots the comparison of thermal responses of one pair of dual-peaks with orthogonal polarisations for the 7°-, 13°- and 19°-TFG at central wavelength of the radiation profile, respectively. Thermal sensitivities for resonances of the 7°-TFG at ~1530nm have been demonstrated in Table.4.1. The measured thermal sensitivities for the resonances of the 13°-TFG at 1476.0 and 1476.3nm are 9.68 and 10.03pm/°C and those for resonances of the 19°-TFG at 1380.6 and 1380.7nm are 8.80 and 8.94pm/°C, respectively. From this figure, we can see that the thermal sensitivity for small tilted structure TFGs at central wavelength decreases with increasing tilt angle, which is mainly attributed to the wavelength dependence of the thermal sensitivity, while the influence to the thermal sensitivity by the refractive index changes for different modes is small and not a dominant factor.

4.7.2. THERMAL RESPONSES OF LARGE ANGLE TFGS

Since the radiation profiles of large angle TFGs cover very broad wavelength ranges, in order to study their thermal responses, only two pairs of dual-peaks of the 75°- and 81°-TFGs at ~1410 and ~1620nm were selected. By increasing the temperature from 10 to 60°C with an increment of 5°C, Thermal sensitivities for these dual-peaks were measured and the results are plotted in Fig.4.26. Thermal sensitivities for the two sets of the dual-peaks of the 75°- and 81°-TFG were measured as shown Table 4.2.

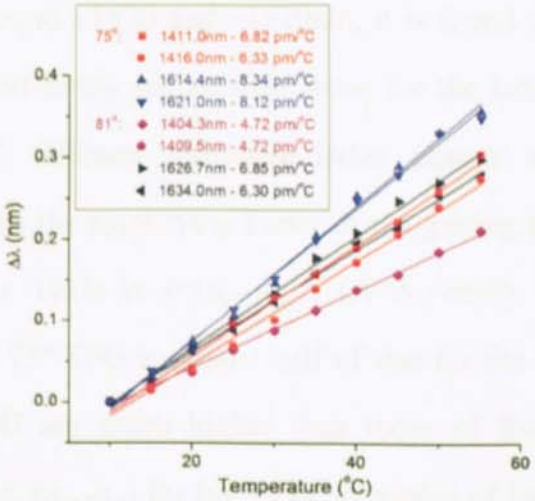

Fig.4.26. Thermal responses for two pairs of dual-peaks of the 75°- and 81°-TFGs at ~1410 and ~1620nm.

Table 4.2. Thermal sensitivities for resonances of a 75°- and an 81°-TFG.

Wavelength (nm)	75°-TFG	1411.0	1416.0	1614.4	1621.0
Thermal sensitivity (pm/°C)		6.82	6.33	8.34	8.12
Wavelength (nm)	81°-TFG	1404.3	1409.5	1626.7	1634.0
Thermal sensitivity (pm/°C)		4.72	4.72	6.85	6.30

It is clear that they are significantly lower than that of normal and small tilted structure FBGs. From these sets of data, it is noted that thermal sensitivities for the dual-peaks with orthogonal polarisations are similar. Quantitatively speaking, the thermal sensitivities for resonances of the 81°-TFG in the range from 1400-1620nm are only half or even less than that of normal structure FBGs around 1550nm range (10.6pm/°C) [18]. This is because the thermal-optic effect on the refractive indices of core an cladding, n_{co} and n_{cl}, will have a cancellation result in the forward-coupling regime (n_{co}-n_{cl}) instead of an adding effect in the backward-coupling regime (n_{co}+n_{cl}). Thus, we see lower temperature sensitivity of the large angle TFGs than that of FBGs with normal and small tilted structures. These results indicate that when these large angle gratings are used in application, the thermal cross-sensitivity induced error is relatively small in comparison with small tilted and normal structure FBGs.

Comparing two sets of dual-peaks of the 75°- and 81°-TFGs in the two same

wavelength ranges around ~1420 and ~1620nm, it is found that thermal sensitivities of the former are significantly higher than those for the latter. This phenomenon is attributed to both (i) different refractive index change against temperature for different modes and (ii) the amplifying factor of the grating period size, as the phase match for large angle TFGs is $\lambda=(n_{co}-n_{cl})\Lambda$ ($\Lambda=\Lambda_G/\cos\theta$). In my experiment, the period size, Λ for the 75°-TFG is almost half of that for the 81°-TFG. But the mode orders of the 75°-TFG are much higher than those of the 81°-TFG in the same wavelength range, thus, $(n_{co}-n_{cl})$ for higher order modes of large angle TFG are more sensitive to temperature change, and this factor influences the general thermal sensitivity more greatly than the amplifying factor. Therefore, the thermal sensitivities for resonances of the 75°-TFG are higher than those for resonances at the same wavelengths of the 81°-TFG.

4.7.3. THERMAL INFLUENCE ON PDL OF 45°-TFGS

As described in section §4.6.2, 45°-TFGs have the potential to be developed into polarisation devices based on their high PDL effect. I then mainly focused on the thermal influence on the PDL of the 45°-TFGs. By subjecting these gratings to elevated temperatures from 10°C to 60°C with an increment of 5°C, it is found that only the resonance ripples changed the shape and shifted irregularly, but no significant total PDL change appeared. This is evident from Fig.4.27 (a) which shows the PDLs of a 45°-TFG measured at temperatures of 10°C, 30°C, 50°C and 60°C, respectively. In order to study the thermal influence on the PDL more accurately, the 45°-TFG was immersed in the index-matching gel and the thermal effect measurement was repeated.

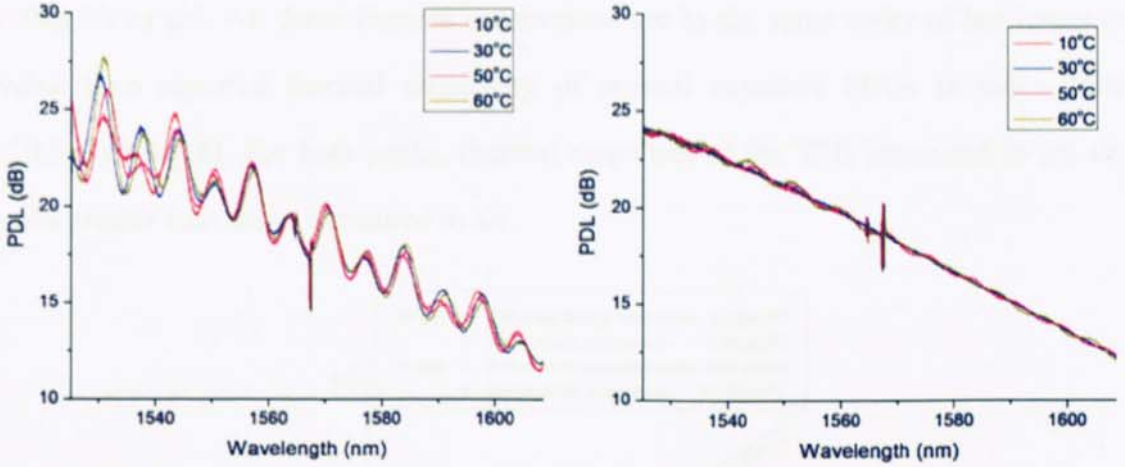

Fig.4.27. PDLs of the 45°-TFG measured at 10°C, 30°C, 50°C and 60°C with the fibre surrounded by (a) air and (b) index-matching gel.

Fig.4.27 (b) shows the PDLs of the 45°-TFG immersed in the gel at temperatures of 10°C, 30°C, 50°C and 60°C, respectively. Now, the existence of very shallow ripples can be seen on the overall PDL profiles, which may be caused by the slightly mismatch of refractive index at the cladding/gel boundary as the refractive index of the gel changes with increasing temperature. From this figure, no significant PDL change with increasing temperature can be found. This is of a great significance for 45°-TFG applications, since the PDL functions of these devices will not affected by environmental temperature fluctuation, providing desirable stability.

Since there is an intrinsic 2nd order Bragg resonance and a ghost peak existing within the PDL profile range of a 45°-TFG, their thermal responses were evaluated as well. Fig.4.28 shows the thermal responses of the 2nd order Bragg resonance and the ghost mode peak measured when the 45°-TFG was surrounded by air and index-matching gel. When the TFG is placed in air, the thermal sensitivities of the 2nd order Bragg and the ghost mode resonance are measured as 9.35 and 9.96pm/°C; when the fibre is surrounded by index gel, those are measured as 9.91 and 10.52pm/°C, respectively. It is clear that the thermal sensitivity of ghost mode resonance is measured slightly greater than that of the 2nd order Bragg resonance with the 45°-TFG surrounded by

either air or gel. All these thermal sensitivities are in the same order of but lower in value than reported thermal sensitivity of normal structure FBGs in silica fibre (10.6pm/°C) [18]. For both peaks, thermal responses of the TFG measured in gel are ~6% greater than those measured in air.

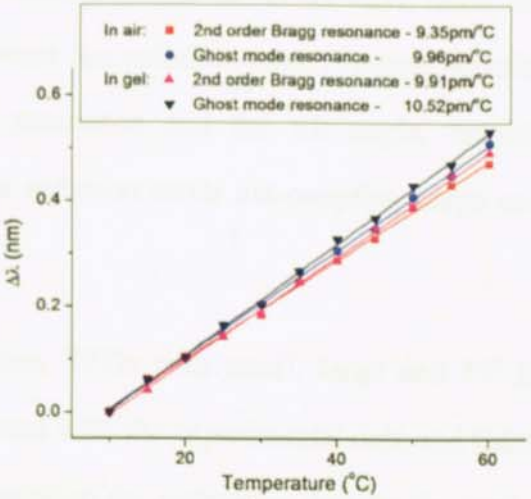

Fig.4.28. The thermal responses of the 2nd order Bragg resonance and the ghost mode resonance measured with the 45°-TFG surrounded by air and index-matching gel.

4.8. *CHAPTER CONCLUSIONS*

In this Chapter, I have firstly and systematically investigated the structures, inscription methods and spectral, PDL and thermal characteristics of TFGs with small, large and 45° tilted structures. Based on the mode-coupling theory, some characteristics of the cladding modes of TFGs have been theoretically analysed, giving relationships between the radiation angle, central wavelength of the radiation profile and the Bragg resonance and the tilt angle, respectively. Furthermore, relationships between the radiation mode out-coupling range and PDL and tilt angle were also introduced.

For studies on real devices, TFGs with small, large and 45° tilted structures were fabricated. Good consistence with the experimental data and the theoretical ones were found, which provide foundation for optimising designs for grating devices with tilted structures. For small and large angle TFGs, I have examined in detail the polarisation effect on coupled cladding mode resonances, such as polarisation induced mode separation and shift for different wavelength ranges. For 45°-TFGs, the PDL effect was analysed in the wavelength range from 1525-1608nm and a 2^{nd} order Bragg resonance was found at the ~1568nm, which may be used in combination to realise fibre laser with single polarisation and single wavelength output. It is also discovered that the PDL ripples can be greatly eliminated by immersing the 45°-TFG in index matching gel and by doing this a very smooth PDL response can be achieved over a very broad wavelength range.

Finally, thermal responses have been measured for these three types of TFGs. For small angle TFGs, thermal sensitivities of three pairs of dual-peaks with orthogonal polarisation states of a 7°-TFG in the wavelength range 1500-1555nm were measured, obtaining the thermal sensitivities ranging from 10.35-11.08pm/°C, which were in the same order of but slightly lower than reported normal structure FBGs made in silica

fibre. Thermal sensitivities then were measured for dual-peaks with orthogonal polarisations for 7°-, 13°- and 19°-TFG, showing a trend that the thermal sensitivity of small angle TFG decreases with increasing tilt angle. The thermal property investigation on TFGs with two large tilted structures at 75° and 81° were carried out. For comparison, thermal sensitivities of two paired polarisation dual-peaks for 75°- and 81°-TFGs at ~1410 and ~1620nm were measured, respectively. For dual-peaks in a similar wavelength range, thermal sensitivities for 75°-TFG resonances are higher than those for 81°-TFG resonances. It is noted that thermal sensitivities for resonances of 81°-TFG in the range from 1400-1620nm are very low (~6.85pm/°C), which are only half or even less than that of small tilted and normal structure FBGs at 1550nm, giving application advantage of low thermal cross-sensitivity. The investigation carried out on 45°-TFGs clearly show that no significant PDL change was found by variation of temperature. This is of a desirable application advantage as all 45°-TFGs can be used as in-fibre high polarisation function devices with great stability.

Chapter 5

Applications of Fibre Gratings with Tilted Structures

5. Applications of Fibre Gratings with Tilted Structures

5.1. INTRODUCTION

Since the first report of TFGs by Meltz *et al.* in 1990 [93], a range of applications using TFGs have been reported including an in-fibre spectrometer [31], WDM channel monitoring [32], EDFA gain flattening [33] and optical sensor interrogation systems [34-38]. Because of their unique polarisation property, TFGs have also been implemented as in-line polarimeters [39, 40], polarisation dependent loss equalisers [41, 42], and high-extinction-ratio polarisers [43].

However, in all these reports, the grating structures were tilted at relatively small angles or at most 45°, therefore, the light is only coupled from the forward-propagating core mode to backward-propagating cladding modes or to radiation modes. Recently, Zhou *et al.* reported the theoretical and experimental investigation of TFGs with tilted structures larger than 45° [185], revealing the characteristics of forward propagating mode coupling and demonstrating the advantages of temperature, strain and refractive index sensitivities [186-188]. The unique characteristics of large angle TFGs have great potential to be applied in optical sensing.

Based on the spectral characteristics discussed in chapter 4, this chapter will report the applications of TFG devices with tilted structures at small and large angles based on their unique properties of cladding and radiation mode coupling, including 800nm 10°-TFG based interrogation system and 81°-TFG based twist and load sensing systems. Firstly I will report the 800nm 10°-TFG based interrogation system will be reported, which is a typical application of the small angle TFG and can be utilised as a spectrometer or refractive index sensor. After that, I will demonstrate the 81°-TFG based transverse load and twist sensing system, which is the application of the large

angle TFG and can transfer the load and twist change to the change of the polarisation and to be measured. Finally, conclusions will be drawn at the end of this chapter.

5.2. *800NM 10°-TFG BASED SIDE DETECTION SYSTEM*

The first TFG patent was filed by Meltz *et al* [192] following their 1990 publication of the potential applications of TFGs as optical taps [93]. Since then, some TFG based interrogation techniques including a system which consists of three TFGs separated in wavelength and three photo-detectors [31], a spectrometer composed of a chirped TFG and a detector array (addition of chirp has been recognised [193] to give such a tap the ability to focus the light) and a demodulation system which consists of a TFG, convex lenses and a charge-coupled device array (CCD-array) [37] have been reported.

This section demonstrates an 800nm-interrogation system based on TFG-convex lens-CCD structure developed from the 1550nm-interrogation system reported by Simpson *et al* [37] by utilising the same WDM interrogation principle. As most commercial CCD-arrays are sensitive and low-cost in 800nm range, and the light sources covering 800nm wavelength range are cheaper than that in 1550nm range, 800nm-interrogation system has the advantages of low-cost, compact size, and ability to interrogate multiplexed information over wavelength range for 800-850nm.

With a fixed probe light, the system can also be applied to measure the surrounding-medium refractive index (SRI) of the TFG. Thus, the spectrum analyser system has the capability of detecting bio/chemical samples, which may have a potential use for medicine, environmental monitoring and life science applications.

5.2.1. SYSTEM SETUP AND CONFIGURATION

5.2.1.1. Principle of interrogation system

The 800nm-interrogation system is a TFG-convex lens-CCD structure, the schematic

diagram of which is shown in Fig.5.1.

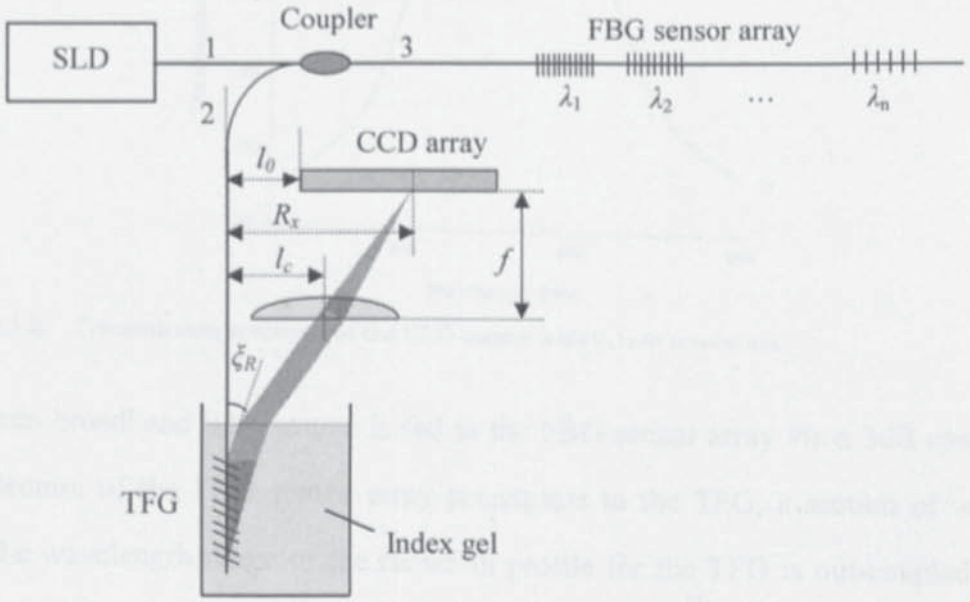

Fig.5.1. Schematic diagram of the apparatus used for the 800nm TFG-CCD interrogation system.

A pigtailed super luminescent diode (SLD)-371, made by Super-lum Ltd., is used as a broadband light source. The transmission spectrum of the SLD plotted in Fig.5.2 is measured by an optical spectrum analyser (OSA) with the resolution of 0.1nm, showing a centre wavelength of 830nm, the full optical bandwidth of 60nm (800-860nm) and the output power is higher than -40dBm. Since the radiation profile of a TFG is determined by the period of the grating and the tilt angle, it is possible to achieve the whole spectrum bandwidth of SLD light source by adjusting the tilt angle of TFG in the range 7° - 13°.

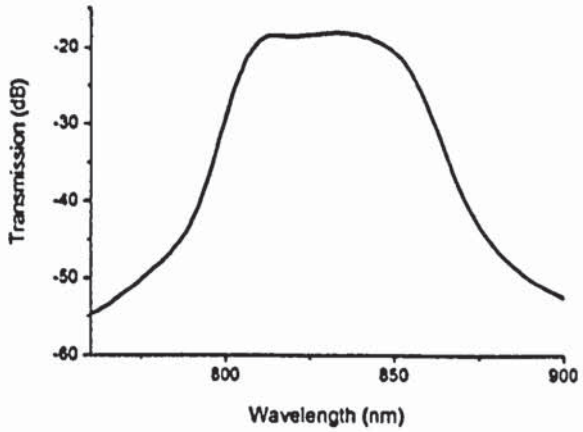

Fig.5.2. Transmission spectrum of the SLD output with 0.1nm resolution

Light from broadband light source is fed to the FBG sensor array via a 3dB coupler. The reflection of the FBG sensor array propagates to the TFG, a section of which within the wavelength range of the radiation profile for the TFG is out-coupled and irradiated to the CCD-array. As discussed in section §4.3.2.1, the direction (ξ) of radiation mode coupling from the fibre core to cladding is related to the parameters of TFG and the fibre used, *i.e.*

Equation 4.7 $$\tan\xi = \frac{\lambda \sin\theta}{\lambda\cos\theta - n\Lambda_G}$$

Therefore, when the fibre is immersed in the gel with the refractive index of n_x, the radiation angle ξ_R in index gel indicated in Fig.5.1 is derived as:

Equation 5.1 $$\sin\xi_R = \sin\xi \cdot \frac{n_x}{n}$$

A 10°-TFG fabricated in 820nm-SMF was selected for this interrogation experimental system. Based on Equation 4.7, the calculated radiation angle in the fibre cladding ξ is ~20°. The refractive index of the gel, which the TFG immersed in, is very close to that of the fibre cladding; hence the radiation modes in the fibre out-couple into the air. The CCD-array could record the signals of far-field radiated light focused by the convex lens which is related to the wavelength change of sensing FBGs. Therefore,

the reflection spectrum of sensing FBGs can be obtained from the CCD signals based on the spectral-spatial transformation function.

5.2.1.2. Spectral property of the sensing FBG and 10°-TFBG

A 10°-TFG used for light out-coupling, fabricated in hydrogen-loaded 820nm-SMF using phase-mask method, has been selected for this interrogation experimental system. Fig.5.3 (a) depicts the transmission spectrum of the TFG. The resonances are resulted from core-cladding coupling, by immersing the TFG into index-matching gel, which can be replaced by a smooth envelop profile representing the coupling to a continuum radiation modes. The radiation range of this 10°-TFG is ~30nm (800-830nm).

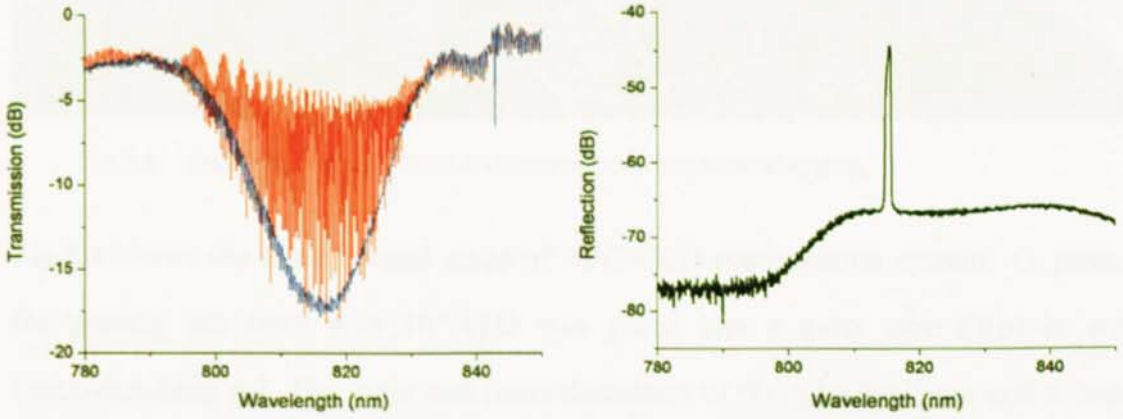

(a) (b)

Fig.5.3. (a) Transmission spectrum of a 10°-TFG. The comb-like resonances are measured with the TFG in air; whilst the smooth curve is measured with the TFG immersed in the index-matching gel. (b) Reflection spectrum of a sensing FBG

Several FBGs used as grating sensors with the wavelengths of Bragg resonances in the TFG radiation range (800-830nm) were fabricated by UV-inscription in hydrogen-loaded 820nm-SMF employing the two-beam holographic technique. Fig.5.3 (b) shows one of the FBG reflection spectra with a Bragg resonance at 816.4nm.

5.2.1.3. Setup of TFG-CCD interrogation system

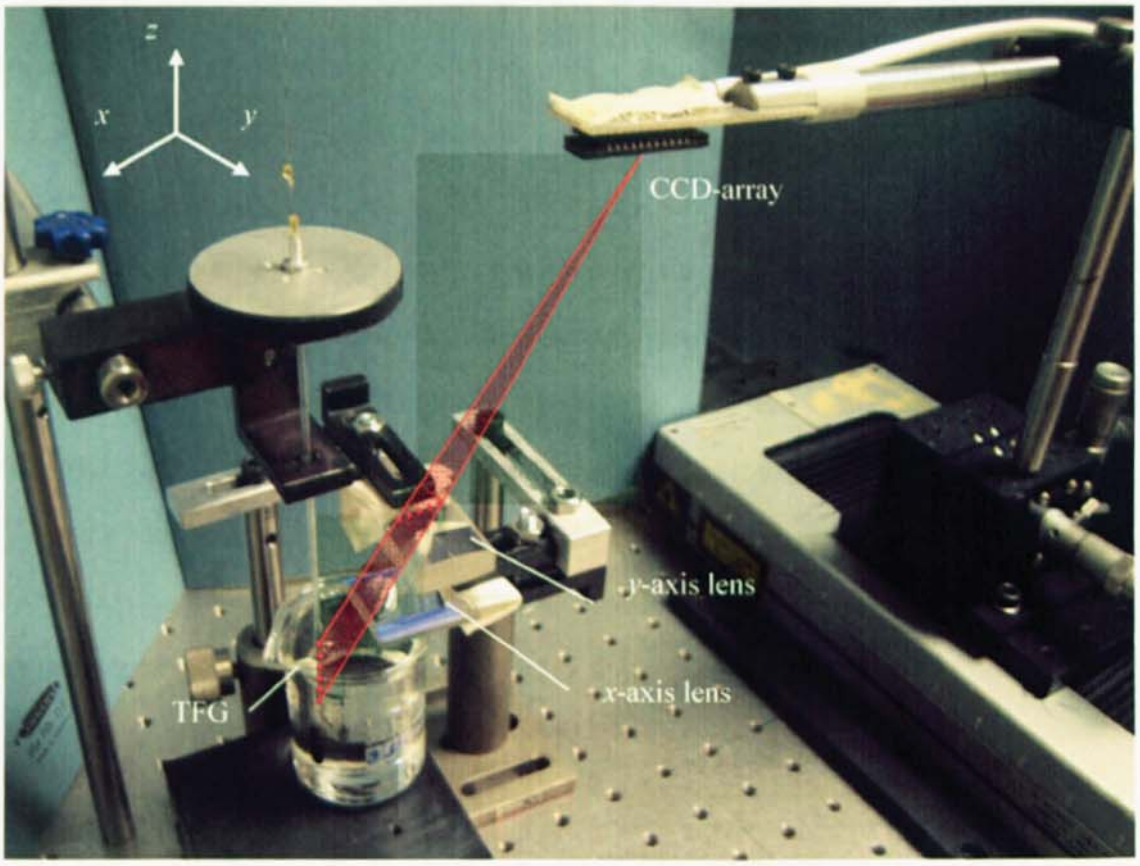

Fig.5.4. Photograph of the TFG-CCD interrogation experiment system.

Fig.5.4 shows the experimental setup of TFG-CCD interrogation system. To protect the grating, the fibre with 10°-TFG was glued into a glass tube filled in with index-matching gel. The outer and inner diameters of the tube are 2mm and 0.7mm, respectively. The higher position end of the tube is mounted on a rotational stage adjusting the direction of the radiated light to the CCD-array. The refractive index of the gel which the TFG and glass tube immersed in is very close to that of the fibre cladding; hence the radiation mode light of the TFG out-couples into the air. Two cylindrical lenses are used to focus the light radiated from the TFG onto the CCD-array along the *x*- and *y*-axis, respectively. The one on the top is the master lens, by which the bandwidth and the resolution of the spectrometer system are defined. The other lens with the focal length of 5cm situated below the first one is used to enhance the intensity of the radiation light. Without any attribution to the sensing

function, the second lens is not drawn in the schematic diagram shown in Fig.5.1.

A SONY ILX511 linear CCD-array is used as the detector array. The device is comprised of 2048-14μm pixels and is shown below with dimensional details in Fig.5.5 (a). CCD-arrays are desirable to use in comparison with photodiode arrays because they offer longer arrays with smaller pixel size at a fraction of the cost of an InGaAs photodiode array. CCD-arrays are most sensitive to light in the visible portion of the spectrum. From the spectral sensitivity (as shown in Fig.5.5 (b)) given by the manufacturer, this type of CCD-array is intrinsically sensitive to 800nm-illumination. Compared with 1550nm-interrogation system reported by George *et al* [37], the CCD-array can be directly used for detection in 800nm system without coating, which reduces the cost in coating and avoids the highly nonlinearity of the response in measurement spectral range.

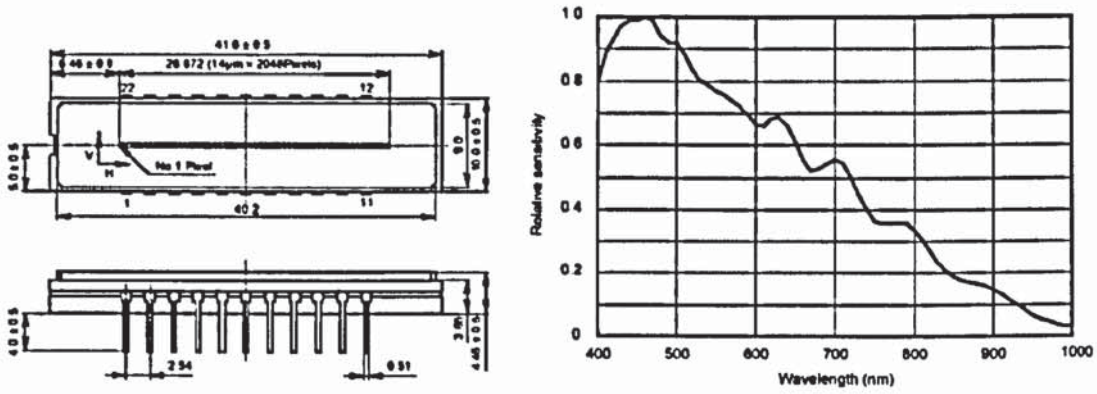

(a) (b)

Fig.5.5. (a) The physical dimensions of Sony ILX511 CCD-array; (b) the relative sensitivity to 400 - 1000nm radiation range.

The CCD-array is positioned along *x*-axis in the focal plane of *y*-axis cylindrical lens as shown in Fig.5.4 and mounted on a computer-controlled translation stage moveable along *y*-axis direction.

5.2.1.4. System alignment

In order to align the system, a 633nm He-Ne was initially coupled to the TFG input and therefore radiated outwards by the grating. A screen in the *x*-*y* plane was placed at the position of CCD-array shown in Fig.5.4. Consequently, the orientations of the TFG and CCD-array were approximately set using the visible output. Subsequent alignment and focusing were achieved with the real-time feedback of the CCD-array using SLD light source.

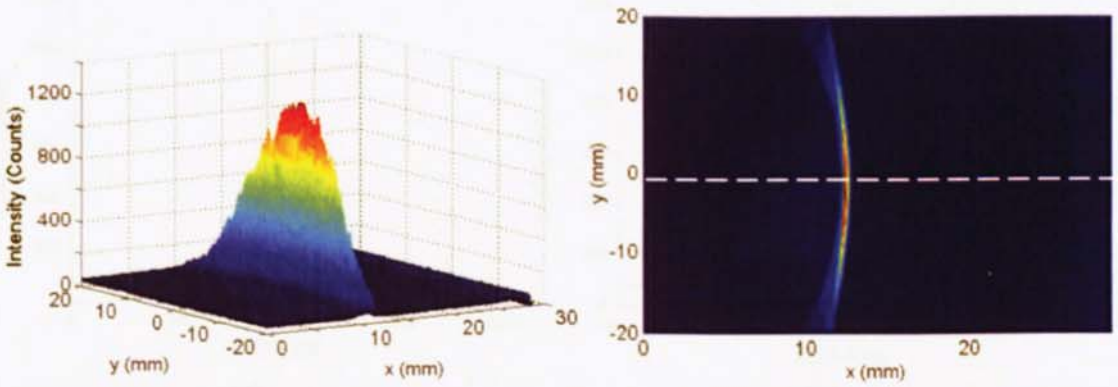

(a) (b)

Fig.5.6. Far-field image of radiated light captured by CCD-array: (a) 3D-image; (b) contour plot in *x*-*y* plane. The dashed line in (b) indicates the centre position where the TFG radiated light is the strongest.

The CCD-array was then placed along the *x*-axis and scanned along *y*-axis. The distribution of the radiation beam in the *x*-*y* plane out-coupled by the TFG and focused by cylindrical lenses can be captured by the CCD-array and displayed on a PC. Fig.5.6 (a) and (b) demonstrate a 3D-image intensity plot and a contour plot of the radiation pattern. Both shape and intensity of the pattern are approximately symmetrical to the dashed line. As long as a good alignment achieved, the radiation pattern distributes always symmetrically to this line and shifts along it when the experimental factors (the reflection wavelength of the sensing FBG and the refractive index of the surrounding gel, *etc*) change.

5.2.1.5. CCD-detected signal and pixilation

With the CCD-array positioned at the centre of the radiated light (the dashed line shown in Fig.5.6 (b)), an example of the radiation signal captured by the CCD-array is shown in Fig.5.7 (a). Once the experimental factors, such as the reflection wavelength of the sensing FBG and the refractive index of the surrounding gel change, the signal shifts along the CCD-array at the same time. Therefore, the change of experimental factors to be measured can be decoded from the shift of the signal.

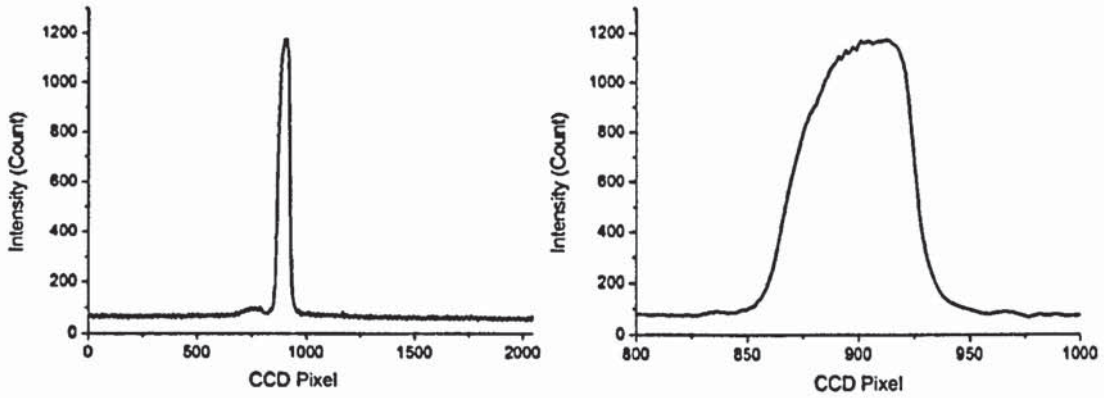

Fig.5.7. (a) Examples of signal captured by the CCD-array along the dashed line plotted from 0 to 2047 pixels; (b) Zoomed signal plotted from 800 to 1000 pixels.

Pixilation is a simple consequence of the finite width (14μm) of the pixels used in the CCD-array and represents the minimum physical resolution of the system. Fig.5.7 (b) shows the zoomed signal plotted in Fig.5.7 (a), from which it is clear that this signal can be hardly represented by just using the pixel reading corresponding to the maximum intensity which will not give the most accurate results. Therefore a function is demanded to transfer the signal profile to radiation wavelength. This problem may be addressed in software with simple techniques which significantly improve the system performance and fractionise the basic detection unit of the CCD-array - pixel - to achieve a finer resolution of the system. There are many different algorithms which can be applied to a dataset to improve the resolution [194] and there would be little worth in reviewing them in this thesis; suffice to say that one of the simplest

approaches yields excellent results and requires only minimal computation time. The centroid detection algorithm (CDA) takes the amplitude weighted mean of the data according to the following equation [195]:

Equation 5.2
$$\hat{x} = \frac{\sum_{1}^{2048} x_i \cdot y_i (> y_{\min})}{\sum_{1}^{2048} y_i}$$

where $\hat{x}$ is the centroid fitted peak value, x_i is the wavelength of the *ith* element and $y_i(> y_{\min})$ is the amplitude of the *ith* element greater than the noise floor $y_{\min}$.

5.2.2. SPECTRUM ANALYSER FUNCTION

The side detection system was originally used as a spectrometer, and the relationship between the radiation angle ξ_R in the gel and the wavelength of the radiation light could be deduced from Equation 4.7, 5.1 and 5.2. In the following subsection, I will introduce the spectrum analyser function of the 800nm TFG-CCD based side detection interrogation system.

5.2.2.1. System bandwidth and resolution

It is a trade-off which must be balanced between the resolution and bandwidth in this system, since the wider the bandwidth of the system is, the lower the resolution will be. The system bandwidth is limited by the detection length of the CCD-array, the focal length of the lens and the radiation range of the TFG. With the given 10°-TFG and CCD-array, the bandwidth of the system is only determined by the focal length, which may be simply calculated by multiplying the spectral resolution and the number of pixels. The system parameters (bandwidth, spectral resolution) for two focal

lengths are calculated as shown in Table 5.1:

Table 5.1. System parameters summary for two lenses

Focal length(mm)	Bandwidth (nm)	Gradient (nm/mm)	Physical resolution (pm/pixel)
45	60	3.34	46.6
155	26	0.91	12.7

Considering the radiation profile of the 10°-TFG from 800nm to 830nm and using the maximum length of the CCD-array, a cylindrical lens with a focal length of 155mm was employed in the experimental system, therefore the bandwidth and resolution of the system are 26nm and 12.7pm respectively.

5.2.2.2. Transfer function

Since the interrogation system is based on the spectral-spatial encoding function of the TFG-CCD structure, the correlation between the wavelength shift and the CCD pixel needs to be calibrated first.

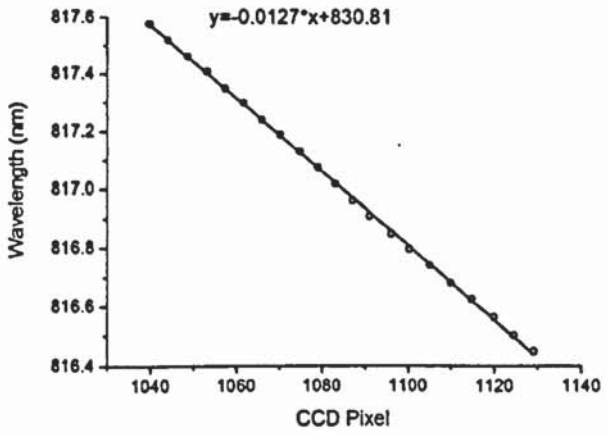

Fig.5.8. The relationship between the Bragg wavelength shift and the CCD pixel reading of this 800nm-interrogation system is linear fitted (straight line) from the experimental data (circles).

The transfer function was obtained by implementing a strain sensing experiment. An FBG with 816.45nm Bragg resonance was employed as sensor inserted between the

port-3 of the 3dB coupler and an OSA. With tension applied on the FBG, its wavelength drifting was monitored by an OSA and our interrogation system at the same time. Fig.5.8 shows the linear relationship between the Bragg wavelength and the CCD reading of this 800nm-interrogation system using a lens of 155mm focal length. The conversion coefficient is 12.7pm/pixel, thus the spectral resolution of the system is 12.7pm. The root mean square (RMS) of the residuals is 6.01pm.

5.2.2.3. Strain and temperature sensing interrogation

Fig.5.9 (a) shows the spectral shifts of a sensing FBG with a Bragg resonance at 816.5nm measured by the TFG-CCD interrogation system when the strain on the grating increased from 0 to 1904.8με, whilst Fig.5.9 (b) shows the results of the same FBG measured when the temperature changed from 0 to 60°C with an incremental step of 2°C. From Fig.5.9 (a) and (b), the strain and temperature sensitivities are estimated as 0.59pm/με and 5.6pm/°C respectively, which are in good agreement with the reported typical results of 0.64pm/με and 6.8pm/°C near the wavelength of 830nm [229].

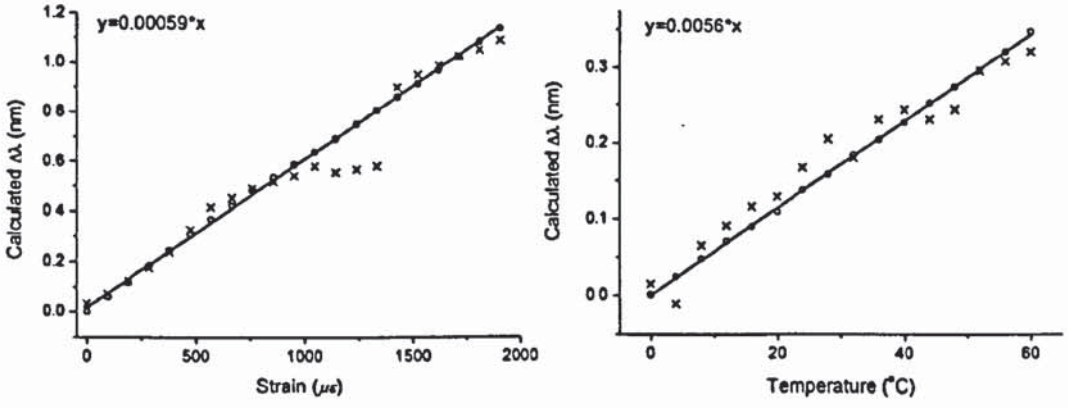

(a) (b)

Fig.5.9. Spectral shift measured by the interrogation system against (a) strain and (b) temperature on sensing FBG. In both (a) and (b), the points marked with 'o' are the data obtained by CDA; whilst those marked with '×' are simply obtained from maximum reading.

The points marked with 'o' in Fig.5.9 represent the shift in the Bragg wavelength

calculated by the CDA, whilst those marked with '×' are the values calculated simply on maximum points of the signals. The RMSs of the residuals for strain experiment are 8.61pm and 75.7pm for CDA and maximum point methods respectively. And those for temperature experiment are 1.66pm and 20.6pm for CDA and maximum point methods respectively. It is clear that the CDA improves the system performance significantly.

5.2.2.4. System stability analysis

Stability is an important factor to consider when designing a sensor interrogation system. The change over time in practical experiment is a contributing factor to overall system error. To model this, the system was used to monitor the reflected spectrum from a sensing FBG, held at the temperature of 20°C, for approximately 45 min with a sample rate of 1Hz.

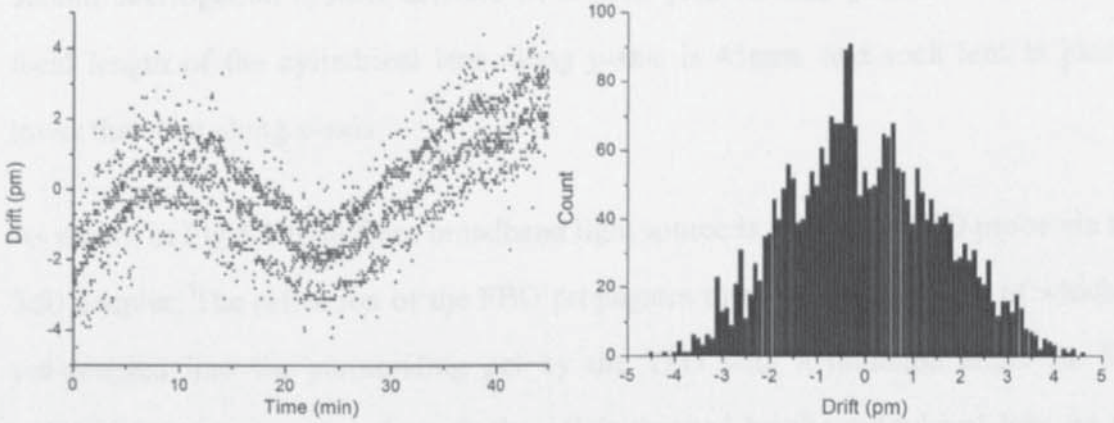

(a) (b)

Fig.5.10. Spectral drifts over time of the sensing FBG measured with the TFG-CCD system: (a) Wavelength shifts of λ against time. (b) Histogram to show the distribution of the spectral drifts over a 45-min period.

Fig.5.10 (a) shows the wavelength drifts recorded over a period of 45 min. The slow fluctuation in the central wavelength may be induced by the perturbation of room temperature of ±0.5°C. Fig.5.10 (b) shows a histogram displaying the distribution of the spectral drifts that clearly forms a normal distribution. The RMS deviation from

the mean of this histogram is merely 1.6pm, which indicates that the system is inherently stable.

5.2.3. REFRACTIVE INDEX SENSING FUNCTION

With a fixed reflection wavelength of the probe FBG, the system can also be applied to measure the surrounding-medium refractive index (SRI) of the TFG. Thus, the above described spectrum analyser system has the capability of detecting bio/chemical samples, which may have a potential use for medicine, environmental monitoring and life science applications.

5.2.3.1. Principle and setup of the refractive index sensing function

The setup of the refractive index sensing system is almost the same as that of 800nm-interrogation system detailed in section §5.2.1.3 and §5.2.2 except that the focal length of the cylindrical lens along *y*-axis is 45mm, and such lens is placed lower than that along *x*-axis.

As shown in Fig.5.1 light from broadband light source is fed to the FBG probe via the 3dB coupler. The reflection of the FBG propagates to the TFG, a section of which is out-coupled into the surrounding gel by the TFG with a radiation angle ξ_R. The radiated light propagating through the gel is focused by the cylindrical lens on the CCD-array which is placed at the focal plane. As the discussion in Section 5.2.1.1, the direction (ξ) of radiation mode coupling in the fibre cladding is calculated as ~20° based on the Equation 4.7 when a 10°-TFG is employed in the system. With the given tilted angle θ, the distance from the fibre to the focus point along *x*-axis in Fig.5.1, R_x (named as radiation radius) is related to the refractive index of the gel, n_x as follows:

Equation 5.3 $$R_x = l_c + f\sqrt{\frac{n_x^2 - n^2\cos^2\xi}{1 - n_x^2 + n^2\cos^2\xi}}$$

where l_c represents the distance between the centre of the cylindrical lens and the fibre along x-axis, f is the focal length of the cylindrical lens and n is the refractive index of the fibre.

With a selected position in the CCD-array, the relationship between the CCD pixel and the radiation radius can be derived as:

Equation 5.4 $$N_x = (R_x - l_0)/0.014$$

where, l_0 represents the distance between the first (No. 0) pixel in the CCD-array and the fibre along x-axis indicated in Fig.5.1, and 0.014 is the length of one CCD pixel in mm.

From the Equation 5.3, we can derive the refractive index change of the sample liquid, n_x, which has a limited dynamic range as:

Equation 5.5 $$n\cos\xi < n_x < \sqrt{1 + n^2\cos^2\xi}$$

Substituting the system parameters: ξ and n, the measurable SRI range n_x is limited from 1.362 to 1.689.

When the refractive index of the sample liquid varies, the radiation beam illuminates the CCD-array at the different position. Therefore, the refractive index of the sample liquid can be decoded from the CCD signals.

5.2.3.2. The refractive index liquids

In the experiment, I employed glycerin (molecular formula: $C_3H_5(OH)_3$, the refractive

index: 1.4735) solution as sample liquid, which is soluble in water in any mixing ratio. Theoretically, the glycerin solution can be produced with the refractive index from 1.3333 (the refractive index of the water) to 1.4735, which provides a good dynamic range for the SRI experiment. Table 5.2 shows the refractive indices of the glycerin solutions with some volume mixing ratio.

Table 5.2. The refractive indices of the glycerin solutions with some volume mixing ratio.

Volume ratio (Glycerin: Liquid)	0	0.1	0.2	0.3	0.4	0.5
Refractive index	1.333	1.34531	1.35804	1.37119	1.38476	1.39875
Volume ratio (Glycerin: Liquid)	0.6	0.7	0.8	0.9	1	
Refractive index	1.41316	1.42799	1.44324	1.45891	1.4735	

5.2.3.3. The limitation on measurement range induced by the dimension of cylindrical lens

Similar to the spectroscopy system, the dynamic range here is also limited by the focal length of the cylindrical lens and the size of the detecting area of the CCD-array. Substituting the system parameters: l_c=24mm, n=1.446 and considering a common SRI range from 1.3712 to 1.4735, the radiation radius, R_x, can be calculated according to Equation 5.3. Table 5.3 lists the calculated values of R_x for two focal lengths: 45mm and 155mm.

Table 5.3. The radiation radii using different cylindrical lenses

n_x	1.333	1.34531	1.35804	1.37119	1.38476	1.39875
R_x (f=45mm)	-	-	-	31.52	35.82	39.29
R_x (f=155mm)	-	-	-	49.90	64.72	76.66
n_x	1.41316	1.42799	1.44324	1.45891	1.4735	
R_x (f=45mm)	42.46	45.52	48.57	51.74	54.74	
R_x (f=150mm)	87.58	98.13	108.70	119.56	129.89	

Considering that the detection-length of CCD-array is 28mm, from Table 5.3, it can be seen that with given $l_0 \sim 33$mm and for SRI range from 1.3712 to 1.4735, a lens of 45mm focal length is more suitable for using most CCD-array detection area.

However, in real experiment, the measurement range is also limited by the size of the cylindrical lens, as the lens cannot be placed very close to the TFG. From Fig.5.11 (a), with given cylindrical lens, when different sample liquids were employed, the radiation pattern illuminated to different position of the cylindrical lens along x-axis and covered different area, which has been depicted in Fig.5.11 (a) and (b).

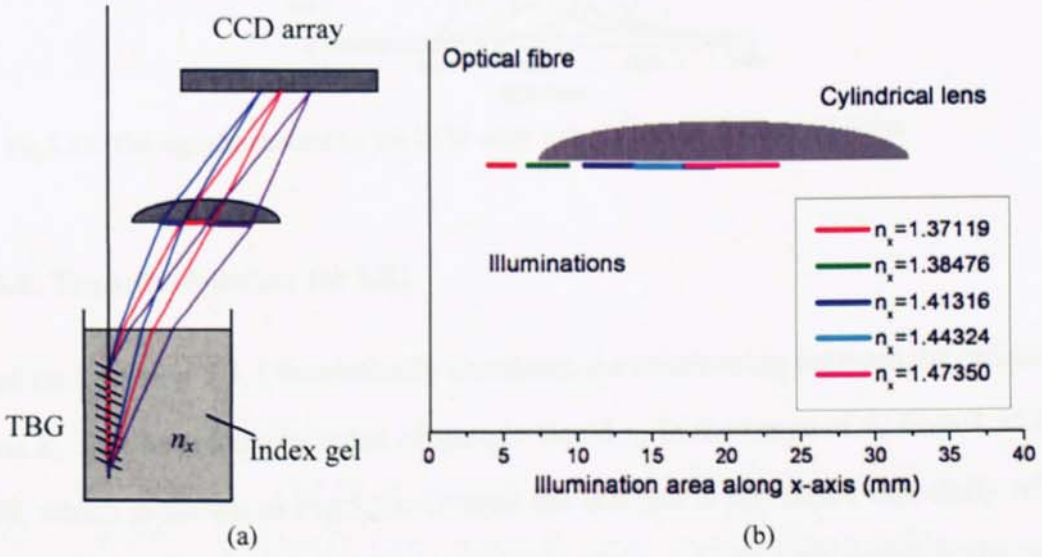

Fig.5.11. (a) The schematic diagram of the illuminations with different sample liquids. (b) The calculated illuminations positions and areas of the output light at the optical plane of cylindrical lens along x-axis when sample liquids with different refractive index were employed.

In Fig.5.11 (b), it is found that the lower refractive index of the sample liquid is used, the less distance between the illumination on the cylindrical lens and the optical fibre along x-axis would be and the smaller area the illumination pattern covered. Fig.5.12 shows the signals detected by the CCD-array using different sample liquids with SRIs above 1.4 at the same fluid level, from which it is found that when the radiation pattern illuminates the edge of the cylindrical lens along x-axis, the amplitude of the CCD signal reduces and the noises increases at the same time. On the other hand, for

practical reason, the cylindrical lens cannot be placed contiguously to glass tube housing the optical fibre and the edge of the cylindrical lens cannot focus the light well. During our experiment, it has been recognised that light will not be collected and focused effectively by the cylindrical lens when the refractive index of the liquid is below 1.4.

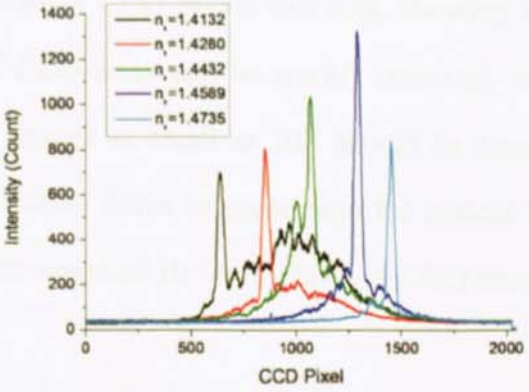

Fig.5.12. The signals detected by the CCD-array using different glycerin solutions

5.2.3.4. Transfer function for SRI

Based on Equation 5.3, I theoretically simulated the relationship between the radiation radius R_x and the refractive index of sample liquid n_x in the range of n_x from 1.362 to 1.689, which is shown in Fig.5.13. Overall the relation is nonlinear, especially when n_x is close to 1.689; however, it is nearly linear from 1.41 to 1.48, which is the most common range for bio/chemical sensing applications.

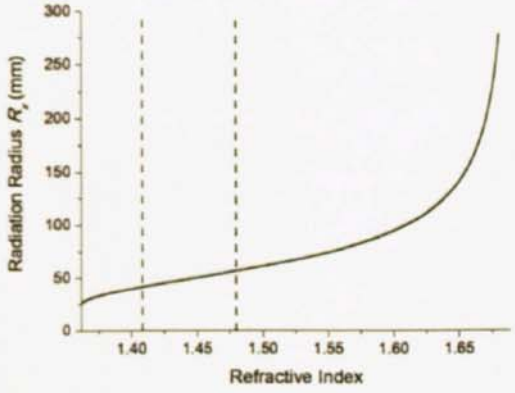

Fig.5.13. The theoretical simulation of the relationship between the radiation radius R_x and the refractive index of sample liquid n_x in the range from 1.362 to 1.689.

5.2.3.5. Experimental results

Considering the length of the CCD-array and the size of the cylindrical lens, sample liquids with refractive indices in the almost linear range (1.41 ~ 1.48) of the simulation curve were selected in Fig.5.13. The refractive indices of sample liquid n_x used in the experiment varied from 1.4132 to 1.4735. Based on Equation 5.4, Fig.5.14 plots the correlation between CCD pixels and SRI, showing a near-linear response. Since a single pixel of CCD-array can be readily resolved, from the plot it can be estimated that the SRI change as small as 10^{-5} should be detectable by this system. Considering that the detection limits of some reported optical fibre based biosensors are in the refractive index range of 10^{-4}-10^{-7} [228], my SRI sensor has the potential to be used as a biosensor.

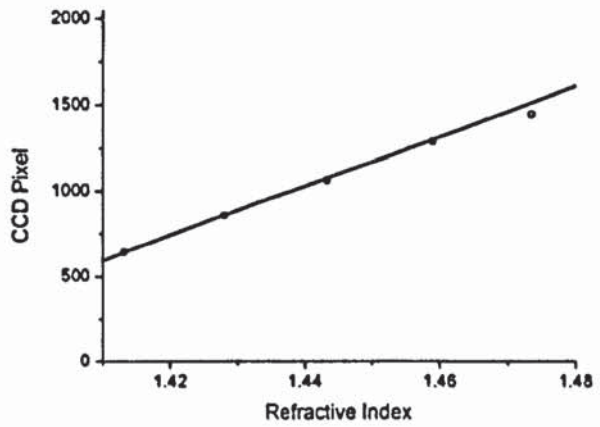

Fig.5.14. The CCD pixel shift against refractive index change in the range from 1.41 to 1.48.

5.3. *LARGE ANGLE TFG BASED SENSING APPLICATION*

TFGs with relatively large tilt angle have shown not only the forward mode coupling characteristics but also a strong polarisation dependent spectral response. These properties have been utilised to implement in-fibre polarimeters [39, 40], PDL equaliser [41, 42] and high extinction ratio polarisers [43]. Recently, Zhou *et al* reported the successful implementation of optical sensors based on large angle TFGs, showing forward-propagating operation and strong polarisation dependence. These devices' responses to temperature, strain and SRI have been evaluated, demonstrating a significantly lower thermal sensitivity and higher strain and SRI sensitivities than normal or slightly tilted FBGs and conventional LPGs [186]. The intrinsically low thermal cross-sensitivity which has been further verified in chapter 4 and narrow spectral responses of such TFGs are particularly attractive as optical sensors which require low thermal cross-sensitivity and high resolution measurement.

In this section, I will demonstrate the large angle TFG based transverse load and twist sensors. With the application of their distinctive polarisation properties, these sensors are capable of transferring the load and twist change to the polarisation spectral evolution to be measured optically. Because the measurement using our sensors can be intensity based, the bulky and expensive OSA is not necessary and the sensing system can be developed using low-cost and high sensitivity sensors by employing cheap single wavelength light sources and photodiodes. With the surrounding temperature change, the grating peaks will shift at the same time. Thus errors may be induced by the thermal cross-sensitivity effect, which is one of disadvantages of such intensity based sensors.

5.3.1. POLARISATION EFFECT AND FABRICATION OF THE LARGE ANGLE TFGS

5.3.1.1. Polarisation effect of the large angle TFGs

With the tilted grating structure, the fibre core of TFG becomes asymmetric along the equivalent slow-axis as shown in Fig.5.15 (a), thus inducing a birefringence in the fibre especially when $\theta > 45°$. As experimentally observed, large angle TFGs exhibit pronounced polarisation mode splitting [185]. In analogy to a polarisation-maintaining (PM) fibre, two orthogonal polarisation axes to a large angle TFG structure may be assigned. As shown in Fig.5.15 (a), the direction perpendicular to the grating fringe plane may be regarded as the fast-axis and the direction in the plane as the slow-axis. The effective refractive index along the fast-axis and slow-axis can then be expressed as n_f and n_s, and we have $n_f < n_s$.

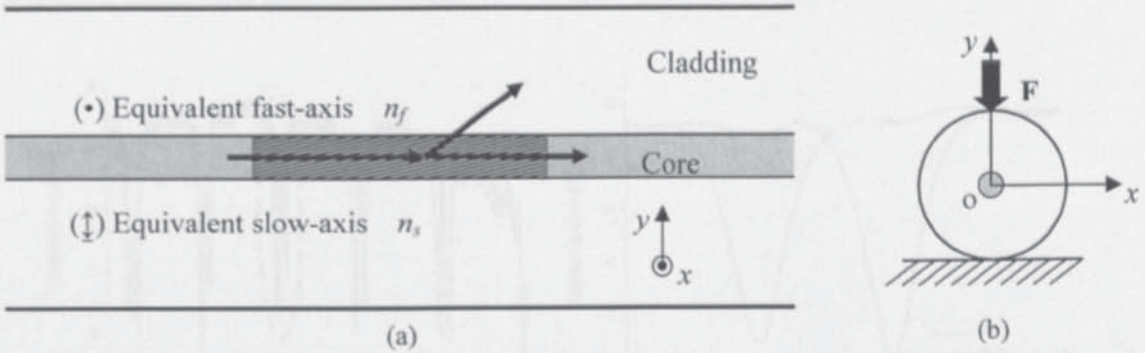

Fig.5.15. (a) Schematic diagram of the large angle TFG with two assigned orthogonal polarisation axes; (b) The cross section of a fibre in an assigned x-y coordinate system with transverse load applied along y-axis. The x-y coordinate system is also depicted in (a) when the force is applied along the slow-axis of the TFG.

5.3.1.2. Fabrication of the large angle TFG

In order to investigate the polarisation property of large angle TFGs and their application in sensing, large angle TFGs of 12mm long with internal tilt fringes at 81° were UV-inscribed in hydrogen-loaded Corning SMF-28 employing the scanning phase-mask technique and a frequency doubled CW Ar^+ laser. The tilted structure was

realised by rotating the phase-mask in the fabrication system. The mask used in the fabrication is custom-designed with a period of 6.6μm purchased from Edmund Optics Ltd.

Fig.5.16 (a) shows the transmission spectrum of an 81°-TFG in the range from 1400 to 1700nm, exhibiting a clear polarisation mode-splitting feature. In this figure a series dual-peak resonances, corresponding to the two sets of coupled cladding modes with orthogonal polarisation states can be seen. I then added a polariser and a polarisation controller before the TFG to change the polarisation state of the probing light. Fig.5.16 (b) shows the transmission spectra of one pair of dual-peaks for two orthogonally polarised states (labelled as P1 and P2). When the light is switched to P1 or P2, one of the dual-peaks grows to its full strength (~9dB) whereas the other almost disappears. The separation between the paired peaks is about 6.16nm, giving an estimated combined fibre birefringence ~ 2×10^{-4} based on Equation 2.36.

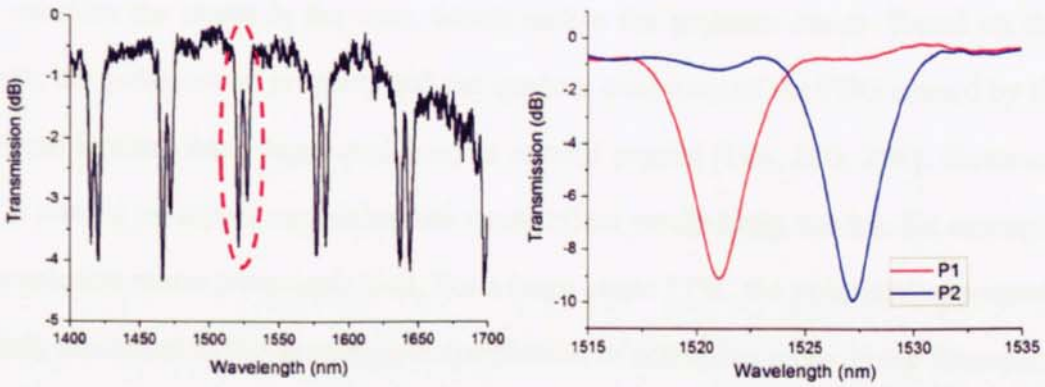

(a) (b)

Fig.5.16. (a) The transmission spectrum of an 81°-TFG in the range from 1400 to 1700nm. (b) The transmission spectra of one pair of dual-peaks for two orthogonally polarised states.

5.3.2. TRANSVERSE LOAD SENSOR BASED ON 81°-TFG

Transverse load measurement using FBGs and LPGs made in low-bi and hi-bi, multi-core and conventional fibre have been reported [196-200]. The majority of these

gratings exhibited a pronounced polarisation mode split effect resulted from the birefringence induced by the transverse loading.

In this section, I report a unique polarisation mode coupling property of large angle TFGs under directional transverse load, which may be explored for vector load sensors. Furthermore, the distinct encoding relationship between the load and the mode coupling strength make it possible to interrogate such an in-fibre load sensor using low-cost light source and detector.

5.3.2.1. Principle of the transverse load sensing system using large angle TFGs

The stress distribution in the optical fibre induced by the transverse loading has been analysed in many papers [201-203]. When the transverse load is applied to an FBG, the Bragg resonance may split into two peaks which is caused by the load induced birefringence. For an FBG, the mode coupling happens in the fibre core, thus we only need consider the stress in the core, which makes the problem easier. Based on this analysis, the polarisation property and the spectral evolution of the FBG caused by the transverse loading have been explained in several papers [196, 200, 204]. However, there is almost no report explaining the stress effect on cladding modes, for example, LPG evolution under transverse load. For a large angle TFG, the polarisation property is mainly attributed to the asymmetric distribution of refractive index in the fibre core. Considering the complexity of analysis for the cladding mode, in this section, an explanation for transverse load sensing using an large angle TFG is given based on the analysis of the stresses also just in the fibre core.

For a standard telecom fibre, when the transverse load is applied to y-axis as shown in Fig.5.15 (b), with a given compressive force F, the stresses in the fibre core can be simplified as those at the geometrical centre. The stresses in x- and y-direction, σ_x and σ_y can be expressed in Hertz equations [205] as:

Equation 5.6 $$\sigma_x = \frac{2F}{\pi DL}, \quad \sigma_y = -\frac{6F}{\pi DL}$$

where D is the fibre diameter, F is the applied force and L is the length of the region under stress. It is noted that the horizontal normal stress σ_x is always positive (tensile) and the vertical normal stress σ_y is negative (compressive), which means $(\sigma_x - \sigma_y) > 0$. The refractive index changes in the cross section due to the photo-elastic effect can be evaluated by [204]:

Equation 5.6 $$\Delta n = n_x - n_y = (n_{x0} - n_{y0}) + (C_1 - C_2)(\sigma_x - \sigma_y)$$

where n_{x0} and n_{y0} are the effective refractive indices of the unstressed fibre; C_1 and C_2 denote the stress-optical coefficients, for silica glass, $C_1 - C_2 = 3.36\times10^{-5}\text{mm}^2/\text{kg}$ [201]. For a large angle TFG, when the transverse load is applied to the slow-axis, we have $n_{x0} = n_f$ and $n_{y0} = n_s$. Thus, the first term in Equation 5.6 will be negative resulting in a reduction in birefringence Δn, *i.e.* the grating structure is less PM-like. In this case, we may expect that the light coupling to the two orthogonally polarised modes is more subjected to perturbation. On the contrary, when the transverse load is applied to the fast-axis of the TFG, we have $n_{x0} = n_s$ and $n_{y0} = n_f$ and the first term in Equation 5.6 will be positive, resulting in increase in birefringence Δn. In this case, the large angle TFG behaves more towards a PM-like fibre, preventing the change of the light coupling to the two polarised modes.

5.3.2.2. Implementation of transverse loading experiment on large angle TFG

The schematic diagram of the transverse loading experiment is shown in Fig.5.17 (a). The 81°-TFG fibre with the grating length of 12mm and a dummy fibre of the same type were laid between two flat-surface aluminium plates. The loading length is 32mm. As shown in Fig.5.17 (b), the distances from the support fibre and the TFG to the two edges of the upper plate were the same. The load F was employed to the

geometrical centre of the upper plate. Therefore the load on the each fibre was $F/2$.

The light from a broadband light source (BBS) was launched into the one end of the grating fibre and the output was monitored from the other end by an OSA. A linear polariser and a polarisation controller were inserted between the BBS and the TFG to change the polarisation state of the probing light. Before the transverse load was applied, the polarisation state was set to fully excite the P1 mode by adjusting the polarisation controller. And then gradually increase the load on the top of the plate.

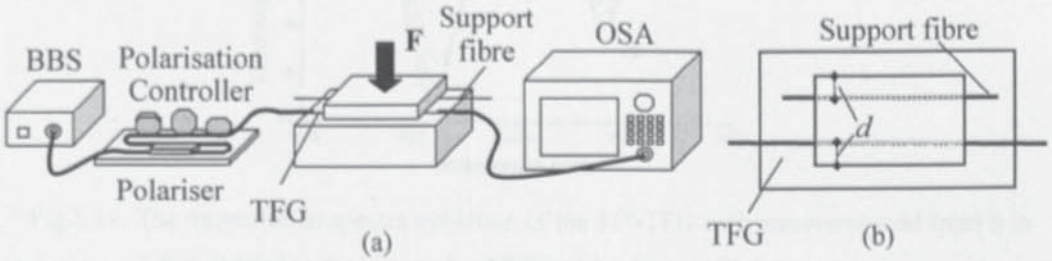

Fig.5.17. (a) The schematic diagram of the transverse loading experiment system. (b) The top view of the two fibres and the aluminium plates.

5.3.2.3. Transverse loading experiment on large angle TFG

The transverse load was applied to the TFG firstly to the slow-axis ($\psi = 0°$) from 0 to 2.6kg (for the two fibres) in an elevation step of 0.2kg, as shown in Fig.5.18 (a).

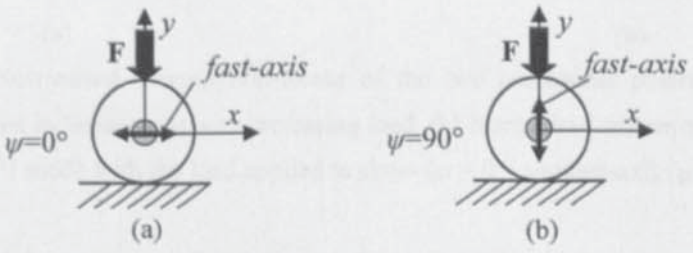

Fig.5.18. The cross section of the TFG in an x-y coordinate system with transverse load applied along (a) slow- and (b) fast-axis; ψ is the angle between the fast-axis of the TFG and x direction.

The transmission spectrum for each applied load is plotted in Fig.5.19. It is clear from

Fig.5.19 that with increasing load, the light coupling to the P1 mode is gradually decreased and to the P2 mode increased. Fig.5.20 (a) plots the normalised transmission-losses against applied load for both peaks in linear scale. We can see from the figure that for the loading range from 3 to 31kg/m, the transmission-loss changes for P1 and P2 peaks are almost linear.

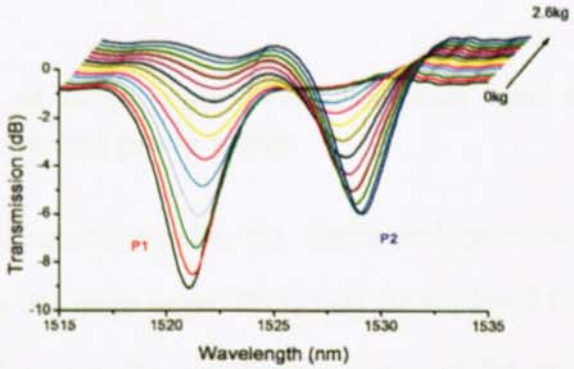

Fig.5.19. The transmission spectra evolution of the 81°-TFG with transverse load from 0 to 2.6kg applied to the slow-axis of TFG and a dummy fibre.

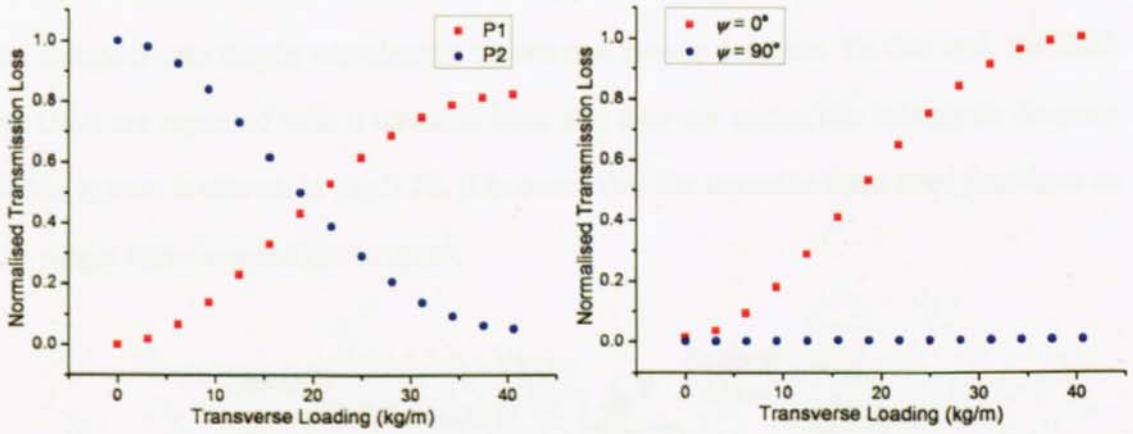

(a) (b)

Fig.5.20. (a) Normalised transmission-losses of the two orthogonal polarisation modes plotted in linear scale with increasing load. (b) Normalised transmission-losses of the P1 mode with the load applied to slow- ($\psi = 0°$) and fast-axis ($\psi = 90°$).

The loading experiment was then repeated by applying the transverse load to the grating fast-axis ($\psi = 90°$), as shown in Fig.5.18 (b), no light coupling change was observed on the two peaks, as shown in Fig.5.20 (b). This distinctive directional polarisation mode coupling behaviour may be explained by the analysis on the

PM-like property of large angle TFGs given in section §5.3.2.1. When the load is applied to the slow-axis, the 81°-TFG is less resisting to the perturbation and light coupling transfers between the two polarisation modes easily, whereas when the load applied to the fast-axis, the grating is much more resisting. This directional coupling property could be the basis of vector load sensor with capability of not just measuring amplitude but also recognising the direction of the loading.

5.3.2.4. Interrogation of large angle TFG transverse load sensor using single wavelength laser and power meter

Based on above experimental results, the directional polarisation mode coupling behaviour exhibited by the large angle TFGs may be explored for implementation of vector load sensors. However, the transmission-losses of the polarisation dual-peaks of the TFG shown in Fig.5.20 were decoded using the BBS and OSA, both are expensive laboratory instruments. In real applications, it is desirable to use low-cost and compact-size single wavelength source and power detector. To this end, the BBS and OSA are replaced with a tuneable laser and a power meter, the schematic diagram of this system is shown in Fig.5.21. It is noted that the tuneable laser here functions as two single wavelength light sources.

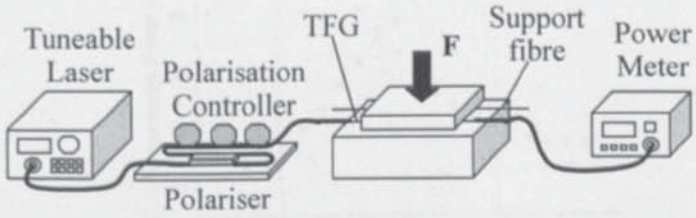

Fig.5.21.The schematic diagram of the transverse loading experiment system using a tuneable laser and a power meter.

A loading measurement on a different 81°-TFG was carried out using this power-measurement system. The spectra of a pair of dual-peaks (at 1537.52 and 1543.22nm) of this TFG under loading are shown in Fig.5.22. I firstly tuned the laser

to the P1 peak at 1537.52nm and applied the load from 0 to 3.8kg with an incremental step of 0.2kg to the TFG and recorded the power levels for each load, and then set the tuneable laser to the P2 peak at 1543.22nm and repeated the measurement. The output power of the tuneable laser was set at 0.126mW (-9dBm). Fig.5.23 plots the measured power values against the load for the two wavelengths.

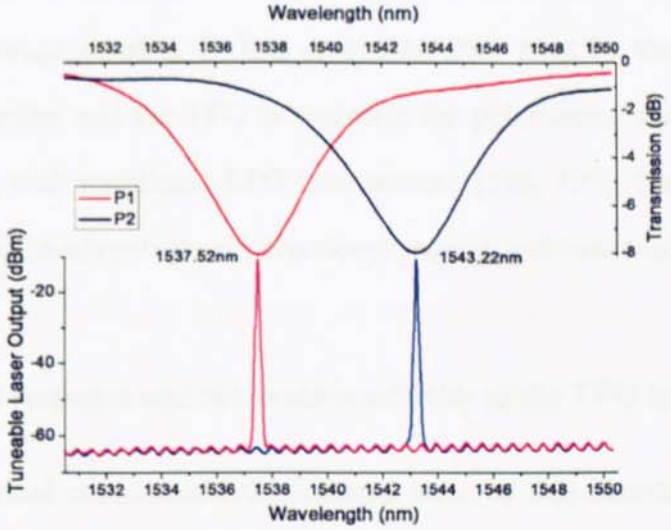

Fig.5.22. The upper plot is the transmission spectra of a pair of dual-peaks of the second 81°-TFG; the wavelength of P1 loss peak is 1537.52nm and that of the P2 peak is 1543.22nm. The lower plot is the output spectra of a tuneable laser set at the wavelength of 1537.52 and 1543.22nm, separately.

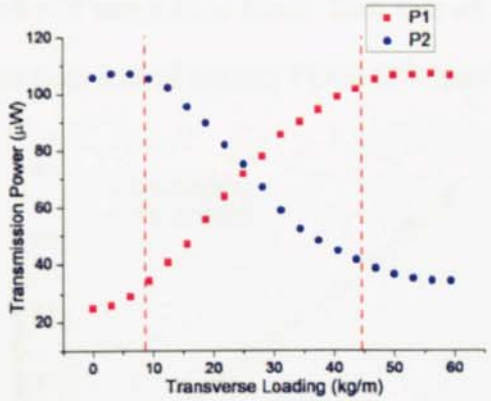

Fig.5.23. Transmission powers for the two orthogonal polarisation modes measured using a tuneable laser and a power meter.

From Fig.5.23, it is clear that the trends of the two plots are similar to the transmission-loss plots shown in Fig.5.20 (a) measured using the BBS and OSA for the first 81°-TFG. In Fig.5.23, although the entire plots are not linear, there is an

almost linear loading response range from 9 to 44kg/m in which the loading sensitivity is estimated at approximately 2.04μW/(kg/m). Thus, if we use a standard detector with a minimum detection power of 1nW, this 81°-TFG based sensor system may detect a load change as small as 1.6×10^{-2}g. In real applications, the tuneable laser can be replaced by two low-cost single-wavelength light sources, and the TFG loading sensor can be placed a bit further away from the light sources and power meters for long-range sensing. In this case, PM fibre may be used to connect the polarisation controller and the TFG to maintain the polarisation state of the incident light. Comparing with traditional LPG load sensors [198, 199], our TFG based load sensor system has the advantages of directional sensing and low-cost of interrogation.

5.3.2.5. Thermal response and the cross-sensitivity of the TFG based sensors

To study the thermal cross-sensitivity induced error of this measurement system, a temperature response evaluation experiment was then carried out with the second 81°-TFG. As shown in Fig.5.24, both measured peaks exhibit a linear thermal response, showing temperature sensitivities 8.2 and 8.1pm/°C. The thermal-sensitivity values are at least an order of magnitude lower than that of conventional LPGs [27] and even also much lower than that of normal FBGs (10.6pm/°C) [18].

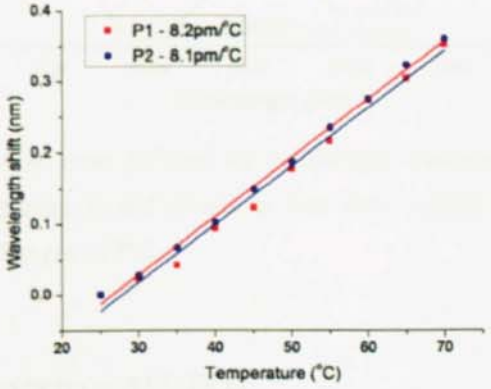

Fig.5.24. Wavelength shifts of paired polarisation peaks of the second 81°-TFG at 1537.52 and 1543.22nm against temperature change, showing linear thermal responses with low thermal coefficients.

Based on the low temperature sensitivity of 81°-TFGs, it is estimated that the spectrum of TFG will shift only ±0.15nm with the temperature change in the range of ±18°C. In Fig.5.25, the attenuation profiles of P1 and P2 are quite rounded (near flat) in the range 1537.52±0.15nm and 1543.22±0.15nm, respectively. In these small wavelength ranges, the maximum difference of the amplitude between the highest and lowest points in the spectral profile is less than ~ 0.06dB, and the measurement error induced by the thermal cross-sensitivity effect is less than 0.2%. This means that the system output power reading is almost insensitive to the moderate temperature change when an 81°-TFG is employed. Thus, for practical applications not under dramatic temperature changes, the power-to-load measurement performed by the 81°-TFG is almost free from thermal cross-sensitivity effect, because the peak profiles are quite broad and the measurement power errors induced by the temperature change are small.

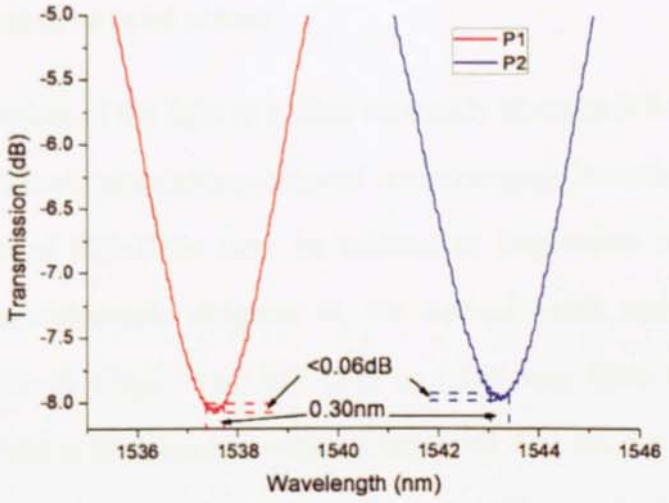

Fig.5.25. The measurement error induced by the thermal cross-sensitivity effect for the 81°-TFG employed in the system is less than 0.06dB when the surrounding temperature changes ±18°C.

5.3.3. TWIST SENSOR BASED ON 81°-TFG

Wang and Rao *et al* have reported a twist sensor employing LPG structure induced by

high-frequency CO_2 laser pulses, and the torsion measurement using such a device was based on the detection of birefringence change induced wavelength shift [206, 207]. Conventionally, LPGs associating with forward mode coupling have relatively long device size and broad spectral width, thus giving low stability and poor spectral resolution.

In this section, I will demonstrate an implementation of an in-fibre twist sensor utilising large angle TFGs. As discussed in section §5.3.2, such gratings exhibit pronounced polarisation mode-splitting features. If torsion is applied to these TFGs the mode-splitting will increase, making them ideal twist or rotation sensors. It has been demonstrated that the TFG based twist sensor is capable of monitoring both direction and amplitude of torsion with added potential advantage of employing low-cost intensity demodulation technique.

5.3.3.1. Implementation of twist sensor

The polarisation direction of the light in a fibre inevitably changes if the fibre is under twist. Thus, the observed polarisation-induced interchanging coupling between the birefringence modes of 81°-TFGs may be utilised to implement optical twist or torsion sensors. The schematic diagram of the optical twist sensing system is illustrated in Fig.5.26. A 12mm long 81°-TFG in 1.5m long fibre was fixed by a clamp on one side and a fibre rotator with an engraved dial on the other end. The length between the clamp and the rotator, L, was 160mm. And the TFG was positioned in the middle section. L_c was defined as the length between the incident light side clamp point and the centre of the TFG, thus we had L_c=80mm. In order to eliminate measurement errors from axial-strain and bending effects, a small axial tension was applied to the fibre maintaining it straight. The light from the BBS was launched into the one end of the fibre and the output was monitored from the other

end by an OSA. A linear polariser and a polarisation controller were inserted between the BBS and the TFG; thus, the light after them was linear polarised.

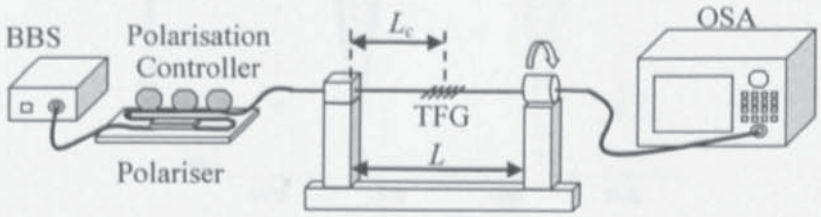

Fig.5.26. Schematic diagram of the experimental setup for implementation of TFG based twist sensor.

5.3.3.2. Twist experiment on 81°-TFG

Before the fibre was twisted, the pre-polarisation state was set at P1 by adjusting the polarisation controller and thus the peak labelled as P1 on the shorter wavelength side was fully excited (~21.6dB), as the first trace shown in Fig.5.27. Then, the twist was applied to the fibre in the clockwise direction from 0° to 190° with an incremental step of 5° and the transmission spectrum for each applied twist was recorded and plotted in Fig. 5.27. As soon as the fibre was twisted, the strength of P1 decreased but P2 increased. When the fibre was rotated by 190°, P1 completely vanished and P2 reached its maximum strength (~21.7dB). In the experiment, this process was repeated by twisting the fibre in anticlockwise direction, and a repeating spectral evolution process for the paired peaks has been recorded.

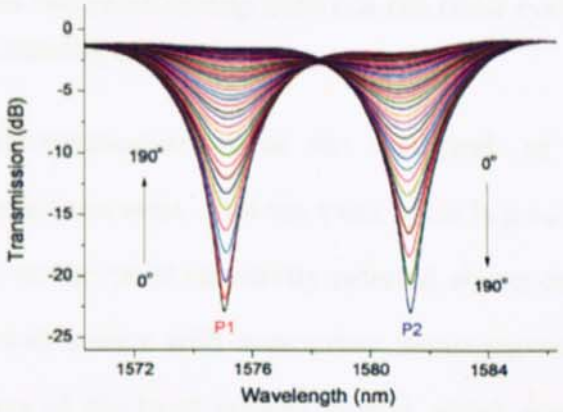

Fig.5.27. Spectra evolution of 81°-TFG under twist in clockwise direction from 0° to 190°.

Fig.5.28 plots the measured transmission-losses of both peaks for clockwise (0° to 190°) and anti-clockwise (0° to -190°) directions in dB and linear scale. In the linear scale figure, the two curves are quasi-sinusoidal like and changes periodically in opposite phases. And the two peaks reached their maximum and minimum strength at the same time. By measuring the adjacent two maximum or minimum points of P1 or P2, the twist cycle of this TFG based twist sensor is around 380°. Additionally, though the two curves are nonlinear in the whole twist cycle, it can be identified two highly linear ranges of ±45° around two cross-points at +95° and -95° on the curves, in which can be used for twist sensing.

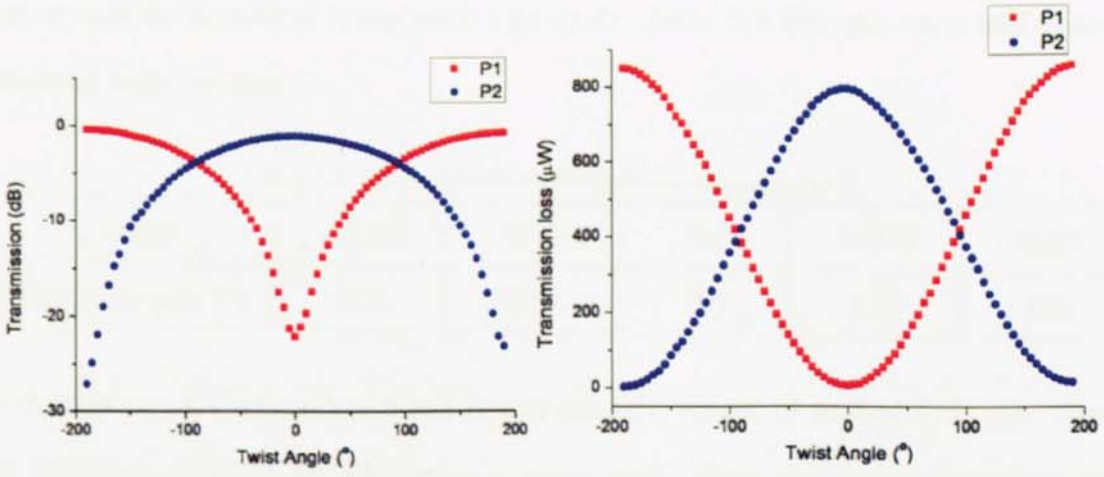

(a) (b)

Fig.5.28. Transmission-losses of the paired-peak under twist in clockwise and anticlockwise directions measured in (a) dB and (b) linear scale.

5.3.3.3. The study on the relationship between the twist cycle and the parameters of the twist sensing system

In Fig.5.28, the transmission-losses of the dual-peak of the 81°-TFG evolve periodically with continuous twist. And the twist cycle is a very important parameter for the twist sensor, as the twist sensitivity referred above can be limited by it. In order to achieve a twist sensor with appropriate measurement range, I then further studied the parameters of the twist sensing system which might influence the twist cycle. In the twist experiment, the spectra evolution might be caused by the change of the polarisation state in the fibre induced by twist. It is obvious that the twist cycle can be related to the distance between the fixed clamp point and the centre of the TFG, L_c and the length of the twisted fibre, L.

With the same 81°-TFG, I first repeated the experiment with the TFG fixed at different position (with different L_c). With L=160mm, the polarisation state was preset at P1 by adjusting the polarisation controller and the fibre was twisted in the clockwise direction until P2 was fully excited. Then the twist half-cycle (half of the full twist cycle) can be recorded, which is achieved more conveniently than the whole cycle. In the following paragraphs, the periodic property of the TFG based twist sensor will be described using twist half-cycle. Table 5.4 lists the twist half-cycles achieved with different L_c.

Table 5.4. The twist half-cycle achieved with different L_c

L_c (mm)	23.5	47.0	79.5	113.0	136.5
Twist half-cycle (°)	520	299	190	127	112

In my system, L (160mm) is much longer than the length of grating (12mm). Thus, the influence induced by difference in twist angle along the grating length is not significant. In this case, the sensitivity of the twist sensor increases with increasing L_c/L and the twist half-cycle is inversely proportional to L_c, which has been verified

from Table 5.4. With a given L, the appropriate twist sensitivity and measurement range of the twist sensor can be selected by using different L_c. If high twist sensitivity is required, a large L_c with a small twist half-cycle can be selected; on the contrary, if large linear measurement range is more important, a small L_c with a large twist half-cycle can selected.

I then further studied the relationship between the twist half-cycle and the length of twisted fibre, L. With the TFG positioned at the centre section between the two clamp points, the twist experiment was repeated using different L. In the case of L=160mm, the twist half-cycle was achieved as 190°; while L=80mm, the twist half-cycle was measured as 195°. The discrepancy between the two measured half-cycles may be caused that the TFG is not positioned at the exact centre section of the twist length.

5.3.3.4. Interrogation of large angle TFG twist sensor using single wavelength laser and power meter

Similar to the loading measurement system mentioned previously, the twist sensing system can also be developed into a twist sensor using single wavelength lasers and power meter, the scheme diagram of which is shown in Fig.5.29.

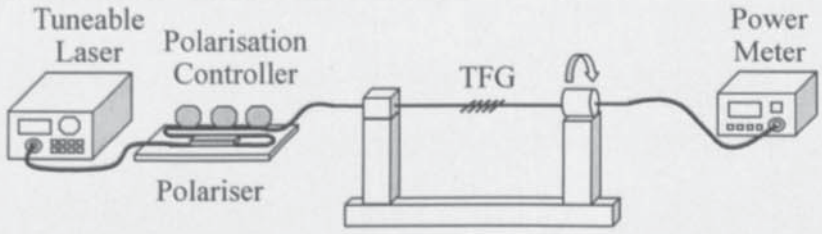

Fig.5.29. The scheme diagram of the twist sensing system using a tuneable laser and a power meter.

I set the output power at 0.4mW (-4dBm) and wavelengths of the tuneable laser at 1575.02 and 1581.36nm individually corresponding to the wavelengths of P1 and P2 when they are fully excited. With a medium twist sensitivity and measurement range

selected, the TFG was positioned at the centre section of the 160mm-length between the clamp point and rotator. With the output wavelength set at 1575.02nm (P1), I firstly adjusted the polarisation controller to achieve the minimum power reading, then switched the output wavelength to 1581.36nm (P2) and recorded the new power reading, which should be around the maximum. With the increment of 5°, the TFG was twisted in clockwise until the power reading for 1581.36nm reached minimum. For each angle, the output wavelength of the tuneable laser is switched at the wavelengths of P1 and P2 one by one and the power readings are recorded individually. Fig.5.30 shows the recorded power readings with the wavelengths at P1 and P2 for different the twist angles.

In Fig.5.30, the trends of the two plots are similar to those shown in Fig.5.28 (b) measured using the BBS and OSA. In the almost linear range ±45° around the cross-points at 95° mentioned in section §5.3.3.2, the twist sensitivity for the two plots were calculated as 166.41 (P1) and 145.90 (P2) μW/rad. The small difference in twist sensitivities measured from the two polarisation loss peaks is mainly caused by the wavelength of the output laser which was a little off the maximum loss peak of P2. In real applications, such error can be eliminated by better calibration to the system and the twist angles can be calculated from power readings corresponding to two peaks using different sensitivities individually.

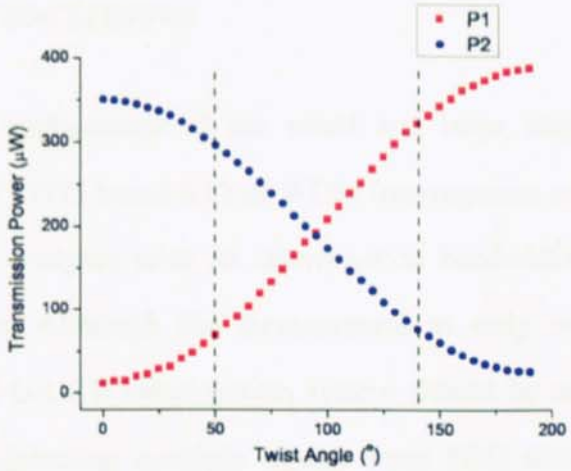

Fig.5.30. Transmission powers for the two orthogonal polarisation modes measured using a tuneable laser and a power meter.

If the twist rate is defined as θ/L, where θ is the twist angle and L represents the twist length, twist sensors, such as the ones referred in [206, 207], are sensitive to the twist rate. But in our experiment, it is demonstrated that the twist sensor is only sensitive to the twist angle. Additionally, the measurement sensitivity and range can be selected by changing the position of the TFG along the twist length.

The 81°-TFG based sensor is capable of detecting both direction and amplitude of the torsion if the initial operation state is set at 95°, where P1 and P2 have the same strength. In this situation, relative variations of the two loss peaks give a clear indication of the twist or torsion direction. It should be noted that the torsion may be easily measured by a simple and low-cost intensity measurement based interrogation system, involving only a single wavelength source and a photo-detector. This is an advantage over other reported grating based twist sensors as they require high cost spectrum analyse systems and broadband sources [206, 207]. Using a standard detector with a minimum detection power of 1nW, the 81°-TFG based sensor can detect a twist rate change as small as 6.9×10^{-6}rad. In other words, if this device is used as an angle sensor, it can detect the rotation as small as 3.9×10^{-5} degrees.

5.4. *CHAPTER CONCLUSIONS*

In this chapter, the applications of the small and large angle TFGs have been demonstrated. The 10°-TFG based 800nm WDM interrogation system can function as an in-fibre spectrum analyser with an interrogation bandwidth up to 60nm and a resolution of 12.7pm. Although the measurement to only one FBG sensor was demonstrated, this TFG-CCD interrogation system should be capable of performing WDM interrogation detecting multiple signals form FBG sensors array within its dynamic range. In addition, the system was further evaluated for sensing the refractive index of sample liquids. In the near-linear range from 1.4132 to 1.4735, it is estimated that the SRI change as small as 10^{-5} can be detected by this low-cost high-resolution TFG WDM interrogation system.

With the utilisation of their distinctive polarisation properties, the 81°-TFG based sensors are capable of transferring the load and twist change to polarisation dependent spectral evolution of the large angle TFGs to be measured optically. By employing single wavelength light source and photodiode, the large angle TFG sensing system can be developed into low-cost and high-sensitivity sensors. Using single wavelength source and a power meter, I have implemented such a load interrogation experiment giving a load sensitivity of 2.04μW/(kg/m) and twist sensing system with the twist sensitivity of 145.90μW/rad. If the power meter is replaced by a photodiode with detectivity of 1nW, our TFG based load and twist sensor systems may detect the load and twist change as small as 1.6×10^{-2}g and 6.9×10^{-6}rad, respectively.

Chapter 6

Fibre Grating Structures Inscribed by Femtosecond Lasers in Silica and Mid-Infrared Glass Fibres

6. Fibre Grating Structures Inscribed by Femtosecond Lasers in Silica and Mid-Infrared Glass Fibres

6.1. INTRODUCTION

The technique of laser inscription in transparent dielectric materials by means of focused femtosecond laser irradiation has attracted considerable interest. The method has been applied to bulk glasses, optical fibres, crystals and polycrystalline or ceramic like media. The method appears to be a promising and flexible technology for optical device fabrication. At present, the detailed mechanism for index and structure changes induced by femtosecond laser is not fully understood, but femtosecond lasers are being used more widely to fabricate microstructure and grating based devices. The possible mechanisms of the femtosecond-laser-induced index change have been discussed in Chapter 3.

Recently, there have been increasing number of reports on inscription of LPGs and FBGs employing femtosecond laser. However, at present, inscriptions of LPGs and FBGs by femtosecond laser using direct point-by-point [168, 172] or phase-masks technique [176] are mainly in silicate-based glass fibres. In this chapter, an initial but systematic investigation is reported on the fabrication of LPGs and FBGs in mid-IR glass fibres by near-IR femtosecond laser.

This chapter will mainly report the LPGs and FBGs inscriptions by femtosecond laser using both point-by-point and phase-mask methods in standard telecom fibre and single- and multi-core mid-IR glass fibres. Firstly the special, physical and composite properties of the mid-IR fibres and the butt-coupling method with characterised transmission spectra will be presented. Subsequently, grating inscriptions using point-by-point and phase-mask method will be introduced respectively in the

following sections. The two different inscription systems and the corresponding inscription methods will be demonstrated. In these two sections, I will further analyse grating structures and spectral, thermal and strain properties of the LPGs and FBGs written in standard telecom fibre and mid-IR glass fibres using femtosecond laser. Finally, conclusions are drawn in the last section of this chapter.

6.2. *CHARACTERISTICS OF MID-IR GLASS FIBRES: TELLURITE AND GERMANATE GLASS FIBRES*

Germanate and tellurite glass fibres have attracted considerable attention for fibre devices in near- and mid-IR regions. Their high refractive index and optical nonlinearity, resistance to corrosion, low melting temperature and good transmission properties from the visible to mid-IR region (0.35-6μm) [208] make them promising fibre hosts for bio/chemical and gas sensing [209, 210], nonlinear optical signal processing [211] and optical amplifier and laser [212, 213] devices. In recent years, we have also seen that there are increasingly reports for multi-core fibres (MCFs). MCFs can offer new device designs such as arrayed fibre sensors for load and bend measurement with direction recognition and temperature compensation capability [200, 214] and arrayed fibre lasers and amplifiers which can scale up output powers [215]. Very recently, germanate and tellurite glass fibres with single- and three-core have been fabricated [216, 217]. More significantly, the three-core tellurite glass fibre has been actively doped with $Ho^{3+}/Tm^{3+}/Yb^{3+}$, Er^{3+}/Ce^{3+}, and Tm^{3+}/Yb^{3+} in three cores, respectively. In each core the emissions from the visible to mid-IR have been observed [218].

6.2.1. CHARACTERISTICS OF GERMANATE AND TELLURITE GLASS FIBRES

Germanate and tellurite-based glass fibres were manufactured by a standard rod-in-tube technique [216, 217] and drawn from the compositions of GeO_2-PbO-Na_2O-Ga_2O_3 (GPNG) and TeO_2-ZnO-Na_2O (TZN), respectively, by the Institute for Materials Research of Leeds University. Fig.6.1 shows the cross section images of these GPNG and TZN fibres taken under microscope. It is noted that the D-shape-like end images are attributed to cleaving defects. Limited by the fabrication technique, fibre cores of two kinds of GPNG fibres shown in Fig.6.1 (a) and (b) were

drawn off the geometrical centre.

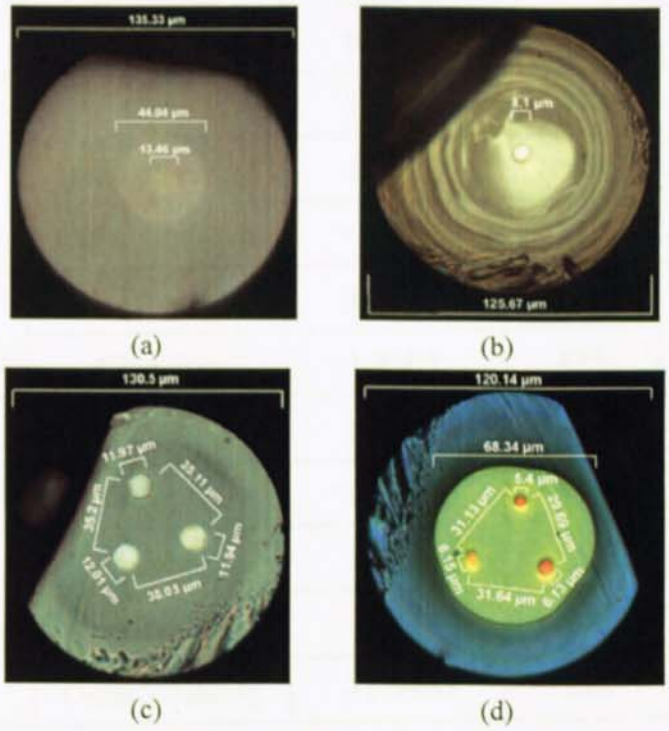

Fig.6.1. Microscope images of the cross sections of GPNG single-core of (a) double-clad and (b) single-clad fibre and TZN (c) passive and (d) active three-core fibres. Note, the D-shape-like end images are attributed to cleaving defects, as the fibres are not standard and fragile to achieve nice-finish cleaving.

The germanate fibres in the work reported in this chapter were drawn from glass compositions (mol %): $55GeO_2$-$30PbO$-$11Na_2O$-$4Ga_2O_3$. And the passive and active tellurite fibres were drawn from compositions (mol %): $79TeO_2$-$14ZnO$-$7Na_2O$ and $80TeO_2$-$10ZnO$-$10Na_2O$, respectively. All three cores of the active TZN fibre were doped with Er^{3+}/Ce^{3+}, while the rest three kinds of fibre were passive fibres. Table 6.1 depicts the geometry parameters and the refractive indices of four kinds of GPNG and TZN fibres.

Table 6.1. The geometry parameters and the refractive indices of GPNG and TZN fibres.

Fibre Type	Structures	Refractive index at 633nm	Diameter (μm)	Separations between cores (μm)
GPNG double-clad fibre	Core	1.8622	13	-
	Inner cladding	1.8505	40	
	Outer cladding	<1.8505	135	
GPNG single-clad fibre	Core	1.8622	8	-
	Cladding	1.8505	125	
TZN passive fibre	Core	2.0475	~12	~35
	Cladding	2.0224	130	
TZN active fibre	Core	2.0448	~6	~31
	Inner cladding	2.0224	68	
	Outer cladding	~1.9900	120	

GPNG and TZN fibres have much lower softening point for glass fabrication at approximately 480°C and 320°C, respectively, which are substantially lower than that (~1200°C) of silica glass.

Fig.6.2 shows the absorption spectra of cladding glass of GPNG and TZN fibres and transmission-losses of these two kinds of fibres in mid-IR range given by our collaborators who provide these fibres. It is noted that the multi-mode GPNG fibre shown in Fig.6.2 (b) is not included in this thesis. From Fig.6.2, it is clear that both materials absorb UV greatly, therefore, LPG and FBG structures cannot be produced in such fibres by UV-inscription as the cladding will absorb all the UV light before it reaching the core.

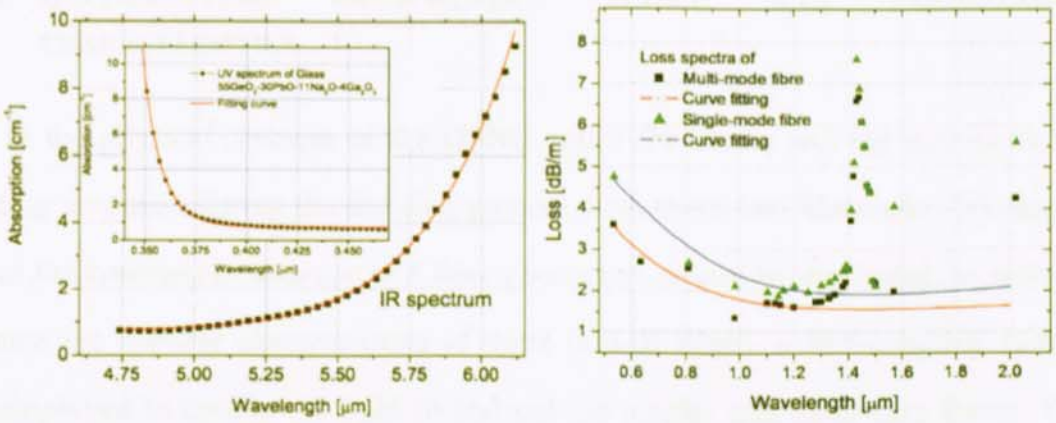

(a) (b)

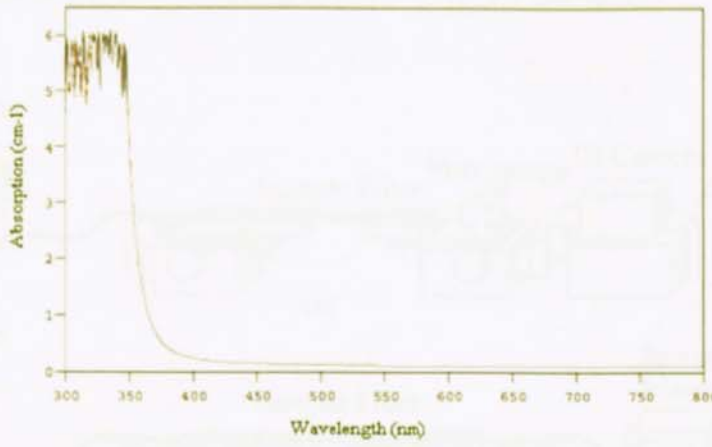

(c)

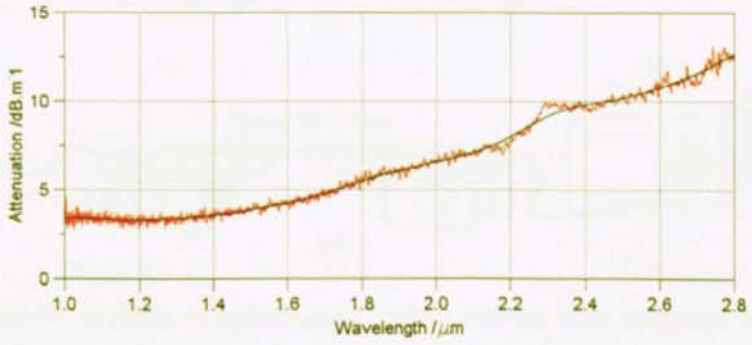

(d)

Fig.6.2. (a) UV/visible and IR absorption spectra of the cladding glass of GPNG fibre, showing the cut-off wavelengths in the UV and IR parts. Both spectral curves in (a) are fitted for calculating the glass intrinsic loss (red lines). (b) Transmission-losses of GPNG multi- (not included in this thesis) and single-mode fibres in the mid-IR range. The continuous blue line in (b) is fitted based on the experimental data (green triangles). (c) UV/visible absorption spectra of the cladding glass of TZN fibre, showing the cut-off wavelengths in the UV parts. (d) Transmission-loss of TZN fibre in the mid-IR range. The red line in (d) is the measured result and the black curve is the calculated one.

6.2.2. BUTT-COUPLING MEASUREMENT SYSTEM AND TRANSMISSION CHARACTERISTICS

Due to the physical softness of the GPNG and TZN fibres, and the defects in the cladding produced during the drawing process, both these two fibres are very fragile so that the commercial cleavers and fibre connecters cannot be employed. In order to examine the spectral characteristics of these mid-IR fibres, a butt-coupling system was employed to couple the light in and out the single- and multi-core fibres. The schematic diagram of the butt-coupling system is shown in Fig.6.3.

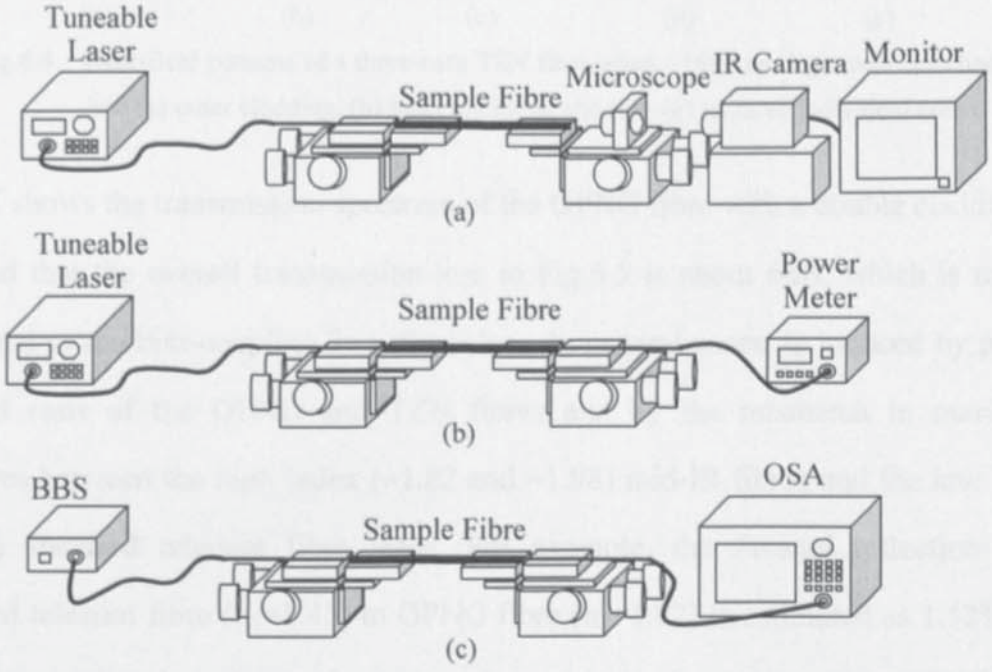

Fig.6.3. Schematic diagram of butt-coupling system and the three operation procedures: (a) left end coupling; (b) right end coupling; (c) transmission spectrum measurement.

To ensure the light coupled into the individual cores of the three-core TZN fibres, I first examined the near-field patterns from the output end of the fibre as shown in Fig.6.3 (a). Fig.6.4 (a)-(e) show the near-field images captured by an IR camera when the light was coupled into the outer cladding, inner cladding and the three individual cores, respectively. When the light was coupled into fibre cores, the cores were seen clearly from the output end, as shown for example in Fig.6.4(c)-(e). And the output

signal was then butt-coupled into a fibre lead to a power meter as shown in Fig.6.3 (b). Tuning the stage on the right side of the system until the power meter reading is maximum, an OSA can be employed to replace the power meter to view the transmission spectrum as shown in Fig.6.3 (c). Note, following this procedure, the spectra of LPGs and FBGs made in GPNG and TZN fibres can be fully characterised.

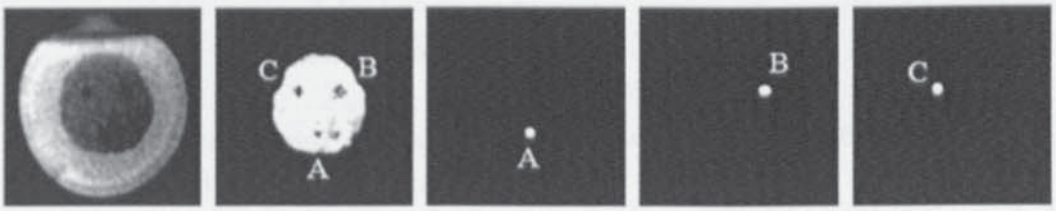

(a) (b) (c) (d) (e)

Fig.6.4. Near-field patterns of a three-core TZN fibre when ~1680 nm light was launched into (a) outer cladding, (b) inner cladding, and (c) - (e) its three individual cores.

Fig.6.5 shows the transmission spectrum of the GPNG fibre with a double cladding. It is noted that the overall transmission-loss in Fig.6.5 is about 6dB, which is mainly attributed to the butt-coupling loss. Such loss, in general cases, is induced by poorly cleaved ends of the GPNG and TZN fibres and by the mismatch in numerical apertures between the high index (~1.82 and ~1.98) mid-IR fibres and the low index (~1.45) standard telecom fibre leads. For example, the Fresnel reflection from standard telecom fibre (n_1=1.45) to GPNG fibre (n_2=1.82) is estimated as 1.12% and thus, the coupling loss due to the mismatch in numerical apertures from GPNG fibre to standard telecom fibre is estimated as ~3.4dB. During butt-coupling, it is noticed that the noise level on the spectrum is greatly influenced by the coupling position; the further away from the centre, the noisier the spectrum is.

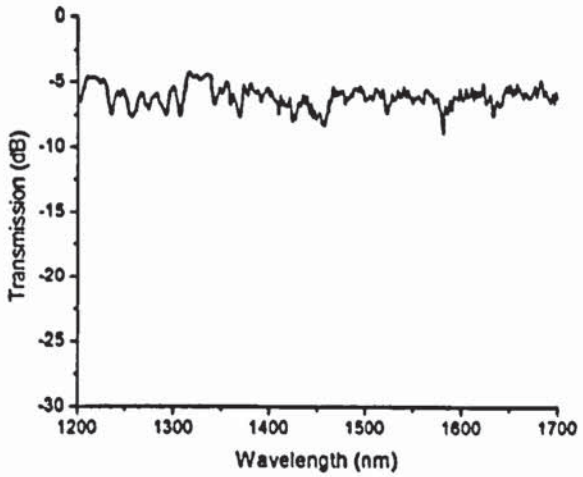

Fig.6.5. The transmission spectrum of a virgin double-clad GPNG fibre showing the overall transmission-loss of ~7dB.

6.3. *FEMTOSECOND-LASER-INSCRIPTION OF LPGS AND FBGS USING POINT-BY-POINT TECHNIQUE*

The use of intense femtosecond pulses to create a permanent refractive index change in glass materials has led to recent interest in FBG fabrication. By means of focusing the femtosecond pulses into the fibre core, point-by-point FBG inscription can be achieved without the need of a phase-mask. In recent years, the direct point-by-point inscription to create fibre grating structures have been demonstrated, including both LPGs [168-170] and FBGs [172, 175].

In this section, I will introduce the point-by-point femtosecond-laser-inscription system, and the properties of LPGs and FBGs inscribed in standard telecom fibres (Corning SMF-28) and LPGs in double-clad GPNG fibre.

6.3.1. INSCRIPTION SYSTEM AND ALIGNMENT

6.3.1.1. Inscription setup

The grating inscription setup using point-by-point method is shown in Fig.6.6. An amplified femtosecond laser system operated at a wavelength of 800nm. This laser system produced 120fs-long (measured before the objective lens) pulses at a repetition of 1kHz and maximum output energy of ~1mJ. Pulse energy employed for inscription is adjusted by a half-wave plate which rotates the direction of the linearly polarised light and a Glan prism which transmits only the vertically polarised component.

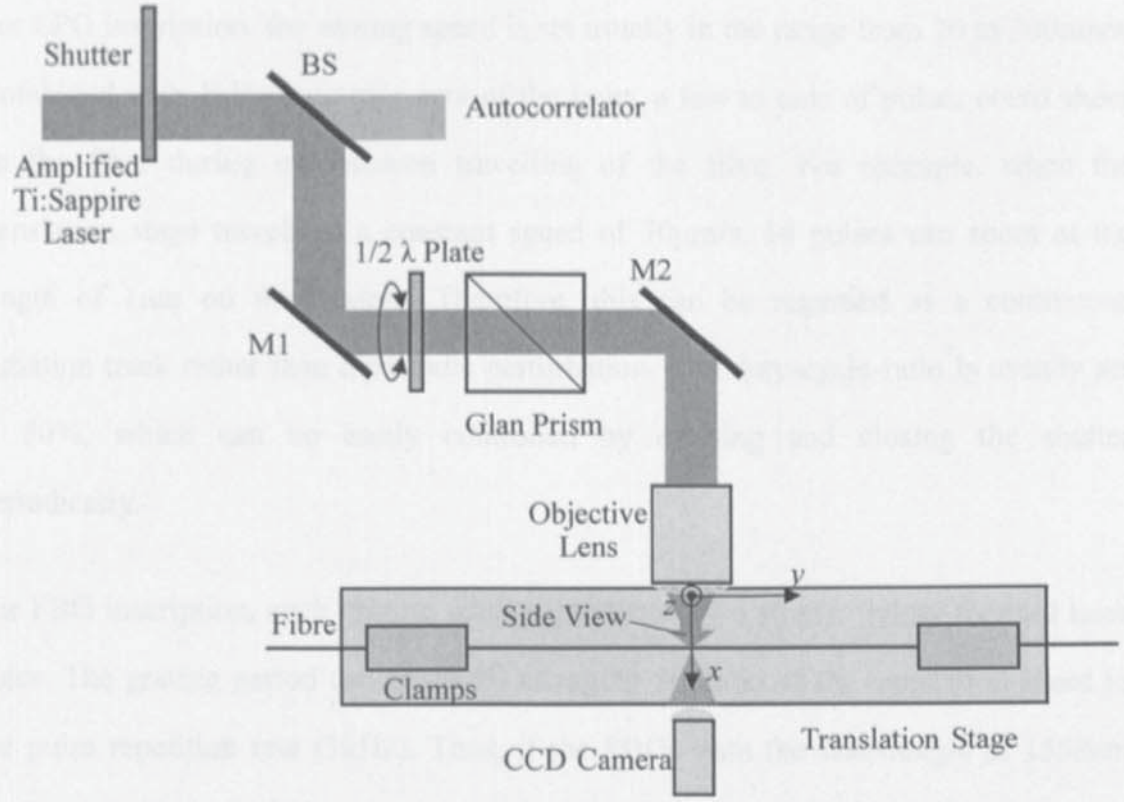

Fig.6.6. Schematic diagram of the point-by-point inscription system using femtosecond laser.

A 100× objective lens with a numerical aperture of 0.55 and specially designed with a long working distance is employed in the system. A CCD camera is placed behind the fibre to image the diffraction pattern for alignment. The laser pulse can be tightly focused by the objective lens. If the self-focusing effect of the optical fibre is neglected, the beam radius in the focal point and the Rayleigh length can be estimated as ~0.9μm and ~3.6μm. In the system, the fibre is placed on a computer controlled 5-dimentional stage, providing linear movement with a resolution of 10nm along *x*, *y* and *z* axes and rotations with a resolution of 0.21μrad around *x* and *z* axes. Due to the long working distance of objective lens, inscription can be carried out with 13mm separation between the surface of the lens and the fibre. During inscription, the stage is moved at a constant speed along the fibre axis, translating the fibre with respect to the focal point of the beam. Limited by the movement range of the translation stage along *y*-axis, the maximum grating length is less than 50mm.

For LPG inscription, the writing speed is set usually in the range from 20 to 200μm/s. Combined with 1kHz repetition rate of the laser, a few to tens of pulses could shoot on the fibre during one micron travelling of the fibre. For example, when the translation stage travels at a constant speed of 70μm/s, 14 pulses can shoot at the length of 1μm on the sample. Therefore, this can be regarded as a continuous radiation track rather than a periodic perturbation. The duty-cycle-ratio is usually set at 50%, which can be easily controlled by opening and closing the shutter periodically.

For FBG inscription, each grating pitch is produced by a single, tightly focused laser pulse. The grating period can be set by changing the ratio of the translation speed to the pulse repetition rate (1kHz). Thus, if the FBGs with the wavelength at 1550nm need to be inscribed in Corning SMF-28, writing speeds from 0.535mm/s to 1.605mm/s can produce first, second and third order FBGs as described by

Equation 6.1 $$\lambda_N = 2n_{eff}\Lambda / N$$

where λ_N is the Bragg wavelength of the N^{th} order FBG, n_{eff} is the effective refractive index of the fibre core and Λ represents the period of the grating structure.

6.3.1.2. System alignment

The good alignment can be achieved by examining the diffraction pattern imaged by the CCD camera. The general alignment procedure has been employed over a long period and improved in recent years by my colleagues Yicheng Lai and Kaiming Zhou. Fig.6.7 shows the diffraction patterns captured by the camera when the fibre is moving towards the focal point of the laser beam.

(a) (b) (c) (d) (e)

Fig.6.7. CCD images taken when the laser beam focal point is (a) far, (b), (c), (d) near and (e) hitting the fibre air/cladding interface. Images of diffraction patterns shown in (a), (b) and (e) indicate the fibre placed symmetrical to the focal point; and images shown in (c) and (d) indicate the fibre axis a little higher and lower than focal point.

Limited by the movement range of the translation stage along *y*-axis of the system (Fig. 6.6), two alignment points are usually selected in the fibre with the distance between them of ~45mm. The whole alignment procedure is described as following. The fibre is firstly moved away (~1mm) from the focal point along *x*-axis using the translation stage and then moved back slowly until the focused beam hits the air/cladding interface of the fibre. This can be indicated by the diffraction pattern displayed on the screen as shown in Fig. 6.7 (e). During the movement, if the height of the fibre axis is off the beam focal point, the diffraction pattern will show asymmetrical shape, as shown in Fig. 6.7 (c) and (d); then the fibre can be moved in *z*-direction until the diffraction pattern is symmetrical. I repeat this alignment procedure for the two far side alignment points of the fibre and record the *x*, *y* and *z* positions of two air/cladding interface points on the control PC. By rotating the fibre around *x* and *z* directions with calculated angles based on above two position readings, the fibre is in parallel to the *y*-direction of the translation stage. When this whole alignment procedure finishes, the new *x*, *y* and *z* positions of the air/cladding interface are recorded and used as the start reference position. Then, the fibre is moved along the *x*-axis towards the objective lens by approximately a distance of the cladding radius (for example, if it is the Corning SMF-28, the moving distance is 62.5μm). Thus the femtosecond beam focal point is assumed now in the fibre core and the femtosecond-laser-inscription can be started. For standard telecom fibre and other

commercial fibres, this is an accurate positioning method to find the fibre core, however, for the mid-IR fibre, *e.g.* the double clad GPNG fibre, the core position was still easy to miss as the fibre was not drawn uniformly and the core was not symmetrically located in the centre of the cladding. For this case, several trials have to be carried out to find the core position.

6.3.2. LPG INSCRIPTION

LPGs inscribed by 800nm femtosecond lasers have been reported for several years [168-170]. But in some cases [168, 169], smooth spectra like UV inscribed gratings were found difficult to achieve by femtosecond-laser-inscription. This may mainly attribute to the uneven refractive index modulation in the fibre core induced by the highly focused femtosecond pulses. In one recent reported case [170], LPGs with high quality spectra were achieved. However, the inscription was too slow (it took more than 4 hours for one grating), and the results might highly rely on the stability of the system.

In my experiments of LPGs inscription using femtosecond laser, when the LPG structures were written in the fibre core using relative high energy and scan speed (comparing with LPGs in [170]), the overall transmission-loss increased greatly as the light was tapped out of fibre core by the femtosecond-laser-induced damages and the cladding mode peaks split. However, smooth and regular LPG spectra were also achieved when the LPG structures were fabricated in the cladding very close to the fibre core or on the cladding/core interface with relative high inscription speed.

In this chapter, the LPG inscription in standard telecom fibre and GPNG fibres will be introduced. To improve the quality of LPG spectra, LPG structures inscribed at the core/cladding interface were demonstrated. Using this method, LPGs were successfully written in standard telecom fibre with smooth and regular spectra.

6.3.2.1. LPGs in standard telecom fibre

LPGs were written in Corning SMF-28 using femtosecond laser and the point-by-point method. The pulse energy was set at ~0.36μJ. After alignment as described in section §6.3.1.2, the laser pulse was focused at or very close to the interface of the fibre core and cladding. The scan speed was selected in the range of 0.1-0.3mm/s and the duty cycles were 50%. Fig.6.8 (a) and (b) show the inscribed grating structures with a period of 560μm viewed from both top and side (beam incident direction) directions under 20× and 10× objective lenses, respectively. The grating structures are clearly physical damages induced by femtosecond laser pulses with relatively high intensity. The total grating length was 31.36mm.

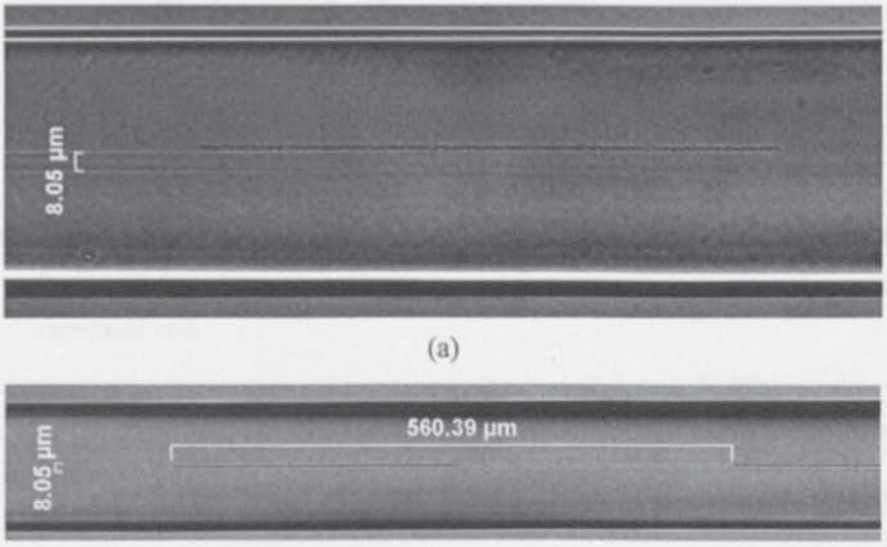

Fig.6.8. Microscope images of LPG with period of ~560μm taken under (a) 20× objective lens from top and (b) 20× objective lens from side direction (laser incident direction). The diameter of fibre core is measured as ~8μm.

From Fig.6.8 we can see that the grating pitches are inscribed at the interface of the fibre core and cladding with the width of ~1μm. Therefore, the pulse intensity is estimated as ~2.4×10^{14}W/cm^2. With a BBS and an OSA, the transmission spectrum of the above LPG was measured as shown in Fig.6.9. In the figure, the spectrum is smooth and the overall transmission-loss is less than 3dB and the greatest loss peak with strength of ~13dB appears at ~1370nm. The LPG spectrum was then simulated

using the Integrated & Fibre Optical Gratings (IFO Gratings) design software and the same parameters employed in the LPG inscription. The simulated spectrum is shown as dash dot line in Fig.6.9. Comparing the simulated transmission spectrum and experimentally measured one, we can see that the spectral resonances from the simulation are in reasonable agreement with the measured ones in position but quite diverse in strength.

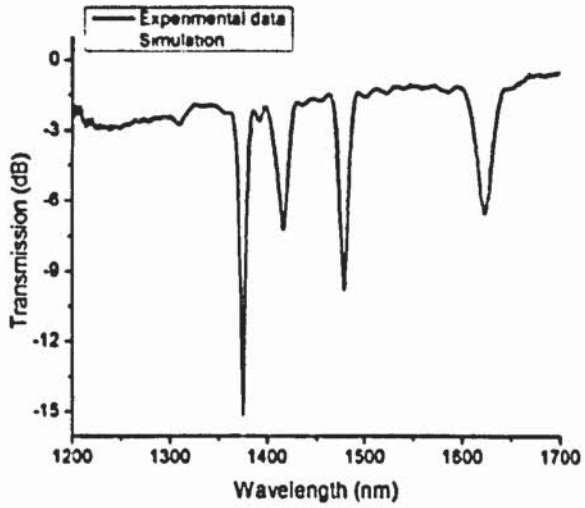

Fig.6.9. Transmission spectrum of the LPG with a period of 560μm. The black continuous line is the experimental measured spectrum and the dash dot curve represents the simulated one.

In addition, the polarisation dependence of this LPG was further analysed by inserting a polariser and a polarisation controller between the BBS and the grating. As the polarisation state of the light is changed, each resonance shifts by different amounts. The polarisation controller was optimised to reach the maximum shift position and the spectrum was recorded. From Fig.6.10 we can see that the third resonance of the 560μm-LPG around 1500nm has shifted by ~6nm and strength reduced by 2.2dB. This marked polarisation dependence effect could be attributed to the off-core position of the grating structure in the fibre.

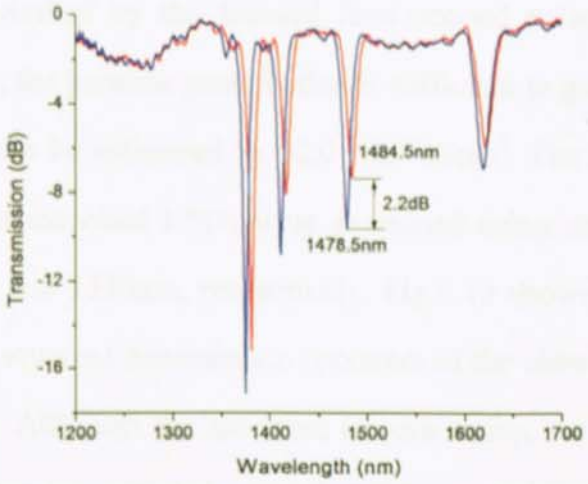

Fig.6.10. Transmission spectra of the 560μm-LPG measured with lights of two orthogonal polarisation states, demonstrating the polarisation induced spectral shift of the third resonance at ~1500nm is about 6.0nm and the peak attenuation variation of 2.2dB.

6.3.2.2. LPGs in germanate glass fibre

LPGs were then inscribed in double-clad GPNG fibre described in section §6.2.1 (Fig.6.1 (a)) using femtosecond laser. LPGs in GPNG fibre were femtosecond-laser-inscribed with the energy of ~0.3μJ and the scan speeds of 0.1-0.2mm/s. Fig.6.11 shows the optical microscope image of one of the femtosecond-laser-inscribed LPGs with designed period of 150μm viewed under a 10× objective lens from top direction, on which we can see clearly the femtosecond-laser-induced regular index structure with a period very close to 150μm in the fibre core positioned off the core centre.

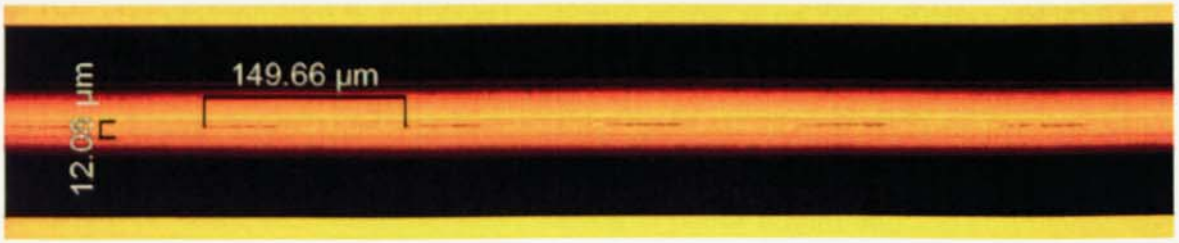

Fig.6.11. Microscope image of the femtosecond-laser-induced LPG structure in GPNG fibre showing a period of ~150μm and is created off the core centre position. Core diameter measured from the image is ~12μm. The image is viewed under a 10× objective lens from top direction.

Although pitches inscribed by the focused femtosecond pulse are much narrower (<1μm) than the core, the periodic perturbation is sufficient to generate LPG coupling. The pulse intensity can be estimated as ~2.0×10^{14}W/cm^2. The spectral responses of the femtosecond-laser-inscribed LPGs were examined using an OSA and two BBS centred around 1200 and 1550nm, respectively. Fig.6.12 shows a concatenated (two spectra from the two sources) transmission spectrum of the above LPG over the range from 900 to 1700nm. Although the spectrum is quite noisy, we can see clearly there are three LPG resonances situated around 1200nm, 1490nm and 1540nm. The attenuation of the strongest loss peak around 1490nm is about 13dB.

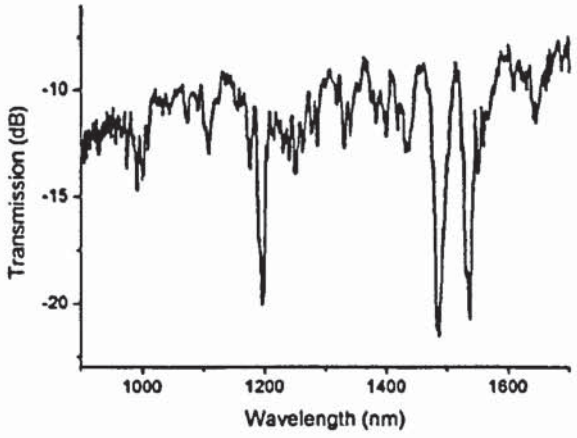

Fig.6.12. The transmission spectrum of one of the femtosecond-laser-inscribed LPGs in GPNG double-clad fibre over the range from 900nm to 1700nm.

In addition, the polarisation dependence of this femtosecond-laser-inscribed LPG was examined by changing the polarisation state of the probing light using a linear fibre polariser and a polarisation controller inserted between the light source and grating. The grating response showed noticeable polarisation dependence. Fig.6.13 shows two sets of spectra for two orthogonal polarisation states, showing the polarisation induced maximum shift for the resonance at ~1540nm is about 6.8nm and the corresponding peak attenuation variation was measured as 5.9dB. This polarisation dependence effect could also be attributed to the off-centre position of the grating structure in the fibre core.

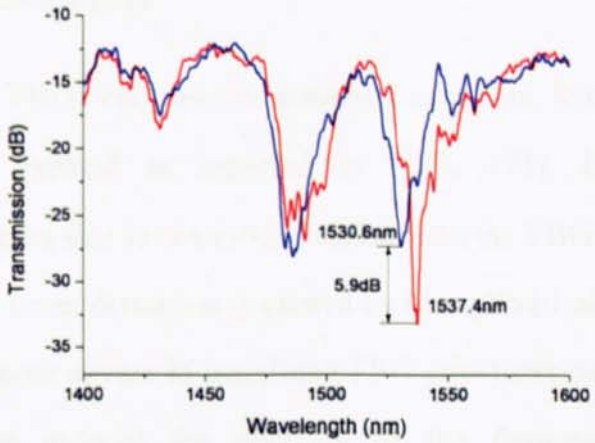

Fig.6.13. The spectral separation between two orthogonal polarisation states of resonance at ~1540nm is 6.7nm and the strength difference is about 5.9dB.

6.3.3. THERMAL RESPONSE OF LPGS IN GERMANANTE FIBRE

The thermal response of the femtosecond-laser-inscribed LPG in GPNG fibre was then examined by subjecting the grating to elevating temperatures. The wavelength shifts of resonances at ~1200 and 1500nm versus the temperature changes from 10 to 60°C with the incensement of 5°C are shown in Fig.6.14. The measured temperature sensitivities of the loss peaks at ~1200nm and 1500nm are very close, with values of 92 and 96pm/°C. These values are ten times higher than the thermal sensitivities of FBGs [18] and similar to that of the LPGs [27] made in standard telecom fibre.

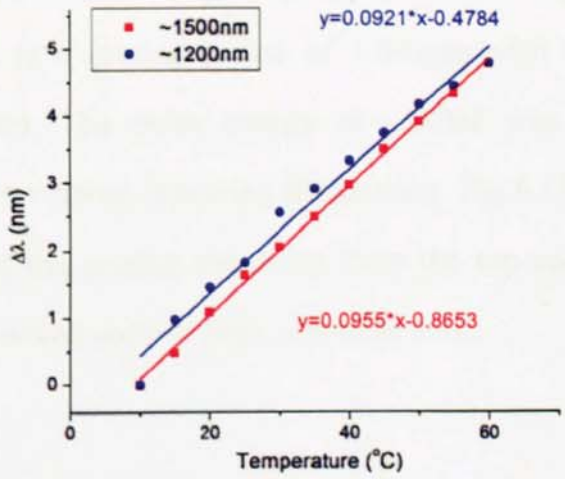

Fig.6.14. The wavelength shift of the resonances at ~1200 and 1500nm against temperature change, showing a similar thermal sensitivity of ~95pm/°C.

6.3.4. FBG INSCRIPTION

Besides LPGs, FBGs can also be inscribed using our femtosecond laser system and point-by-point method as reported in [172, 175]. However, as the focused femtosecond beam size is not much smaller than the FBG grating period (~1μm), the effect from the beam distortion is caused by the cylindrical geometry of the fibre [149, 175] is much more severe in inscribing FBG structures using point-by-point method. Such distortion reduces the intensity of the femtosecond-laser-inducing index modification drastically and severely limits to achieve first order FBGs. In order to avoid this effect, the fibre was placed in a square micro-capillary tube filled with index-matching oil so that the surface geometry presented to the path of the incident femtosecond laser beam is becoming flat [175]. By using this approach, grating fringes with high visibility can be achieved as they can be observed clearly under the microscope.

6.3.4.1. FBGs in standard telecom fibre

By housing the fibre in a square micro-capillary tube filled with index-matching oil, I have successfully inscribed FBGs in Corning SMF-28. After focusing the pulse at the centre of the fibre core, a 5mm-long grating was inscribed using a translation speed of 1.069mm/s. This led to a grating period of 1.069μm with a second-order Bragg resonance at ~1550nm. The pulse energy of ~180nJ was employed in grating inscription in the fibre without removing the coating. Fig.6.15 (a) and (b) show the microscope images of the grating structures from the top and side (beam incident direction) directions viewed under a 100× objective lens.

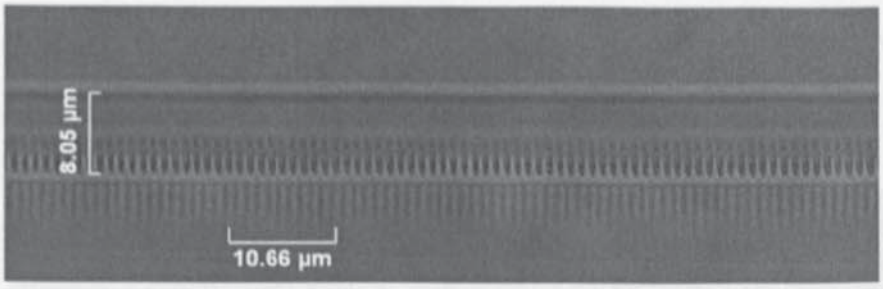

(a)

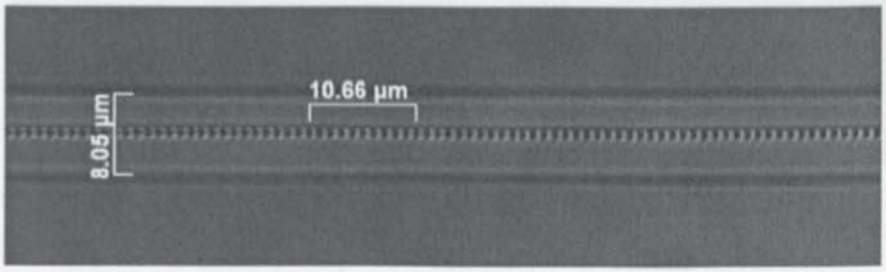

(b)

Fig.6.15. Microscope images of the femtosecond-laser-induced FBG structure in Corning SMF-28 viewed from the (a) top and (b) side direction, showing a period measured as 1.066µm. The core diameter measured from the image is ~8µm. The image is viewed under a 100× microscope lens.

From Fig.6.15 (a) we can see that the grating structure is created off the centre position of the fibre core. The femtosecond-laser-inscription induced grating structure consists of an array of individual ellipsoidal index perturbation, each formed by a single laser pulse, with measured width and depth of ~0.8µm and ~9.0µm respectively. The inscription pulse intensity can be estimated as 1.9×10^{14}W/cm^2. As shown in Fig.6.15 (a) and (b), the grating period is measured as 1.066µm, which is very close to the designed one.

For inscription of 1st order FBG using point-by-point method, the above grating structure inscribed by femtosecond laser is too large in size. By removing the fibre coating before inscription and further reducing the pulse energy to ~90nJ, the size of focused femtosecond beam pulse can be even reduced for 1st order FBG structure inscription since the cross section of the beam above the energy threshold decreases. By doing this, a 5mm-long grating was inscribed using a translation speed of 0.536mm/s. This led to a grating period of 0.536µm with a 1st order Bragg resonance

at ~1554nm. The microscope image taken under a 100× objective lens from the top direction is shown in Fig.6.16.

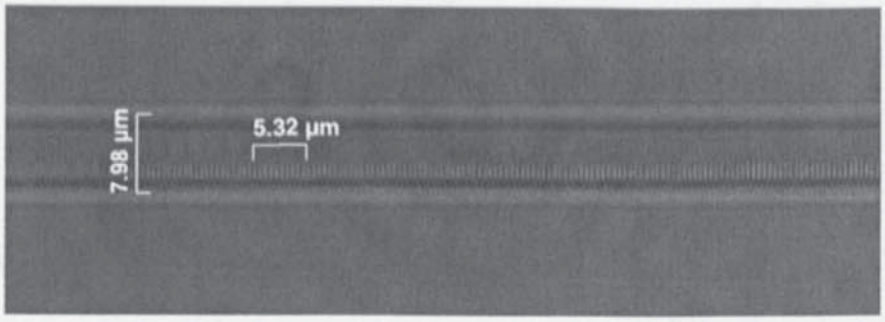

Fig.6.16. Microscope image of the femtosecond-laser-induced FBG structure in Corning SMF-28 viewed from the top direction, showing a period of 0.532µm. The core diameter measured from the image is ~8µm. The image is viewed under a 100× microscope lens.

In Fig.6.16, the observed width and depth of the arrayed ellipsoidal index perturbations are ~0.3µm and ~3.5µm, respectively. Despite the close proximity of the grating fringes, the ~0.53µm periodic index modulation is readily visible. The inscription pulse intensities can by estimated as 6.7×10^{14}W/cm^2. Fig.6.17 (a), (b) and (c) show the spectra of the 1st and 2nd order gratings and the simulated spectra only for the 1st order resonance (note, the IFO software cannot simulate the 2nd order resonances with sinusoidal index modulation). The reflectivities of these two FBGs are measured as ~4.2 and ~5.1dB, respectively. Based on the simulation, the effective index modulation, δn for the 1st order grating can be estimated as 1.1×10^{-4}.

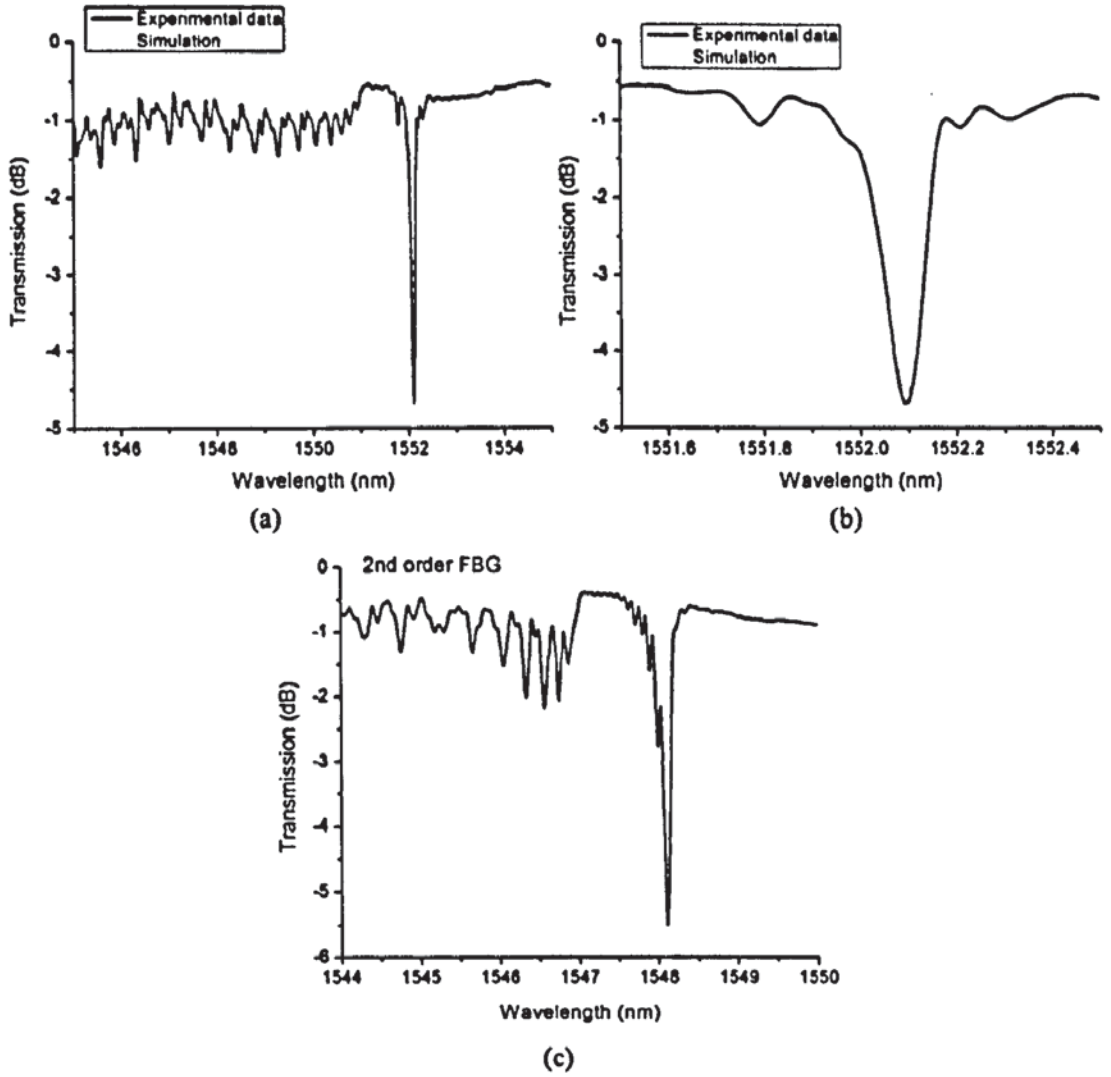

Fig.6.17. (a) Transmission spectra of the 1st order FBG and (b) the zoomed one. The black continuous line is the experimental measured spectrum and the green dash dot curve represents the simulated one using IFO. (c) Transmission spectrum of the 2nd order FBG.

The asymmetry of the induced index profile with respect to the circular cross section area of the fibre core suggests that the gratings would exhibit polarisation-dependent spectral responses. Using a polarised light source and a high-resolution OSA, the transmission profiles of these two gratings for two orthogonal polarisation states were measured as shown in Fig. 6.18.

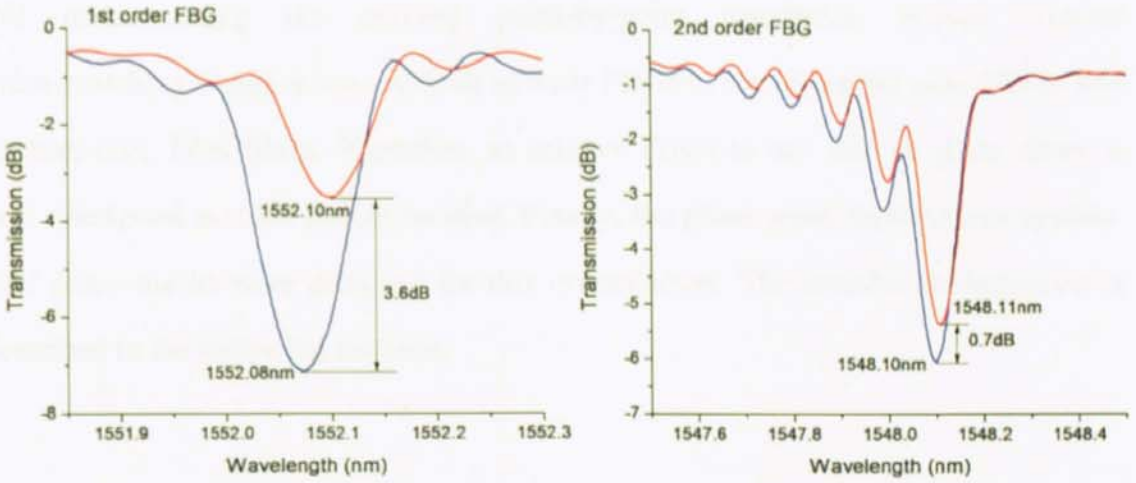

(a) (b)

Fig.6.18. Transmission spectra of the (a) 1st order and (b) 2nd order FBGs measured using light with two orthogonal polarisation states.

As shown in Fig.6.18 (a) and (b), the differences in Bragg wavelengths between the orthogonal polarisation spectral profiles for the 1st and 2nd order FBGs are measured as 0.02 and 0.01nm, respectively. And the peak attenuation variations for these two FBGs are 3.6 and 0.7dB, respectively. Based on the simulation of the 1st order FBG, the effective birefringence Δn_{eff} can be estimated as 1.9×10^{-5} and the effective index modulation, δn, along each polarisation state, are $\sim1.5\times10^{-4}$ and $\sim0.9\times10^{-4}$, respectively.

6.3.4.2. FBGs in germanante and tellurite fibres

Following the success of the FBG inscription in standard telecom fibre, I then tried to write FBGs in GPNG and TZN fibres using the same femtosecond-laser-inscription system and point-by-point method. The fibre is required to be housed in a square tube filled with index-matching oil to successfully write FBG structures by focused femtosecond beam. However, I could not find safe liquids with high refractive index (>1.80), as those liquids with high refractive index are either highly toxic or extremely corrosive. In addition, as shown in Fig.6.1, the GPNG fibre core is off the geometrical centre and the three cores of TZN fibre are distributed in the cladding,

this means using the existing point-by-point inscription system without index-matching liquid, it was difficult to write FBGs in the off-centre core GPNG and in three-core TZN fibres. Therefore, to achieve FBGs in our mid-IR glass fibres, a new inscription method should be used. Finally, the phase-mask method was applied. And phase-masks were designed for this investigation. The detailed investigation is described in the following sections.

6.4. *FEMTOSECOND-LASER-INSCRIBED FBGS BY PHASE-MASK TECHNIQUE*

For grating inscription using a femtosecond laser, the point-by-point technique is a flexible way to create gratings with various wavelengths and different lengths, but it requires a critically focused beam and careful selection of intensity threshold, which is very difficult to obtain. Comparing with the point-by-point system, the phase-mask system is much simpler and easier to perform alignment. Although gratings inscribed using phase-mask technique are of fixed wavelengths and of short grating length, the fibre core can be quickly located by the diffraction pattern, which makes the inscription much more simple and straight forward.

FBGs inscribed using 800nm femtosecond laser and phase-mask was firstly reported by Stephen J. Mihailov *et al* in 2003 [176]. In their paper, they reported FBGs of different orders inscribed using femtosecond laser and phase-masks for several different periods. After that, a series of papers have been reported on FBGs inscribed using femtosecond laser and phase-mask, including the work on FBG inscription method [177], the analysis of grating structures and spectra [178-182], and the annealing properties of femtosecond laser induced FBGs [181, 219].

In this section, I will describe the FBG femtosecond-laser-inscription method and system, especially used for FBG fabrication in mid-IR fibres. The work started by using standard telecom fibre. By improving the inscription system and optimising the condition, FBGs in single- and multi-core mid-IR glass fibres have been written successfully.

6.4.1. FBG INSCRIPTION SYSTEM USING PHASE-MASK

6.4.1.1. Design of phase-mask

Since the femtosecond laser in our lab is operating at 800nm and the mid-IR glasses have high refractive indices, it was impossible to produce 1st order FBGs at wavelength in the range of 1200-1700nm in mid-IR fibres using commercial +1/-1 order interference phase-masks, as the mask pitch required is too small (Λ=~850nm for 1st order FBG in GPNG fibre at 1550nm) and the 0 order diffraction takes most of energy of the transmission light through the phase-mask. I then decided to purchase the masks for 2nd order FBG fabrication using femtosecond-laser-inscription. To achieve an N^{th} order FBG with Bragg wavelength of λ_N the pitch of the grating structure in the fibre, Λ, is defined by Equation 6.2.

With good zero-order nulling, we have $\Lambda=\Lambda_{PM}/2$ (Equation 2.39), where Λ_{PM} is the mask pitch. Therefore, different mask pitches, Λ_{PM}, can be selected to achieve corresponding N^{th} order Bragg resonances λ_N. For standard telecom fibre, 1st - 4th order Bragg resonances occurred at 1550nm can be produced using phase-masks with different pitches of 1.071, 2.142, 3.213 and 4.284μm, respectively. However, the transmission efficiency is quite different for phase-masks with different orders. Table 6.2 lists coupling of 800nm radiation into various phase-mask orders, obtained from reference [176].

Table 6.2. Coupling of 800nm radiation into various phase-mask orders. [176]

Our phase-masks were custom designed +1/-1 order phase-masks from Ibsen. Aiming for femtosecond-laser-inscribing FBGs around 1500 - 1700nm, 2nd order phase-masks with pitches of 2.142 and 1.697μm were selected for standard telecom and mid-IR glass fibres to achieve good zero order nulling (<2%).

6.4.1.2. Inscription system

The schematic diagram of FBG inscription system using femtosecond laser and phase-mask is shown in Fig.6.19. The 800nm femtosecond laser was from an amplified Ti:sapphire system with a repetition rate of 1kHz and a maximum output energy of ~1mJ. The pulse duration measured before the attenuator was <120fs. The inscription energy can be adjusted using an attenuator.

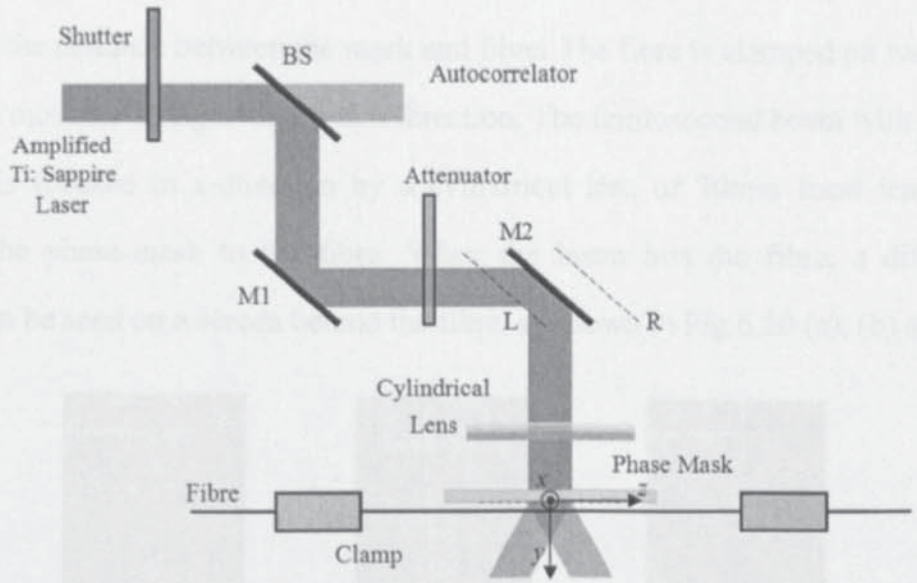

(a)

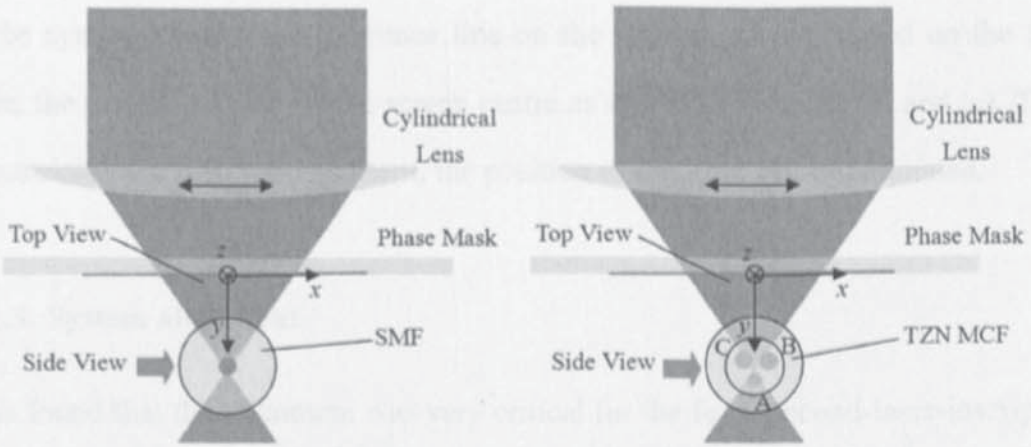

Fig.6.19. (a) Schematic diagram of FBG inscription system using femtosecond laser and phase-mask for (b) single-core and (c) three-core (TZN) fibres. The *x*-axis is parallel to the phase-mask and perpendicular to the mask grooves; the *y*-axis is normal to the phase-mask; *z*-axis is the direction along the fibre axis.

In the system, the phase-mask is placed normal to the incident beam and mounted on a two-dimension stage movable along *y*- and *z*-axis for adjusting the position of the mask and the distance between the mask and fibre. The fibre is clamped on two stages which are movable along *x*- and *y*-axis direction. The femtosecond beam with a radius of 5mm is focused in *x*-direction by a cylindrical lens of 30mm focal length and through the phase-mask to the fibre. When the beam hits the fibre, a diffraction pattern can be seen on a screen behind the fibre, as shown in Fig.6.20 (a), (b) and (c).

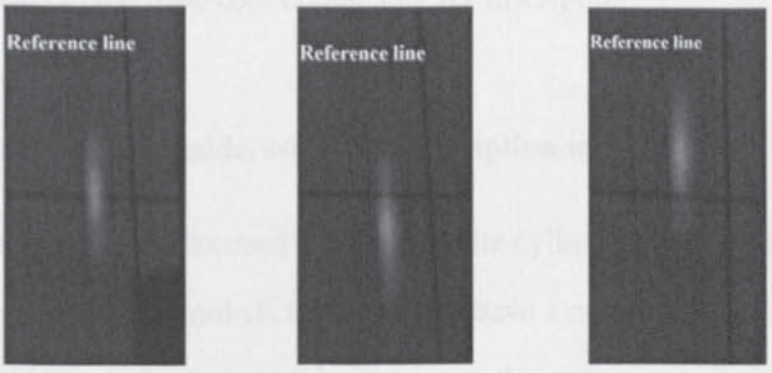

Fig.6.20. The diffraction pattern displayed on the screen when the femtosecond laser beam is focused (a) on or (b), (c) off the centre of the fibre. Note: the horizontal black line is the reference line.

As shown in Fig.6.20 (a), if the laser beam is focused on the fibre centre, the pattern

will be symmetrical to the reference line on the screen; if not focused on the fibre centre, the pattern will be off the screen centre as shown in Fig.6.20 (b) and (c). Thus, by examining the diffraction pattern, the position of the fibre can be estimated.

6.4.1.3. System alignment

It was found that the alignment was very critical for the femtosecond-laser-inscription of FBGs in mid-IR fibres using phase-mask. In the alignment process, the two stages clamping the fibre were firstly adjusted along *y*-axis until the fibre was parallel to the phase-mask. And then the fibre was moved by adjusting the stages along *x*-axis until a clear symmetrical diffraction pattern was displayed on the screen. After that, the height of the lens was adjusted along *y*-axis until the whole diffraction pattern length became minimum, which indicating the beam focal point was hitting the fibre core. This procedure was repeated to the two far side positions on the fibre by moving the mirror M2 mounted on a PC controlled translation stage along *z*-direction to L and R positions, as shown in Fig.6.19 (a). Eventually, the mounted fibre was parallel to the movement direction of the PC controlled translation stage mounting the mirror M2. By presetting the cylindrical lens parallel to this movement direction as well, the laser beam was focused to the fibre core completely for inscription.

6.4.1.4. Focusing effect consideration and inscription method

The laser beam was highly focused by not only the cylindrical lens but also the fibre cladding, especially for the mid-IR fibres as they have a much higher refractive index. Hence, the width of femtosecond-laser-inscribed grating structures in standard telecom and mid-IR glass fibres along *x*-axis (in Fig.6.19) are merely 2-3μm. Fig.6.21 (a) and (b) show the grating structures with 2-3μm widths in Corning SMF-28 and GPNG fibres taken under a 40× microscope from the top direction (beam incident

direction, as shown in Fig.6.19). It is noted that the grating structure in GPNG fibre was inscribed off the fibre core because the core of this fibre was drawn slightly off the geometrical centre of the cladding.

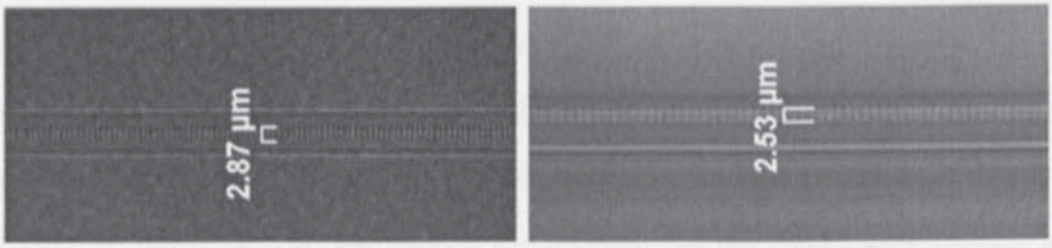

(a) (b)

Fig.6.21. The microscope images of grating structures in (a) Corning SMF-28 and (b) GPNG fibre from the top view (the laser incident direction, as shown Fig.6.19). Note, the structure in (b) was inscribed off the fibre core.

Such a thin-layer of FBG structure gives a much weaker reflectivity than if the structures cover the whole fibre core. In addition, if the fibre is not drawn with uniform in geometry (the mid-IR fibres fabricated by Leeds University have very poor uniformity), and it is easy to miss the core region with the highly focused beam, as shown in Fig.6.21 (b). To ensure maximum coverage of femtosecond-laser-inscription in the core region to write FBGs with strong reflections, the incident beam was scanned along the *x*-axis by shifting the cylindrical lens while the femtosecond beam was exposing the fibre. To maximise the femtosecond beam coverage region on the core, the lens may be scanned along *x*-axis by a distance larger than the core size. Because the laser beam is further focused by the fibre cladding (due to the round shape of the cladding), with the same shift amount of the lens along *x*-axis, the femtosecond laser beam will cover different areas of the fibre for standard telecom and mid-IR glass fibres, due to their different refractive indices. In my experiment, when fibre is placed very close to the phase-mask, by shifting the cylindrical lens from -15 to 15μm, the femtosecond beam coverage area in SMF-28 is around 5mm×20μm, whist in TZN fibre is only 5mm×14μm.

It was noted that when the energy level of femtosecond pulses was increased to improve the efficiency of the inscription in GPNG and TZN fibres, the fibre cladding upper surface was burnt easily as shown in Fig.6.22 before the grating structures had been inscribed in the fibre core. The reason lay in the low melting temperatures of the mid-IR glasses. Therefore, the energy level of femtosecond pulses is very critical for inscribing FBG structures in mid-IR fibre core without burning the fibre. In the system, a 30mm-focal-length cylindrical lens was selected to increase the energy intensity on the fibre core and reduce the intensity on the fibre upper surface at the same time.

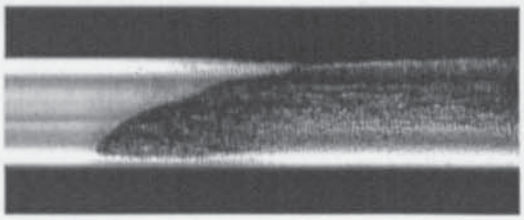

Fig.6.22. Microscope image of a TZN fibre with upper cladding surface burnt by high energy level femtosecond pulses from the top view.

6.4.2. ORDER WALK-OFF EFFECT AND INTERFERENCE STRUCTURE IN OPTICAL FIBRE INDUCED IN THE INSCRIPTION BY FEMTOSECOND LASER AND PHASE-MASK

6.4.2.1. Order walk-off effect and simulation

When I examined the FBG structures inscribed by the femtosecond laser using phase-mask under the microscope in the initial stage, very often interference structures with different periods could be seen from the side direction (as shown in Fig.6.19), as evidently shown in Fig.6.23. It seems that these multi-period structures could be generated by multi-beam interference. This led to our investigation on the propagation property of the femtosecond laser beam after the phase-mask.

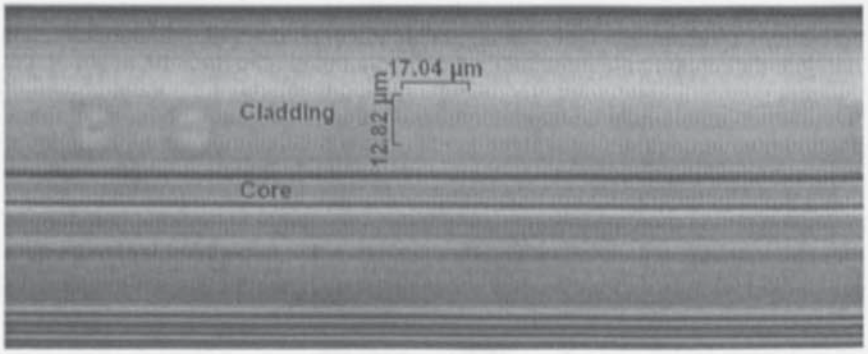

Fig.6.23. Microscope image of three-beam interference pattern generated grating structures in a GPNG fibre viewed from the side direction (as shown in Fig.6.19).

When femtosecond pulses encounter the phase-mask, different order diffractions after the mask travel in different directions. The diffraction angle θ_m ($m = 0, \pm1, \pm2 \ldots$) can be defined by the grating equation:

Equation 6.2 $$\sin\theta_m = m\lambda / \Lambda_{PM}$$

where m is the order number, Λ_{PM} is the mask pitch and λ is the wavelength in the medium. As different order diffractions travel in different directions, their velocity components along the direction normal to the mask are different. Comparing with CW beam and long pulse lasers, femtosecond pulse length is very short (<150fs). Therefore, after travelling only a few millimetres, different diffraction orders will separate completely; this is the order walk-off effect.

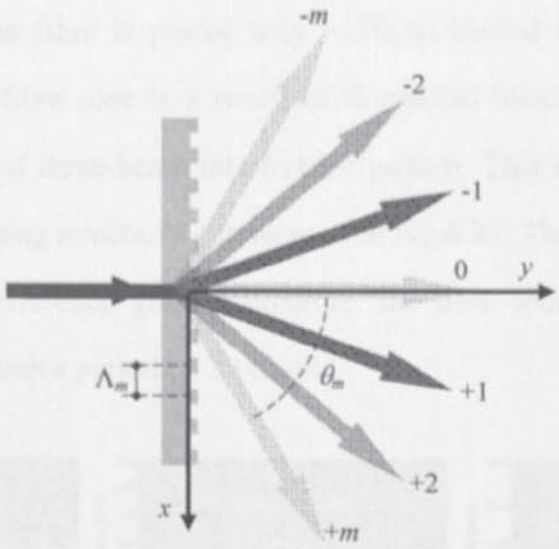

Fig.6.24. Schematic diagram showing different diffraction directions for different orders of the beam after the phase-mask.

The x-axis is defined parallel to the phase-mask while the y-axis is normal to it as shown in Fig.6.24. The laser pulse was assumed to be Gaussian module with the duration of τ =150fs:

Equation 6.3 $$I(t) = I_0 \exp\left[-4\ln 2\left(\frac{t}{\tau}\right)^2\right] \approx I_0 \exp\left[-2.77\left(\frac{t}{\tau}\right)^2\right]$$

where I_0 is the energy when t=0.

To examine the order walk-off effect of the mask with a period of 2.142μm, the propagation of different order beams were simulated as function of the travelling distance from the mask and the results are shown in Fig.6.25. These images in the figure were generated by superimposing Gaussian intensity profiles travelling at angles set by the grating equation. Each order travels at the speed of light. From Fig.6.25 (a)-(c) we can see that when the 0 order travelled just 100μm from the mask, the diffractions of 0, ±1 and ±2 orders are entirely overlapping, when travelled 800μm, the 0 and ±1 orders are still very close together but ±2 order diffractions lag behind, and when travelled about 1600μm from the mask, all 0, ±1 and ±2 orders are

separated. Thus, if the fibre is placed only ~100μm behind the mask, the grating structure area in the fibre core is a result of five-beam interference pattern and if ~800μm behind it is of three-beam interference pattern. This clearly explained why multi-interference grating structures can be seen in Fig.6.23. Thus, in order to achieve a pure two-beam interference grating structure, the fibre should be placed 1.6mm away from the mask with a period of 2.142μm.

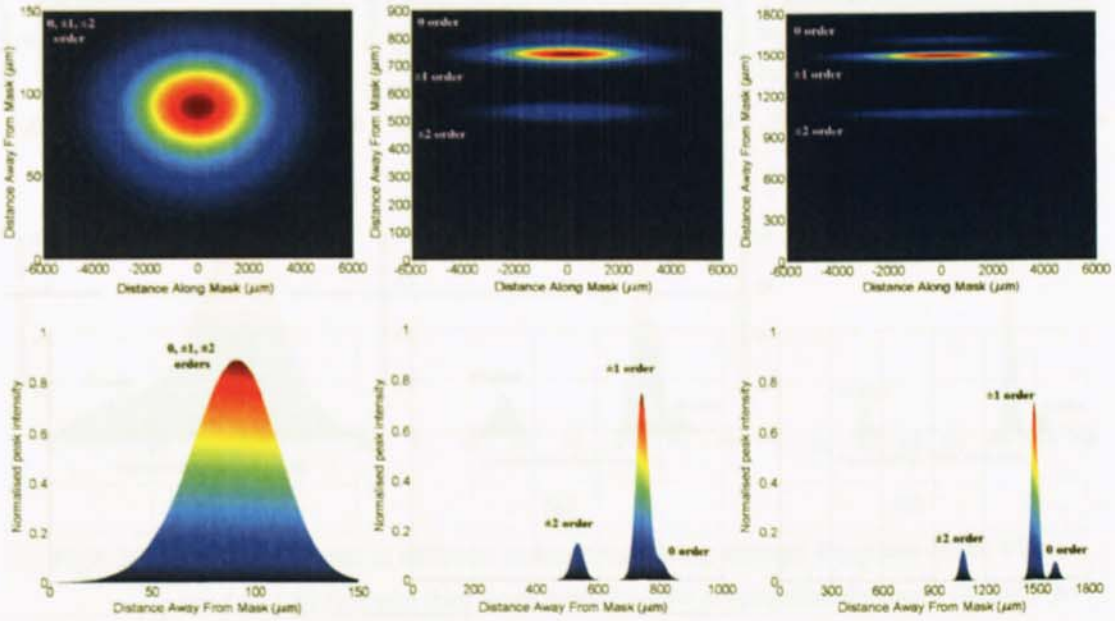

(a) (b) (c)

Fig.6.25. Diffraction beams of different orders propagating through the phase-mask with a period of 2.142μm and their peak intensities for propagation distances (a) 100, (b) 800 and (c) 1600μm, showing interference areas in x-y plane and the normalised amplitude for each area. The phase-mask position is set at $y = 0$.

From Fig.6.25, when the 0 order beam propagates 100, 800 and 1600μm beyond the mask, we have the main peak intensities in these three cases of 89%I_0, 75%I_0 and 71%I_0. It is clear that the peak intensity reduces significant with the distance of the propagation beam from the mask. The reason of intensity reduction attributes to the order walk-off and pulse evolution.

Similar results on the order walk-off effect have been obtained for the mask with a period of 1.697μm, as shown in Fig.6.26 (a), (b) and (c). Here we see that when the

fibre is placed 1200μm away from the mask, a pure two-beam interference grating structure can be achieved. From Fig.6.26 it is estimated that when the 0 order propagates 100, 500 and 1200μm beyond the mask, we have the main peak intensities in these three cases of 82%I_0, 75%I_0 and 71%I_0.

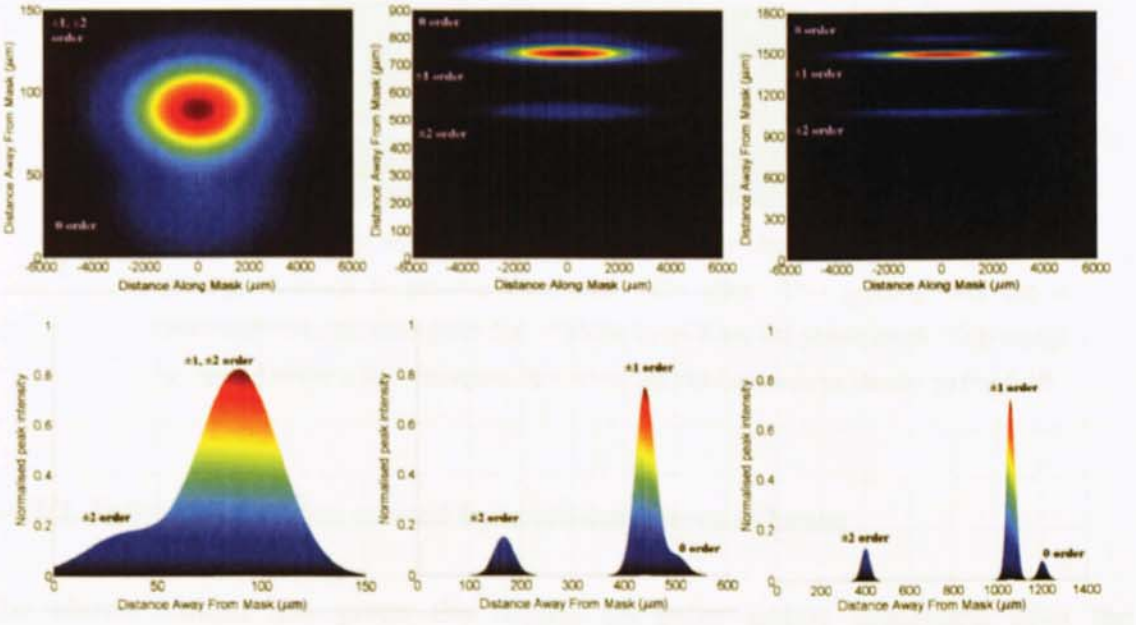

(a) (b) (c)

Fig.6.26. Diffraction beams of different orders propagating through the phase-mask with a period of 1.697μm and their peak intensities for propagation distances (a) 100, (b) 500 and (c) 1200μm, showing interference areas in x-y plane and the normalised amplitude for each area. The phase-mask position is set at $y = 0$.

From the above simulation, pure two-beam interference grating structures can be achieved by placing the fibre 1600 and 1200μm away from the two purchased custom-designed masks with periods of 2.142 and 1.697μm, respectively. However, in the experiment it is also noticed that if the fibre is placed too close to the phase-mask, the mask can be damaged when high energy pulse is used, because the energy density outside the fibre is sufficient to damage the phase-mask although the focal point is in the fibre core.

It should also be pointed out that although the fibre can be placed with a right distance from the mask to eliminate the multi-interference effect, because we need to scan the

cylindrical lens along the *x*-direction to make strong gratings, this could cause some phase-errors. This phase-error effect is clearly seen in Fig. 6.27, indicated by several slightly misaligned grating structures in the fibre. This effect may be overcome by using more precise position and control in moving the lens in future.

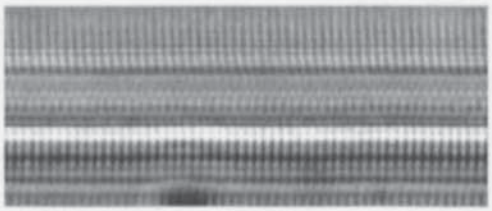

Fig.6.27. Microscope image of the phase-error appeared in femtosecond-laser-inscribed grating structure in passive three-core TZN fibre. This grating structure is inscribed with the fibre placed at ~300μm away from the phase-mask. This image is viewed under a 40× objective lens from the top direction as shown in Fig.6.19.

6.4.2.2. Index modulation caused by multi-interference beam

The above section has given the results on pulse orders separation after the phase-mask. In this section, the simulated multi-interference induced index fringe modulation is presented and compared them with the actual femtosecond-laser-inscribed grating structure in the fibre. For this work, a CW beam interference model was used to simulate grating structures in fibres. Unlike previous models [220-222], it was not necessary to take into account the propagation of the pulse envelope. Thus, the resulting interference field would have the form [179]

Equation 6.4 $$|E(x,y)|^2 = \left|\sum_m a_m \exp[ikx\sin(\theta_m) + iky\cos(\theta_m)]\right|^2$$

where a_m is the amplitude of the diffracted orders, and k is the wave-vector amplitude. We have $k = 2\pi n/\lambda$. The employed order amplitudes were the parameters in Table 6.2 Λ_{PM}=2.142μm. As shown in Fig.6.19, the *x*-axis is parallel to the phase-mask and perpendicular to the grooves and the *y*-axis is normal to the phase-mask. Therefore,

the propagation angle of the m^{th} diffraction order in the fibre can be expressed as:

Equation 6.5 $$\sin\theta_m^{'} = \frac{m\lambda}{n\Lambda_{PM}}$$

Fig.6.28 (a) and (b) are the microscope images of the FBG structures resulted from three- and two-beam interference inscribed by femtosecond laser in single-clad GPNG fibres which were placed 100 and 1200μm behind the mask, respectively. In Fig.6.28 (a) we can clearly see a multi-period structure.

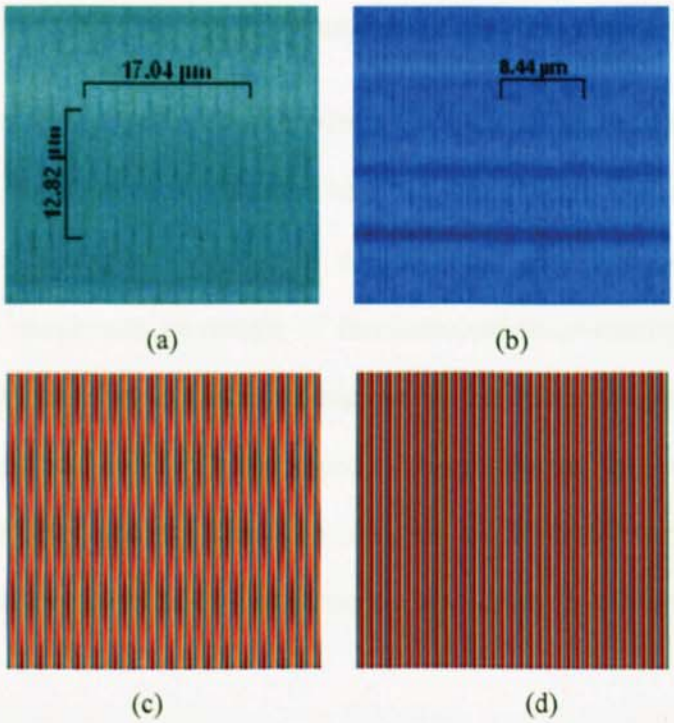

Fig.6.28. Experimental grating structures in GPNG fibres (viewed from the side direction) resulted from (a) three-beam and (b) two-beam interfernce and simulation structures for (c) three-beam and (d) two-beam.

With the wavelength λ set at 800nm and the refractive index n assumed to be 1.8039. The simulated three- and two-beam interference patterns are plotted in Fig.6.28 (c) and (d). Like the experimental results, we also see that the three-beam interference simulation gives a multi-period structure in Fig.6.28 (c). As shown in Fig.6.28 (b) and (d), a clear one-period FBG structure in the fibre with only two-beam interference can be achieved from both experimental and simulated results. The period of the grating

structure measured from Fig.6.28 (a) is around 1.70μm, which is not the half period of the phase-mask. This can be taken as an example of Talbot effect [221]. The Talbot length (structure period along *y*-axis) is calculated as ~12.75μm, which is very close to the measured one, 12.82μm, as shown in Fig.6.28 (a). The period of the grating structure measured from Fig.6.28 (b) is about 0.844μm, which is very close to that of theoretical pure two-beam interference pattern (0.849μm).

6.4.3. FBG INSCRIPTION AND CHARACTERISTICS

6.4.3.1. FBGs in standard telecom fibre and their spectral characteristics

The FBG structures were fabricated in Corning SMF-28 using femtosecond laser and a phase-mask with a period of 2.142μm. The fibre was placed 1.6mm away from the phase-mask in the inscription system to achieve the pure two-beam interference pattern. To ensure maximum coverage of femtosecond-laser-inscription in the core region, the incident beam was scanned along the *x*-axis in the range from -5 to 5μm by shifting the cylindrical lens with the speed of 3μm/s during the exposure. Fig.6.29 (a) and (b) show the grating structure images in SMF-28 without and with hydrogen-loading taken under a 40× microscope lens from the side direction (shown in Fig.6.19).

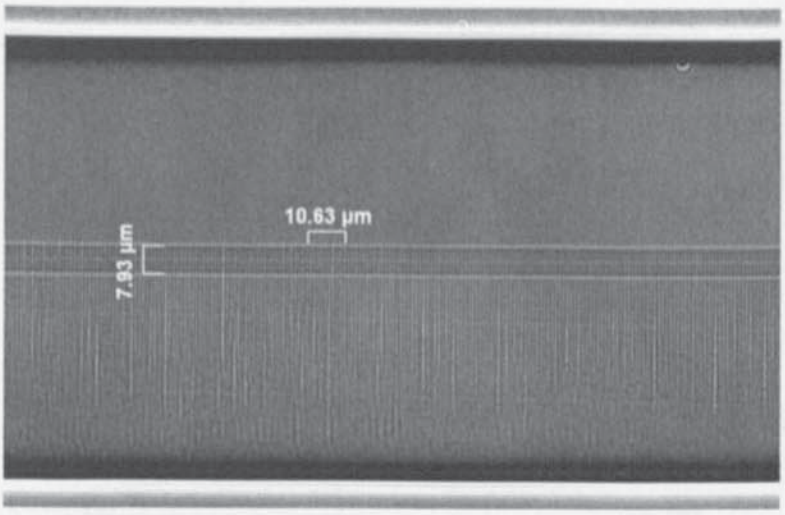

(a)

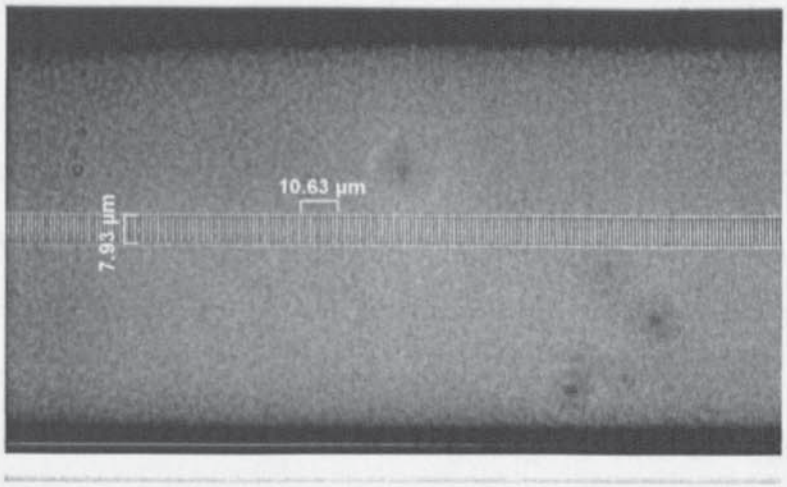

(b)

Fig.6.29. Microscope images of FBG structures in Corning SMF-28 (a) without and (b) with hydrogen-loading taken under a 40× objective lens viewed from the side direction. The core diameter measured is measured as ~8µm in both (a) and (b).

As seen from Fig.6.29 (a), it is clear that the grating structure covers the whole core region and also extends into the cladding region. The period of the structure is measured as 1.063µm, which is very close to the half period of the phase-mask (1.071µm). Fig.6.30 (a) shows the transmission spectrum of this second order FBG with a peak-strength of ~11dB at 1549.2nm.

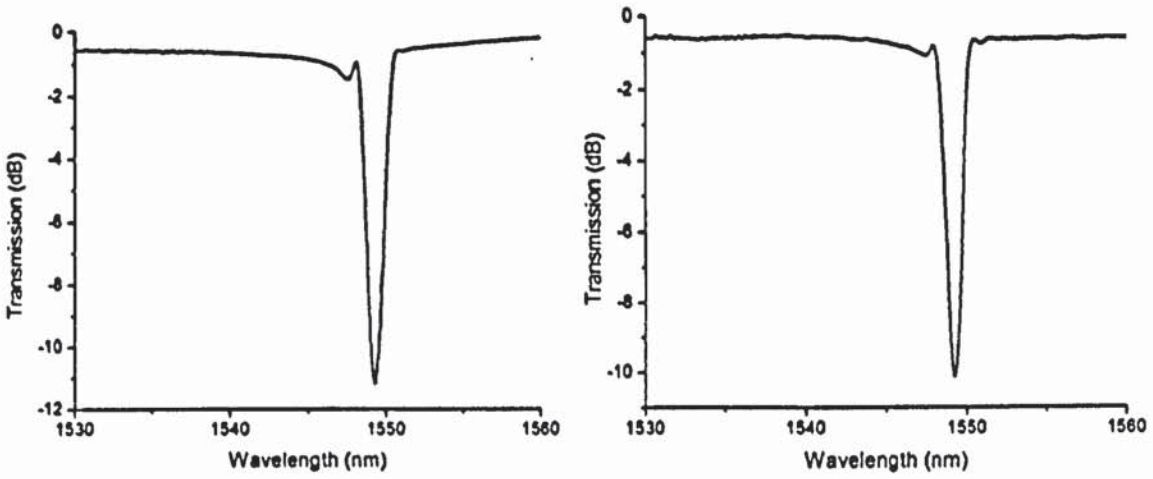

Fig.6.30. Transmission spectra of the FBGs in Corning SMF-28 (a) without and with hydrogen-loading inscribed using phase-mask with a period of 2.142μm.

I then further studied FBG inscription in hydrogen-loaded SMF-28 using the same phase-mask and placing the fibre 1.6mm away from the mask. The photosensitivity of fibre was found increased greatly after the hydrogen-loading, and a much lower femtosecond laser threshold energy was needed to write strong FBGs. Considering the focused beam size of 5mm×2.5μm, Table 6.3 presents threshold energies and intensities of the femtosecond-laser-inscribed gratings in SMF-28 without and with hydrogen-loading.

Table 6.3. Threshold energies and intensities of femtosecond-laser-inscribed gratings in SMF-28.

Fibre	Pulse Energy (μJ)	Intensity (W/cm^2)
Corning SMF-28	67	5.7×10^{12}
hydrogen-loaded Corning SMF-28	28	2.4×10^{12}

If we only consider the contribution of the ±1 orders, which contain ~80% of the incident energy, and ignore rest orders, the interference of these two orders will result in a peak intensity of ~160% of the incident energy. Therefore, the threshold peak intensity, I_{th}, can be calculated from [180]:

Equation 6.6
$$I_{th} = \frac{E_{th} \times 1.6}{Area \times \tau}$$

where, E_{th} is the incident threshold energy, τ is the pulse duration, and *Area* presents the focused beam area.

The grating structures inscribed in hydrogen-loaded SMF-28 using femtosecond laser and phase-mask is shown in Fig.6.29 (b). It is noted that the grating structure covers only the fibre core because the inscription energy employed was much lower than the threshold energy for SMF-28 without hydrogen-loading. The period of the structure is measured as 1.063μm, which is very close to the half period of the phase-mask.

From the transmission spectra of the femtosecond-laser-inscribed FBGs in standard telecom fibre, it is noticed that there is almost no light coupling to the cladding modes, as no resonances can be seen on the shorter wavelength sides of the main Bragg peaks, as shown from Fig.6.30 (a) and (b), whereas the cladding mode coupling resulted resonances are always visible and even very strong for the UV-inscribed FBGs in hydrogen-loaded standard telecom fibre. Similar result has been reported in [223]; and the reason of this phenomenon was explained as the partially apodized grating structure due to the Gaussian profile of the incident beam and low average induced index change though no explicit apodization process is implemented. This could be advantage to devices as there would be no cladding mode coupling induced cross-talk effect. Due to limited time for this project, I could not carry on more study on this unique cladding-mode-suppressed feature in FBGs. This should be further verified and studied before the definitive conclusion can be drawn.

6.4.3.2. FBGs in germanate glass fibre

The FBG structures were produced in the single-clad single-core GPNG fibre using femtosecond-laser-inscription through a custom-designed phase-mask with a period of 1.697μm. Because of the high refractive index of the GPNG fibre, the mask was designed aiming to inscribe 2nd order FBGs in this kind of fibre with response around

1540nm. The output beam with a radius of 5mm was focused in x-axis by a cylindrical lens of 30mm focal length and through the mask to the fibre core. As mentioned in section §6.4.1.4, due to the focusing effect of the cladding with high refractive index, the width of femtosecond-laser-inscribed grating structure along x-axis, as shown in Fig.6.21 (b), is merely ~2.5μm.

To ensure maximum coverage of femtosecond-laser-inscription in the core region, the incident beam was scanned along the x-axis from -30 to 30μm with an incremental step of 2μm for the single-core GPNG fibre. After each shift, the translation stage was paused for 3min letting the laser expose the focused fibre position.

The femtosecond pulse energy is critical for inscribing FBG structure in the core to avoid burning the fibre cladding. Via systematic tests, critical femtosecond energy of ~22μJ is identified to be suitable for inscribing FBGs in the GPNG fibres and the threshold peak intensity for GPNG fibres can be calculated as 1.9×10^{12}W/cm^2.

After inscription by femtosecond laser, the FBG fringe structures was firstly examined under the microscope. Fig.6.31 (a) shows the top view image of grating structures inscribed in GPNG single-core fibre, from which we can see the core is fully covered by the continuous fringes. Fig.6.31 (b) exhibits the side view image of grating structure. In this image, the grating structures appear also in the cladding region and show a typical three-beam interference pattern. The pitch length in these microscope images are measured as 1.704μm, which is close to the period of the phase-mask (1.697μm), instead of a half of it. This is also attributed to the Talbot effect [221]. From Fig.6.31 (b), the Talbot length is measured as 12.82μm, which is in good agreement with the simulated one in section §6.4.2.2.

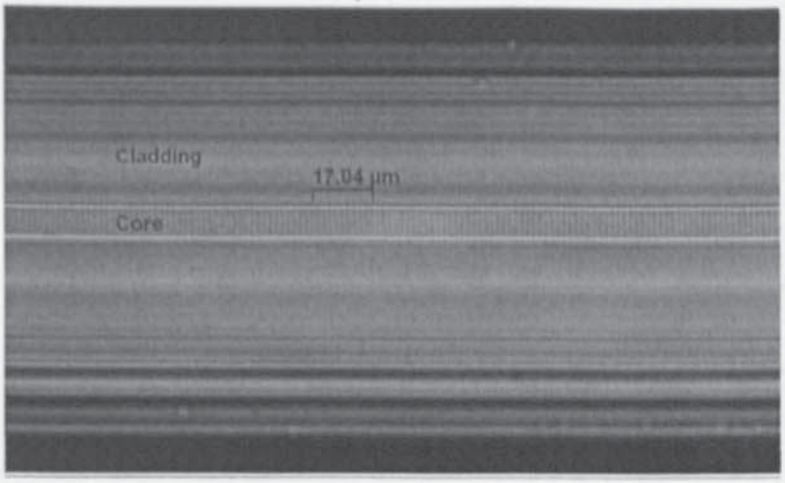

(a)

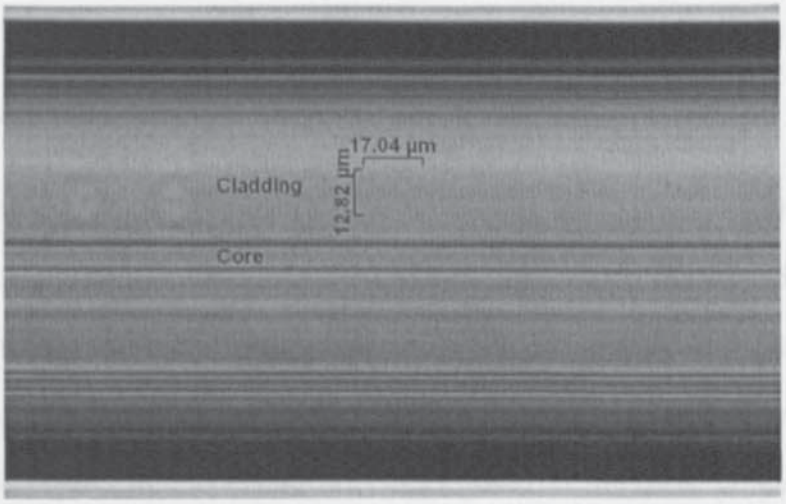

(b)

Fig.6.31. Microscope images of FBG structure from (a) the top and (b) side view in the GPNG fibre. The period of the structure is measured as 1.704μm in both (a) and (b). And Talbot length is measured in (b) as 12.82μm.

A super continuum BBS from Koheras with an output wavelength up to 1800nm was employed to examine the transmission spectra of the fabricated FBGs in GPNG fibres using butt-coupling method. Fig.6.32 (a) shows a 2nd order Bragg resonance at 1540.42nm with the strength of 6.5dB. It is noted that Fabry-Perot resonances at the shorter wavelength side of the Bragg peak is due to the Gaussian beam shape. A very weak 3rd order resonance at 1033.74nm is also observed with the strength of only 1.2dB, as shown in Fig.6.32 (b). From the wavelengths of these two resonances, we calculated the refractive indices of the GPNG fibre as ~1.8156 and ~1.8271 at 1540 and 1034nm, respectively.

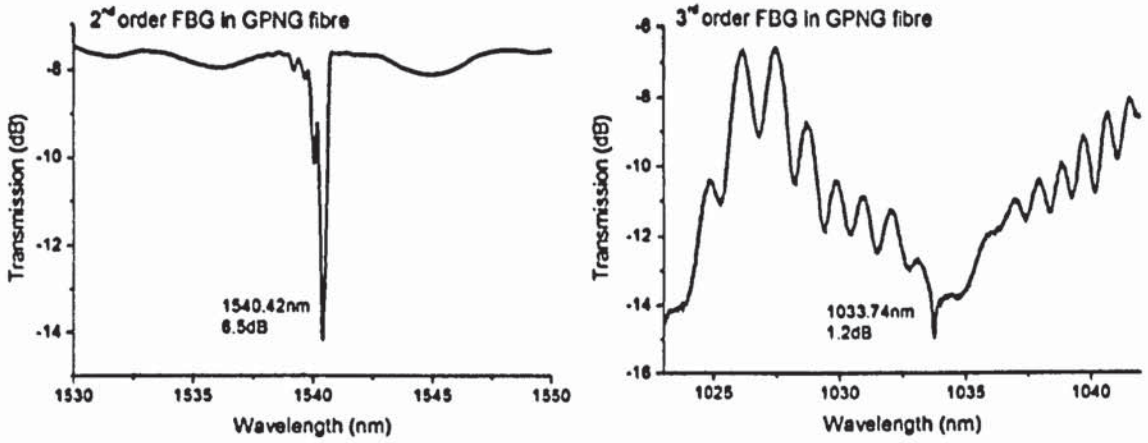

(a) (b)

Fig.6.32. (a) 2nd and (b) 3rd order FBG resonances of the grating made in GPNG fibre.

6.4.3.3. FBGs in tellurite glass fibre

The FBG structures were produced in the three-core passive and active TZN fibres using femtosecond-laser-inscription through the same phase-mask with a period of 1.697μm. Using similar inscription parameters, 2nd order FBGs were inscribed in the passive and active TZN fibres with Bragg resonances at ~1680nm. To ensure maximum coverage of femtosecond-laser-inscription in the three cores, the incident beam was scanned along the *x*-axis from -50 to 50μm with an incremental step of 2μm. After each shift, the translation stage was also paused for 3min letting the laser expose the focused fibre position. The critical pulse energy of ~14μJ was identified via systematic tests for inscribing FBGs in the TZN fibres, and the corresponding femtosecond pulse peak intensity was calculated as 1.3×10^{12}W/cm^2.

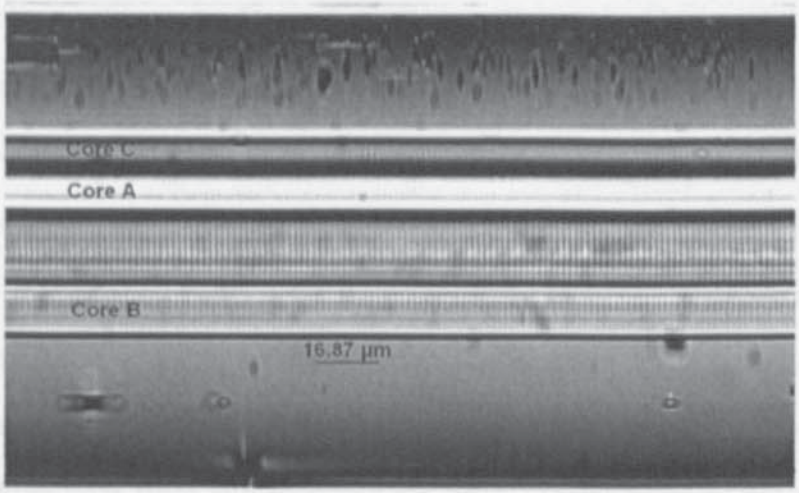

(a)

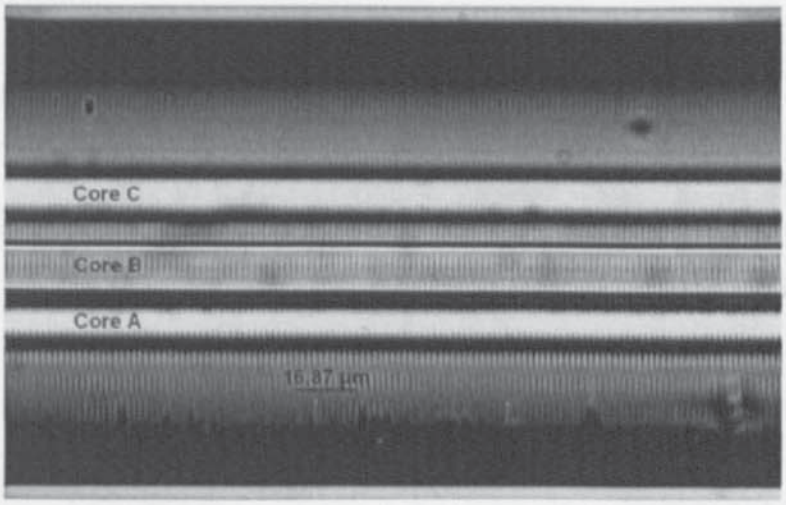

(b)

Fig.6.33. Microscope images of grating structure from (a) the top view and (b) side view of the TZN passive fibre. In both (a) and (b), the periods of the structures are measured as 1.687µm.

Fig.6.33 (a) shows the top view image of grating structures inscribed in three-core TZN passive fibre, from which we can see all the cores and part of the cladding in the fibre are covered by the continuous fringes. In the side view image of grating structures (Fig.6.33 (b)), the grating structures covering the almost the whole cladding section indicates a typical three-beam interference pattern. Similar to the grating structures in GPNG fibres, the pitch lengths in these microscope images are measured as 1.687µm, which are close to the period of the PM (1.697µm), instead of a half of it.

Due to higher refractive index and larger size of the core, the passive three-core TZN

fibre is actually multi-mode fibre at ~1694nm. This is evidenced by the multiple Bragg resonance feature exhibited by the FBGs in all three cores, as shown in Fig.6.34 (a) - (c). In the fabrication, the femtosecond beam was more focused to the core A, thus the grating resonance in core A is the strongest, giving 14.3dB transmission-loss for the lowest order mode and the FBG resonances in core B and C achieved a similar strength in an order of ~4dB. As a prototype device, this result is encouraging and more uniform FBG structures in all three cores should be possible by rotating the three-core fibre and focusing the femtosecond beam to the targeted core during the inscription.

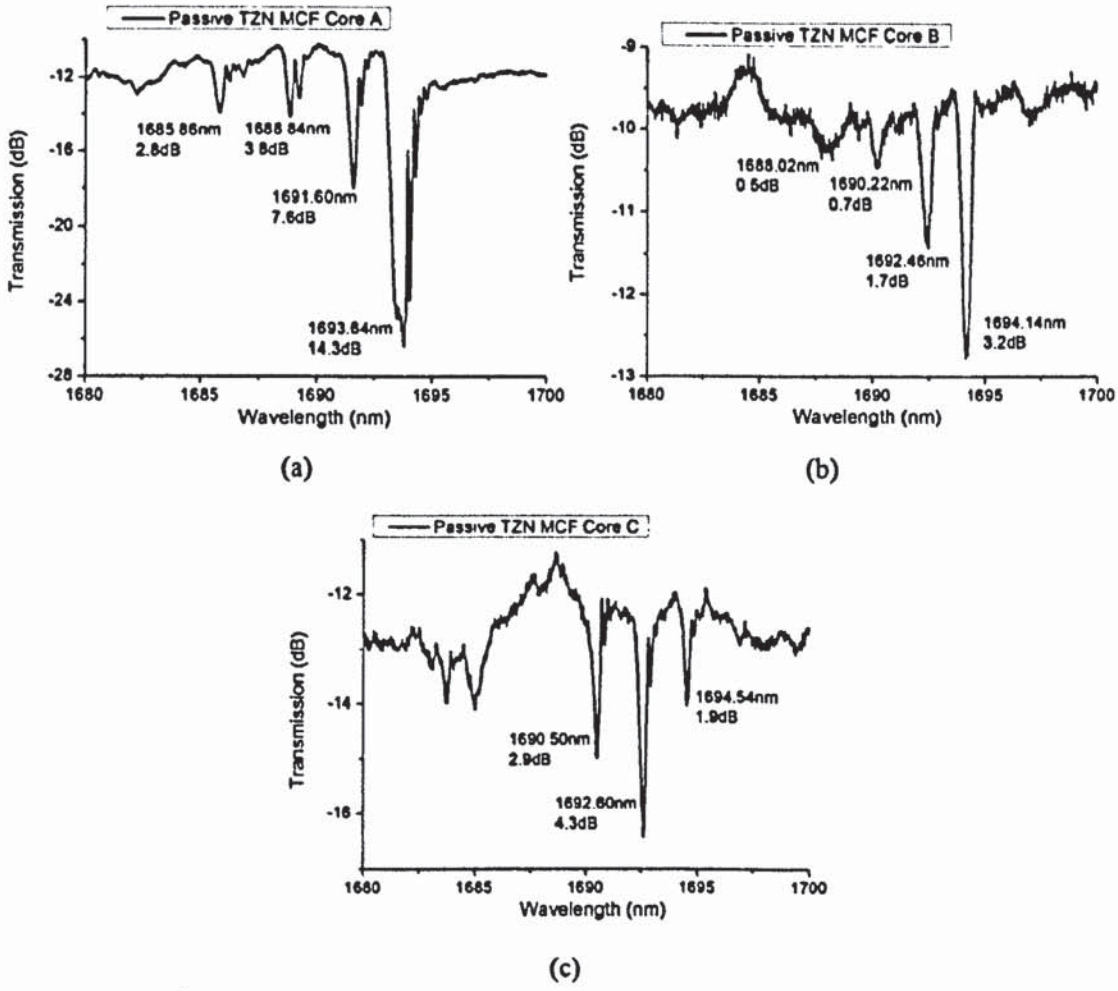

Fig.6.34. 2nd order FBG resonances in the passive three-core TZN fibre: (a) core A, (b) core B and (c) core C.

FBG structures were also inscribed by femtosecond laser in the active three-core TZN

fibre. The 2nd order FBG resonances in the three cores are shown in Fig.6.35. (a) - (c). Here, we only see single resonance in each core indicating the fibre is single mode structure, because its core diameters are smaller than that of passive TZN fibre. The 2nd order FBGs are more uniform across the three cores in this active fibre, as we see the strengths of the three resonances at 1678.05, 1676.05 and 1676.85nm in the three cores are 10.6, 5.6 and 6.8dB, respectively. The refractive index of the TZN fibre core at ~1677nm can be estimated as ~1.9760.

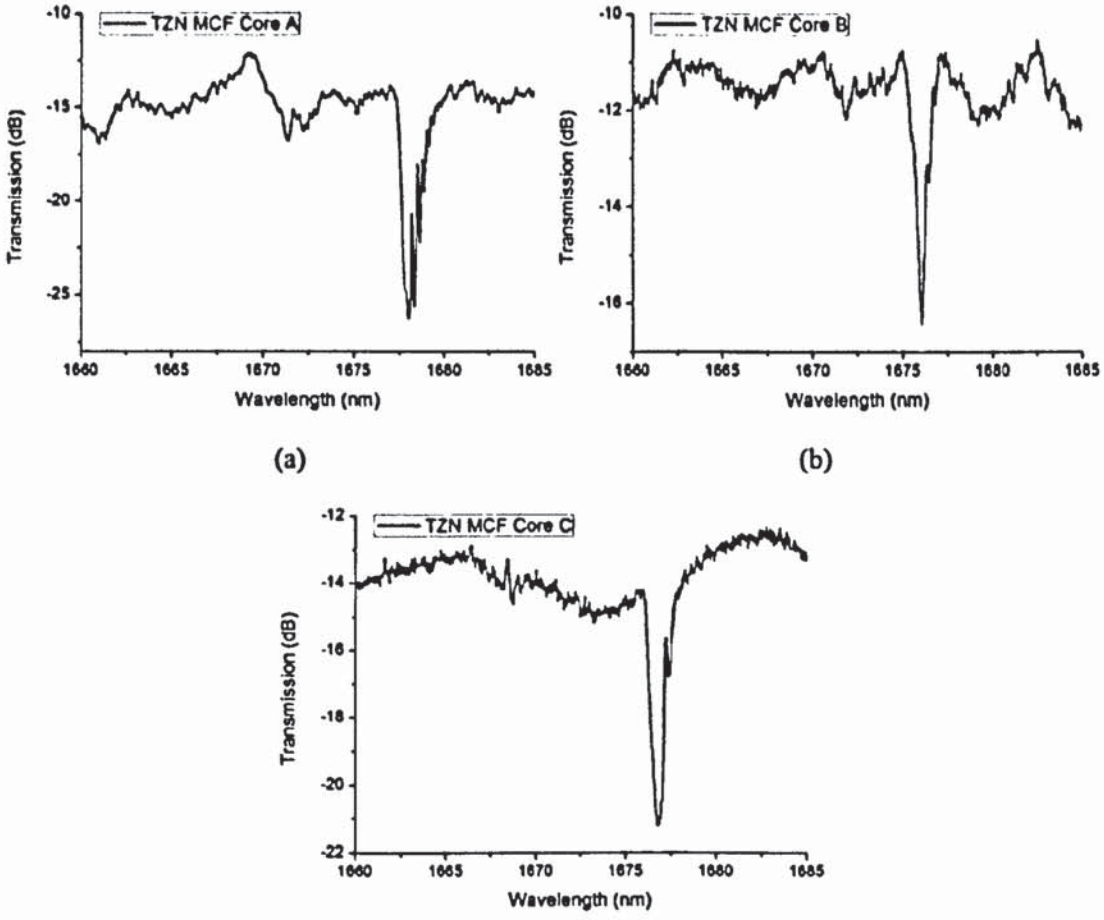

Fig.6.35. 2nd order FBG resonances in (a) core A, (b) core B and (c) core C of the active TZN fibre.

It is noted from Fig.6.34 and Fig.6.35 that some pronounced type of Fabry-Perot structures appears at the longer wavelength side of the Bragg resonances for the TZN fibres, which is different from the normal FBG spectra. Note, due to the Gaussian

beam shape, very often there is Fabry-Perot resonances at the shorter wavelength side of the Bragg peak, for example, in Fig.6.32 (a). A similar phenomenon was observed for UV-inscribed B/Ge fibre [224] and the simulation suggested that this may be caused by a negative refractive index modulation induced during inscription. The refractive index distribution induced by femtosecond laser in TZN fibre is assumed negative and can be expressed as:

Equation 6.7
$$\delta n(x) = \delta n_0 \left[1 - \exp\left(\frac{B(x - L_g/2)^2}{L_g^2} \right) \right]$$

where B = 4 is used in our calculation, L_g is the grating length, x is the axis along the grating length, δn_0 is the maximum refractive index change that can be reached for type I gratings. With the parameters used as δn_0=0.0018, L_g=5mm, the spectrum in one of the cores of the active TZN MCF was simulated as shown in Fig.6.36. Limited by the simulation software, the 1st order harmonic resonance with half of the period was employed in simulation, but the profile is very like the experimental one in Fig.6.35 (a). This explanation needs to be verified by further experiment in TZN fibres using femtosecond-laser-inscription.

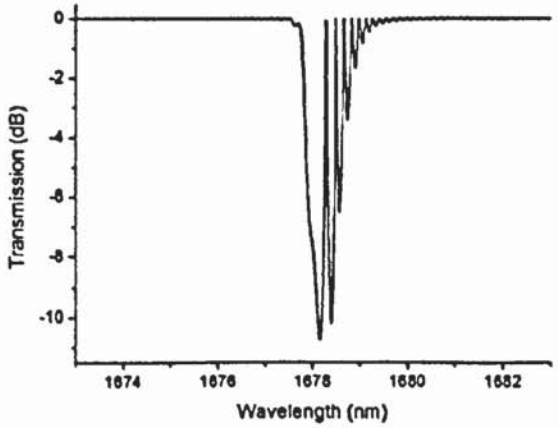

Fig.6.36. The spectral simulation of the 1st order harmonic resonance with half of the period in the core A in the active TZN MCF.

6.4.4. THERMAL AND STRAIN RESPONSE OF FBGS INSCRIBED IN MID-IR GLASS FIBRES BY FEMTOSECOND LASER

6.4.4.1. Thermal responses of the grating resonance in germanante and tellurite glass fibres

I have also examined the thermal responses of the femtosecond-laser-inscribed FBGs in GPNG and TZN fibres by subjecting the grating fibres to elevating temperatures. The wavelength shifts of the 2nd and 3rd order Bragg resonances of GPNG fibre at 1540 and 1033nm versus the temperature changes from 10 to 70°C with incremental step of 5°C are shown in Fig.6.37 (a), showing the measured thermal sensitivities of 24.71 and 16.80pm/°C, respectively. Fig.6.37 (b) shows the thermal sensitivities of the active three-core TZN fibre for elevating temperature from 10 to 60°C. The thermal sensitivities of cores A - C are measured as 20.21, 18.61 and 19.25pm/°C, respectively.

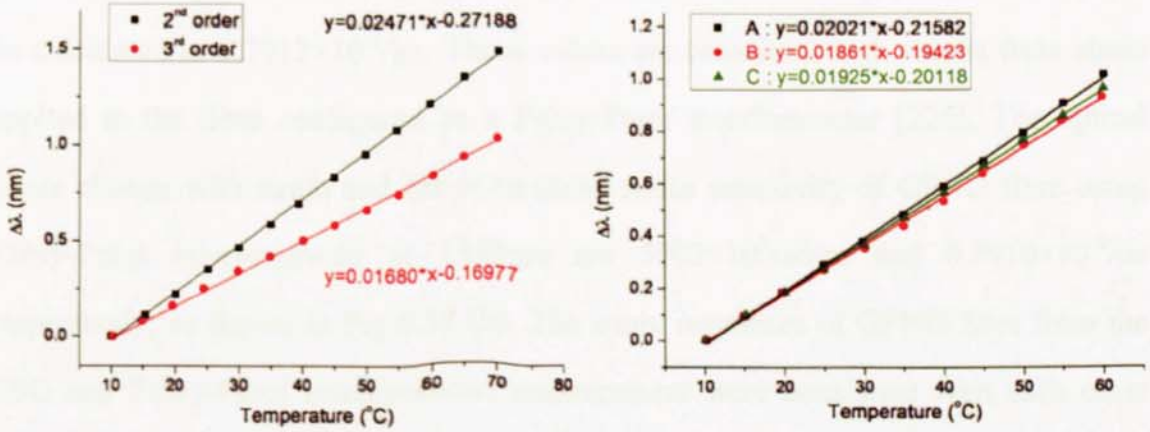

(a) (b)

Fig.6.37. The wavelength shift of (a) the 2nd and 3rd order resonances of the GPNG fibre at ~1540 and 1033nm and (b) the 2nd order resonances of the core A - C of the active three-core TZN fibre at ~1677nm against temperature change.

The thermal sensitivity can be expressed as:

Equation 6.8

$$\frac{\Delta\lambda}{\Delta T} = \lambda_B \left(\alpha + \frac{\beta}{n_{eff}} \right)$$

where $\alpha = \frac{1}{\Lambda}\frac{d\Lambda}{dT}$ is the thermal expansion coefficient, and $\beta = \frac{dn}{dT}$ is the thermo-optic coefficient. For GPNG fibre, α and β given in [225] are 1.09×10^{-5} and 9.0×10^{-6}/°C. Therefore, using the value of refractive index n_{eff}=1.8156, the thermal sensitivity for 1540 and 1033nm can be calculated as 24.43 and 16.39pm/°C, respectively. For TZN fibre, using $\alpha=1.86\times10^{-5}$/°C, $\beta=-1.64\times10^{-5}$/°C from [226] and n_{eff}=1.9760, we can derive the thermal sensitivity for 1676nm with the value of 17.26pm/°C. From the above calculation, the experimental thermal sensitivities are in good agreement with the theoretical ones.

6.4.4.2. Strain responses of the FBGs in germanante glass fibre

The strain response of the femtosecond-laser-inscribed FBGs in GPNG fibres was also examined by applying longitudinal strain to the grating fibres. The strain sensitivity of the 2nd order Bragg resonance of GPNG fibre at 1540nm was measured to be 1.219pm/με, as shown in Fig.6.38 (a). And the normalised strain sensitivity can be calculated as 0.7912×10^{-6}/με. These values are consistent with results from strain applied to the fibre configured as a Fabry-Perot interferometer [226]. The optical phase change with strain and the normalised strain sensitivity of GPNG fibre using Fabry-Perot interferometer at 1540nm are 5902×10^{3}rad/m and 0.7910×10^{-6}/με respectively, as shown in Fig.6.38 (b). The strain responses of GPNG fibre from the FBG and Fabry-Perot interferometer measurement were consistent with each other with only 0.025% difference in the normalised strain sensitivity.

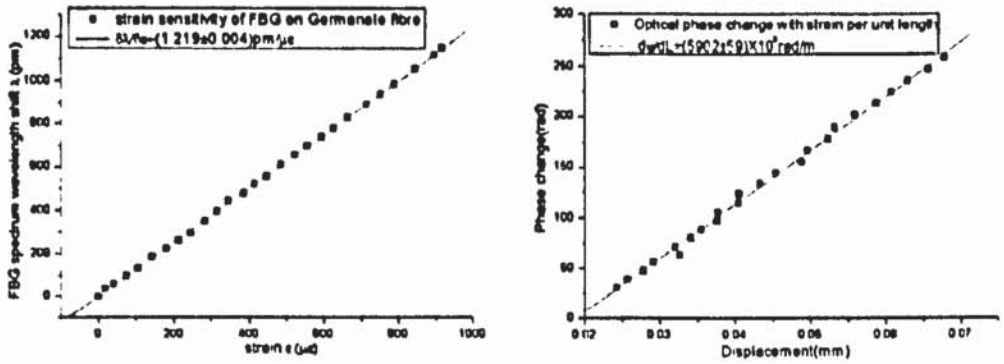

(a) (b)

Fig.6.38. The strain sensitivity of the 2nd order resonances of (a) the GPNG fibre at ~1540nm and (b) the optical phase change with strain per unit length of GPNG fibre at ~1540nm from Fabry-Perot interferometer.

The strain sensitivity of FBGs can be expressed as:

Equation 6.9
$$\frac{\Delta\lambda_B}{\varepsilon} = \lambda_B \cdot \left\{1 - \frac{1}{2} \cdot n^2 \left[(1-\mu)p_{12} - \mu p_{11}\right]\right\}$$

The optical phase change per unit strain per unit fibre length of the Fabry-Perot interferometer can be express as:

Equation 6.10
$$\frac{\Delta\phi}{\varepsilon L} = \frac{\Delta\phi}{\Delta L} = \frac{2n\pi}{\lambda}\left\{1 - \frac{1}{2} \cdot n^2 \left[(1-\mu)p_{12} - \mu p_{11}\right]\right\}$$

Then the normalised strain sensitivity of the fibre from FBGs and Fabry-Perot interferometer can be expressed as:

Equation 6.11
$$\frac{1}{\beta} \cdot \frac{\Delta\phi}{\Delta L} = \frac{1}{\lambda_B} \cdot \frac{\Delta\lambda_B}{\varepsilon} = 1 - \frac{1}{2} \cdot n^2 \left[(1-\mu)p_{12} - \mu p_{11}\right]$$

where β is the propagation constant of the mode in the fibre, ε is the longitudinal strain applied to the fibre, μ is Poisson's ratio, p_{11} and p_{12} are the strain-optic coefficients. Using p_{11}=0.225, p_{12}=0.235 and μ=0.232 for germanate glass with composition (mol%) of $30PbO\text{-}10Bi_2O_3\text{-}60GeO_2$ from [227], the strain sensitivity of

FBGs and optical phase change with strain of Fabry-Perot interferometer for 1540nm can be calculated as 1.270pm/με and 6318×10^{3}rad/m, respectively. The normalised strain sensitivity of germanate glass fibre at 1540nm can be derived with the value of 0.8243×10^{-6}/με. From the above calculations, the experimental strain responses are also in good agreement with values calculated using published data for fibre with similar compositions, and the small difference between these experimental and predicted values may be due to the slightly different glass compositions being compared.

6.5. *CHAPTER CONCLUSIONS*

In this chapter, I have demonstrated the fabrication of LPGs and FBGs in standard telecom and mid-IR germanante and tellurite glass fibres using femtosecond laser inscription employing point-by-point and phase-mask methods and presented a systematic investigation on the spectral, thermal and strain characteristics of these gratings.

Using the point-by-point method, LPGs and FBGs were inscribed in Corning SMF-28 and double-clad GPNG fibres with femtosecond pulse intensities estimated in the order of 10^{14}W/cm^2. An LPG with period of 560μm was fabricated at the core/cladding interface in SMF-28 in order to achieve high spectral quality with a relatively high inscription speed. The strongest LPG loss peak with strength of ~13dB has been obtained. The LPG spectral resonances are in good agreement with simulated results. An LPG with period of 150μm was inscribed in GPNG double-clad fibre and the strength of its strongest loss peak around 1500nm was about 13dB. The temperature sensitivities of the loss peaks of this LPG at ~1200 and 1500nm were measured as 92 and 96pm/°C, respectively.

1st and 2nd order FBGs with periods of 0.536 and 1.069μm were inscribed in SMF-28 also using the point-by-point method and placing the fibre in a square micro-capillary tube filled with index-matching oil. The reflectivities of these two FBGs with wavelengths at ~1550nm were measured as ~4.2 and 5.1dB, respectively. Due to asymmetry of the structures inscribed in the fibre using the point-by-point method, transmission spectra of both LPGs and FBGs exhibit strong polarisation dependences.

FBG inscription using phase-mask method in standard telecom, single-core GPNG and three-core passive and active TZN fibres has been studied on both grating structures and spectral properties. A theoretical analysis has been carried out on the

walk-off effect of the femtosecond beam propagation through the phase-mask, and identified the optimal distance to place the fibre behind the phase-mask. Pure two-beam interference 2nd order FBG structures can be achieved by placing the standard telecom fibre 1.6mm away from the mask with the period of 2.142μm and mid-IR fibre 1.2mm away from the mask with the period of 1.697μm. The 2nd order FBGs in Corning SMF-28 without and with hydrogen-loading have been achieved with reflectivity reaching the value of ~11dB.

Using the phase-mask of 1.697μm period, FBGs were inscribed in germanate and tellurite glass single- and multi-core fibres. With peak intensities in the order of 10^{12}W/cm^2, FBGs in passive and active GPNG and TZN fibres were achieved. In the single-core GPNG fibre, the 2nd and 3rd order Bragg resonances are at 1540 and 1033nm with strengths of 6.5 and 1.2dB. In the three-core TZN fibres, the 2nd order resonances are situated at ~1677nm in all three cores with the strongest peak, exhibiting a strength of 10.6dB.

In addition, thermal sensitivities of FBGs made in these two kinds of mid-IR glass fibres have been characterised. The thermal sensitivities of the 2nd and 3rd order Bragg resonances in GPNG fibre were measured as 24.7 and 16.8pm/°C and those of the 2nd order resonances in the three individual cores of the TZN fibre were measured as 20.2, 18.6 and 19.3pm/°C, respectively. The experimental thermal sensitivities are in good agreement with the theoretically calculated ones. The strain and normalised strain sensitivity of 2nd order FBG in GPNG fibre were also measured and calculated as 1.219pm/με and 0.7912×10^{-6}/με, respectively. The normalised strain sensitivity from the FBG is consistent with the value of 0.7910×10^{-6}/με from a Fabry-Perot interferometer measurement using the same fibre. The experimental strain response is also in good agreement with the value calculated using published data for fibre with similar compositions.

Chapter 7

Conslusions and Future Work

7. Conslusions and Future Work

7.1. CONCLUSIONS

7.1.1. SPECTRAL CHARACTERISTICS OF TFGS AND THEIR APPLICATIONS

In this thesis, I have presented the results from theoretical and experimental investigation on the structures, inscription methods and spectral, PDL and thermal characteristics of TFGs with small, large and 45° tilted structures. Based on the mode-coupling theory, I have theoretically analysed the TFGs, revealing the relationships between the radiation angle, central wavelength of the radiation profile, Bragg resonance and the tilt angle and identifying design rules for the dependence of the radiation mode out-coupling range and PDL on the tilt angle of TFGs.

TFGs with small, large and 45° tilted structures have been fabricated for studies on real devices. These TFGs have been systematically characterised, obtaining typical spectral, polarisation and thermal properties, which are in good agreement with theoretically analysed results. For TFGs tilted at small and large angles, I have examined in detail the polarisation effect on coupled cladding mode resonances, such as polarisation induced mode separation and shift for different wavelength ranges. For 45°-TFGs, the PDL effect was analysed in the wavelength range from 1525-1608nm and a 2^{nd} order Bragg resonance was identified at ~1568nm, which may be used in combination with its in-fibre polariser function to realise fibre laser with single polarisation and single wavelength output. Further studies on the 45°-TFG demonstrate that the PDL ripples can be greatly eliminated by immersing the grating in index-matching gel, showing a very smooth PDL response over a broad wavelength range.

Additionally, thermal responses have been measured for these three types of TFGs.

For small angle TFGs, the thermal sensitivities of three pairs of resonances with orthogonal polarisation states of a 7°-TFG in the wavelength range 1500-1555nm were measured, obtaining the thermal sensitivities ranging from 10.35-11.08pm/°C, which were in the same order of but slightly lower than reported normal structure FBGs made in silica fibre. For large angle TFGs, the thermal sensitivities for 75°- and 81°-TFGs with polarisation dual-peaks around ~1410 and ~1620nm have been measured, showing that thermal sensitivities for 75°-TFG resonances were higher than those for 81°-TFG resonances in the similar wavelength range. It is noted that thermal sensitivities for resonances of 81°-TFG in the range from 1400-1620nm have been observed low as ~6.85pm/°C, which is only half or even less than that of small tilted and normal structure FBGs at 1550nm, giving application advantage of low thermal cross-sensitivity. The investigation carried out on 45°-TFGs clearly show that no significant PDL change was found under the variation of temperature. This is of a desirable application advantage as all 45°-TFGs can be used as in-fibre high polarisation function devices with great stability.

Based on the unique optical properties of TFGs, applications using small and large angle TFGs have been demonstrated. The 10°-TFG based 800nm WDM interrogation system has been studied, showing a function as an in-fibre spectrum analyser with an interrogation bandwidth up to 60nm and a resolution of 12.7pm. Additionally, this system was further evaluated for sensing the refractive index of sample liquids. In the near-linear range from 1.4132 to 1.4735, it is estimated that the SRI change as small as 10^{-5} can be detected by this low-cost high-resolution TFG WDM interrogation system. By utilising the polarisation signatured dual-peak property of large angle TFGs, their high sensitivity loading and twisting sensing capability has been demonstrated. The 81°-TFG based sensors are capable of encoding the transverse load and twist change to polarisation dependent spectral evolution of the paired polarisation resonances. The large angle TFG based sensing system can be further

developed into low-cost and high-sensitivity sensors by employing single wavelength light source and photodiode. Using this low-cost power measurement scheme, a load interrogation experiment have been implemented employing an 81°-TFG, giving a load sensitivity of 2.04μW/(kg/m) and a twist sensitivity of 145.90μW/rad. If the power meter is replaced by a photodiode with detectivity of 1nW, our TFG load and twist sensor systems may detect the load and twist change as small as 1.6×10^{-2}g and 6.9×10^{-6}rad, respectively.

7.1.2. Optical fibre gratings inscribed by femtosecond laser in silica and mid-IR glass fibres

Germanante and tellurite glasses have been taken as good candidates for mid-IR glass fibres due to their high refractive index and optical nonlinearity, resistance to corrosion, low melting temperature and good transmission properties in the mid-IR region. In addition to the work on UV-inscribed TFGs, another major research work is carried out on femtosecond-inscription of FBGs and LPGs in standard telecom and mid-IR germanante and tellurite glass fibres using the point-by-point and phase-mask techniques and I have systematically investigated the spectral, thermal and strain characteristics of these gratings.

Using the point-by-point inscription technique, LPGs and FBGs were inscribed in standard telecom and double-clad GPNG fibres with femtosecond pulse intensity estimated in the order of 10^{14}W/cm^2. An LPG with a period of 560μm was inscribed at the core/cladding interface in standard telecom fibre in order to achieve high spectral quality with a relatively fast inscription speed. The strongest LPG loss peak with a strength of ~13dB has been obtained. The LPG spectral resonances are in good agreement with simulated spectrum. An LPG with a period of 150μm was inscribed in GPNG double-clad fibre and the strength of its strongest loss peak around 1500nm was about 13dB. The thermal sensitivities of the loss peaks of this LPG at ~1200 and

1500nm were measured as 92 and 96pm/°C, respectively. For FBG fabrication, 1st and 2nd order FBGs with period of 0.536 and 1.069μm were inscribe in standard telecom fibre by placing the fibre in a square micro-capillary tube filled with index-matching oil. The reflectivities of these two FBGs with wavelengths at ~1550nm were measured as ~4.2 and 5.1dB, respectively. Due to asymmetry of the structures inscribed in the fibre by the point-by-point method, transmission spectra of both LPGs and FBGs exhibit strong polarisation dependence.

Using the phase-mask technique, FBGs have been inscribed in standard telecom, single-core GPNG and three-core passive and active TZN fibres with femtosecond pulse intensity estimated in the order of 10^{12}W/cm^2. Both grating structures and spectral properties have been studied. To achieve FBGs with high quality in transmission spectra, a theoretical analysis has been carried out on the walk-off effect of the femtosecond laser beam propagation through the phase-mask to identify the optimal distance to place the fibre behind the phase-mask. Based on the theoretical analysis, pure two-beam interference induced 2nd order FBG structures were fabricated by placing the standard telecom fibre 1.6mm away from the mask with a period of 2.142μm and by placing the mid-IR fibre 1.2mm away from the mask with a period of 1.697μm. The 2nd order FBGs have been studied in standard telecom fibres with and without hydrogenation and the highest reflectivity of ~11dB have been realised in these gratings. FBGs in germanate and tellurite glass single- and multi-core fibres were inscribed using the phase-mask with the period of 1.697μm to achieve Bragg resonances in the wavelength range from 1200 to 1700nm. In the single-core GPNG fibre, an FBG was written with the 2nd and 3rd order Bragg resonances measured at 1540 and 1033nm with strengths of 6.5 and 1.2dB. In the three-core TZN fibres, the 2nd order resonances are situated at ~1677nm in all three cores with the strongest peak exhibiting a strength of 10.6dB.

In addition, thermal sensitivities of the FBGs in these two types of mid-IR glass fibres have been characterised. The thermal sensitivities of the 2nd and 3rd order Bragg resonances in GPNG fibre were measured as 24.7 and 16.8pm/°C and those of the 2nd order resonances in the three individual cores of the TZN fibre were measured with an average value of ~20pm/°C, which were in good agreement with the theoretically calculated ones based on the parameters from references.

Finally, the strain sensitivity of the FBG in GPNG fibre have been measured. The strain sensitivity and normalised strain sensitivity of the 2nd order Bragg resonance of GPNG fibre at 1540nm were measured to be 1.219pm/με and 0.7912×10^{-6}/με, respectively, which were in good agreement with values calculated using published data for fibre with similar compositions. The normalised strain sensitivity of the GPNG fibre was also measured using Fabry-Perot interferometer as 0.7910×10^{-6}/με, which was consistent with the result of FBG-based measurement.

7.2. *SUGGESTION FOR FUTURE WORK*

7.2.1. 45°-TFG BASED SIDE DETECTION SPECTROMETER

TFGs tap the light out of fibre core and this function has been utilised for realisation of side detection spectrometers using small angle TFGs in several cases [31, 37, 93, 193] and also reported in Chapter 5 in this thesis. However, because they are tilted at small angles, the detection dynamic range is limited by the narrow radiation mode profile, for example, the radiation range of the 10°-TFG employed in this thesis is only ~30nm (800-830nm). Additionally, to tap the light out, the fibre has to be immersed in the index-matching gel, which increases the complexity and limitation of the setup.

Recently, with the development of the grating inscription technique, 45°-TFGs can be inscribed easily, which could be a better candidate to replace small angle TFGs in the spectrometer system. As mentioned in section §4.6, the radiation range of the 45°-TFG usually covers a wavelength range over 200nm, providing a much broader dynamic range for the spectrometer. In addition, the light can be tapped out from the side of the fibre directly by a 45°-TFG without using the index-matching gel, which makes the system more simple and compact. These two advantages make such TFG-based side detection spectrometers more applicable.

It is noted that the light intensity tapped by the 45°-TFG is highly polarisation dependent, which has been clearly described in section §4.3.4 and §4.6. In real applications, a polariser and polarisation controller can be used to change polarisation state of the incident light to the TFG and ensure the maximum out-coupling. Additionally, PM fibres may be used between the polarisation controller and the TFG to eliminate the polarisation effect on the out-coupling efficiency and accuracy for the interrogation system proposed.

7.2.2. Optimisation of the femtosecond-laser-inscription setup using phase-mask

As mentioned in section §6.4.1, a cylindrical lens with a 30mm focal length was used in our femtosecond-laser-inscription system for FBG writing and in this system, the laser beam was highly focused by the lens and the fibre itself. Thus, the FBG structures created in standard telecom and mid-IR glass fibres are only 2-3μm, which covers only 20-30% of the fibre core area, making weak gratings. In my thesis, to ensure maximum coverage of femtosecond-laser-inscription in the core region to achieve strong FBG resonances, the incident beam was scanned along the direction across the fibre axis by shifting the cylindrical lens while the femtosecond laser beam was exposing the fibre. And the grating structures in mid-IR glass fibres are the combination of many layers of structures, which may induce some noises in transmission spectra of FBGs.

For a Gaussian beam approximation, the radius of the focal spot size is $w = \lambda f / \pi w_0$ [223], where λ is the wavelength. From this equation we can see, by using a lens with longer focal length, the focal spot size is increased, and fewer layers of structures are required for the grating inscription. Thus, the quality of the grating spectra may be improved and the FBG inscription in mid-IR glass fibre may be more efficient.

Additionally, in section §6.4.3.3, the strengths of the FBG resonances in multi-core TZN fibre varied in different cores. The strongest one was written in the core placed along the y-axis shown in Fig. 6.19. To achieve strong FBGs in all the cores, the fibre clamps can be replaced by two rotators. Therefore, the multi-core fibre can be rotated until the destination core is along the y-axis. By fabricating the grating structure one by one in each fibre core, the FBG resonances with strong strengths in all cores can be achieved.

7.2.3. TFG INSCRIPTION USING FEMTOSECOND LASER

FBGs with high quality in spectrum are realisable by femtosecond laser now, but there are still more questions in relation to the photosensitivity mechanism and scopes for further development in inscription. So far, there is no report on inscription of TFGs using femtosecond laser.

For the inscription of TFGs using +1/-1 order phase-mask and UV laser, the interference region of laser reduces greatly with increasing tilt angle of the phase-mask. Thus, due to the very small size of the UV beam (hundreds of micrometres), it is difficult to write a TFG with larger tilt angle, especially a 45°-TFG. For most femtosecond laser used for FBG inscription in conjunction with a phase-mask, the diameter of laser spot are usually a few millimetres. From this point of view, TFGs could be written using femtosecond laser by rotating the phase-mask or using a tilted phase-mask. If this is workable, 45°-TFG structures can be produced in a range of fibres and planar waveguides in non silica materials.

7.2.4. QUESTIONS TO BE CLARIFIED

As reported previously, the cladding modes coupling can be suppressed [223] due to partially apodized grating structure induced by the Gaussian profile of the incident beam. In section §6.4.3.1, as we do not see any resonances on the shorter wavelength sides of the main Bragg peaks the femtosecond-laser-inscribed FBGs in standard telecom fibre, further study is needed to identify what is the mechanism responsible for the cladding mode coupling suppression. The finding from this will provide an effective way to inscribe better quality FBGs using femtosecond laser.

Additionally, in section §6.4.3.3, some pronounced Fabry-Perot structures appears at the longer wavelength side of the Bragg resonances for the FBGs inscribed in TZN fibres, which is different from the normal FBG spectra. In my thesis, this phenomenon

was explained by a negative refractive index modulation induced during inscription. However, this should be further verified and studied before the definitive conclusion can be drawn.

References

1. R. J. Bates, *Optical Switching and Networking Handbook*. New York: McGraw-Hill, Chapter 1, 2001.

2. K. O. Hill, Y. Fujii, D. C. Johnson, and B. S. Kawasaki, "Photosensitivity in optical fiber waveguides: Application to reflection filter fabrication," *Appl. Phys. Lett.*, **32**, 647-649, 1978.

3. R. A. Bergh, H. C. Lefevre, and H. J. Shaw, "Single-mode fiber-optic polarizer," *Opt. Lett.*, **5**, 479-481, 1980.

4. R. B. Dyott, J. Bello, and V. A. Handerek, "Indium-coated D-shaped-fiber polarizer," *Opt. Lett.*, **12**, 287-289, 1987.

5. W. Eickhoff, "In-line fibre-optic polariser," *Electron. Lett.*, **16**, 762-764, 1980.

6. K. O. Hill and G. Meltz, "Fibre Bragg Grating Technology Fundamentals and Overview," *J. Lightwave Technol.*, **15**, 1263-1276, 1997.

7. J. A. R. Williams, I. Bennion, K. Sugden, and N. J. Doran, "Fiber dispersion compensation using a chirped in-fire Bragg grating," *Electron. Lett.*, **30**, 985-987, 1994.

8. R. Kashyap, S. V. Chernikov, P. F. McKee, and J. R. Taylor, "30 ps chromatic dispersion compensation of 400 fs pulses at 100 Gbits/s in optical fibers using an all fiber photoinduced chirped reflection grating," *Electron. Lett.*, **30**, 1078-1080, 1994.

9. K. O. Hill, B. Malo, F. Bilodeau, S. Th'eriault, D. C. Johnson, and J. Albert, "Variable-spectral-response optical waveguide Bragg grating filters for optical signal processing," *Opt. Lett.*, **20**, 1438-1440, 1995.

10. K. O. Hill, D. C. Johnson, F. Bilodeau, and S. Faucher, "Narrow-bandwidth optical waveguide transmission filters: A new design concept and applications to optical fiber communications," *Electron. Lett.*, **23**, 465-466, 1987.

11. F. Bilodeau, D. C. Johnson, S. Th'eriault, B. Malo, J. Albert, and K. O. Hill, "An all-fiber dense-wavelength-division multiplexer/demultiplexer using photoimprinted Bragg gratings," *IEEE Photon. Technol. Lett.*, **7**, 388-390, 1995.

12. M. Shigehara, T. Satoh, A. Inoue, and Y. Hattori, "Optical fiber identification system using fiber Bragg gratings," *Conf. Optic. Fiber Commun., OFC'95*, San Jose, CA, USA, 1995.

13. G. A. Ball and W. W. Morey, "Efficient integrated Nd^{3+} fiber laser," *IEEE Photon. Technol. Lett.*, **3**, 1077-1078, 1991.

14. G. A. Ball and W. H. Glenn, "Design of a single-mode linear-cavity erbium fiber laser

utilizing Bragg reflectors," *J. Lightwave Technol.*, **10**, 1338-1343, 1992.

15. G. A. Ball, W. W. Morey, and W. H. Glenn, "Standing-wave monomode erbium fiber laser," *IEEE Photon. Technol. Lett.*, **3**, 613-615, 1991.

16. A. Othonos and K. Kalli, *Fiber Bragg gratings: Fundamentals and applications in telecommunications and sensing*, Chapter 2-5, Artech House, Inc. 1999.

17. R. Kashyap, *Fiber Bragg gratings*, Chapter 2-4, Academic Press, 1999.

18. B. Guan, H. Tam, S. Ho, W. Chung and X. Dong, "Simultaneous strain and temperature measurement using a single fibre Bragg grating," *Electron. Lett.*, **36**, 1018-1019, 2000.

19. A. M. Vengsarkar, P. J. Lemaire, J. B. Judkins, V. Bhatia, T. Erdogan, and J. E. Sipe, "Long-period fiber gratings as band-rejection filters, " *J. Lightwave Technol.*, **14**, 58-65, 1996.

20. R. Kashyap, R. Wyatt, and P. F. McKee, "Wavelength flattened saturated erbium amplifier using multiple side-tap Bragg gratings," *Electron. Lett.*, **29**, 154-156, 1993.

21. A. A. Abramov, A. Hale, R. S. Windeler, and T. A. Strasser, "Widely tunable long-period fibre gratings," *Electron. Lett.*, **35**, 81-82, 1999.

22. K. S. Chiang, Y. Liu, M. N. Ng, and S. Li, "Coupling between two parallel long-period fibre gratings," *Electron. Lett.*, **36**, 1408-1409, 2000.

23. V. Bhatia, D. Campbell, R. O. Claus, and A. M. Vengsarkar, "Simultaneous strain and temperature measurement with long-period gratings," *Opt. Lett.*, **22**, 648-650, 1997.

24. V. Bhatia and A. M. Vengsarkar, "Optical fiber long-period grating sensors," *Opt. Lett.*, **21**, 692-694, 1996.

25. V. Bhatia, D. K. Campbell, D. Sherr, G. D. Tiffanie, A. Z. Noel, A. Gregory, A. M. Kent, and R. O. Clau, "Temperature-insensitive and strain-insensitive long-period gratings sensor for smart structures," *Opt. Eng.*, **36**, 1872-1876, 1997.

26. V. Bhatia, G. D. Tiffanie, A. Z. Noel, and R. O. Clau, "Temperature-insensitive long-period grating for strain and refractive index sensing," *Smart Structures and Materials 1997: Smart Sensing, Proc. SPIE.*, San Diego, CA, USA, **3042**, 194-202, 1997.

27. V. Bhatia, "Applications of long-period gratings to single and multi-parameter sensing," *Opt. Express.*, **4**, 457-466, 1999.

28. T. Allsop, L. Zhang, and I. Bennion, "Detection of organic aromatic compounds in paraffin by a long period fiber grating optical sensor with optimized sensitivity," *Opt. Commun.*, **191**, 181-190, 2001.

29. S. James and R. Tatam, "Optical fibre long-period grating sensors: characteristics and

application," *Meas. Sci. Technol.*, 14, R49-R61, 2003.

30. H. J. Patrick, A. D. Kersey, and F. Bucholtz, "Analysis of the response of long period fiber gratings to external index of refraction," *J. Lightwave Technol.*, 16, 1606-1612, 1998.

31. K. S. Feder, P. S. Westbrook, J. Ging, P. I. Reyes, and G. E. Carver, "In-fiber spectrometer using tilted fiber gratings," *IEEE Photon. Technol. Lett.*, **15**, 933-935, 2003.

32. R. S. Westbrook, K. S. Feder, P. I. Reyes, P. Steinvurzel, B. J. Eggleton, R. G. Ernst, L. A. Reith and D. M. Gill, "Application of fiber Bragg grating filter/tap module to a wavelength-locked low-chirp directly-modulated 10Gb/s RZ transmitter," *Optical Fiber Communication Conference*, Anaheim, California, USA, 680-682, 2002.

33. R. Kashyap, R. Wyatt, and R. J. Campbell, "Wideband gain flattened erbium fibre amplifier using a photosensitive fibre blazed grating," *Electron. Lett.*, **29**, 154-156, 1993.

34. C. Jáuregui, A. Quintela, and J. M. López-Higuera, "Interrogation unit for fiber Bragg grating sensors that uses a slanted fiber grating," *Opt. Lett.*, **29**, 676-678, 2004.

35. C. Jáuregui, J. M. López-Higuera, and A. Quintela, "Interrogation of interferometric sensors with a tilted fiber Bragg grating," *Opt. Express*, **12**, 5646-5654, 2004.

36. Y. Liu, L. Zhang, and I. Bennion, "Fabricating fibre edge filters with arbitrary spectral response based on tilted chirped grating structures," *Meas. Sci. Tech.*, **10**, L1-L3, 1999.

37. A. G. Simpson, K. Zhou, L. Zhang, L. Everall, and I. Bennion, "Optical sensor interrogation with a blazed fiber Bragg grating and a charge-coupled device linear array," *Appl. Opt.*, **43**, 33-40, 2004.

38. A. G. Simpson, K. Zhou, L. Zhang, and I. Bennion, "Wide bandwidth, high resolution spectral interrogation using a BFBG-CCD array for optical sensing applications," *16th International Conference on Optical Fibre Sensors*, Nara Japan, 534-537, 2003.

39. P. S. Westbrook, T. A. Strasser, and T. Erdogan, "In-line polarimeter using blazed fiber gratings," *IEEE Photon. Technol. Lett.*, **12**, 1352-1354, 2000.

40. J. Peupelmann, E. Krause, A. Bandemer, and C. Schäffer, "Fibre-polarimeter based on grating taps," *Electron. Lett.*, **38**, 1248-1250, 2002.

41. S. L. Mihailov, R. B. Walker, T. J. Stocki, and D. C. Johnson, "Fabrication of tilted fibre-grating polarisation-dependent loss equaliser," *Electron. Lett.*, **37**, 284-286, 2001.

42. P. I. Reyes and P. S. Westbrook, "Tunable PDL of Twisted-Tilted Fiber Gratings," *IEEE Photon. Technol. Lett.*, **15**, 828-830, 2003.

43. K. Zhou, G. Simpson, X. Chen, L. Zhang, and I. Bennion, "High extinction ratio in-fiber

polarizer based on a 45° tilted fiber Bragg gratings," *Opt. Lett.*, 30, 1285-1287, 2005.

44. D. P. Hand and J. S. Russell, "Photoinduced refractive index changes in fibre Bragg gratings," *Appl. Phys. Lett.*, **15**, 102-104, 1990.

45. C. Fiori and R. Devine, "Evidence for a wide continuum of polymorphs in *a*-SiO_2," *Phys. Rev. B*, **33**, 2972-2974, 1986.

46. D. Wong, S. B. Poole, and M. G. Sceats, "Stress-birefringence reduction in elliptical-core fibers under ultraviolet irradiation," *Opt. Lett.*, **17**, 1773-1775, 1992.

47. A. Attard, "Fermi level shift in $Bi_{12}SiO_{20}$ via photon-induced trap level occupation," *J. Appl. Phys.*, **71**, 933-937, 1992.

48. D. L. Williams, "Photosensitive index changes in germania doped silica fibres and waveguides," *Photosensitivity and Self-Organization in Optical Fibers and Waveguides*, Quebec, Canada, Proceedings SPIE, **2044**, 55-68, 1993.

49. N. Lawandy, "Light induced transport and delocalisation in transparent amorphous systems," *Opt. Commun.*, **74**, 180-184, 1989.

50. A. Miotello and R. Kelly, "Laser irradiation effects in Si^+-implanted SiO_2," *Nuclear Instruments and Methods in Physics Research B*, **65**, 217-222, 1992.

51. M. J. Yuen, "Ultraviolet absorption studies of germanium silicate glasses," *Appl. Opt.*, **21**, 136-140, 1982.

52. P. S. Russell, L. J. Poyntz-Wright, and D. P. Hand, "Frequency doubling, absorption and grating formatting in glass fibres: Effective defective defects or defective effects?" *Fiber Laser Sources and Amplifiers II*, San Jose, USA, Provedings SPIE, **1373**, 126-139, 1990.

53. P. St. J. Russell, D. P. Hand, and Y. T. Chow, "Optically-induced creation, transformation and organisation of defects and colour-centres in optical fibres," *International Workshop on Photoinduced Self-Organization Effects in Optical Fibre*, Quebec City, Quebec, Proceedings SPIE, **1516**, 47-54, 1991.

54. R. M. Atkins, V. Mizrahi, and T. Erdogan, "248-nm induced vacuum UV spectral changes in optical fibre preform cores: Support for a colour centre model of photosensiticity," *Electron. Lett.*, **28**, 2210-2211, 1993.

55. K. D. Simmons, S. LaRochelle, V. Mizrahi, G. I. Stegeman, and D. L, Griscom, "Correlation of defect centers with a wavelength-dependent photosensitive response in germania-doped silica optical fibers," *Opt. Lett.*, **16**, 141-143,1991.

56. H. Hosono, M. Mizuguchi, H. Kawazoe, and J. Nishii, "Correlation between Ge E' centers and optical absorptionbands in SiO_2:GeO_2 glasses," *Jpn. J. Appl. Phys.*, **35**, L234-L236, 1996.

57. R. M. Atkins and V. Mizrahi, "Observations of changes in UV absorption bands of singlemode germanosilicate core optical fibres on writing and thermally erasing refractive index gratings," *Electron. Lett.*, 28, 1743-1744, 1992.

58. D. L. Williams, S. T. Davey, R. Kashyap, J. R. Armitage, and B. J. Ainslie, "Direct observation of UV induced bleaching of 240 nm absorption band in photosensitive germanosilicate glass fibres," *Electron. Lett.*, 28, 369-371, 1992.

59. T. E. Tsai, E. J. Friebele, and D. L. Griscom, "Thermal stability of photoinduced gratings and paramagnetic centers in Ge- and Ge/P-doped silica optical fibers," *Opt. Lett.*, 18, 935-937, 1993.

60. T. Tsai, G. M. Williams, and E. J. Friebele, "Index structure of fiber Bragg gratings in Ge-SiO_2 fibers," *Opt. Lett.*, 22, 224-226, 1997.

61. B. Leconte, W. Xie, M. Douay, P. Bernage, P. Niay, J. F. Bayon, E. Delevaque, and H. Poignant, "Analysis of color-center-related contribution to Bragg grating formation in Ge:SiO_2 fiber based on a local Kramers-Kronig transformation of excess loss spectra," *Appl. Opt.*, 36, 5923-5930, 1997.

62. W. X. Xie, P. Niay, P. Bernage, M. Douay, J. F. Bayon, T. Georges, M. Monerie, and B. Poumellec, "Experimental-Evidence of 2 Types of Photorefractive Effects Occurring During Photo inscriptions of Bragg Gratings Within Germanosilicate Fibres," *Opt. Commun.*, 104, 185-195, 1993.

63. P. Cordier, J. C. Doukhan, E. Fertein, P. Bernage, P. Niay, J. F. Bayon, and T. Georges, "TEM Characterization of Structural-Changes in Glass Associated to Bragg Grating Inscription in a Germanosilicate Optical-Fibre Preform," *Opt. Commun.*, 111, 269-275, 1994.

64. P. Niay, P. Bernage, S. Legoubin, M. Douay, W. X. Xie, J. F. Bayon, T. Georges, M. Monerie, and B. Poumellec, "Behaviour of Spectral Transmissions of Bragg Gratings Written in Germania-Doped Fibres - Writing and Erasing Experiments Using Pulsed or CW UV Exposure," *Opt. Commun.*, 113, 176-192, 1994.

65. M. Rothschild, D. J. Ehrlich, and D. C. Shaver, "Effects of excimer laser irradiation on the transmission, index of refraction, and density of ultraviolet grade fused silica," *Appl. Phys. Lett.*, 55, 1276-1278, 1989.

66. D. C. Allan, C. Smith, N. F. Borrelli, and T. P. Seward III, "193-nm excimer-laser-induced densification of fused silica," *Opt. Lett.*, 21, 1960-1962, 1996.

67. M. Douay, W. X. Xie, T. Taunay, P. Bernage, P. Niay, P. Cordier, B. Poumellec, L. Dong, J. F. Bayon, H. Poignant, and E. Delevaque, "Densification involved in the UV-based photosensitivity of silica glasses and optical fibres," *J. Lightwave Technol.*, 15, 1329-1342, 1997.

68. D. L. Williams, B. J. Ainslie, J. R. Armitage, R. Kashyap, and R. Campbell, "Enhanced UV photosensitivity in boron codoped germanosilicate fibres," *Electron. Lett.*, 29, 45-47, 1993.

69. P. J. Lemaire, "High-pressure H_2 loading as a technique for achieving ultrahigh UV photosensitivity and thermal sensitivity in GeO_2 doped optical fibres," *Electron. Lett.*, 29, 1191-1193, 1993.

70. F. Bilodeau, "Photosensitization of optical fiber and silica-on-silicon/silica waveguides," *Opt. Lett.*, 18, 953-955, 1993.

71. L. Dong, J. L. Cruz, L. Reekie, M. G. Xu, and D. Payne, "Enhanced photosensitivity in tin-co doped germanosilicate optical fibres," *IEEE Photon. Technol. Lett.*, 7, 1048-1050, 1995.

72. L. Dong, J. L. Cruz, J. A. Tucknott, L. Reekie, and D. N. Payne, "Strong photosensitive gratings in tin-doped phosphosilicate optical fibers," *Opt. Lett.*, 20, 1982–1984, 1995.

73. R. M. Atkins, P. J. Lemaire, T. Erdogan, and V. Mizrahi, "Mechanisms of Enhanced UV Photosensitivity Via Hydrogen Loading in Germanosilicate Glasses," *Electron. Lett.*, 29, 1234-1235, 1993.

74. K. Noguchi, N. Shibata, N. Uesugi, Y. Negishi, "Loss increase for optical fibers exposed to hydrogen atmosphere," *J. Lightwave Technol.*, 3, 236-243, 1985.

75. J. Stone, "Interactions of hydrogen and deuterium with silica optical fibers: A review," *J. Lightwave Technol.*, 5, 712-733, 1987.

76. D. L. Williams and R. P. Smith, "Accelerated lifetime tests on UV written intra-core gratings in boron germania codoped silica fibre," *Electron. Lett.*, 31, 2120-2121, 1995.

77. S. Kannan, J. Z. Y. Guo, and P. J. Lemaire, "Thermal stability analysis of UV-induced fibre Bragg gratings," *J. Lightwave Technol.*, 15, 1478-1483, 1997.

78. T. Erdogan, V. Mirrahi, P. Lemaire, and D. Monroe, "Decay of ultraviolet-induced fibre Bragg gratings," *J. Appl. Phys.*, 76, 73-80, 1994.

79. H. Patrick, S. L. Gilbert, A. Lidgard, and M. D. Gallagher, "Annealing of Bragg gratings in hydrogen-loaded optical-fibre," *J. Appl. Phys.*, 78, 2940-2945, 1995.

80. S. R. Baker, H. N. Rourke, V. Baker, and D. Goodchild, "Thermal decay of fibre Bragg gratings written in boron and germanium co doped silica fibre," *J. Lightwave Technol.*, 15, 1470-1477, 1997.

81. S. Pal, J. Mandal, T. Sun, and K. T. V. Grattan, "Analysis of thermal decay and prediction of operational lifetime for a type I boron-germanium co doped Fibre Bragg grating," *Appl. Opt.*, 42, 2188-2197, 2003.

82. G. Brambilla and H. Rutt, "Fiber Bragg gratings with enhanced thermal stability," *Appl. Phys. Lett.*, 80, 3259-3261, 2002.

83. M. Fokine, "Formation of thermally stable chemical composition gratings in optical fibers," *J. Opt. Soc. Amer. B*, 19, 1759-1765, 2002.

84. A. Yariv, "Coupled-mode theory for guided-wave optics," *IEEE J. Quantum Electron.*, 9, 919-933, 1973.

85. H. Kogelnik, and C. W. Shank, "Coupled wave theory of distributed feedback lasers," *J. Appl. Phys.*, 43, 2327-2335, 1972.

86. T. Erdogan, "Fiber grating spectra," *J. Lightwave Technol.*, 15, 1277-1294, 1997.

87. T. Erdogan, "Cladding-mode resonances in short- and long- period fiber grating filters," *J. Opt. Soc. Am. A*, 14, 1760-1773, 1997.

88. B. S. Kawasaki, K. O. Hill, D. C. Johnson, and Y. Fujii, "Narrow-band Bragg reflectors in optical fibers," *Opt. Lett.*, 3, 66-68, 1978.

89. D. K. W. Lam and B. Garside, "Characterization of single-mode optical fibre filers," *Appl. Opt.*, 20, 440-445, 1981.

90. G. Meltz, W. W. Morey, and W. H. Glenn, "Formation of Bragg gratings in optical fibres by a transverse holographic method," *Opt. Lett.*, 14, 823-825, 1989.

91. D. Z. Anderson, V. Mizrahi, T. Erdogan, and A. White, "Production of in-fibre gratings using a diffractive optical element," *Electron. Lett.*, 29, 566-567, 1993.

92. K. O. Hill, B. Malo, F. Bilodeau, D.C. Johnson, and J. Albert, "Bragg gratings fabricated in monomode photosensitive optical fibre by UV exposure through a phase mask," *Appl. Phys. Lett.*, 62, 1035-1037, 1993.

93. G. Meltz, W. W. Morey, and W. Glenn, "In-Fibre Bragg grating tap," *Optical Fibre Communications*, San Francisco, California, USA, 1990 OSA Technical Digest Series 1, TuG1, 1990.

94. B. Eggleton, P. Krug, and L. Poladian, "Experimental demonstration of compression of dispersed optical pulses by reflection from self-chirped optical fibre Bragg gratings," *Opt. Lett.*, 19, 877-880, 1994.

95. R. Kashyap, J. R. Armitage, R. Wyatt, S. T. Davey, and D. L. Williams, "All-fibre narrow-band reflection gratings at 1500 nm," *Electron. Lett.*, 26, 730-732, 1990.

96. H. G. Limberger, P. Y. Fonjallaz, P. Lambelet, R. P. Salathé, C. Zimmer, and H. H. Gilgen "OLCR characterization of efficient Bragg gratings in optical fiber," *Photosensitivity and Self-Organization in Optical Fibers and Waveguides*, Quebec, Canada, Proceedings SPIE, 2044, 272-283, 1993.

97. K. C. Byron, K. Sugden, T. Bricheno, and I. Bennion, "Fabrication of chirped Bragg gratings in photosensitive fiber," *Electron. Lett.*, 29, 1659-1660, 1993.

98. J. Albert, K. O. Hill, B. Malo, S. Theriault, F. Bilodeau, D. C. Johnson, and L. E. Erickson, "Apodization of the spectral response of fiber bragg gratings using a phase mask with variable diffraction efficiency," *Electron. Lett.*, 31, 222-223, 1995.

99. J. Albert, K. O. Hill, D. C. Johnson, F. Bilodeau, and M. J. Rooks, "Moire phase masks for automatic pure apodisation of fiber Bragg gratings," *Electron. Lett.*, 32, 2260-2261, 1996.

100. R. Kashyap, P. F. Mckee, and D. Armes, "UV written reflection grating structures in photosensitive optical fibers using phase-shifted phase mask," *Electron. Lett.*, 30, 1977-1978, 1994.

101. J. Canning and M. G. Sceats, "π phase shifted periodic distributed structures in optical fibers by UV post-processing," *Electron. Lett.*, 30, 1344-1345, 1994.

102. L. Zhang, K. Sugden, I. Bennion, and A. Molony, "Wide-stopband chirped fiber moire grating transmission filters," *Electron. Lett.*, 31, 477-479, 1995.

103. S. Legoubin, E. Fertein, M. Douay, P. Bernage, P. Niay, F. Bayon, and T. Georges, "Formation of moire grating in core of germanosilicate fiber by transverse holographic double exposure method," *Electron. Lett.*, 27, 1945-1946, 1991.

104. B. J. Eggleton, P. A. Krug, L. Poladian, and F. Ouellette, "Long periodic superstructure Bragg gratings in optical fibers," *Electron. Lett.*, 30, 1620-1622, 1994.

105. J. D. Prohaska, E. Snitzer, S. Rishton, and V. Boegli, "Magnification of mask fabricated fibre Bragg gratings," *Electron. Lett.*, 29, 1614-1615, 1993.

106. Q. Zhang, D. A. Brown, L. Reinhart, T. F. Morse, J. Q. Wang, and G. Xiao, "Tuning Bragg wavelength by writing gratings on pre-strained fibres," *IEEE Photon. Technol. Lett.*, 6, 839-841, 1994.

107. K. C. Byron and H. N. Rourke, "Fabrication of chirped fibre gratings by novel stretch and write technique," *Electron. Lett.*, 31, 60-61, 1995.

108. D. Du, X. Liu, G. Korn, J. Squier, and G. Mourou, "Laser-induced breakdown by impact ionization in SiO_2 with pulse widths from 7 ns to 150 fs," *Appl. Phys. Lett.*, 64, 3071-3073, 1994.

109. P. D. Maker, R. W. Terhune, and C. M. Savage, "Optical third harmonic generation," *Proc. 3rd Int. Con. J. Quantum Electronics*, Paris: Dunod, 1559-1576, 1964.

110. C. B. Schaffer, A. Brodeur, and E. Mazur, "Laser-induced breakdown and damage in bulk transparent materials induced by tightly focused femtosecond laser pulses," *Meas. Sci. Technol.*, 12, 1784-1794, 2001.

111. J.W. Chan, T. R. Huser, S. H. Risbud, and D. M. Krol, "Waveguide fabrication in fused silica using tightly focused femtosecond laser pulses," *Integrated Optics: Devices, Materials, and Technologies VI*, Proc. SPIE, San Jose, CA, USA, 4640, 129-136, 2002.

112. J. W. Chan, T. Huser, S. Risbud, and D. M. Krol, "Structural changes in fused silica after exposure to focused femtosecond laser pulses," *Opt. Lett.*, 26, 1726-1728, 2001.

113. C. H. Fan and J. P. Longtin, "Modeling optical breakdown in dielectrics during ultrasfast laser processing," *Appl. Opt.*, 40, 3124-3131, 2001.

114. R. W. Boyd, *Nonlinear optics*, third edition, Chapter 12, Academic Press, 2008.

115. S. C. Jones, P. Braunlich, R. T. Casper, X. Shen, and P. Kelley, "Recent progress on laser-induced modifications and intrinsic bulk damage of wide-gap optical materials," *Opt. Eng.*, 28, 1039-1068, 1989.

116. B. C. Stuart, M. D. Feit, S. Herman, A. M. Rubenchik, B. W. Shore, and M. D. Perry, "Nanosecond-to-femtosecond laser-induced breakdown in dielectrics," *Phys. Rev. B*, 53 1749-1761, 1996.

117. B. C. Stuart, M. D. Feit, S. Herman, A. M. Rubenchik, B. W. Shore, and M. D. Perry, "Optical ablation by high-power short-pulse lasers," *J. Opt. Soc. Am. B*, 13, 459-468, 1996.

118. D. Du, X. Liu, and G. Mourou, "Reduction of multi-photon ionization in dielectrics due to collisions," *Appl. Phys. B*, 63, 617-621, 1996.

119. M. Lenzner, J. Krüger, S. Sartania, Z. Cheng, Ch. Spielmann, G. Mourou, W. Kautek, and F. Krausz, "Femtosecond optical breakdown in dielectrics," *Phys. Rev. Lett.*, 80, 4076-4079, 1998.

120. N. Bloembergen, "Laser-induced electric breakdown in solids," *IEEE J. Sel. Top. Quant. Electron.*, 10, 375-386, 1974.

121. A. M. Streltsov and N. F. Borrelli, "Fabrication and analysis of a directional coupler written in glass by nanojoule femtosecond laser pulses," *Opt. Lett.*, 26, 42-43, 2001.

122. M. Will, S. Nolte, B. N. Chichkov, and A. Tunnermann, "Optical properties of waveguides fabricated in fused silica by femtosecond laser pulses," *Appl. Opt.*, 41, 4360-4364, 2002.

123. C. Florea, and K. A. Winick, "Fabrication and characterization of photonic devices directly written in glass using femtosecond laser pulses," *J. Lightwave Tech.*, 21, 246-253, 2003.

124. R. Osellame, N. Chiodo, V. Maselli, A. Yin, M. Zavelani-Rossi, G. Cerullo, P. Laporta, L. Aiello, S. De Nicola, P. Ferraro, A. Finizio, and G. Pierattini, "Optical properties of waveguides written by a 26 MHz stretched cavity Ti: sapphire femtosecond oscillator,"

Opt. Express, **13**, 612-620, 2005.

125. K. Miura, J. R. Qiu, H. Inouye, T. Mitsuyu, and K. Hirao, "Photowritten optical waveguides in various glasses with ultrashort pulse laser," *Appl. Phys. Lett.*, **71**, 3329-3331, 1997.

126. R. Bruckner, "Properties and structure of vitreous silica. I," *J. Non-Cryst. Solids*, **5**, 123, 1970.

127. E. N. Glezer and E. Mazur, "Ultrafast-laser driven micro-explosions in transparent materials," *Appl. Phys. Lett.*, **71**, 882-884, 1997.

128. A. M. Streltsov and N. F. Borrelli, "Study of femtosecond-laser-written waveguides in glasses," *J. Opt. Soc. Am. B*, **19**, 2496-2504, 2002.

129. C. B. Schaffer, J. F. Garcia, and E. Mazur, "Bulk heating of transparent materials using a high repetition-rate femtosecond laser," *Appl. Phys. A*, **76**, 351-354, 2003.

130. L. Sudrie, M. Franco, B. Prade, and A. Mysyrowicz, "Study of damage in fused silica induced by ultra-short IR laser pulses," *Opt. Commun.*, **191**, 333-339, 2001.

131. E. Bricchi, B. G. Klappauf, and P. G. Kazansky, "Form birefringence and negative index change created by femtosecond direct writing in transparent materials," *Opt. Lett.*, **29**, 119-121, 2004.

132. JM. Hopkins and W. Sibbett, "Ultrashort-pulse lasers: big payoffs in a flash," *Sci. Am.*, **283**, 72-79, 2000.

133. E. N. Glezer, M. Milosavljevic, L. Huang, R. J. Finlay, T. H. Her, J. P. Callan, and E. Mazur, "Three-dimensional optical storage inside transparent materials," *Opt. Lett.*, **21**, 2023-2025, 1996.

134. P. P. Pronko, S. K. Dutta, J. Squier, J. V. Rudd, D. Du, and G. Mourou, "Machining of submicron holes using a femtosecond laser at 800 nm," *Opt. Commun.*, **114**, 106-110, 1995.

135. U. Keller, "Recent developments in compact ultrafast lasers," *Nature*, **424**, 831-838, 2003.

136. T. Brabec and F. Krausz, "Intense few-cycle laser fields: Frontiers of nonlinear optics," *Rev. Mod. Phys.*, **72**, 545-591, 2000.

137. K. M. Davis, K. Miura, N. Sugimoto, and K. Hirao, "Writing waveguides in glass with a femtosecond laser," *Opt. Lett.* **21**, 1729-1731, 1996.

138. R. Osellame, S. Taccheo, M. Marangoni, R. Ramponi, P. Laporta, D. Polli, S. D. Silvestri, and G. Cerullo, "Femtosecond writing of active optical waveguides with astigmatically shaped beams," *J. Opt. Soc. Am. B*, **20**, 1559-1567, 2003.

139. L. Shah, A. Arai, S. Eaton, and P. Herman, "Waveguide writing in fused silica with a femtosecond fiber laser at 522 nm and 1 MHz repetition rate," *Opt. Express*, **13**, 1999-2006, 2005.

140. V. Apostolopoulos, L. Laversenne, T. Colomb, C. Depeursinge, R. Salathe, M. Pollnau, R. Osellame, G. Cerullo, and P. Laporta, "Femtosecond irradiation induced refractive-index changes and channel waveguiding in bulk Ti^{3+}:sapphire," *Conference on Lasers and Electro-Optics/International Quantum Electronics Conference and Photonic Applications Systems Technologies*, Technical Digest (CD), paper CMY4, OSA 2004.

141. M. V. Dubov, I. Khrushchev, I. Bennion, A. G. Okhrimchuk, A. V. Shestakov, "Waveguide inscription in YAG:Cr^{4+} *crystals by femtosecond laser irradiation*," *Conf. of Lasers and Electro-Optics, Washington DC, USA, CThV5, OSA conf. Proc.*, 2004.

142. W. K. Swainson and S. D. Kramer, "Three-dimensional patterned media," U.S. patents 4466080, 1984.

143. W. K. Swainson and S. D. Kramer, "Method and media for accessing data in three dimensions," U.S. patents 4471470, 1984.

144. D. A. Parthenopolous and P. M. Rentzepis, "Three-dimensional optical storage memory," *Science*, **245**, 843-845, 1989.

145. W. Denk, J. H. Strickler, and W. W. Webb, "Two-photon laser scanning fluorescence microscopy," *Science*, **248**, 73-76, 1990.

146. A. Marcinkevičius, S. Juodkazis, M. Watanabe, M. Miwa, S. Matsuo, H. Misawa, and J. Nishii, "Femtosecond laser-assisted three-dimensional microfabrication in silica," *Opt. Lett.*, **26**, 277-279, 2001.

147. V. Maselli, R. Osellame, G. Cerullo, R. Ramponi, and P. Laporta, "Fabrication of long microchannels with circular cross section using astigmatically shaped femtosecond laser pulses and chemical etching," *Appl. Phys. Lett.*, **88**, 191107, 2006.

148. S. Campopiano, R. Bernini, L. Zeni, and P. M. Sarro, "Microfluidic sensor based on integrated optical hollow waveguides," *Opt. Lett.*, **29**, 1894-1896, 2004.

149. Y. Lai, K. Zhou, L. Zhang, and I. Bennion, "Microchannels in conventional single-mode fibers," *Opt. Lett.*, **31**, 2559-2561, 2006.

150. K. Zhou, X. Chen, Y. Lai, K. Sugden, L. Zhang, and I. Bennion, "In-fiber polymer-glass hybrid waveguide Bragg grating," *Opt. Lett.*, **33**, 1650-1652, 2008.

151. A. Martinez, K. Zhou, I. Bennion, and S. Yamashita, "In-fiber microchannel device filled with a carbon nanotube dispersion for passive mode-lock lasing," *Opt. Express*, **16**, 15425-15430, 2008.

152. A. Vogel, J. Noack, G. Huttman, and G. Paltauf, "Mechanisms of femtosecond laser

nanosurgery of cells and tissues," *Appl. Phys. B*, **81**, 1015-1047, 2005.

153. W. Watanabe and N. Arakawa, "Femtosecond laser disruption of subcellular organelles in a living cell," *Opt. Express*, **12**, 4203-4213, 2004.

154. N. Shen, D. Datta, C. B. Schaffer, P. LeDuc, D. E.Ingber, and E. Mazur, "Ablation of cytoskeletal filaments and mitochondria in live cells using a femtosecond laser nanoscissor," *Mech. Chem. Biosystems*, **2**, 17-25, 2005.

155. W. Supatto, D. Débarre, B. Moulia, E. Brouzés, JL. Martin, E. Farge, and E. Beaurepaire, "*In vivo* modulation of morphogenetic movements in *Drosophila* embryos with femtosecond laser pulses," *Proc. Natl. Acad. Sci. USA*, **102**, 1047-1052, 2005.

156. C. B. Schaffer, A. Brodeur, J. F. García, and E. Mazur, "Micromachining bulk glass by use of femtosecond laser pulses with nanojoule energy," *Opt. Lett.*, **26**, 93-95, 2001.

157. W. Chen, S. M. Eaton, H. Zhang, and P. R. Herman, "Broadband directional couplers fabricated in bulk glass with high repetition rate femtosecond laser pulses," *Opt. Express*, **16**, 11470-11480, 2008.

158. W. Watanabe, T. Asano, K. Yamada, K. Itoh, and J. Nishii, "Wavelength division with three-dimensional couplers fabricated by filamentation of femtosecond laser pulses," *Opt. Lett.*, **28**, 2491-2493, 2003.

159. R. R. Thomson, H. T. Bookey, N. D. Psaila, A. Fender, S. Campbell, W. N. MacPherson, J. S. Barton, D. T. Reid, and A. K. Kar, "Ultrafast-laser inscription of a three dimensional fan-out device for multicore fiber coupling applications," *Opt. Express*, **15**, 11691-11697, 2007.

160. Y. Sikorski, A. A. Said, P. Bado, R. Maynard, C. Florea, and K. A. Winick, "Optical waveguide amplifier in Nd-doped glass written with near-IR femtosecond laser pulses," *Elec. Lett.*, **36**, 226-227, 2000.

161. S. Taccheo, G. Della Valle, R. Osellame, G. Cerullo, N. Chiodo, P. Laporta, O. Svelto, A. Killi, U. Morgner, M. Lederer, and D. Kopf, "Er:Yb-doped waveguide laser fabricated by femtosecond laser pulses," *Opt. Lett.*, **29**, 2626-2628, 2004.

162. S. Juodkazis, S. Matsuo, H. Misawa, V. Mizeikis, A. Marcinkevicius, H. B. Sun, Y. Tokuda, M. Takahashi, T. Yoko and J. Nishii, "Application of femtosecond laser pulses for microfabrication of transparent media," *Appl. Surf. Sci.*, **197-198**, 705-709, 2002.

163. H. Hosono, K. Kawamura, S. Matsuishi, and M. Hirano, "Holographic writing of micro-gratings and nanostructures on amorphous SiO_2 by near infrared femtosecond pulses," *Nuclear Instruments and Methods in Physics Research B*, **191**, 89-97, 2002.

164. J. Zhai, Y. Shen, J. Si, J. Qiu and K. Hirao, "The fabrication of permanent holographic gratings in bulk polymer medium by a femtosecond laser," *J. Phys. D: Appl. Phys.*, **34**

3466-3469, 2001.

165. J. D. Mills, P. G. Kazansky, and E. Bricchi, "Embedded anisotropic microreflectors by femtosecond-laser nanomachining," *Appl. Phys. Lett.*, 81, 196-198, 2002.

166. C. N. LaFratta, J. T. Fourkas, T. Baldacchini, and R. A. Farrer, "Multiphoton Fabrication," *Angew. Chem. Int. Edn*, 46, 6238-6258, 2007.

167. H. B. Sun and S. Kawata, "Two-photon photopolymerization and 3D lithographic microfabrication," *NMR/3D Analysis. Photopolymerization*, Springer-Verlag Berlin, Berlin, 170, 169-273, 2004.

168. Y. Kondo, K. Nouchi, T. Mitsuyu, M. Watanabe, P. G. Kazansky, and K. Hirao, "Fabrication of long-period fiber gratings by focused irradiation of infrared femtosecond laser pulses," *Opt. Lett.*, 24, 646-648, 1999.

169. E. Fertein, C. Przygodzki, H. Delbarre, A. Hidayat, M. Douay, and P. Niay, "Refractive-Index Changes of Standard Telecommunication Fiber through Exposure to Femtosecond Laser Pulses at 810 cm," *Appl. Opt.*, 40, 3506-3508, 2001.

170. F. Hindle, E. Fertein, C. Przygodzki, F. Dürr, L. Paccou, R. Bocquet, P. Niay, H. Georg Limberger, and M. Douay, "Inscription of Long-Period Gratings in Pure Silica and Germano–Silicate Fiber Cores by Femtosecond Laser Irradiation," *IEEE Photon. Technol. Lett.*, 16, 1861-1863, 2004.

171. Alexey I. Kalachev, David N. Nikogosyan, *Fellow, OSA*, and Gilberto Brambilla, "Long-Period Fiber Grating Fabrication by High-Intensity Femtosecond Pulses at 211 nm," *J. Lightwave Technol.*, 23, 2568-2578, 2005.

172. A. Martinez, M. Dubov, I. Khrushchev and I. Bennion, "Direct writing of fibre Bragg gratings by femtosecond laser," *Elec. Lett.*, 40, 1170-1172, 2004.

173. A. Martinez, I.Y. Khrushchev and I. Bennion, "Thermal properties of fibre Bragg gratings inscribed point-by-point by infrared femtosecond laser," *Elec. Lett.*, 41, 176-177, 2004.

174. A. Martinez, I. Y. Khrushchev, and I. Bennion, "Direct inscription of Bragg gratings in coated fibers by an infrared femtosecond laser," *Opt. Lett.*, 31, 1603-1605, 2006.

175. Y. Lai, K. Zhou, K. Sugden, and I. Bennion, "Point-by-point inscription of first-order fiber Bragg grating for C-band applications," *Opt. Express*, 15, 18318-18325, 2007.

176. S. J. Mihailov, C. W. Smelser, P. Lu, R. B. Walker, D. Grobnic, H. Ding, G. Henderson, and J. Unruh, "Fiber Bragg gratings made with a phase mask and 800-nm femtosecond radiation," *Opt. Lett.*, 28, 995-997, 2003.

177. S. J. Mihailov, C. W. Smelser, D. Grobnic, R. B. Walker, P. Lu, H. Ding, and J. Unruh, "Bragg gratings written in all-SiO_2 and Ge-doped core fibers with 800-nm femtosecond

radiation and a phase mask," *J. Lightwave Technol.*, **22**, 94-100, 2004.

178. C. W. Smelser, S. J. Mihailov, D. Grobnic, P. Lu, R. B. Walker, H. Ding, and X. Dai, "Multiple-beam interference patterns in optical fiber generated with ultrafast pulses and a phase mask," *Opt. Lett.*, **29**, 1458-1460, 2004.

179. C. W. Smelser, D. Grobnic, and S. J. Mihailov, "Generation of pure two-beam interference grating structures in an optical fiber with a femtosecond infrared source and a phase mask," *Opt. Lett.*, **29**, 1730-1732, 2004.

180. C. W. Smelser, S. J. Mihailov, and D. Grobnic, "Hydrogen loading for fiber grating writing with a femtosecond laser and a phase mask," *Opt. Lett.*, **29**, 2127-2129, 2004.

181. C. W. Smelser, S. J. Mihailov, and D. Grobnic, "Rouard's method modeling of type I-IR fiber Bragg gratings made using an ultrafast IR laser and a phase mask," *J. Opt. Soc. Am. B*, **23**, 2011-2017, 2006.

182. C. W. Smelser, S. J. Mihailov, and D. Grobnic, "Impact of index change saturation on the growth behavior of higher-order type I ultrafast induced fiber Bragg gratings," *J. Opt. Soc. Am. B*, **25**, 877-883, 2008.

183. S. J. Mihailov, D. Grobnic, and C. W. Smelser, "Efficient grating writing through fibre coating with femtosecond IR radiation and phase mask," *Elec. Lett.*, **43**, 442-443, 2007.

184. T. Erdogan and J. E. Sipe, "Tilted fiber phase gratings," *J. Opt. Soc. Amer. A*, **13**, 296-313, 1996.

185. K. Zhou, L. Zhang, X. Chen, I. Bennion, "Low thermal sensitivity grating devices based on ex-45° tilting structure capable of forward-propagating cladding modes coupling," *J. Lightwave Technol.*, **24**, 5087-5094, 2006.

186. K. Zhou, L. Zhang, X. Chen, and I. Bennion, "Optic sensors of high refractive-index responsivity and low thermal cross sensitivity that use fiber Bragg gratings of >80° tilted structures," *Opt. Lett.*, **31**, 1193-1195, 2006.

187. K. Zhou, L. Zhang, X. Chen, R. Suo, and I. Bennion, "Implementation of optical fibre sensors with low thermal cross-sensitivity utilising ex-45° tilting grating structures," *18th International Conference on Optical Fibre Sensors*, Cancun, Mexico, TuD-3, 2006.

188. X. Chen, K. Zhou, R. Suo, L. Zhang, and I. Bennion, "In-fibre twist sensor based on TFBG structures," *18th International Conference on Optical Fibre Sensors*, Cancun, Mexico, TuE-29, 2006.

189. S. J. Mihailov, R. B. Walker, P. Lu, H. Ding, X. Dai, C. Smelser and L. Chen, "UV-Induced polarisation-dependant loss (PDL) in tilted fibre Bragg gratings: application of a PDL equaliser," *IEE Proc. Optoelectronics*, **149**, 211-216, 2002.

190. Y. Li, M. Froggatt, and T. Erdogan, "Volume current method for analysis of tilted fiber

gratings," *J. Lightwave Technol.*, 19, 1580-1591, 2001.

191. L. Dong, B. Ortega, and L. Reekie, "Coupling characteristics of cladding modes in tilted optical fiber Bragg gratings," *Appl. Opt.*, 37, 5099-5105, 1998.

192. G. Meltz, W. Morey, A. L. Wilson, "Optical waveguide embedded light redirecting and focusing Bragg grating arrangement," U.S. patent, 5061032, 1991.

193. J. L. Wagener, T. A. Strasser, J. R. Pedrazzani, J. Demarco, "Fiber grating optical spectrum analyzer tap," *11th International Conference on Integrated Optics and Optical Fibre Communications. 23rd European Conference on Optical Communications (IOOC-ECOC 97)*, Edinburgh, UK, 65-68, 1997.

194. W. H. Press, B. P. Flannery, A .S. Teukolsky, and W. Vetterling, *Numerical Recipes*, Cambridge University Press, 2nd Edition, 1987.

195. A. Ezbiri, S. E. Kanellopoulos, and V. A. Handerek, "High resolution instrumentation system for fibre-Bragg grating aerospace sensors," *Opt. Commun.*, 150, 43-48, 1998.

196. R. B. Wagreich, W. A. Atia, H. Singh and J. S. Sirkis, "Effects of diametric load on fibre Bragg gratings fabricated in low birefringent fibre," *Electron. Lett.*, 32, 1223-1224, 1996.

197. I. Abe, H. J. Kalinowski, O. Frazão, J. L. Santos, R. N. Nogueira and J. L. Pinto, "Superimposed Bragg gratings in high-birefringence fibre optics: three-parameter simultaneous measurements," *Meas. Sci. Technol.*, 15, 1453-1457, 2004.

198. L. Zhang, Y. Liu, L. Everall, J. A. R. Williams and I. Bennion, "Design and realization of long-period grating devices in conventional and high birefringence fibers and their novel applications as fiber-optic load sensors," *IEEE J. Sel. Top. Quantum Electron.*, 5, 1373-1378, 1999.

199. X. Shu, K. Chisholm, I. Felmeri, K. Sugden, A. Gillooly, L. Zhang and I. Bennion, "Highly sensitive transverse load sensing with reversible sampled fiber Bragg gratings," *Appl. Phys. Lett.*, 83, 3003-3005, 2003.

200. M. Silva-López, W. N. MacPherson, C. Li, A. J. Moore, J. S. Barton, J. D. C. Jones, D. Zhao, L. Zhang and I. Bennion, "Transverse load and orientation measurement with multicore fiber Bragg gratings," *Appl. Opt.*, 44, 6890-6897, 2005.

201. N. Imoto, N. Yoshizawa, J. Sakai, and H. Tsuchiya, "Birefringence in single-mode optical fiber due to elliptical core deformation and stress anisotropy," *IEEE J. Quantum Electron.*, 16, 1267-1271, 1980.

202. K. Okamto, T. Hosaka, and T. Edahiro, "Stress analysis of optical fibers by a finite element method," *IEEE J. Quantum Electron.*, 17, 2123-2129, 1981.

203. P. D. Gianino and B. Bendow, "Calculations of stress-induced changes in the transverse

refractive-index profile of optical fibers," *Appl. Opt.*, 20, 430-434, 1981.

204. R. Gafsi and M. A. El-Sherif, "Analysis of induced birefringence effects on fiber Bragg gratings," *Opt. Fiber Technol.*, 6, 299-323, 2000.

205. R. A. Steinberg and T. G. Giallorenzi, "Performance limitation imposed on optical waveguide switches and modulator by polarization," *Appl. Opt.*, 15, 2440-2453, 1976.

206. Y. P. Wang and Y. J. Rao, "Long period fibre grating torsion sensor measuring twist rate and determining twist direction simultaneously," *Electron. Lett.*, 40, 164-166, 2004.

207. C. Y. Lin, L. A. Wang, and G. W. Chen, "Corrugated long-period fiber gratings as strain, torsion, and bending sensors," *J. Lightwave Technol.*, 19, 1159-1167, 2001.

208. S. Shen, A. Jha, X. Liu, M. Naftaly, K. Bindra, H. J. Bookey, and A. K. Kar, "Tellurite glasses for broadband amplifiers and integrated optics," *J. Am. Ceram. Soc.*, 85, 1391-1395, 2002.

209. T. Uemura, K. Nishida, M. Sakakida, K. Ichinose, S. Shimoda, and M. Shichiri, "Non-invasive blood glucose measurement by Fourier transform infrared spectroscopic analysis through the mucous membrane of the lip: application of a chalcogenide optical fiber system," *Frontiers Med. Biol. Eng.*, 9, 137-153, 1999.

210. J. Mulrooney, J. Clifford, C. Fitzpatrick, and E. Lewis, "Detection of carbon dioxide emissions from a diesel engine using a mid-infrared optical fibre based sensor," *Sens. Actuators A: Physical.*, 136, 104-110, 2007.

211. K. S. Bindra, H. T. Bookey, A. K. Kar, B. S. Wherrett, X. Liu, and A. Jha, "Nonlinear optical properties of chalcogenide glasses: Observaton of multiphoton absorption," *Appl. Phys. Lett.*, 79, 1939-1941, 2001.

212. A. Mori, H. Masuda, K. Shikano, and M. Shimizu, "Ultra-wide-band tellurite-based fiber Raman amplifier," *J. Lightwave Technol.*, 21, 1300-13106, 2003.

213. A. Céreyon, B. Champagnon, V. Martinez, L. Maksimov, O. Yanush, and V. N. Bogdanov, "xPbO-(1-x)GeO_2 glasses as potential materials for Raman amplification," *Opt. Mater.*, 28, 1301-1304, 2006.

214. G. M. H. Flockhart, W. N. MacPherson, J. S. Barton, J. D. C. Jones, L. Zhang, and I. Bennion, "Two-axis bend measurement with Bragg gratings in multicore optical fiber," *Opt. Lett.*, 28, 387-389, 2003.

215. P. Glas, M. Naumann, A. Schirmacher, and Th. Pertsch, "The multicore fiber - a novel design for a diode pumped fiber laser," *Opt. Commun.*, 151, 187-195, 1998.

216. X. Jiang, J. Lousteau, and A. Jha, "Raw materials purification for the development of high performance infrared transmitting germanate glass fibre," *Glass Technology: The European Journal of Glass Science & Technology Part A*, in press, 2008.

217. J. Lousteau, H. Bookey, X. Jiang, C. Hill, A. Kar, and A. Jha, "Fabrication of multicore tellurite glass optical fibres," *Proceedings of IEEE International Conference on Transparent Optical Networks, Institute of Electrical and Electronics Engineers*, Rome, Italy, 504-509, 2007.

218. H. T. Bookey, J. Lousteau, A. Jha, N. Gayraud, R. R. Thomson, N. D. Psaila, H. Li, W. N. MacPherson, J. S. Barton, and A. K. Kar, "Multiple rare earth emissions in a multicore tellurite fiber with a single pump wavelength," *Opt. Express*, **15**, 17554-17561, 2007.

219. D. Grobnic, C. W. Smelser, S. J. Mihailov and R. B. Walker, "Long-term thermal stability tests at 1000 °C of silica fibre Bragg gratings made with ultrafast laser radiation," *Meas. Sci. Technol.*, **17**, 1009-1013, 2006.

220. P. E. Dyer, R. J. Farley, and R. Giedl, "Analysis of grating formation with excimer laser irradiated phase masks," *Opt. Commun.*, **115**, 327-334, 1995.

221. N. M. Dragomir, C. Rollinson, S. A. Wade, A. J. Stevenson, S. F. Collins, G. W. Baxter, P. Farrell, and A. Roberts, "Nondestructive imaging of a type I optical fiber Bragg grating," *Opt. Lett.*, **28**, 789-791, 2003.

222. J. D. Mills, C. W. J. Hillman, B. H. Blott, and W. S. Brocklesby, "Imaging of Free-Space Interference Patterns Used to Manufacture Fiber Bragg Gratings," *Appl. Opt.*, **39**, 6128-6135, 2000.

223. D. Grobnic, C. W. Smelser, S. J. Mihailov, R. B. Walker, and P. Lu, "Fiber Bragg Gratings With Suppressed Cladding Modes Made in SMF-28 With a Femtosecond IR Laser and a Phase Mask," *IEEE Photon. Technol. Lett.*, **16**, 1864-1866, 2004.

224. X. Shu, K. Sugden, D. Zhao, F. Floreani, L. Zhang and I. Bennion, "Complex growth behaviour of hybrid-type fibre Bragg gratings," *Electron. Lett.*, **39**, 274-276, 2003.

225. S. S. Bayya, G. D. Chin, J. S. Sanghera, and I. D. Aggarwal, "Germanate glass as a window for high energy laser systems," *Opt. Express*, **14**, 11687-11693, 2006.

226. H. Li, J. Lousteau, W. N. MacPherson, X. Jiang, H. T. Bookey, J. S. Barton, A. Jha, and A. K. Kar, "Thermal sensitivity of tellurite and germinate optical fibers," *Opt. Express*, **15**, 8857-8863, 2007.

227. A. I. Rabukhin, "Concentration dependences of elastooptic coefficients of germanate glasses containing lead and bismuth oxides," *Glass and Ceramics.*, **37**, 87-90, 1995.

228. X. Fan, I. M. White, S. I. Shopova, H. Zhu, J. D. Suter and Y. Sun, "Sensitive optical biosensors for unlabeled targets: A review," *Analytica. Chimica. Acta.*, **620**, 8-26, 2008.

229. Y. J. Rao, "In-Fibre Bragg grating sensors," *Meas. Sci. Technol.*, **8**, 355-375, 1997.

230. X. Shu, L. Zhang and I. Bennion, "Sensitivity characteristics near the dispersion turning

points of long-period fiber gratings in B/Ge codoped fiber," *Opt. Lett.*, 26, 1755-1757, 2001.

Publications

Tilted Fibre Gratings:

1. R. Suo, X. Chen, K. Zhou, L. Zhang and I. Bennion, "In-fibre directional transverse loading sensor based on excessively tilted fibre Bragg gratings," *Meas. Sci. & Tech.*, 20, 034015, 2009.

2. R. Suo, X. Chen, K. Zhou, L. Zhang, and I. Bennion, "800nm WDM interrogation system for strain, temperature and refractive index sensing based on tilted fibre Bragg grating" *IEEE Sensors J*, 8, 1273-1279, 2008.

3. C. Mou, K. Zhou, R. Suo, L. Zhang, and I. Bennion, "Fibre laser torsion sensor system using an excessively tilted fibre grating and low-cost time domain demodulation," *20th International Conference on Optical Fibre Sensors (OFS-2009)*, Edinburgh, UK, 2009, accepted.

4. R. Suo, X. Chen, K. Zhou, L. Zhang and I. Bennion, "Polarisation mode coupling of excessively tilted fibre Bragg gratings with directional transverse loading," *19th International Conference on Optical Fibre Sensors (OFS-2008)*, Perth, Australia, 7004-176, 2008.

5. R. Suo, X. Chen, K. Zhou, L. Zhang, I. Bennion and B. Liu, "Tilted fibre Bragg grating based 800nm WDM interrogation system for strain, temperature and refractive index sensing," *Third European Workshop on Optical Fibre Sensors (EWOFS-2007)*, Napoli, Italy, 66192N, 2007.

6. K. Zhou, L. Zhang, X. Chen, R. Suo, and I. Bennion, "Implementation of optical fibre sensors with low thermal cross-sensitivity utilising ex-45° tilting grating structures", *18th International Conference on Optical Fibre Sensors (OFS-2006)*, Cancun, Mexico, TuD3, 2006.

7. X. Chen, K. Zhou, R. Suo, L. Zhang and I. Bennion, "In-fibre twist sensor based on TFBG structures," *18th International Conference on Optical Fibre Sensors (OFS-2006)*, Cancun, Mexico, TuE-29, 2006.

Femtosecond Laser Inscription in Mid-IR Glass Fibres:

8. R. Suo, J. Lousteau, H. Li, X. Jiang, K. Zhou, L. Zhang, W. N. MacPherson, H. T. Bookey, J. S. Barton, A. K. Kar, A. Jha, and I. Bennion, "Fiber Bragg gratings inscribed using 800nm femtosecond laser and a phase mask in singleand multi-core mid-IR glass fibers," *Opt. Express.*, 17, 7540-7548, 2009.

9. R. Suo, J. Lousteau, H. Li, X. Jiang, K. Zhou, L. Zhang, H. Bookey, W. MacPherson, J.

Barton, A. Kar, A. Jha and I. Bennion, "Fiber Bragg grating structures inscribed using 800nm femtosecond laser in single- and multi-core mid-IR glass fibers with their spectral, thermal and strain properties," *International Conference on Materials for Advanced Technologies (ICMAT) 09: Symposium P*, Singapore, P-S10.9, 2009.

10. H. Li, J. Lousteau, R. Suo, X. Jiang, W. N. MacPherson, H. T. Bookey, J. S. Barton, A. K. Kar, L. Zhang, A. Jha, and I. Bennion, "Sensing properties of germanate and tellurite glass optical fibres," *20th International Conference on Optical Fibre Sensors (OFS-2009)*, accepted.
11. R. Suo, Y. Lai, K. Zhou, L. Zhang, I. Bennion, X. Jiang, J. Lousteau and A. Jha, "Long-period gratings in near-single-mode GeO_2 glass fiber by IR femtosecond laser inscription," *Bragg Gratings, Photosensitivity and Poling in Glass Waveguides (BGPP-2007)*, Quebec, Canada, BWB5, 2007.

12. R. Suo, Y. Lai, K. Zhou, L. Zhang, I. Bennion, X. Jiang, J. Lousteau and A. Jha, "Fibre gratings in GeO_2 glass fiber by IR femtosecond laser inscription," *PHOTONEX-2007, Institute of Physics*, Coventry, UK, 2007.

Other Publications:

13. A. Fender, W. N. MacPherson, R. R. J. Maier, J. S. Barton, D. S. George, R. I. Howden, G. W. Smith, B. J. S. Jones, S. McCulloch, X. Chen, R. Suo, L. Zhang, and I. Bennion, "Two-Axis Temperature-Insensitive Accelerometer Based on Multicore Fiber Bragg Gratings," *IEEE Sensors J.*, 8, 1292-1298, 2008.

14. A. Fender, W. N. MacPherson, R. R. J. Maier, J. S. Barton, J. D. C. Jones, K. S. Ellis, C. L. Leppard, P. G. Blackwell, J. R. Miller, B. J. S. Jones, S. McCulloch, X. Chen, R. Suo, and L. Zhang, "Radial deformation measurement of a cylinder under compression using multicore fibre," *19th International Conference on Optical Fibre Sensors (OFS-2008)*, Perth, Australia, 7004-88, 2008.

15. A. Fender, W. N. MacPherson, R. R. J. Maier, J. S. Barton, D. S. George, R. I. Howden, G. W. Smith, B. J. S. Jones, S. McCulloch, X. Chen, R. Suo, L. Zhang, and I. Bennion, "Two-axis accelerometer based on multicore fibre Bragg gratings," *Third European Workshop on Optical Fibre Sensors (EWOFS-2007)*, 66190Q, Napoli, Italy, 2007.

16. X. Chen, C. Zhang, D. J. Webb, R. Suo, G. D. Peng, and K. Kalli, "Optical bend sensor for vector curvature measurement based on Bragg grating in eccentric core polymer optical fibre", *20th International Conference on Optical Fibre Sensors (OFS-2009)*, Edinburgh, UK, 2009. Accepted.

17. H. Fu, X. Shu, R. Suo, L. Zhang, S. He, and I. Bennion, "Transversal-load sensor by using local pressure on a chirped fiber Bragg grating" accepted by *IEEE Sensors J.*